Developing Plasma Spectroscopy and Imaging Diagnostics to Understand Astrophysically-Relevant Plasma Experiments: Megameters, Femtometers, and Everything in Between

Thesis by

Ryan S. Marshall

In Partial Fulfillment of the Requirements for the
Degree of
Doctor of Philosophy

CALIFORNIA INSTITUTE OF TECHNOLOGY
Pasadena, California

2020
Defended April 16, 2020

Ryan S. Marshall
ORCID: 0000-0003-0429-3923

ACKNOWLEDGEMENTS

There are many people that I would like to thank for their contributions throughout the past six years and beyond.

First, I would like to thank my candidacy committee, Professors Kerry Vahala, Kieth Schwab, Fiona Harrison, and Paul Bellan, and my thesis committee, Professors Kerry Vahala, Geoff Blake, Fiona Harrison, and Paul Bellan. I appreciate the feedback that you have given me and the insightful questions posed.

I would like to thank Christy Jenstad and Jennifer Blankenship for everything they do for Applied Physics. I could always count on them when I needed an afternoon piece of candy. I cannot thank Connie Rodriguez enough for maintaining the group finances. Whether it was my complicated travel reports or the 130+ purchase invoices that I sent her over almost six years (I counted), she always made sure things got handled correctly.

I would also like to thank the resident electrical engineer Dave Felt. Dave is an extremely capable engineer who has built some amazing electronics for the lab.

I am also grateful to each and every one of my Bellan group labmates. I am very lucky to have joined the lab while Bao Ha, Xiang Zhai, and Vernon Chaplin were the senior graduate students. Thank you for all the hours you took while wrapping up your degrees and working on your theses to make sure the next generation of students could continue where you left off. Your knowledge fast-tracked my generation. Now to my junior labmates. Andre Nicolov, I am extremely jealous of the next generation dusty plasma experiment that you get to work on. Yang Zhang, although we sat in different offices, I am glad that we got to do some experiments together on the solar experiment. Yi Zhou, the future of the X-ray research is in great hands with you. I will miss your random questions. Finally, Young Dae Yoon and Pakorn Wongwaitayakornkul and I have overlapped during our Ph.D's from start to finish. From being junior graduate students and taking classes to traveling to conferences and becoming senior graduate students together, it has been a great six years. I look forward to hearing about all the great things you do next.

I am very fortunate to have worked with three very capable post doctoral researchers during my time in the Bellan Lab. I enjoyed working with Byonghoon Seo on the jet experiment. Byonghoon built some awesome diagnostics for the lab. I am fortunate to have had the opportunity to work with now-professor Amelia Greig on the jet as well. I won't ever forget the taste of vegemite. Finally, I could not have completed my Ph.D. without Kil-Byoung (KB) Chai, the man who built the dusty plasma experiment and worked closely with me on both the dusty plasma experiment and jet experiments. I learned an enormous amount from him, my biggest mentor besides Paul and I appreciate all the time he spent with me while he was a post-doc here. Even after he moved back to South Korea, I could still count on KB to answer questions about the dusty plasma experiment as they came up.

Finally Professor Paul M. Bellan. I could not have picked a better advisor if I tried. His kindness, patience, and enthusiasm for laboratory plasma physics are unmatched. Paul possesses the extremely unique quality of being willing to stop whatever he is working on to assist when any one of his 4-7 graduate students knock on his door. Rather than groaning, Paul is often excited to drop whatever more important thing he is working on to come into the lab and get his hands dirty with some hardware –whether it is trying to isolate a noise source in a signal or the conundrum of a slightly leaking vacuum chamber. I don't know how he gets anything done, yet he still finds time to publish papers on his own. On top of all this, Paul is extremely generous when it comes to sending his students to conferences. I have had the good fortune of being able to present my research and learn from experts at a dozen conferences during my time in his lab.

I would also like to give a special shout out to shipping and receiving and the campus post office. You guys signed for and shipped out hundreds of packages for me.

Figure 0.1: Family photo. Mom, dad, grandma, and grandpa braving the 90°F Pasadena summer sun to celebrate two children/grandchildren getting their master's degrees together in 2017.

I would like to thank my parents, Heather and Don Marshall, who always encouraged me to pursue science. My mom always thought I would be a mathematics major in college, clearly I showed her! They always made sure that I was in appropriately challenging classes growing up and took action when I was clearly bored in class. I know I can always count on them whenever I need anything. Not many parents can say that they have a single child who is a graduate student at Caltech, but they can say that they have **two** children who are both getting their Ph.D's at Caltech. The xomrad, my brother Michael Marshall, is a fellow Ph.D. student in the Aerospace Engineering department. I never thought we would go to the same school at the same time again, but it just goes to show that you never know what is going to happen. I'm very glad that you joined me here at Caltech. It's nice to always have someone around that I can see and bother. I know you will do great finishing your Ph.D.

Finally my grandparents, Anne and Murray Pasternack. No matter where my parents moved us, I could always count on grandma and grandpa to live within a roughly 5 mile radius of 33.483289 N latitude, 117.662084 W longitude. It goes without say that without you both (and my parents too), none of my successes would have been possible. I am forever grateful to have had over 27 years with both of you. Grandma and grandpa always made sure I had everything I needed, and some stuff I didn't need like the GameBoy and Pokemon Blue version that my parents wouldn't let me get. I know it's been an incredibly difficult year for us, especially grandpa. It came as a huge shock to learn that grandma would not be here with us to celebrate my Ph.D. But I know she's somewhere up there looking down, cheering, and bragging to everyone she knows.

I would also like to thank the generous funding of i) the U.S. Department of Energy Office of Science, Office of Fusion Energy Science, ii) Air Force Office of Scientific Research, and iii) NASA/NSF Partnership on the Sciences of Dusty Plasmas. Without these funding sources, the research in this thesis would not have been possible. And thus I want to thank every American taxpayer for funding this research.

ABSTRACT

One of the main attractions of using laboratory experiments as a proxy to study solar and astrophysical plasmas is the ability to build diagnostics that directly measure things. This cannot be done on actual solar and astrophysical plasmas as they are either i) extremely distant, ii) in an extreme environment, or iii) both. Fortunately, the lack of intrinsic scales in the MHD equations means that a plasma created in the laboratory with similar β, S, and magnetic topology will evolve similarly to its astrophysical analogs. Thus the use of diagnostics in the laboratory to understand the evolution of laboratory plasmas can assist in understanding complicated astrophysical plasma dynamics.

This thesis is broken up into three main areas. The first is about the development of and results from two new custom X-ray scintillator detectors and a CMOS camera repurposed into an X-ray spectrometer mounted on the Caltech Astrophysical Jet Experiment. Next, water-ice grain growth in a cold dusty plasma is quantified by analyzing the frames in a movie recorded by an ultra-high-speed camera. Finally, the development of and results from a custom, motorized Laser-Induced Fluorescence diagnostic that measures the temperature and flow speed of neutral argon atoms in the dusty plasma experiment are presented.

Two custom-built X-ray scintillator detectors mounted on the jet experiment detect a burst of hard X-rays establishing that this burst occurs simultaneously with a fast magnetic reconnection event taking place in the $T = 2$ eV plasma. A repurposed windowless CMOS camera acting as an X-ray spectrometer confirms the burst consists of non-mono-energetic photons around 6 keV energy. This magnetic reconnection event is triggered after the jet undergoes an ideal MHD kink instability which accelerates the jet laterally inducing a fast-growing secondary Rayleigh-Taylor instability. The Rayleigh-Taylor instability causes the ideal MHD treatment of the jet to be violated when it pinches the jet diameter past c/ω_{pi} causing it to break apart. As it breaks apart, a burst of hard X-rays are detected. These findings lead to the conclusion that an inductive electric field arises at the location of the reconnection event that accelerates a small fraction of electrons to keV energy despite the plasma being so collisional that acceleration is unexpected. This theory leads to the hypothesis that the fine structure of solar prominences consists of many Litz-wire like strands of plasma each on the order of a few ion skin depths in diameter, as opposed to the traditional picture of one monolithic arch.

Analysis of a high-speed video of ice grains growing from 20 to 80 μm inside the dusty plasma experiment leads to the conclusion that the charged ice grains in the experiment grow via accretion of water molecules. The video challenges the common astrophysical assumption that the dusts in dusty plasmas are spherical as they are clearly seen to be elongated, fractal structures in the movie. Another commonly made assumption is that the grains grow via agglomerating collisions and that this results in the grains having a power law dependence on radius. Video of the grains in the Caltech experiment shows a log-normal dependence and absolutely no evidence of agglomerating collisions; or even a case of two grains approaching with a large relative velocity, and then scattering. It is believed that the grains have a large negative charge resulting in strong mutual repulsion and this, combined with their nearly non-existent relative velocities due to undergoing oscillatory motion by a relatively coherent wave, prevents them from agglomerating. This combined with a detailed study of Coulomb repulsion between the grains leads to the conclusion that direct accretion of water molecules is likely the dominant contribution to the observed ice grain growth.

Lastly, a Laser-Induced Fluorescence diagnostic has been developed for the dusty plasma experiment. Whereas the first two projects rely on passive detection instruments, the LIF diagnostic actively uses a pump beam to excite atoms in the plasma, and then detects the resulting emission. The diagnostic is motorized and automated with Labview so that the plasma volume can be scanned in three dimensions. Argon neutral temperature is measured to be slightly above room temperature on the Caltech experiment and the PK4 experimental setup at Baylor University. Challenges such as the lack of absolute calibration of diode lasers and wavelength drift due to slight changes in ambient room conditions are overcome to measure sub-linewidth bulk neutral flow speeds on the order of 1-2 m/s with resolution on the order of 2/3 of a meter per second. The competing influences of a density gradient and wavelength dependent absorption broadening mechanism are separated and quantified. High-speed video shows that introducing an argon flow to a cloud of ice grains causes the cloud of ice grains to move and change shape. This motion is analyzed and found to show agreement with neutral LIF flow measurements. Surprisingly, when the flow ceases, the ice grain cloud reverts to its original location and shape.

PUBLISHED CONTENT AND CONTRIBUTIONS

[1] Ryan S. Marshall, Michael J. Flynn, and Paul M. Bellan. "Hard X-ray bursts observed in association with Rayleigh-Taylor instigated current disruption in a solar-relevant lab experiment". In: *Physics of Plasmas* 25.11 (2018), p. 112101. DOI: https://doi.org/10.1063/1.5054927.
R.S.M. designed and built D_{ext} and D_{int}. R.S.M. worked on D_{CMOS} with M.J.F. R.S.M. prepared the data, analyzed the data, and wrote the manuscript.

[2] Ryan S. Marshall and Paul M. Bellan. "Acceleration of charged particles to extremely large energies by a sub-Dreicer electric field". In: *Physics of Plasmas* 26.4 (2019). DOI: https://doi.org/10.1063/1.5081716.
R.S.M. developed the acceleration model with P.M.B. R.S.M. prepared the figures and wrote the manuscript.

[3] Ryan S. Marshall, Kil-Byoung Chai, and Paul M. Bellan. "Identification of accretion as grain growth mechanism in astrophysically relevant water-ice dusty plasma experiment". In: *Astrophysical Journal* 837.1 (2017). DOI: https://doi.org/10.3847/1538-4357/aa5d11.
R.S.M. and K.B. Chai analyzed the 40,000 images separately and compared results to ensure accuracy. R.S.M. helped with preparing data and assisted in writing the manuscript with K.B. Chai.

[4] Byonghoon Seo, Pakorn Wongwaitayakornkul, Magnus A. Haw, Ryan S. Marshall, Hui Li, and Paul M. Bellan. "Determination of a macro- to micro-scale progression leading to a magnetized plasma disruption". In: *Physics of Plasmas* 27.2 (2020). DOI: https://doi.org/10.1063/1.5140348.
R.S.M. built the X-ray detector (D_{int}) and helped B.H.S. to learn how to operate it.

[5] Ryan S. Marshall and Paul M. Bellan. "Laser-induced fluorescence measurement of very slow neutral flows in a dusty plasma experiment". In: *Review of Scientific Instruments* 91.6 (2020). DOI: https://doi.org/10.1063/5.0006684.
R.S.M. designed and built the LIF diagnostic. R.S.M. wrote the Labview program to automate data collection and incorporated motorization. R.S.M. prepared the data, analyzed the data, and wrote the manuscript.

TABLE OF CONTENTS

LIST OF ILLUSTRATIONS

LIST OF TABLES

Number *Page*

Chapter 1

INTRODUCTION

This thesis presents exciting results from both the Caltech Astrophysical Jet Experiment (often referred to as the *jet experiment*) and the Caltech Water-Ice Dusty Plasma Experiment (often referred to as the *dusty plasma experiment*). The development of novel spectroscopy and imaging diagnostics on both of these experiments serves as the foundation of this thesis.

Chapter 1 is an introduction to the thesis. After a brief introduction to plasma itself, Ch. 1 transitions to a discussion of the current state of research regarding the astrophysical analogs of the jet and the dusty plasma experiments. Subsequently, Ch. 1 establishes the crucial bridge between astrophysically-relevant laboratory plasmas and the astrophysical plasmas they emulate: the dimensionless nature of the magnetohydrodynamic (MHD) equations. The introduction concludes by showcasing the similarities between the Caltech jet experiment and solar prominences. Appendix A contains a mathematical foundation of plasma physics leading up to the origin of the dimensionless nature of the MHD equations.

Following this introduction, the first half of this thesis focuses on MHD-driven flux-rope plasmas. Examples of these plasmas in nature include solar prominences seen arching out of the sun and jets seen shooting out of young stellar objects (YSO) and galactic nuclei (AGN). Chapter 2 contains an introduction to the Caltech Astrophysical Jet Experiment apparatus. Chapter 3 highlights a few important previous results from the nearly 20-year operation of the experiment and then jumps straight into my work detecting X-ray emission from the jet. Chapter 4 presents an original theory that plausibly explains the X-ray observation seen in Ch. 3. The jet portion of the thesis concludes with Ch. 5 which utilizes the dimensionless nature of the MHD equations to make a hypothesis about the fine structure of solar prominences based on the experimental observation in Ch. 3 and proposed acceleration mechanism in Ch. 4. Appendix C contains a detailed look at the construction of the most technical X-ray detector built for this project.

The second half of this thesis transitions to an investigation of cold water-ice dusty plasmas like the ones in noctilucent clouds and Saturn's E-ring. Chapter 6 begins with an introduction to the Caltech Water-Ice Dusty Plasma Experiment apparatus. Chapter 7 investigates the growth of micron-size water-ice grains in the dusty plasma experiment via analysis of an ultra high-speed movie. Chapter 8 presents temperature and flow velocity measurements made on the argon neutral species in room-temperature dust-free and astrophysically-relevant water-ice dusty plasma using a custom-built Tuneable-Diode Laser Induced Fluorescence (TD-LIF) diagnostic. Appendix D contains a detailed look at the hardware developed for LIF.

1.1 Plasmas

A plasma is an ionized gas consisting of electrons, ions, and neutral atoms interacting with each other. The key condition for this group of particles to be considered a plasma is that there must be enough of them such that each species can be treated statistically. This condition is quantified in Appendix A. Irving Langmuir, a 1920's era pioneer of this fledgling field, named this collections of electrons and ions a *plasma* after the blood plasma which is the liquid that holds everything in the blood in suspension. Although there is no actual fluid medium that holds the electrons, ions, and neutrals in suspension, the name stuck and plasma physics was born in 1922 [1].

Microscopically, the electrically neutral atoms that constitute material in the solid, liquid, or gas state interact directly via collisions. On the other hand, plasmas contain electrically charged species and motion at the microscopic level is primarily determined by long-range electric and magnetic fields that would have little to no effect on a solid, liquid, or gas.

The three most important parameters for distinguishing plasmas are number density n, temperature T, and magnetic field $\mathbf{B}$ where the bold-face font denotes a vector quantity. The flavors of plasmas found in industrial settings, in research laboratories, and in nature[1] cover an enormous set in the three parameter $(n, T, \mathbf{B})$-space. Figure 1.1 samples a taste of these endless possibilities. The two bold asterisks superimposed on Fig. 1.1 represent where the Caltech Astrophysical Jet Experiment (red) and Caltech Water-Ice Dusty Plasma Experiment (blue) compare to many other commonly occurring scientific and natural plasmas. To build on these three parameters, the dusty plasma introduces a whole new dimension of flavors with the introduction of a much larger fourth species immersed in the plasma called the *dust species*. The different flavors of plasmas are endless and if you can dream it, it probably exists somewhere in the universe.

[1] where nature means either terrestrially on Earth or elsewhere in the solar system or universe

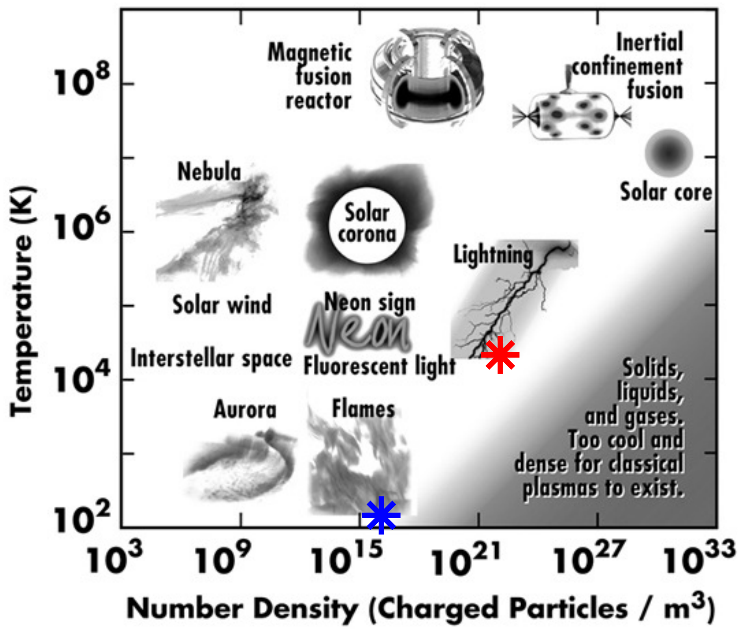

Figure 1.1: Logarithmic chart that shows where many commonly occurring scientific and natural plasmas sit relative to each other based on their number density n and temperature T. Copyright Contemporary Physics Education Project www.CPEPphysics.org, used with permission.

1.2 Astrophysical Plasmas

This thesis draws frequent connection to the astrophysical plasmas that our laboratory experiments are relevant to: MHD-driven braided flux-rope plasmas and weakly ionized cold water-ice dusty plasmas like the ones shown in Figs. 1.2 and 1.3, respectively.

Flux-Rope Plasmas

Figure 1.2 shows three plasma structures spanning many different length scales and lifetimes that the jet experiment is relevant to. Figure 1.2(a) shows the relativistic AGN jet from the supermassive 2.5×10^9 $M_\odot$ black hole (where $M_\odot = 1.99 \times 10^{30}$ kg, the mass of the sun) at the center of the Hercules A galaxy located ~ 2 billion light years from Earth by superimposing visible and radio wavelength images from the Hubble Space Telescope's Wide Field Camera 3 and Karl G. Jansky Very Large Array radio telescope, respectively. The impressive optically invisible jet structure seen in the radio image shooting out of the bright optically yellow galaxy in the center is ~ 1.5 million light years (~ 10^{22} m) long. Figure 1.2(b) shows images of the classical YSO jet associated with the young star HH30 taken by Hubble Space Telescope's Wide Field and Planetary Camera 2 over a five-year period between 1995 and 2000. The images show the 400 AU (~ 10^{14} m) long jet shooting out of the 450 AU diameter disk. The jet has a speed between 1.6×10^5 and 9×10^5 km/hr. There is another jet below the disk not pictured in the images. The pictured jets differ in length scale by approximately eight orders of magnitude, but it is hypothesized that the fundamental mechanism that drives them is the same, barring relativistic effects in the case of the AGN jet. One peculiarity of these astrophysical jets is that they produce high energy super-thermal particles and energetic photons [2, 3].

At first glance, the megameter-size solar prominence shown in Fig. 1.2(c) looks like it might have little in common with the jet structures in Figs. 1.2(a) and (b). However, focusing on one of the bases of the solar prominence in the region accented by the black box in Fig. 1.2(c), the system would closely resemble the jets shown in Figs. 1.2(a) and (b): a collimated, twisted flux-rope. Solar prominences are often stable for weeks or months and suddenly undergo fast eruptions that shoot huge amounts of material into space called coronal mass ejections. These transient, localized eruptions are regularly accompanied by solar flares: bright bursts of high-energy radiation and super-thermal charged particles emitted from near the surface of the sun. The particular prominence pictured in Fig. 1.2(c) produced both a coronal mass ejection and M1 class solar flare during its April 16, 2012 eruption. Solar flares produce electrons with energies up to 10^8 eV and ions up to 10^9 eV even though the corona is only 10^2 eV or less [4–8].

Acceleration of charged particles to energies orders of magnitude larger than the ambient thermal energy is a well-documented but mysterious feature of not only solar and astrophysical plasmas like the ones pictured in Fig. 1.2, but also of many laboratory plasmas. Laboratory observations are numerous starting with the 1950's observation in the ZETA device of neutrons [9] initially interpreted as the by-product of thermonuclear fusion reactions. However, doubt was quickly cast over this interpretation as the ZETA plasma was shown to be only 10-10^2 eV, much colder than the required 10^4 eV temperature for thermonuclear fusion [10–13]. More recent laboratory examples include dense plasma focus devices which use a transient magnetized plasma to produce small quantities of neutrons [14, 15] presumably by the same mechanism that occurred in ZETA. A transient burst of X-rays was observed

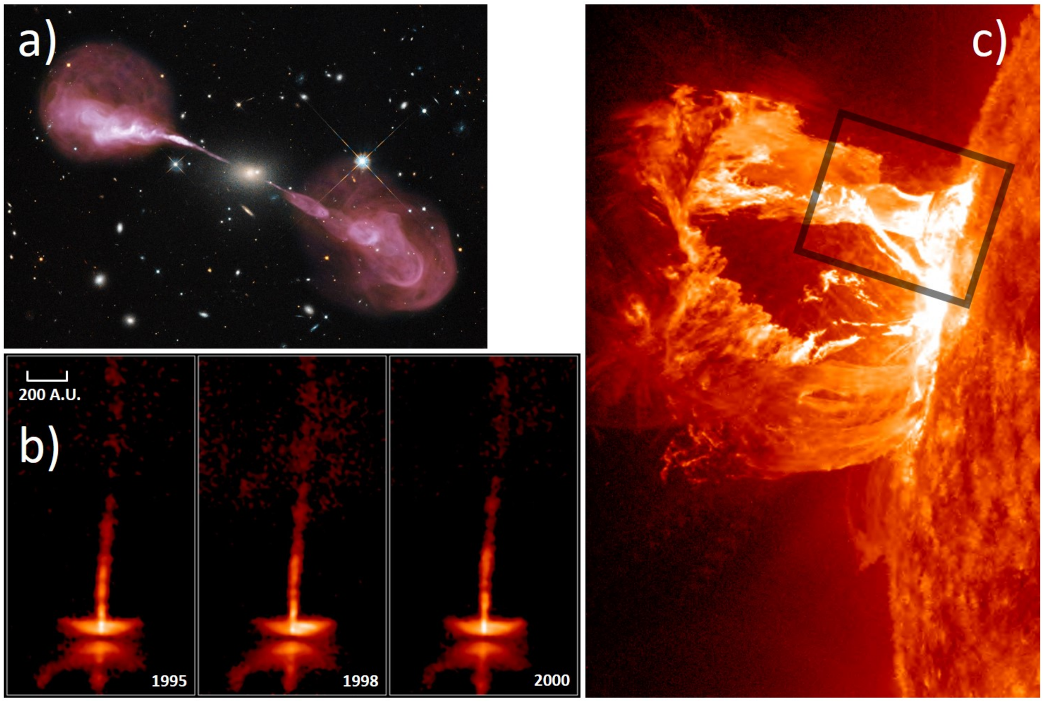

Figure 1.2: Braided flux-rope plasmas in nature. a) Superimposed visible and radio image of Hercules A galaxy. b) Images of the HH30 young stellar object jet taken between 1995 and 2000. (a) and (b) from www.hubblesite.org, News Release numbers STScI-2012-47 and STScI-2000-32, respectively. c) A solar prominence eruption captured by NASA's Solar Dynamics Observatory in the 304 Angstrom wavelength. Credit: NASA/SDO/AIA.

in association with spheromak formation and was believed to be associated with the pinching off of the plasma from the gun electrodes [16]. Other magnetic confinement devices such as tokamaks produce super-thermal particles as well [17]. Recently, a hard X-ray burst has been observed on the Caltech Astrophysical Jet Experiment [18].

The common factors in these very different laboratory and astrophysical regimes are that (i) charged particles are accelerated to energies orders of magnitude larger than thermal, (ii) the process is transient, (iii) magnetic fields and electric currents are involved, and (iv) there appears to be some sort of instability. Mechanisms such as runaway ions in small regions [19], creation of a deuterium beam [11], wave-particle resonance [5], stochastic motion [8], and Fermi acceleration [20] were previously proposed, but magnetic reconnection is now thought to play a crucial role [21–23]. Since the accelerated particles are significantly more energetic than the thermal particles, the energy reservoir powering this acceleration is unlikely to come from the thermal particles and instead is presumed to come from the energy stored in the magnetic field being released through magnetic reconnection.

It is not known exactly how magnetic reconnection accelerates charged particles to super-thermal energy. Key questions such as i) why only a subset of particles are energized, ii) how this subset is selected, and iii) why this subset can be accelerated in an extremely collisional plasma all remain unanswered. The fundamental nature of these questions and the difficulty of studying these plasmas in their natural environments make super-thermal particle acceleration ripe for laboratory investigation. In fact, there are many magnetic reconnection experiments being performed in laboratories across the United States and the world including TREX at the University of Wisconsin [24], MRX at Princeton University [25], and MAGPIE at Imperial College [26]. Due to its magnetic topology and physical properties such as ion skin depth, the MHD-driven jet created here at Caltech with its cascade of instabilities provides a fascinating perspective on the acceleration of super-thermal particles.

Dusty Plasmas

Figure 1.3 shows four photographs of very weakly ionized water-ice dusty plasmas in nature. Figure 1.3(a) shows a photograph of a noctilucent cloud which consists of tiny water-ice grains [27]. Figure 1.3(b) shows Saturn's moon Enceladus which is an exciting area of study. Enceladus has a geyser-like structure at its south pole that continuously ejects frozen water-ice grains into Saturn's E-ring, shown in Fig. 1.3(c). The bright spot in the middle of the ring is the moon Enceladus. Figure 1.3(d) is a radio telescope image of the protoplanetary disk surrounding the star HL Tauri. Protoplanetary disks and molecular clouds are comprised of very weakly ionized plasma with dusts including water-ice grains [28].

The mechanism for grain growth in astrophysical dusty plasma is an active area of study. The water-ice grains in noctilucent clouds are presumed to nucleate on meteorite smoke particles and grow by accreting water molecules [29], but direct observation of the growth process has not been observed. Rocket-borne detectors have measured the water-ice grain size to be a few tens of nm and the charge to be about one electron [27].

Ice grains in Saturn's E-ring are presumed to grow because water molecules and small water-ice grains are continuously ejected from the south pole of Enceladus [30]. There is no other obvious local water source in the E-ring. The Cassini spacecraft Plasma Spectrometer (CAPS) and Cosmic Dust Analyzer (CDA) measured

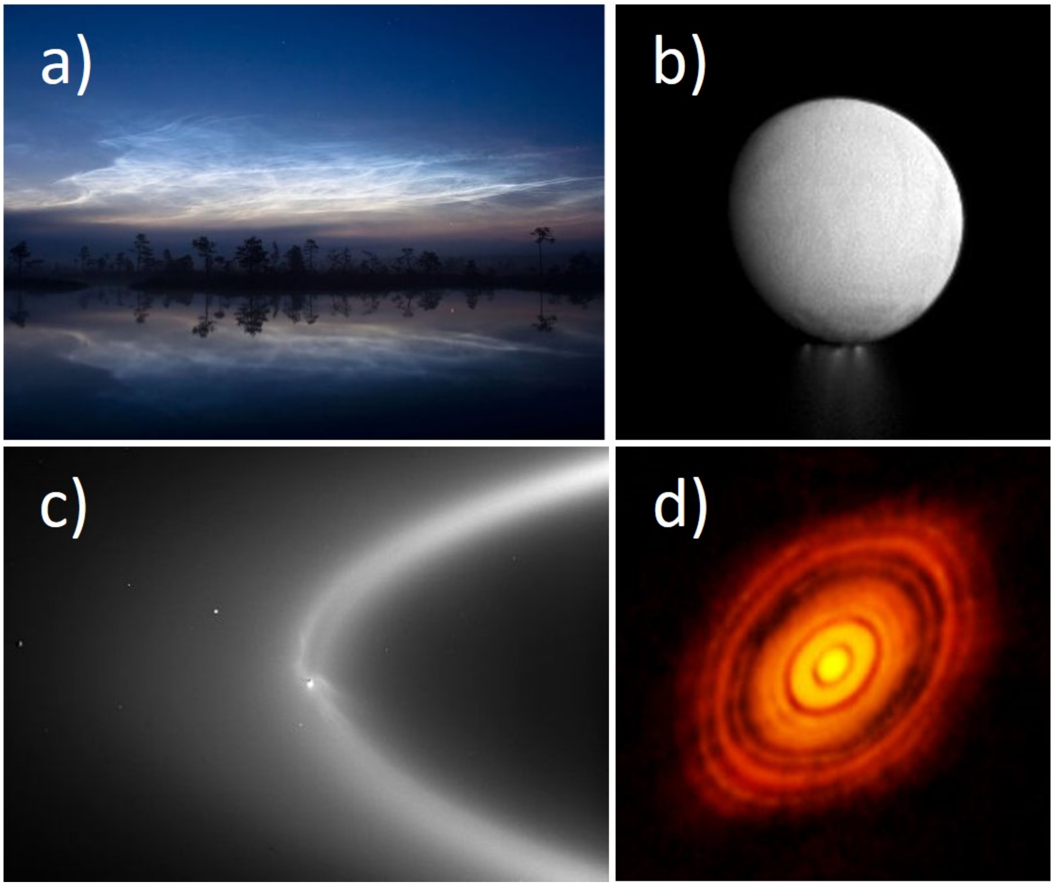

Figure 1.3: Dusty plasmas in nature. a) Noctilucent clouds over Kuresoo Bog, Soomaa National Park, Estonia. Credit: Martin Koitmäe https://commons.wikimedia.org/w/index.php?curid=10752455. b) Image of Enceladus taken by the Cassini Spacecraft on September 23, 2013 in the near infared. c) Image of Saturn's E-ring with Enceladus inside it from about 15 degrees above the ringplane approximately 2.1 million km from Enceladus taken by Cassini Spacecraft on September 15, 2006. (b) and (c) Credit: NASA/JPL/Space Science Institute. d) Image of protoplanetary disk around the young star HL Tauri taken by the Atacama Large Millimeter Array in Chile. Credit: ALMA: ESO/NAOJ/NRAO; A. Isella; B. Saxton NRAO/AUI/NSF.

the size, speed, and charges of ice grains in Saturn's E-ring and Enceladus plume. These measurements indicate that the size of ice grains is $< 10\ \mu$m and that most ice grains are negatively charged while a few are positively charged [31–33]. Once again, direct observation of grain growth is not available.

Planetesimal formation in protoplanetary disks is an entirely different matter. Rather than growth saturating in the nanometer or micron-size regime, planetesimal formation ends with an object that is megameter-sized. On the way from the nanometer-size regime to the megameter-size regime, the dusts must pass through the micron-size regime. Unsurprisingly, the ice grain growth process in protoplanetary disks and molecular clouds is also difficult to observe directly. These structures are extremely distant and presumably have a growth time much longer than the human scale. Indirect, survey-type telescope measurements of multi-wavelength emissions ranging from μm to mm are typically used to estimate the growth process of dusts including ice grains [34–36]. An observed spectral energy distribution (SED) is fitted in these estimates to a standard dust emission model to obtain the maximum or mean size of dusts; these estimates assume that dust grains are spherical and the dust density has a power-law dependence on the radius [2]. The ice grain growth is then deduced by sorting the observed data as a function of the disk age or the evolution stage. Based on the constraints from multi-wavelength observations and laboratory experiments (with non-ice dusts and non-plasma environments) [37–39], several models have been developed to explain planetesimal formation [40–42]. The process which has been proposed is that ice grains are heterogeneously nucleated on refractory materials [43] and that they quickly grow to mm or cm size in the outer disk regions [34, 35, 44].

The lack of actual observation of water-ice grain growth in astrophysical dusty plasma environments makes this another area ripe for laboratory study. Baylor University [45] and Auburn University [46] both operate dusty plasma experiments where the dust grains are prefabricated micron-size plastic spheres. Other experiments in Europe have studied the dust growth process using reactive gases [47–49]. There is even an experiment aboard the International Space Station called Plasmakristall-4 (PK4) that performs dusty plasma experiments in microgravity [50]. The Caltech Water-Ice Dusty Plasma Experiment is unique among its peers because it grows water-ice dust grains by injecting water vapor directly into the plasma where the water vapor freezes into ice grains. The Caltech experiment was designed to be an upgraded version of the apparatus used by Shimizu *et al.* [51].

1.3 Scaling Laws

The common factors in the plasma structures shown in Figs. 1.2 and 1.3 are that they are (i) extremely distant from earth, (ii) in an extreme environment, or (iii) both. These complications make in-situ study extremely challenging or impossible. As such, experimental physicists design and operate machines that create relevant

[2] Results from the Caltech Water-Ice Dusty Plasma Experiment will be presented in this thesis to challenge both of these assumptions.

plasmas in the laboratory to better understand their astrophysical counterparts. The fundamental reason why physicists can do this is because the MHD equations have no intrinsic length scale. The resistive MHD equations can be written in dimensionless form[3] as

$$\bar{\rho}\left(\frac{\partial \bar{\mathbf{U}}}{\partial \bar{t}} + \bar{\mathbf{U}} \cdot \bar{\nabla}\bar{\mathbf{U}}\right) = \left(\bar{\nabla} \times \bar{\mathbf{B}}\right) \times \bar{\mathbf{B}} - \beta\bar{\nabla}\bar{P} \tag{1.1}$$

$$\frac{\partial \bar{\mathbf{B}}}{\partial \bar{t}} = \bar{\nabla} \times \left(\bar{\mathbf{U}} \times \bar{\mathbf{B}}\right) + \frac{1}{S}\bar{\nabla}^2\bar{\mathbf{B}} \tag{1.2}$$

$$\frac{\partial \bar{\rho}}{\partial \bar{t}} + \bar{\nabla} \cdot \left(\bar{\rho}\bar{\mathbf{U}}\right) = 0 \tag{1.3}$$

$$\left(\frac{\partial}{\partial \bar{t}} + \bar{U} \cdot \bar{\nabla}\right)\left(\bar{P}\bar{\rho}^{-\gamma}\right) = 0 \tag{1.4}$$

where $\beta = \mu_0 P_0/B_0^2$ and $S = \frac{\mu_0 l v_A}{\eta}$. Here, a reference magnetic field B_0, a reference density ρ_0, and a reference length l have been prescribed. From these, a reference Alfvén velocity $v_{A0} = B_0/\sqrt{\mu_0\rho_0}$ and a reference time $\tau = l/v_{A0}$ are defined. The various dimensionless quantities (barred variables) then relate to the original variables by

$$\bar{\rho} = \frac{\rho}{\rho_0}, \bar{\mathbf{B}} = \frac{\mathbf{B}}{B_0}, \bar{\mathbf{U}} = \frac{\mathbf{U}}{v_{A0}}, \bar{\mathbf{x}} = \frac{\mathbf{x}}{l}, \bar{t} = \frac{t}{\tau}, \bar{\nabla} = l\nabla,\ \bar{P} = \frac{P}{P_0}. \tag{1.5}$$

β and S are two important dimensionless quantities that show up in the dimensionless resistive MHD equations. β is called the plasma "beta" and S is called the Lundquist Number. β is the ratio of the pressure forces to the magnetic forces. A low-β plasma, or $\beta << 1$, is a plasma where the magnetic forces dominate the pressure forces. S is effectively a measure of how "frozen-in" the magnetic flux is to the plasma. That is to say, S is a measure of how true it is that the plasma and its magnetic field lines convect together. Astrophysical plasmas have very large Lundquist Numbers because l is enormous and this makes ideal MHD a good approximation for them. Although S is not as large as in the astrophysical cases, S is large enough to make the same $S >> 1$ ideal MHD approximation in the Caltech jet experiment.

Ryutov *et al*. [52] showed that the scaling of two different ideal MHD plasmas can be expressed in terms of just three ratios if the two plasmas have the same β, S, and

[3] Appendix A shows where these equations come from.

similar boundary conditions. On scaling a lab plasma to a solar plasma these three parameters are

$$c_1 = \frac{l_{lab}}{l_{solar}}, \ c_2 = \frac{\rho_{0lab}}{\rho_{0solar}}, \ \ c_3 = \frac{P_{0lab}}{P_{0solar}}. \tag{1.6}$$

This results in the following scaling from lab plasma to solar plasma parameters

$$B_{solar} = \frac{1}{\sqrt{c_3}} B_{lab} \tag{1.7}$$

$$v_{A,solar} = \sqrt{\frac{c_2}{c_3}} v_{A,lab} \tag{1.8}$$

$$\tau_{solar} = \frac{1}{c_1}\sqrt{\frac{c_3}{c_2}} \tau_{lab} \tag{1.9}$$

$$\left(\frac{dv}{dt}\right)_{solar} = \frac{c_1 c_2}{c_3}\left(\frac{dv}{dt}\right)_{lab}. \tag{1.10}$$

What these scaling laws say is that if you have two plasmas with similar β and S and you can estimate c_1, c_2, and c_3, you know the scaled values of all the other important quantities in the system.

Marshall and Bellan [53] extended these scalings to electrical quantities. Since Ampere's law gives $2\pi r B = \mu_0 I$, it is seen that current scales as lB and so

$$I_{solar} = \frac{1}{c_1\sqrt{c_3}} I_{lab}. \tag{1.11}$$

Similar arguments can be made to obtain the scaling for inductance, magnetic flux, electric field, voltage, current density, and magnetic energy which respectively scale as

$$L_{solar} = \frac{1}{c_1} L_{lab} \quad (1.12)$$

$$\Phi_{solar} = \frac{1}{c_1^2 \sqrt{c_3}} \Phi_{lab} \quad (1.13)$$

$$E_{solar} = \frac{\sqrt{c_2}}{c_3} E_{lab} \quad (1.14)$$

$$V_{solar} = \frac{\sqrt{c_2}}{c_1 c_3} V_{lab} \quad (1.15)$$

$$J_{solar} = \frac{c_1}{\sqrt{c_3}} J_{lab} \quad (1.16)$$

$$W_{solar} = \frac{1}{c_3 c_1^3} W_{lab}. \quad (1.17)$$

1.4 Astrophysical Jet Experiment as a Proxy for Solar Prominence

The dimensionless nature of the MHD equations showcased in Section 1.3 allows us to use our laboratory experiments to study solar and astrophysical phenomena. Laboratory experiments at Caltech have similar β, S, and magnetic topology to the astrophysical systems in Fig. 1.2 which means that the systems should evolve similarly but with different timescales. Table 1.1 outlines estimated values of key parameters for the Caltech single loop experiment and a Solar Prominence on one side and the Caltech jet experiment and a YSO jet on the other side. All 10 rows of quoted values come from the references listed in the bottom row of each column. The parameters in the top four rows of the table can be used to calculate the middle four and most show very good agreement with the tabulated values. A few are less precise but reasonable enough, likely because the data in the table is compiled from many different sources. In the 10th row of the table, v is the speed the jet propagates which is why there is no value listed for the single loop structure. The astrophysical jet experiment (a major topic in this thesis) and the solar loop experiment (the major topic in Ref. [54]) are the primary tools at Caltech used to understand flux-rope plasmas.

Figure 1.4 illustrates the similar magnetic topology and boundary conditions between solar prominences (a), the single loop experiment (b), and the jet experiment (c). The previously used photograph of a solar prominence is shown again in Fig. 1.4(a). Immediately adjacent, Fig. 1.4(b) shows a photograph of the arched flux rope with two footpoints created in the single loop experiment at Caltech. The incredible similarity makes it an excellent tool to understand solar prominence dynamics.

Parameter	Single Loop Expt	Solar Prominence	Jet Expt	YSO Jet
n [m^{-3}]	6×10^{22}	6×10^{14}	3×10^{22}	10^{10}
$\lvert B\rvert$ [G]	3000	50	10^4	10^{-3}
T [eV]	2	100	2	0.7
L [m]	0.5	2×10^7	0.3	10^{14}
ρ [kg/m^3]	10^{-4}	10^{-12}	2×10^{-3}	2×10^{-17}
P [Pa]	3×10^3	5×10^{-2}	160	10^{-9}
v_A [m/s]	3×10^4	4×10^6	2×10^4	2×10^4
β	0.01	0.002	0.01	0.4
S	$10^1 - 10^3$	$10^8 - 10^{12}$	$10^1 - 10^2$	10^{15}
v [km/s]	N/A	N/A	50	300
Refs	[55–58]	[1, 53, 55, 57]	[53, 59]	[59, 60]

Table 1.1: Table of key parameters for the Caltech single loop experiment and a Solar Prominence on one side and the Caltech jet experiment and a YSO type jet on the other side.

At first glance, the image of the jet experiment shown in Fig. 1.4(c) looks like it does not fit with the other two. While this image more closely resembles the AGN and YSO jets in Fig. 1.2(a) and (b), it is also relevant to solar prominences, particularly near the footpoints. Near each footpoint of the prominence, the system would mirror the jet topology: a collimated, twisted flux-rope. Thus, the jet is a zoomed-in picture looking at the base of the prominence. The dynamics of the jet should mirror the dynamics of the base of the single loop experiment and the solar prominence itself.

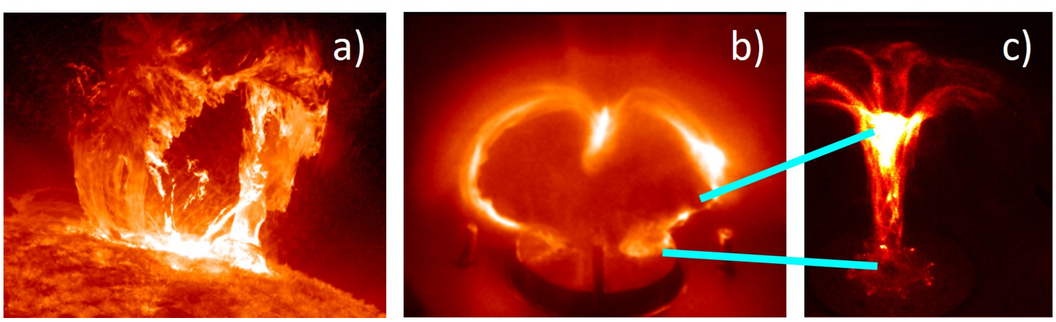

Figure 1.4: Similar magnetic topology between solar prominences and the Caltech laboratory experiments. a) Solar prominence, same as Fig. 1.2(c). b) Plasma created in the single loop experiment. c) Plasma created in the jet experiment.

Chapter 2

JET EXPERIMENT DETAILS

The Caltech Astrophysical Jet Experiment is the longest running currently operational experiment in the Bellan plasma physics laboratory. It has been extensively studied by graduate students and post-docs for nearly 20 years and new physics is still being uncovered. The jet experiment produces a relatively cold, dense, collisional low-β MHD-driven jet with an initial radius of a few cm and a length increasing to several 10's of cm in 30-50 μs. This experiment provides a unique opportunity to study centimeter-scale versions of astrophysical flux-rope plasmas in the laboratory.

Figure 2.1 is a cutaway of the experiment. The jet is created inside a 1.4 m diameter and 1.6 m long vacuum chamber which has a pair of coplanar, concentric copper electrodes mounted on one end. The inner disk electrode is connected to a capacitor bank and the outer annular electrode is connected directly to ground allowing for a potential difference of 3-6 kV to be applied across the electrodes during discharge. A more detailed description of the experimental setup and shot firing process summarized here can be found in Refs. [61–63]. First, a coil behind the electrodes is energized creating a dipole-like poloidal magnetic field that links the inner and outer electrodes. Fast gas valves open and puff a gas cloud into the vacated vacuum chamber through eight radially oriented, equally spaced concentric pairs of holes on the inner and outer electrodes. After gas injection, the 120 μF capacitor bank establishes a large potential difference (3-6 kV) across the electrodes. The applied voltage ionizes the gas cloud in front of the electrodes along the poloidal magnetic field lines from the coil. Electric current driven by the discharging capacitor bank flows along the eight plasma arches. Hydrogen, nitrogen, argon, and krypton gases can be used. A pulse forming network (PFN) can be used to sustain the jet for up to 50 μs.

2.1 Experimental Hardware

The jet experiment is made of a number of hardware components that will each be discussed in the following subsections below.

Vacuum Chamber

The experiment is housed inside a 1.4 m diameter and 1.6 m long stainless steel vacuum chamber. It has 2.75" ConFlat (CF) flange ports around the vessel that provide great flexibility to the user when it comes to installing diagnostics. The vessel has five 10" CF flange ports arranged in a line on each side of the chamber, many of which are used as visible-light windows. An air-powered gate valve is mounted on the single 14" CF flange at the bottom between the chamber and a Marathon CP-12 Cryopump. During normal operation, the Cryopump and HC-8E Compressor keep the base pressure in the chamber at approximtely 10^{-7} Torr as measured by an ion gauge.

Power Supply

The capacitor bank and the electrical connections to the electrodes sit at the heart of the experiment. We use two 60 μF Areovox Industries, Inc. capacitors in parallel for an effective 120 μF capacitance. These capacitors are charged to 3-6 kV over $\sim$ 30 seconds and then each discharged over $\sim$ 15 μs by throwing two GL-7703 size A mercury-vapor ignitrons. The beauty of this sysem is that the capacitors can be charged using relatively ordinary power from the wall and then $\sim$ 100 MW is provided during discharge which is as much power as an entire city like Pasadena consumes.

Between the capacitor bank and the electrodes are four Belden YK-198 low-inductance coaxial cables. The electrodes are an inner 20 cm diameter copper disk and an outer 50 cm diameter copper annulus with a few mm gap between the two.

The capacitor bank outputs a current that looks like a damped sinusoidal wave peaking around $\sim$ 100 kA for a 5 kV charge.

PFN

The Pulse Forming Network (PFN) is an extra power supply whose purpose is to provide extra current to keep the experiment going for longer after the first capacitor bank has discharged. It provides a square voltage pulse using a sequence of inductors and capacitors. A complete description of the Pulse Forming Network (PFN) can be found in Ch. 5 of Ref. [59].

Background Magnetic Field

The background poloidal magnetic field is created by a separate power supply that runs current through a solenoid coil of radius 9.55 cm with 110 turns that is located directly behind the electrodes. The magnetic field lines from this coil link the inner and outer electrodes.

Gas Inlets

Gas enters into the vacuum chamber through eight holes arranged concentrically in the inner and outer electrodes. Behind the holes are four electrically controlled fast gas valves that open and close in a very short amount of time and let in an amount of gas that varies with the voltage provided to them. There is also an additional gas inlet through a side 2.75" CF port that allows gas to be injected inside the vacated vacuum chamber in front of the jet.

Data Acquisition

Diagnostic data is collected using a Struck Systeme SIS3100 VME with an SIS1100 PCI card slot in a PC to interface with it. The PCI card connects to the VME via optical fiber. The system is housed in a large crate with 12 data acquisition boards that can each input 8 channels for a total of 96 channels of data. The system operates with 100 MHz frequency.

2.2 Diagnostics

Over the past nearly 20 years, a whole suit of diagnostics has been developed for the jet experiment. Figure 2.1 shows some of the many diagnostics available on the Caltech jet experiment. The next few subsections will highlight some of the most important diagnostics, both pictured and not pictured on Fig. 2.1. The key X-ray diagnostics including D_{ext}, D_{int}, and D_{CMOS} will be introduced in Ch. 3.

Imacon 200 Camera

The Imacon 200 intensified CCD camera is without a doubt the most important tool in our diagnostic arsenal. In the fast mode of operation, the camera can take 7 black and white 1200 x 980 pixel images at up to 2×10^8 frames per second (FPS). The slow mode has the capability to take 14 images at up to 7×10^6 FPS. Imacon 200 is capable of using DSLR camera lenses giving it a wide range of viewing options.

The photographs provided by the Imacon 200 are invaluable in understanding the physics governing the flux-rope experiments at Caltech.

Magnetic Probes

The radial b-dot magnetic probe array measures the three components of the magnetic field (B_r, B_ϕ, and B_z) at 11 radial locations spaced 2 cm apart. The whole probe array can be translated in the z direction allowing an rz plane view of the magnetic field to be constructed [59, 64, 65].

HV Probe

The jet experiment employs a Tektronix high voltage probe to measure the voltage across the electrodes during each shot. This probe can measure voltages up to 12 kV and outputs the voltage on the probe with 1000x attenuation. Thus 1 kV on the probe would output as 1 V. The probe has a characteristic rise time of $\sim$ 10 ns.

Current Probe

A Rogowski coil outputs a voltage proportional to the derivative of current. The output voltage is coupled with a passive hardware integrator to measure current. The hardware integrator has effective resistance $R_{eff} = 82\ \Omega$ and $C = 2\ \mu$F which gives RC time constant $\tau \approx 170\ \mu$s [66].

EUV Optics

An EUV imaging system with the capability to image photons with energy between 20 eV and 60 eV at frame rates up to 3.3×10^6 frames per second can be used. The key components of this system are a multilayer Mo:Si mirror and a fast decaying YAG:Ce scintillating screen. EUV images of the jet projected onto the scintillating screen are taken by the Imacon 200 camera [67].

Interferometer

A HeNe laser interferometer with unequal path lengths is used to measure line-averaged density of the jet [68]. The path lengths are over 8 meters different and the interferometer still works because what matters is that the path length difference is an integer multiple of the laser cavity length. The interferometer was recently upgraded with a new single mode optical fiber coupling that allows the system to translate and rotate [69].

Thompson Scattering

Thomson scattering with a 532 nm Nd:YAG laser is used to measure electron density and temperature [69].

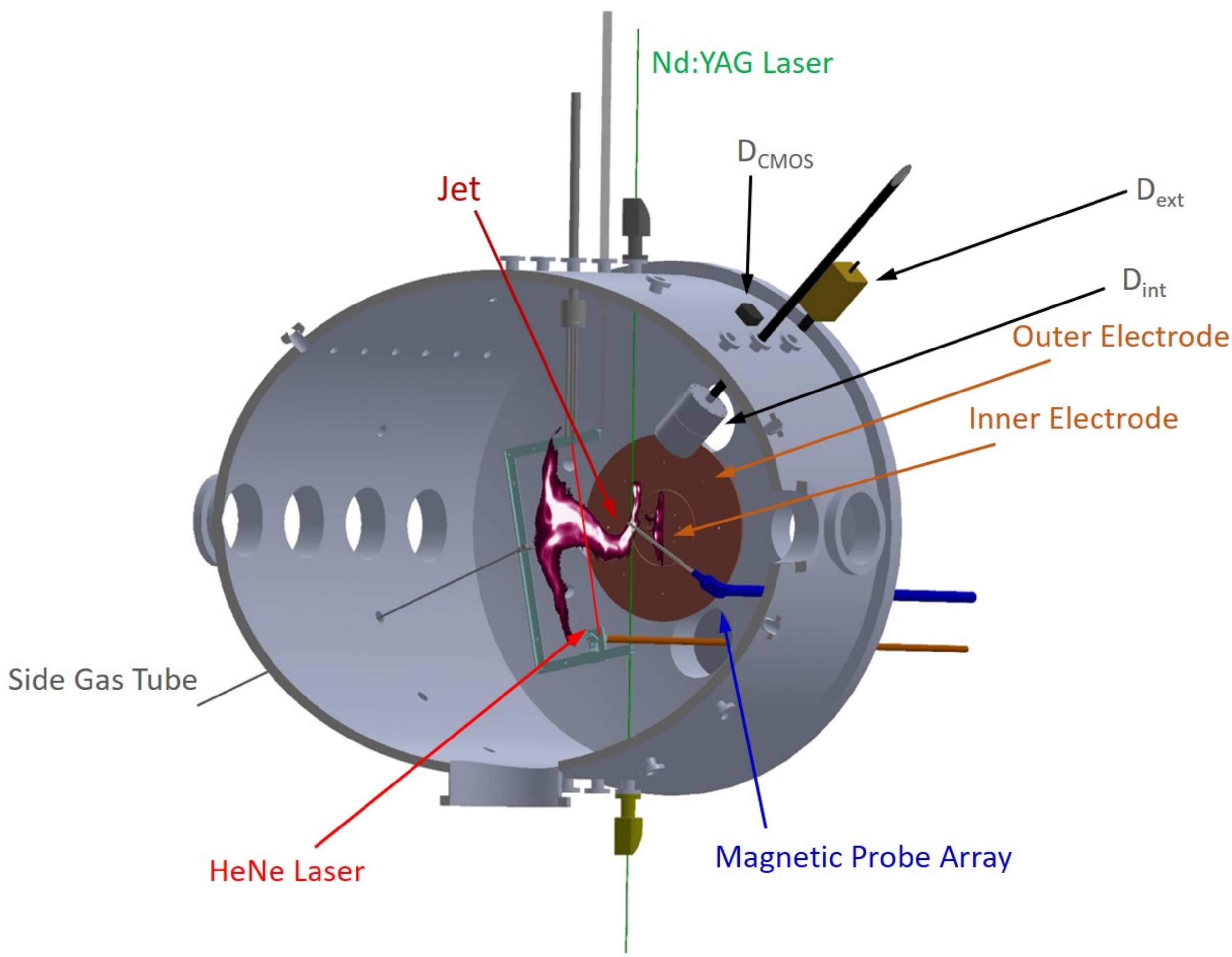

Figure 2.1: Cutaway of the Caltech Astrophysical Jet Experiment showing the position and approximate scale of the jet inside as well as part of the diagnostic suite. Green Nd:YAG laser beam passing vertically through the chamber is part of the Thomson Scattering diagnostic. Red HeNe laser beam is part of the interferometer.

Chapter 3

X-RAY OBSERVATION

[1] R. S. Marshall, M. J. Flynn, and P. M. Bellan. “Hard X-ray bursts observed in association with Rayleigh-Taylor instigated current disruption in a solar-relevant lab experiment”. In: *Physics of Plasmas* 25.11 (2018), p. 112101. DOI: https://doi.org/10.1063/1.5054927.

The Caltech jet experiment produces an MHD-driven jet whose lifetime depends on the gas it is composed of, varying from ~ 10 μs for a hydrogen jet to ~ 40 μs for an argon jet. The more massive the atoms in the jet, the more slowly the jet propagates down the chamber and the longer its lifetime [70].

The Caltech jet experiment operates in three distinct experimental regimes based on magnetic flux through the inner electrode, $\Psi_{ie} = \oint_S \mathbf{B} \cdot d\mathbf{A} \approx \pi a^2 B_z(a)$ [59]. Ψ_{ie} is directly related to the background poloidal magnetic field and it follows that a larger Ψ_{ie} stabilizes the jet against the kink instability [59]. Ψ_{ie} is varied in practice by increasing or decreasing the current running through the solenoid coil behind the electrodes. The three operational regimes are: i) Detached –jet detaches from the electrodes, ii) Kinked –jet stays attached and at some critical length undergoes the ideal MHD kink instability, or iii) Straight –jet stays attached and remains straight [59, 71]. The work presented in this thesis will focus on the physics of the intermediate case ii) where the jet undergoes the kink instability.

Figure 3.1 shows the lifecycle of the jet for a Hydrogen plasma[1]. The first image, while relatively dim, shows the jet 2 μs into the shot. The eight bright dots seen in a circular pattern are eight holes in the inner electrode from where gas is injected into the chamber. Arches of plasma that extend radially out from the eight holes are faintly visible. These arches are what we call the ‘spider legs.’ Each subsequent image shows the jet 500 ns later. The eight legs collimate and form a single jet over the next ~ 2 μs. The straight jet then propagates down the chamber.

When it becomes energetically favorable (which occurs when the jet reaches some critical length), the ideal MHD kink instability sets in [59, 71] and the jet begins to coil up like an inductor. Energy $W = \phi^2/(2L)$ and so during the ideal MHD

[1] Hydrogen is used for the photographs because it creates a particularly nice set of images.

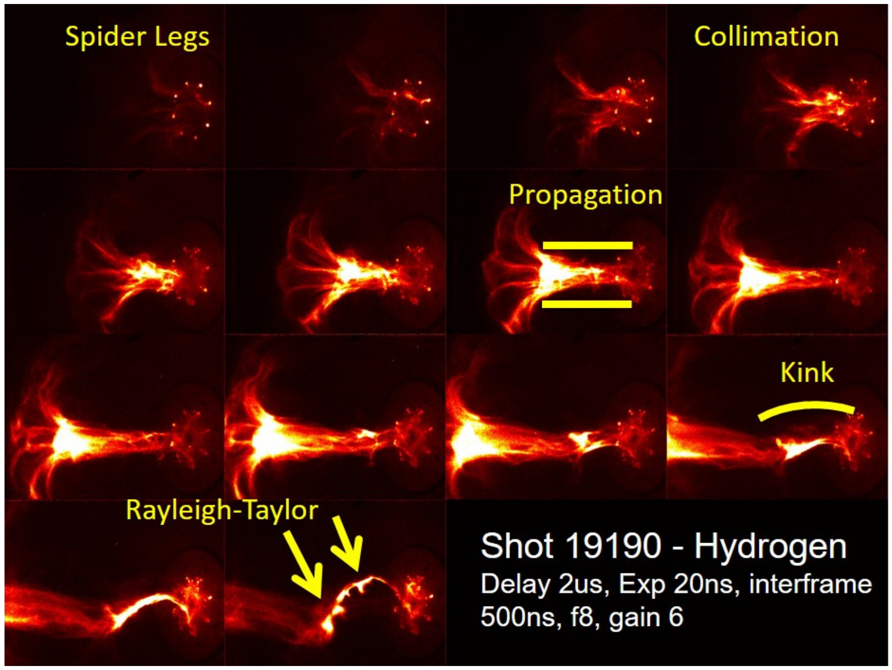

Figure 3.1: Hydrogen jet life-cycle. The first image is taken 2 μs into the shot and each subsequent image is taken 500 ns later. The Imacon 200 images are falsely colored.

kink instability, ϕ is constant because magnetic flux is frozen into the plasma and inductance L is increasing which means that the magnetic energy is decreasing.

The kink is an accelerating reference frame which induces a secondary Rayleigh-Taylor instability on top of it. Rayleigh-Taylor (RT) is an interchange instability that occurs when there is a heavy fluid on top of a light fluid. In the case of the Caltech jet, the heavy fluid is the jet itself and the light fluid is vacuum. The fastest growing RT mode has a growth rate that goes like $\gamma_{RT} = \sqrt{g_{eff}k}$ where $g_{eff} \approx 4 \times 10^{10}$ m/s^2 is the effective gravity and $k \approx 300$ m^{-1} comes from the wavelength of the RT ripples. RT instability ripples pinch down the plasma jet. In the case of a hydrogen plasma, the RT instability does not pinch the plasma down far enough to break it apart. But in the case of the argon plasma, the RT instability pinches the diameter of the jet past the ion skin depth $\delta_i = c/\omega_{pi} \approx 4$ mm, the critical length scale at which the ideal MHD description of the plasma fails because the Hall term has become non-negligible. In this moment, the RT instability causes a magnetic reconnection event [62].

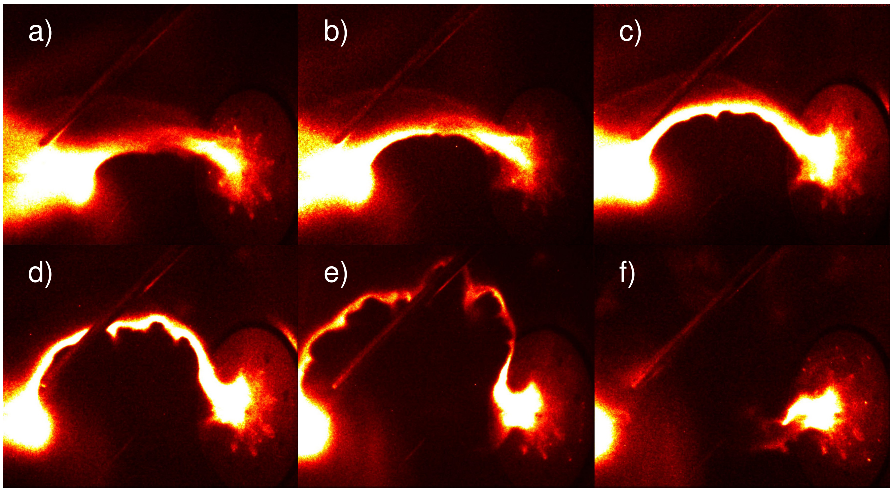

Figure 3.2: Argon jet instability cascade from kink to Rayleigh-Taylor to magnetic reconnection. a) is taken 25 μs into the shot and each subsequent image is 1 μs later. a) and b) show a kinked plasma that is accelerating radially outward. c) and d) show fast-growing Rayleigh-Taylor ripples superposed on the kinking arch. From c) to e), the ripples get larger and in the microsecond between e) and f), the ripples get so large that the plasma breaks apart. The Imacon 200 images are falsely colored.

Spectroscopic line ratios indicate nominal 2 eV electron temperatures while Doppler broadening of spectral lines indicates similar ion temperatures [61]. The laser interferometer [68] indicates a nominal density $n_e \simeq 3 \times 10^{22}$ m^{-3} giving a nominal 0.6 μm electron collision mean free path using the nominal temperature of $T = 2$ eV. The electron and ion temperatures increase to 6 eV and 16 eV, respectively at the time and approximate location of the RT instability [61]. A $Z = 2$ ionization state is assumed based on spectroscopic measurements at the time of the X-ray burst. A set of images showing certain key points in the argon jet's life cycle is shown in Fig. 3.2. Each frame is 1 μs after the previous. Figures 3.2(a)-(c) show the jet undergoing the ideal MHD kink instability and becoming helical [63, 71]. The radially outward acceleration associated with the exponential growth of the helical instability triggers a Rayleigh-Taylor (RT) secondary instability [62] whose ripples are seen growing in Figs. 3.2(c)-(e) on the inboard side of the arch. Figs. 3.2(c)-(e) show the RT instability choking the jet diameter at the interchange ripples. During the microsecond between Figs. 3.2(e) and (f), the plasma breaks apart.

At the time when the argon plasma breaks apart, seven simultaneous, transient measurements provide strong circumstantial evidence that something beyond the scope of ideal MHD, i.e. a magnetic reconnection event, is taking place.

1. The high speed camera shows that the jet appears to undergo a RT instability, and then break apart [62].
2. There is a transient EUV burst at the RT location [61].
3. The spectrometer shows Ar II line emission before the RT instability but Ar III and Ar IV emission during the RT instability, indicating electron heating [61].
4. An rf magnetic probe indicates a burst of high frequency waves, tentatively identified as whistlers [61].
5. The spectrometer shows increased Doppler broadening of the ion lines, indicating ion heating [61].
6. The magnetic probe array shows that the magnetic field morphology after breaking is substantially different from before.
7. A 500-1000V fast transient is recorded across the electrodes by the high voltage probe.

The rest of Ch. 3 will be devoted to adding a surprising new simultaneous measurement to the list of seven transients.

8. There is a transient burst of hard X-rays.

3.1 X-ray Burst and Detector Details

Four different detectors have been used to detect X-ray emission from the jet. These detectors are denoted as: (i) D_{ext}, a single-channel plastic scintillator mounted outside the chamber, (ii) D_{int}, a vacuum-tight 7-channel plastic scintillator detector mounted inside the vacuum chamber, (iii) D_{amptek}, a commercial Amptek XR100 Silicon Drift Detector mounted outside the chamber, and (iv) D_{CMOS}, a windowless CMOS camera mounted outside the chamber.

The Eljen Technology EJ-200 plastic scintillators in D_{ext} and D_{int} are made of Polyvinyltoluene. EJ-200 was chosen because it has a long attenuation length (380 cm), it is fast (rise time $\sim$ 0.9 ns, fall time $\sim$ 2.1 ns), it is cost effective, easy to machine, and easy to maintain and operate. Hamamatsu H10721 photomultipliers were chosen because of their fast rise time (∼ 0.57 ns) and because they do not require a high voltage power supply. Operation simply requires wiring the photomultiplier up to a 4.5-5.5 Volt source. The low current draw means that the PMT can be powered by four standard 1.5 V alkaline batteries wired in series. This is especially important for the jet experiment because it prevents ground loops by enabling each PMT to be electrically isolated from the rest of the experiment. Without this precaution, ground loops would easily overwhelm the small currents produced by each PMT.

Fig. 3.3 indicates how the detectors are positioned. D_{ext}, D_{int}, and D_{Amptek} have time resolution with minimal energy resolution while D_{CMOS} has energy resolution, but no time resolution. The data from these four detectors show that a short $\sim 10^{-6}$ s burst of non-mono-energetic hard X-rays is detected between $t \approx 24 - 40$ μs at the same time as several other distinct transient phenomena.

Detection of a burst of hard X-ray emission from the Caltech jet is surprising because the plasma temperature is ∼ 2 eV. The temperature increases to a few integer multiples of this at the time and location of the RT instability. But even 6-16 eV is barely into the EUV part of the electromagnetic spectrum and the observed hard X-rays are ∼ 3 orders of magnitude more energetic.

External Detector, D_{ext}

The one inch diameter cylindrical plastic scintillator in D_{ext} sits immediately outside the vacuum chamber behind a 2.75” CF flange with a kapton window mounted in it. The scintillator is wrapped with aluminum foil and then by black electrical tape to block visible light. A 2.5 m light pipe carries scintillated blue photons from the tapered end of the scintillator to a battery-powered PMT inside a highly shielded box. The electrodes are outside the field of view of D_{ext} and so cannot be the source of the X-rays, i.e. the X-rays must originate in the plasma.

Figure 3.4 shows a sample dataset. The X-ray data from D_{ext} is shown in blue and the voltage across the electrodes measured by the high voltage (HV) probe is shown in black. At $t \approx 26.5$ μs, D_{ext} detects an X-ray burst and a nearly simultaneous 500 V transient appears across the electrodes.

The X-ray energy is estimated by collecting data from 75 consecutive shots with varying thicknesses of aluminum foil placed in the X-ray path between the kapton window and the scintillator inside D_{ext}. To establish a reference, 20 consecutive shots were taken with no foil (other than the foil wrapping the scintillator). Then

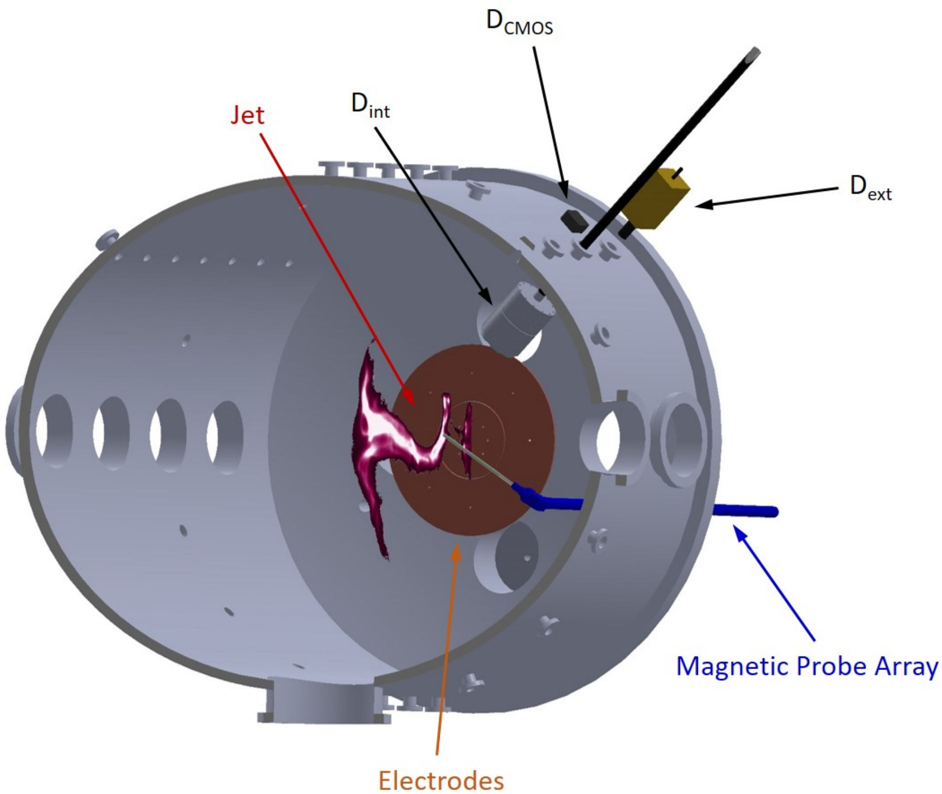

Figure 3.3: Experimental layout showing key diagnostics used in X-ray study. The electrodes are shown in the center. The magnetic probe array shown oriented with the array spanning the center of the electrodes can both move axially and rotate. D_{CMOS} is the small, black rectangular camera on the third flange from the end. D_{int} is mounted next to it on the second flange; its seven scintillators are housed in the cylindrical body located inside the vacuum chamber. The scintillated photons are transmitted through optical fibers coming out of the black tube through the flange. D_{ext} is shown on the flange farthest to the right; it was operated on the second flange currently home to D_{int} prior to its existence. D_{amptek} was operated on the far right flange where D_{ext} is shown. The Imacon 200 camera takes photographs through one of the large side windows.

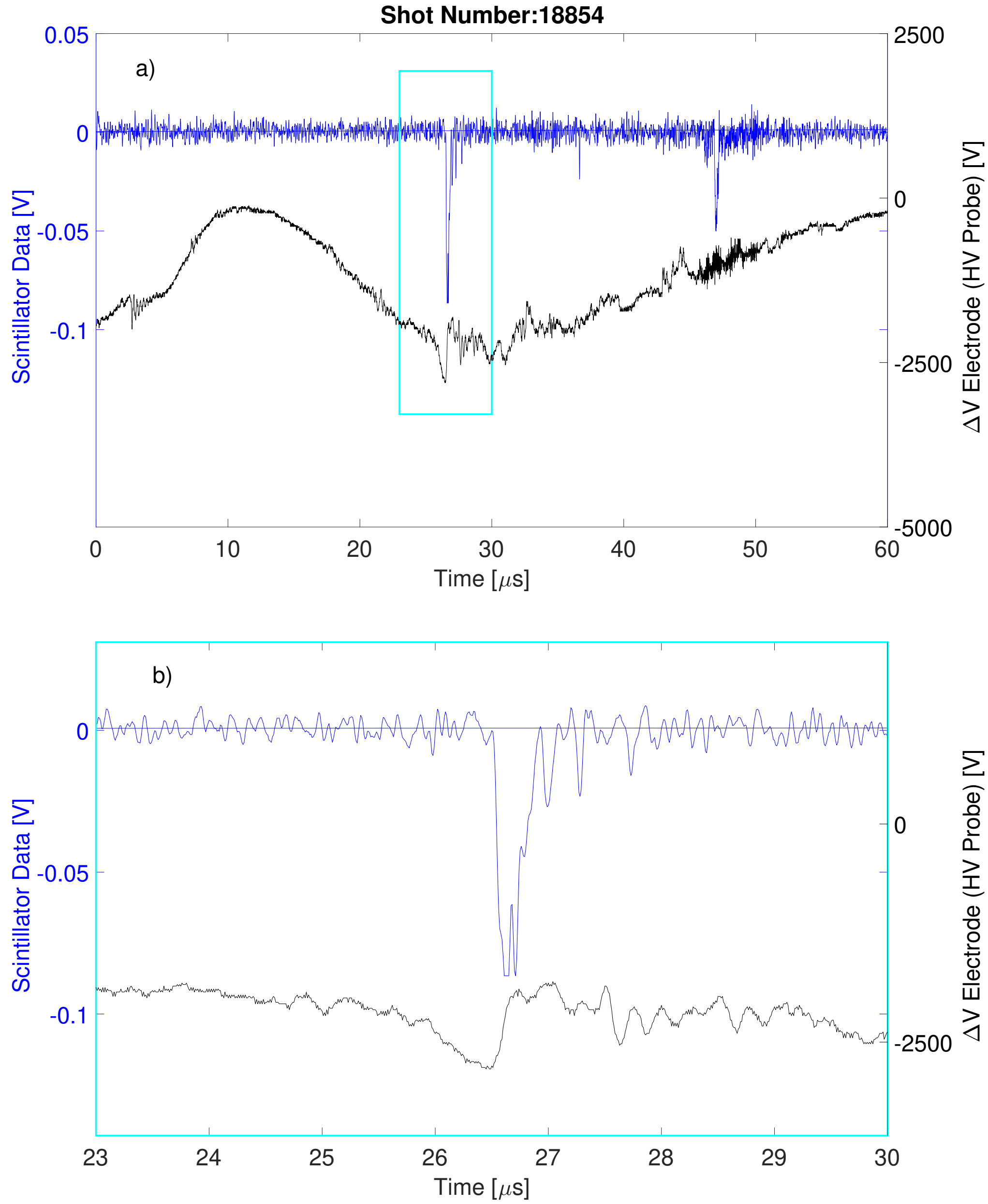

Figure 3.4: Shot 18854 X-ray signal from D_{ext} (top, blue trace) and high voltage probe trace (bottom, black trace). ΔV Electrode is the voltage across the electrodes measured by the high voltage probe. a) shows the full trace of both diagnostics and b) is zoomed in for times $t = 23 - 30$ μs bounded by the cyan box in a).

20, 10, 20, and 5 shots were taken with 86, 124, 173, and 297 microns of additional attenuating foil, respectively. Transmission fractions for the varying thicknesses of foil were least-squares fit with known aluminum transmission data as a function of energy [72]. The best fit was found to be 5.8 keV with 4.3 keV lower bound and 6.4 keV upper bound; this fitting is shown in Fig. 3.5. The D_{ext} data by itself does not provide sufficient information to tell whether the X-rays are mono-energetic or not. The following sections on D_{int} and D_{CMOS} will discuss this in detail.

The histogram in Fig. 3.6 shows that the X-ray burst appears to happen at a random time between 24 and 40 μs. When images from the high-speed camera and the voltage across the electrodes measured by the high voltage probe are compared to the timing of the X-ray pulse, a striking correlation becomes readily apparent. The X-ray pulse does not occur randomly, but instead correlates with both the visual observation of the RT instability breaking the jet and also with a transient jump of the electrode voltage. Figure 3.7 shows this correlation between the times of the X-ray signal, the transient electrode voltage jump, and visual observation of the jet apparent breaking (i.e., dimming of visible light). Figures 3(d) and 3(h) in Ref. [61] provide a more definite definition of the dimming. Figure 3(d) in Ref. [61] is a superimposed image of the jet with visible light in blue and EUV in red whereas Fig. 3(h) in Ref. [61] directly below it is purely visible. Arrows in Fig. 3(h) in Ref. [61] pinpoint the locations in the RT region where visible emission of the jet dims in between consecutive frames. During this time, Fig. 3(d) in Ref. [61] shows a strong burst of EUV emitted from the same region. The visible dimming and EUV emission is a reproducible phenomena. The time when the plasma breaks apart, synonymous with the visible dimming, is determined using images taken with 250 ns interframe time, i.e. a capture rate of 4×10^6 FPS. It follows that Fig. 3.7(b) illustrates less time resolution than Fig. 3.7(a) due to the interframe time being much larger than the time between electrode voltage data points. D_{ext} occasionally detects multiple bursts and these coincide closely with multiple high-voltage probe jumps suggesting multiple events taking place in a single shot. It was not possible to image these multiple events using the high-speed camera because the events were too separated in time for the camera timing to bracket these multiple events. However, the camera frequently captured one of the multiple detected RT-instigated breaking events and the time of the captured event image was simultaneous with an X-ray scintillator signal.

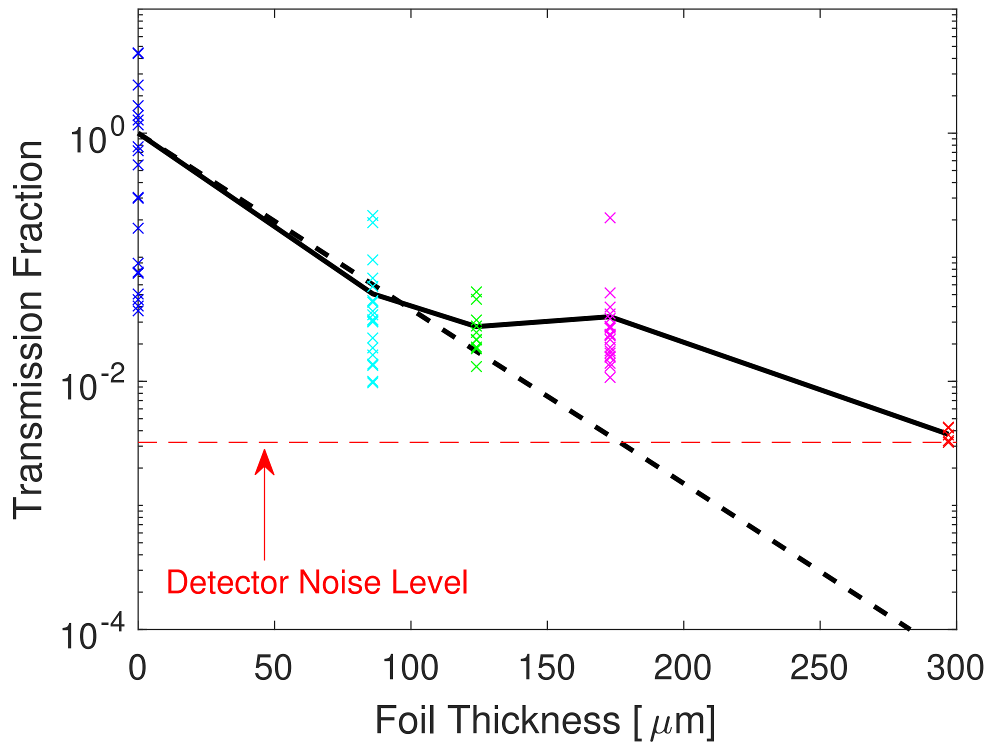

Figure 3.5: Plot shows the exponential attenuation of the X-ray signal measured by D_{ext} with increasing aluminum foil thickness on a logarithmic vertical axis. Each 'x' is a measured signal amplitude normalized to the average amplitude of the 20 measurements taken with no added attenuating foil. Signals were allowed to saturate to increase dynamic range in the more sensitive measurements and as a result some did saturate when no added foil was used. Signal strengths for saturated signals were estimated by fitting their pedestals to the pedestal of a scaled signal with a known strength. The average signal transmission for the number of shots taken with each thickness of aluminum foil is shown in black and used to calculate the best fit, shown as the black dashed line. The red data points and dashed line represent the noise in the system and helps to explain why the best fit diverges at high thickness. The noise is calculated as the standard deviation of the data for the 297 μm foil thickness case where no X-rays were observed above the noise. The best fit is calculated via least-squares using data from Henke *et al.* [72].

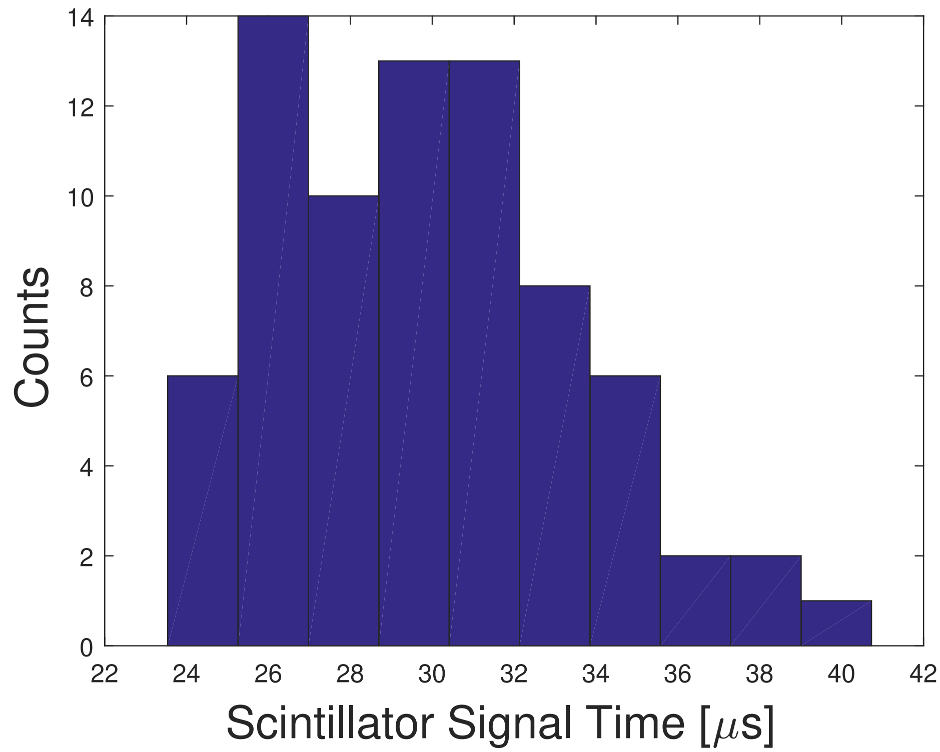

Figure 3.6: Histogram of the times at which the X-ray signal is observed by D_{ext}.

Internal Detector, D_{int}

D_{int} is made of seven one inch diameter scintillators, each individually wrapped by aluminum foil and then black electrical tape. The housing holding the scintillators is vacuum-tight which allows this detector to be mounted inside the vacuum chamber so that the scintillators are only 35 cm from the center axis of the vacuum chamber. Each of the seven scintillators is linked to its own PMT through a 2 mm diameter and 10 m long optical fiber. The PMT outputs are measured by a 1 GHz bandwidth oscilloscope with four input channels. This system has a 5 ns time resolution.

Figure 3.8 shows data from channels 1, 2, 3, and 4 of D_{int}. The signal envelopes show excellent agreement across channels. In the four data sets, there is no signal until $t \approx 25$ μs when all four channels detect an X-ray burst that lasts about 1.5 μs. Camera images from this shot show that the timing coincides with the jet breaking.

Figure 3.9 shows the X-ray data from channel 3 in Fig. 3.8 starting with the complete 15 μs data set at the top of the figure. The middle plot in Fig. 3.9 shows a 1 μs close-up of the X-ray signal. The bottom plot in Fig. 3.9 shows a 100 ns ultra-close-up of the data inside the dashed lines of the middle plot. D_{int}'s dramatically improved

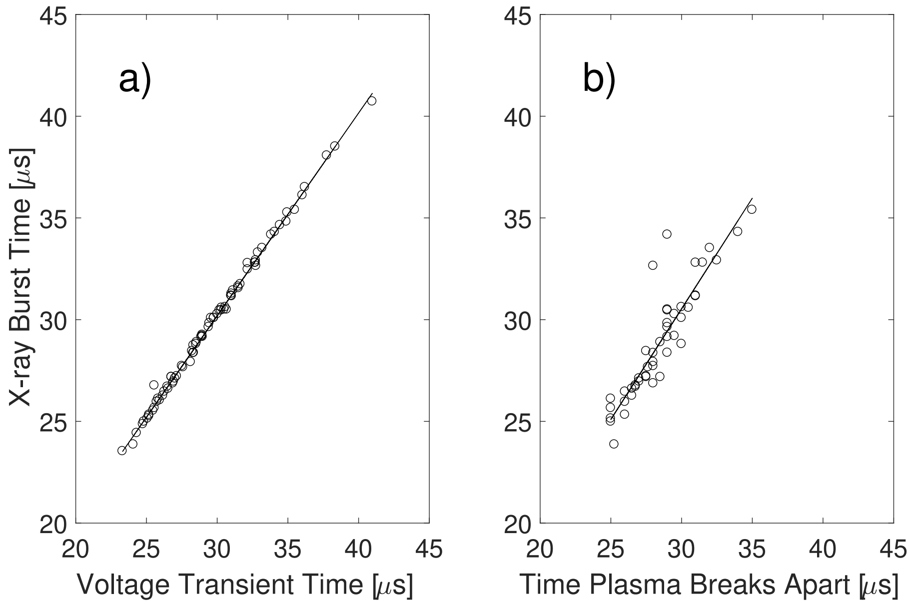

Figure 3.7: Time correlation between X-ray burst, voltage transient measured by HV probe, and time when plasma breaks apart. a) shows the time of the voltage transient measured by the HV probe (horizontal axis) versus the time of the X-ray burst detected by D_{ext} (vertical axis) for each shot. b) shows the time when the plasma breaks apart from the RT instability (horizontal axis) versus the time of the X-ray burst detected by D_{ext} (vertical axis). These figures show that the X-ray burst, voltage transient across the electrodes, and when the plasma breaks apart all happen simultaneously. Lines shown are linear best fits according to a least squares fit.

time resolution shown in Fig. 3.9 builds on the results from D_{ext} by providing two important new pieces of information: (i) the X-ray signal consists of the scintillator collecting dozens to hundreds of discrete X-ray photons during the time when the jet is breaking and (ii) the X-rays are not mono-energetic as the observed signals have varying signal amplitudes.

Amptek Detector, D_{amptek}

The Amptek XR100 Silicon Drift Detector, D_{amptek}, detects X-rays in the 1-10 keV range and has count rates as high as 10^6 counts per second. Data taken by D_{int} shown in Fig. 3.9 shows that X-ray illumination rates during the burst are $\sim 100/1\mu s = 10^8$ per second or more. From these count rates, it is apparent that X-ray emission while the jet breaks is too fast for D_{amptek} to detect individual photons, but D_{amptek} is still useful qualitatively as a commercially produced validation tool.

D_{amptek} and D_{int} were operated simultaneously on the experiment. The two detectors

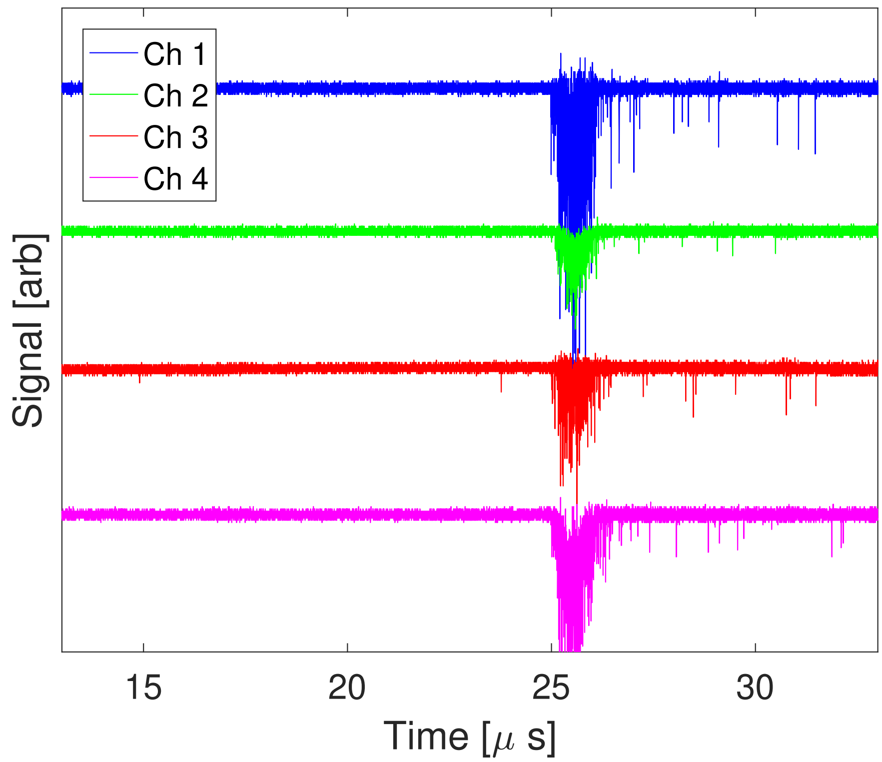

Figure 3.8: X-ray data taken by the four channels of D_{int} going into the 1 GHz oscilloscope. The vertical offset in the data is set manually for presentation purposes. With no added offset, all the data prior to 25 μs would sit at the same level.

validated each other because when one detector saw an X-ray burst, the other did too. Equally as important, when one detector did not see an X-ray signal, the other saw either no X-ray signal or an extremely weak one.

X-ray Camera, D_{CMOS}

D_{CMOS} is a Mightex Systems MCE-B013-UW 1.3 Megapixel Windowless Camera with a sheet of aluminum foil placed in front of the CMOS sensor, a design that yields a reliable, energy-resolving X-ray detector [73–77]. It is important to note here that the term 'X-ray' is used as an all-encompassing term to describe ionizing radiation with energy $E > 124$ eV. X-rays and γ-rays are physically the same, the only distinction is in their origin: X-rays are from electrons outside the nucleus as well as from processes like Bremsstrahlung while γ-rays are from processes inside the nucleus. The windowless construction of the camera is important because most cameras are manufactured with a protective glass sheet glued directly onto the CMOS sensor and glass strongly attenuates X-rays at the relevant energies. This

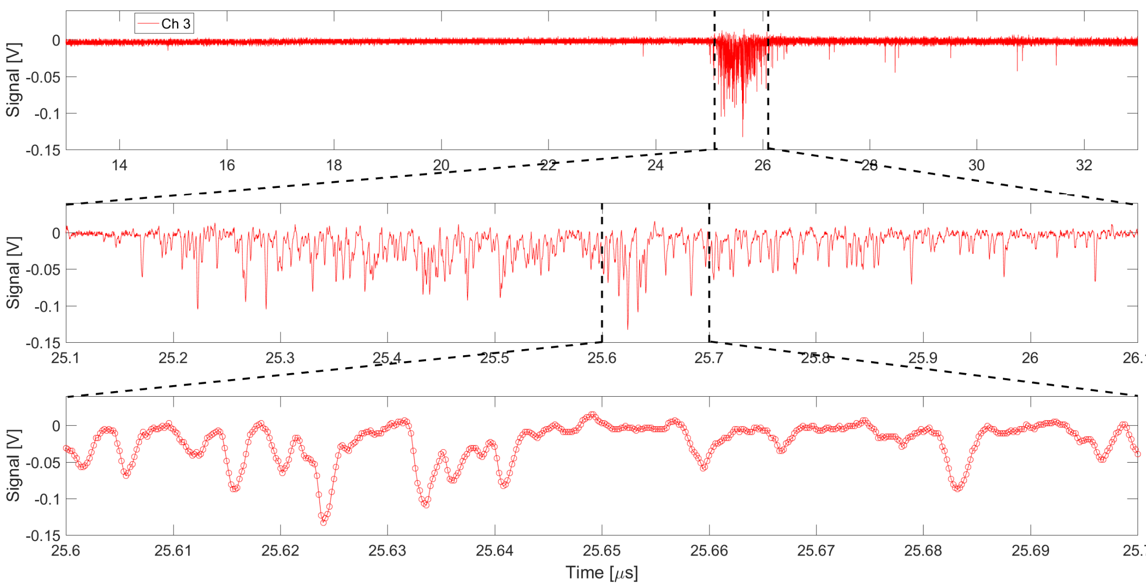

Figure 3.9: Zoomed-in view of D_{int} X-ray signal. The top row is the same data taken by D_{int} that is shown as Channel 3 of Fig. 3.8. The middle plot shows a zoomed-in view of 1 μs inside the dashed vertical lines from the top plot during the X-ray burst. The bottom plot shows a 100 ns snapshot, the region in the middle set of dashed lines blown up.

glass sheet can be removed through careful application of heat to break the glue [73, 76], but a simpler solution is to use a windowless camera[2]. A single sheet of standard, store-bought aluminum foil is $\sim$ 18 μm thick. This foil transmits X-rays with energy $E > 4$ keV [72] while blocking visible light. Pixels impacted by X-rays have an intensity output proportional to the amount of energy deposited by the incoming photon, provided the pixel is not saturated. A histogram of the pixel intensities gives the X-ray energy distribution which can be calibrated using X-ray sources with known energies [73–77].

D_{CMOS} was calibrated using an 87 μCi Co-57 sealed Mössbauer source and an 11 μCi Fe-55 stainless steel encapsulated source. Co-57 emits at 6.4, 14.4, and 122 keV while Fe-55 emits at 5.9 keV. It was observed that X-ray photons incident on D_{CMOS} deposit their energy in multiple neighboring pixels, hereby referred to as clusters, most commonly 2 or 3 pixels total. This seemed at first to contradict results found by Stoeckl *et al.* [75] who report that “a significant fraction of the X-ray

[2] I tried to apply heat to remove the sheet of glass glued to the chip and it was not as easy as it is made out to be. I ended up having a CMOS chip with melted pins on the back and a piece of glass still glued to the front. I recommend the simpler solution.

photons deposit all their energy in one [13.5 μm by 13.5 μm] pixel." However, D_{CMOS} has a pixel size of 5.2 μm by 5.2 μm, less than 1/6 the area of a pixel in the sensor used by Stoeckl *et al.* More than 90% of the incident photons deposit their energy in 6 or fewer pixels suggesting a similar effective deposition area to that in Stoeckl *et al.* To account for deposition in neighboring pixels, we developed a clustering algorithm where neighboring pixels are grouped into a single event. From an initial pixel with an intensity greater than 30, an energy far above the measured background, neighboring pixels are searched for pixels with intensity greater than 12 which represents a threshold greater than 99% of the measured background. If a valid pixel is found, the neighbors of the new pixel are added to the search. All neighboring pixels with an intensity greater than 12 are grouped into a single event with the initial pixel. A sample cluster from a Co-57 X-ray is shown in Fig. 3.10.

The energies from this calibration are displayed in Fig. 3.11. The blue data is made up of 155,000 X-rays detected from the 87 μCi Co-57 sealed Mössbauer source in 2000 images. The peaks, accented with blue vertical dashed lines are assigned using known Co-57 emission energies: the upper peak is the 14.4 keV X-ray emission and the lower peak is the 6.4 keV Kα line of a decay product. A histogram of 54,000 photons detected from the 11 μCi Fe-55 sealed source in 2000 images is superimposed on the same axes in orange. Using the calibration from the Co-57 histogram and assuming a linear relationship between the pixel intensity and energy deposited in a pixel, the orange peak from the Fe-55 data is calculated to be 5.9 keV, an exact match with the Fe-55 emission.

D_{CMOS} is mounted outside the vacuum chamber with the same orientation as D_{ext}. Because D_{CMOS} is not a fast camera, it is triggered before the plasma shot and exposed during the entire duration of the shot. One image is obtained per shot. D_{CMOS} is calibrated using known X-ray energies and so it directly measures the energy deposited by X-rays emitted from the jet. Figure 3.12 is a histogram that shows detected X-ray energies. The blue data labeled '1 layer' shows the X-rays from 50 shots when only a single sheet of aluminum foil is placed in front of the camera sensor. This single sheet has the duty of blocking all visible light as well as passing X-rays. A distribution of energy of the X-rays is shown where the majority have energy between 4 keV and 9 keV. Thus, the 5.8 keV energy estimate from D_{ext} shows excellent agreement with D_{CMOS}.

Aluminum foil is sequentially added in front of D_{CMOS} to illustrate how the spectrum of detected photons changes with attenuation. Like the blue data in Fig. 3.12, each

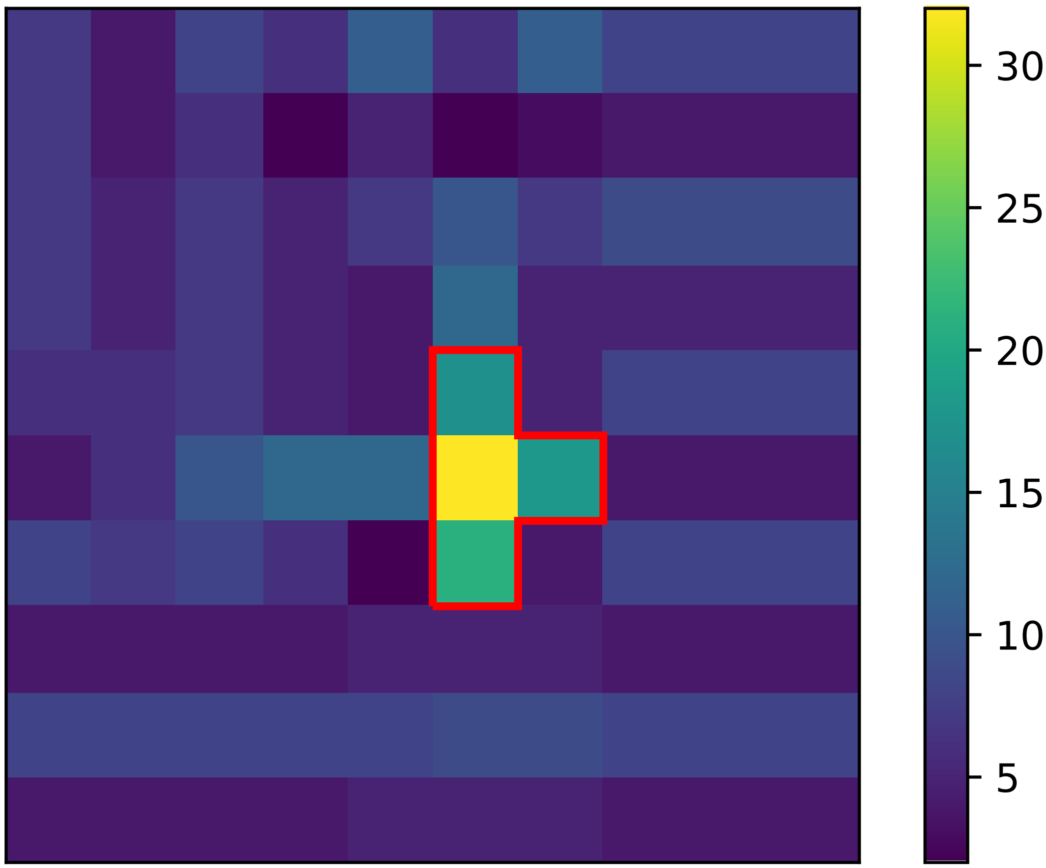

Figure 3.10: A partial image from D_{CMOS} showing a typical energy deposit on the camera sensor. This particular image is a Co-57 X-ray. The four pixels that contain the energy deposited from the X-ray are outlined in red. The yellow pixel contains the largest deposited energy. The pixel intensity of ~ 30 is much larger than where no interaction has occurred, and thus is easily recognized.

subsequent spectrum is also made up of data from 50 shots. As foil is added, the spectrum amplitude in Fig. 3.12 decreases as expected. Also as expected, the foil appears to attenuate a larger fraction of the incident X-ray photons with lower energy.

3.2 Magnetic Field Measurements

The magnetic field evolution has been measured by an axially translatable radial B-dot probe array [59, 64, 65] that records B_r, B_ϕ, and B_z at 11 radial locations spaced 2 cm apart. The probe is aligned normal to the electrode perimeter so that the respective r, ϕ, and z directions of the probe coils correspond to the chamber r, ϕ, and z coordinates. Figure 3.3 shows the magnetic probe array oriented such that it is positioned above the center of the electrodes.

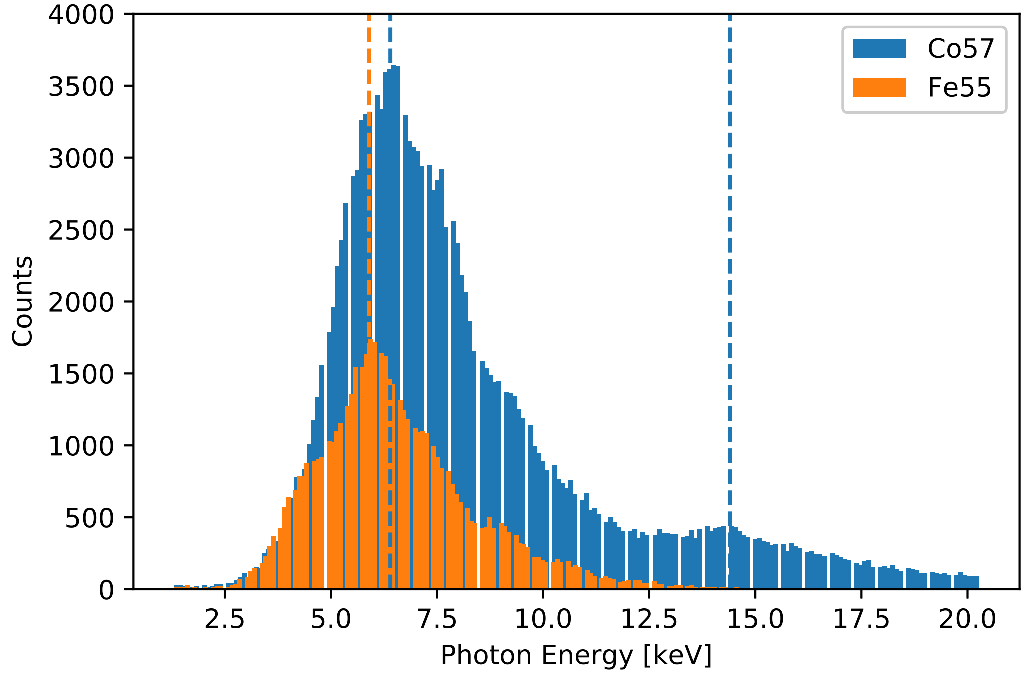

Figure 3.11: Histograms of detected X-ray energies from an 87 μCi Co-57 sealed Mössbauer source (blue) and an 11 μCi sealed Fe-55 source (orange) using D_{CMOS}. Dashed vertical lines highlight the peaks of the respective sources. The two peaks from Co-57 are fitted to known data, 6.4 keV for the lower and 14.4 keV for the upper. By assuming a linear relationship between energy deposited and pixel intensity, the peak associated with the Fe-55 source is calculated to be at 5.9 keV.

By translating the probe through a sequence of z positions for a sequence of plasma shots and measuring B_r, B_ϕ, and B_z at the 11 radial locations, an rz plane view of the magnetic field can be constructed. The magnetic field configuration has high reproducibility before the kink starts, but during the kink and RT instabilities, the plasma has poor reproducibility. At later times, reproducibility is partially restored.

At each axial position z, data from 10 shots is averaged to give $\vec{B}(r, z = z_{probe}, t)$ for fixed z_{probe}. Thus, the measurement indicates an ensemble average. The probe is translated by $\Delta z = 2.5$ cm and the process is repeated. The final 110-point data set is $\vec{B}(r, z, t)$ for grid points $r = 0, 2, 4, ..., 20$ cm and $z = 7.5, 10, 12.5, ..., 30$ cm. The measurements are recorded with 10 ns resolution by 100 megasample per second digitizers. The electrode location defines $z = 0$ and poloidal flux is defined as

$$\psi(r, z, t) = \int_0^r B_z(r', z, t) 2\pi r' dr' \tag{3.1}$$

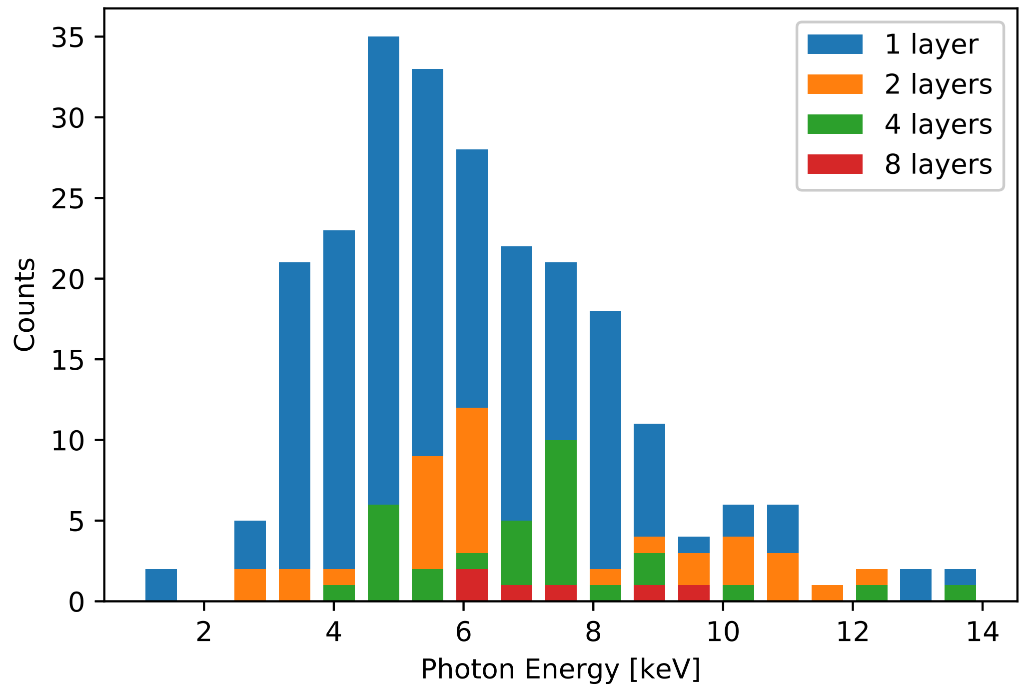

Figure 3.12: Histograms of X-ray energies from the Caltech jet experiment. Each individual histogram is X-ray detection with a different thickness of attenuating aluminum foil between D_{CMOS} and the jet. The number of foil sheets includes the single sheet required for D_{CMOS} to function as an X-ray detector, i.e. there are 0, 1, 3, and 7 layers of additional attenuation material added for attenuation for each spectrum respectively. Each spectrum includes X-rays seen during plasma 50 shots.

which can be discretized as

$$\psi(r,z,t) = \Delta r \sum_{r'=0}^{r'=r} B_z(r',z,t) 2\pi r' \tag{3.2}$$

where $\Delta r = 2$ cm is the radial distance between stations in the B-dot probe array. One key assumption that is evident from this integration is that the ensemble average magnetic field measurement $B(r,z,t)$ is constant in the toroidal $\hat{\phi}$ direction. The poloidal current is defined as

$$I(r,z,t) = \frac{2\pi}{\mu_0} r B_\phi(r,z,t). \tag{3.3}$$

The top row of Fig. 3.13 shows camera frames from 5 to 35 μs. These images show that the jet flows without kinking until about $15-20$ μs and that the RT occurs at $25-30$ μs. The second from top row shows the corresponding evolution of $\psi(r,z,t)$

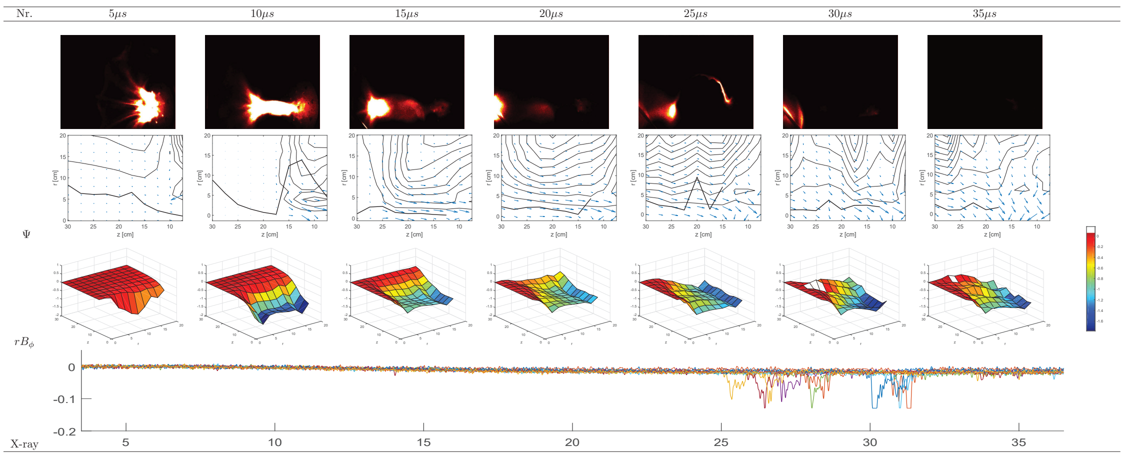

Figure 3.13: Timing relationships for camera images, poloidal magnetic flux, poloidal current, and X-rays. The top row shows false color images of the plasma taken every 5 μs by a high-speed camera. The plasma jet is clearly seen propagating down the chamber from right to left as time increases from 5 to 20 μs. The kink and RT instabilities break apart the plasma at $t \approx 25\mu$s in this set of images. The second row (denoted ψ) shows poloidal flux contours calculated from magnetic probe measurements using Eq. 3.2 for times corresponding to the photos in the top row (black line is where $B_\phi = 0$). As in the photos, the poloidal flux surfaces are clearly stretching from right to left during the 5 to 20 μs interval, coincident with the jet traveling down the chamber. After the RT instability breaks apart the plasma, the flux surfaces change substantially. The third row of images (denoted rB_ϕ) shows the poloidal current in arbitrary units. The colorbar on the right-hand side applies to all seven plots. The jet's right to left motion from 5 to 20 μs can be seen clearly in these plots also. After 20 μs, the poloidal current surfaces become more random and there are locations where the current vanishes or changes sign, i.e., there is a current disruption. The sign change is highlighted by the white color in the colormap which makes it easy to see. The bottom plot is stretched over all 7 columns and shows X-ray scintillator signals for 10 of the 100 shots used to make the poloidal flux and poloidal current plots in the second and third rows. The 10 X-ray signals occur at times 25 μs $< t <$ 32 μs and Fig.3.7 showed that the X-ray signals are coincident with the RT instability and voltage jump. The temporal irreproducibility of the RT signal and associated phenomena is evident from the scatter in the times for the 10 X-ray signals. This scatter indicates that the magnetic plots must be considered as an ensemble average of the poloidal flux and current over many shots.

and the third from top row shows the evolution of $I(r, z, t)$. Once the jet propagates past $z = 7.5$ cm, the magnetic probe array registers a signal and from 7.5 to 20 μs, jet propagation in the $+z$ direction is clearly evident from both the camera frames and the I, ψ plots. This initial segment of the jet evolution has high reproducibility.

The next phase starts at the onset of the kink instability which is then followed by the RT instability breaking the jet. The exact timing varies from shot to shot as was shown in Fig. 3.7. For the particular photograph sequence shown in the top row of Fig. 3.13, the RT instability starts at ~ 25 μs. Figure 3.13 shows that the flux surfaces become irregular with reduced shot-to-shot reproducibility from 25 to approximately 35 μs. It is at times in this interval that X-rays are observed (bottom row).

Figure 3.13 shows that the magnetic flux profile changes abruptly at the time of RT. After the RT, X-rays, and other associated simultaneous phenomena, the ψ profile differs from its prior profile. There is also evidence from the third row of Fig. 3.13 that the shot-averaged $I(r, z, t)$ transiently goes to zero at certain axial locations which indicates a break in the shot-averaged J_z circuit. Observation of the changing magnetic field at the spatial and temporal scale of the RT ripples is not possible because the spatial scale of these ripples is smaller than the probe spatial resolution and because the location of the RT instability varies from shot to shot.

3.3 Energy and Electric Field Estimation

The energy in the capacitor bank driving the jet is $W_c = CV^2/2 = 120\mu\text{F} \times (5\ \text{kV})^2/2 = 1.5$ kJ. The thermal energy in the particles in the breaking region is $W_{th} = nVk_bT$ where n is the particle density, V is the volume of the region assumed to be a cylinder, and T is the temperature. Assuming a nominal radius $r = 2$ cm and length $l = 0.4$ m, this volume is $V = \pi r^2 L = 5 \times 10^{-4}$ m^3. Using the nominal density $n = 3 \times 10^{22}$ m^{-3} from the laser interferometer [68] and temperature $T = 2$ eV, the thermal energy in the particles is $W_{th} = nVk_bT = 5$ J. The circuit magnetic energy at the time of the X-ray burst is $W_{mag} = LI^2/2 = 54\ \text{nH} \times (60\ \text{kA})^2/2 = 100$ J. Calibration of D_{ext} using X-rays from a thorium reference source and taking into account the solid angle subtended by D_{ext} indicate that the radiated X-ray energy is $\sim 10^{-8}$ J indicating that only a tiny fraction of the electrons emit X-rays. This imposes the important constraint that any proposed mechanism for accelerating electrons to high energy in a collisional plasma should work on only a tiny fraction of the electrons.

Since argon's K-shell energy is 3.2 keV [78], atomic line radiation cannot explain the observed $\sim$ 6 keV photons. As additional evidence that the radiation is not from argon's K-shell, Fig. 3.12 shows that the energy of the emitted photons from the plasma is not mono-energetic or at multiple specific lines.

This elimination of K-shell radiation suggests Bremsstrahlung to be the likely mechanism. A 6 keV electron travels at $v \approx 5 \times 10^7$ m/s. The X-ray pulse lasts approximately 1 μs as seen in the top trace in Fig. 3.9. If a 2 eV electron uniformly accelerates to 6 keV in 0.5 μs, an electric field $E = 520$ V/m would be required and the electron would travel 11 meters. If the acceleration time constraint was doubled to 1 μs, the acceleration would result in the electron traveling twice the distance: 22 meters. Such long acceleration distances are not credible because the high-speed imaging shows that the breaking region has a scale length of $\sim$ 10 cm. If, instead, the electron reaches 6 keV in 10 cm, then an $E = 6 \times 10^4$ V/m electric field is required and the acceleration of an individual electron would take only ~4 ns, if it did not collide. This electric field is much smaller than the Dreicer [79] electric field $E_D = 5.6 \times 10^{-18} n_e Z T_e^{-1} \ln \Lambda = 8 \times 10^5$ V/m, so the plasma would be collisional and not running away (i.e, not having all electrons accelerated to high energy). This is an important point that is the foundation of the acceleration theory presented in Ch. 4.

Figure 3.8 shows that the X-ray signal consists of dozens to hundreds of discrete photons emitted throughout the $\sim$ 1 μs time interval when the jet is breaking. This suggests that electron acceleration is continuously occurring during the entire 1 μs interval. This multiplicity of photons is consistent with acceleration of individual electrons in 4 ns over a 10 cm path by $E = 6 \times 10^4$ V/m.

3.4 Discussion

An inductive electric field could arise in a manner similar to (but with more extreme parameters) the spark that occurs when a toaster is unplugged from the wall; this is in effect an opening switch voltage source [80–82]. When a toaster is unplugged, the circuit produces a large LdI/dt voltage that attempts to keep the electric current flowing; here L is the inductance of the wiring up to the wall socket. This situation is also analogous to a log pile-up on a fast-moving river with the river flow velocity corresponding to current, the mass of the upstream river water to inductance, the momentum of this upstream water to magnetic flux, and the pressure drop across the log pile-up analogous to the voltage drop LdI/dt. The RT instability breaking the jet acts like the opening switch because the RT instability chokes the current channel diameter d to be smaller than the ion skin depth c/ω_{pi}.

The reason why the ion skin depth is a critical dimension can be seen by comparing the electron drift velocity along the jet axis $v_d = J_z/ne$ to the Alfvén velocity $v_A = B_z/\sqrt{\mu_0 n m_i}$ [62]. The ratio of these velocities can be expressed as

$$\frac{v_d}{v_A} = \frac{J_z}{ne}\frac{\sqrt{\mu_0 n m_i}}{B_z} = \frac{c}{\omega_{pi}}\frac{1}{rB_z}\frac{\partial}{\partial r}\left(rB_\phi\right) \tag{3.4}$$

so if B_ϕ is of order B_z and the radial scale length is of order c/ω_{pi}, the electron drift velocity becomes of order of the Alfvén velocity and so the current will become kinetically unstable. Thus, when the flux-rope cross-section is choked down to be of the order of the ion skin depth, the plasma no longer behaves like a perfect conductor. The plasma cannot conduct a current requiring such a large electron drift velocity, so in that moment it develops a resistance.

The choke region behaves as an opening switch that interrupts the current and a voltage LdI/dt appears across the gap [83–85]. This is like the pressure drop across the log pile-up in the river analogy.

Modeling the plasma in this electrical circuit picture as an LC circuit where C is from the capacitor bank power supply and L comes from both the plasma and the cabling up to the plasma is a powerful big-picture conceptual tool. Figures 3.14 (a) and (b) show this circuit diagram with the plasma immediately before and after the RT instability breaks the plasma apart. When the circuit is closed before the RT instability, the LC circuit quarter-cycle time is $t_{1/4} = \pi/2\sqrt{LC}$. The observed current rise-time is ~ 4 μs, so using the 120 μF of the fast capacitor bank gives $L \simeq 54$ nH, most of which is in the path from the capacitor to where the circuit opens. The Pulse Forming Network (PFN) cables have a similar inductance. The electric current flowing in the jet at the time of the RT instability is ~ 60 kA and the circuit has $L = 54$ nH, so the RT instability interrupting this circuit produces a voltage of $V = LdI/dt$ across the gap shown in Fig. 3.14 (b). It is important to note that this inductive LdI/dt voltage is not related to the voltage on the capacitor bank and can actually be much larger depending on L, dI, and dt. Jiang *et al.* [81] and Tataki *et al.* [82] discuss this in great detail.

The actual interruption of this current is not instantaneous and likely has shorter duration than the observed X-ray burst. A nominal interruption time of 500 ns is chosen based upon growth rates for the RT instability from Moser [62]. Direct estimation from the images in Ref. [62] yields $\gamma_{RT} = 1 \times 10^6$ /s and calculation

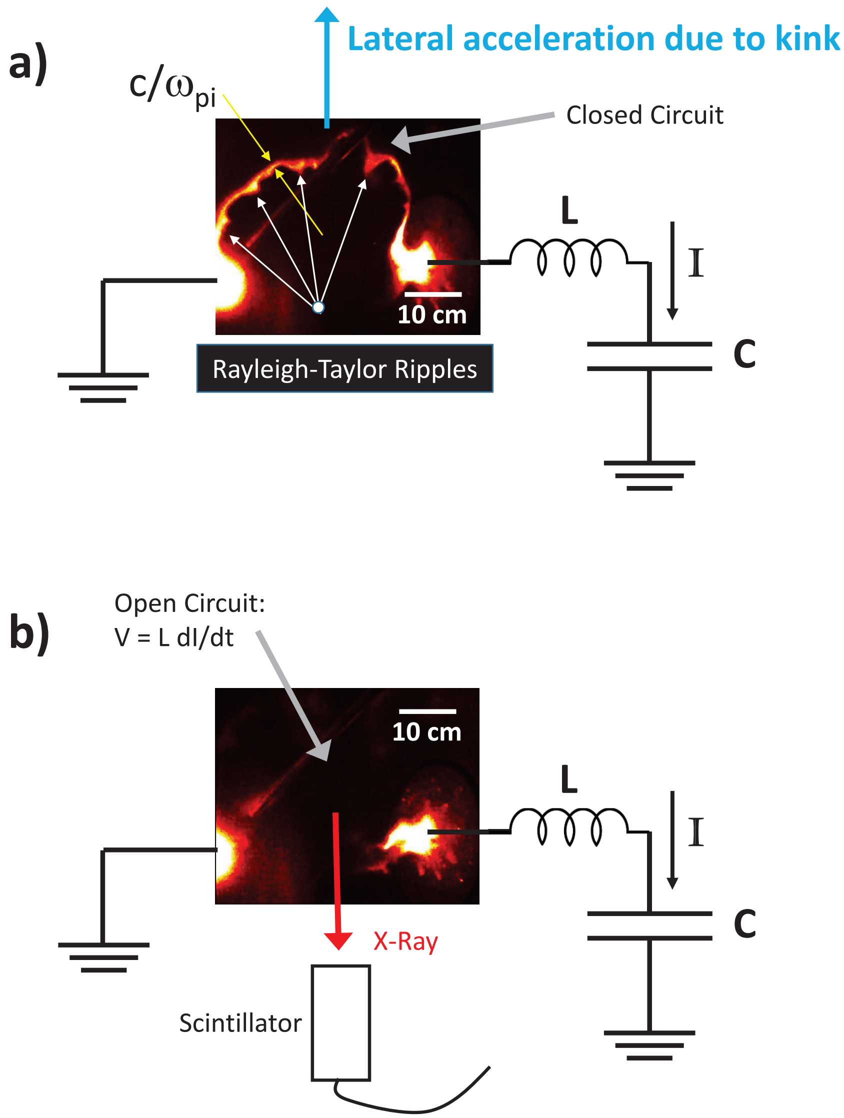

Figure 3.14: Images of the argon plasma just before and after the RT instability in a circuit diagram indicating the power electronics. a) shows the plasma at $t = 29$ μs into shot 18758 as a closed circuit when the RT instability has just started. The plasma is undergoing lateral acceleration caused by the kink instability. The RT ripples are indicated by the white arrows. b) shows the plasma and circuit 1 μs later at $t = 30$ μs, just after the RT instability has broken the jet to form an open circuit. A voltage LdI/dt appears across the gap.

using the measured effective gravity and observed ripple wavelength gives $\gamma_{RT} = \sqrt{g_{eff}k} = 3 \times 10^6$ /s where g_{eff} and k both come from the images in Ref. [62] and were documented at the beginning of Ch. 3. Choosing a nominal interruption time intermediate between the observed and calculated growth rates, 500 ns, will produce an inductive voltage of $V = LdI/dt \simeq 6$ kV ; this is consistent with accelerating electrons to ~ 6 keV. The value of 6 keV is nominal because some electrons may be accelerated to higher energies while only emitting Bremsstrahlung photons of lower energy since their slowing-down collisions can be less than head-on.

The simultaneous substantive change in global shot-averaged poloidal flux structure from before to after the RT instability, the X-ray evidence for a large transient electric field and the six other measurements listed at the beginning of Ch. 3 provide strong circumstantial evidence that a fast magnetic reconnection event is instigated by the RT instability. If one were to argue that there is no magnetic reconnection event, i.e., if one were to argue that magnetic flux remains frozen into the plasma frame throughout the entire time when the above eight phenomena occur, then there would be no electric field in the plasma frame, so no means exist for accelerating electrons to high energy. Furthermore, the voltage transient observed by the high voltage probe indicates there is a sudden change in the magnetic flux linked by the electric circuit going from the inner electrode to outer electrode. If magnetic flux were frozen into the plasma, then no such change in flux linked by this circuit could occur, so no voltage transient would be observed at the electrodes.

At this point, the questions from the introduction to flux rope plasmas in Ch. 1 re-emerge: i) How does a small subset of particles get energized? ii) How is the subset selected? iii) Why can this subset accelerate while the plasma is both cold and collisional?

The following mechanism is postulated. The key ideas are the energy dependence and statistical nature of the mean free path. The plasma is very dense, so there are a large number of electrons and ions in the reconnection region. The reconnection electric field accelerates all the electrons, but because the plasma is very collisional with a mean free path initially on the order of 1 μm, only e^{-1} of the electrons are successfully accelerated over the 1 μm mean free path as $1 - e^{-1} \approx 0.66$ of the electrons are scattered in this distance. The electrons that did not collide are now moving with more kinetic energy than initially, so their next mean free path is longer. Again, e^{-1} are successfully accelerated and gain even more energy than previously. This cycle of acceleration and increasing mean free path repeats over the reconnection distance. Not only can this type of acceleration explain the X-ray observation, but also the EUV observation as particles that only accelerate part of the way before radiating could easily emit EUV. Because of the high density, a tiny but macroscopic number of initially thermal electrons can successfully accelerate to keV energies and then finally collide to emit a large energy photon. A full quantitative description of this proposed mechanism will be presented in Ch. 4.

Chapter 4

X-RAY THEORY

[1] R. S. Marshall and P. M. Bellan. "Acceleration of charged particles to extremely large energies by a sub-Dreicer electric field". In: *Physics of Plasmas* 26.4 (2019), p. 042102. DOI: https://doi.org/10.1063/1.5081716.

This chapter presents the model for how a small subset of thermal particles can be accelerated to high energies in a plasma that is ostensibly so extremely collisional that no such acceleration would be expected. This model involves combining statistical concepts with the predictions of Vlasov-based Fokker-Planck calculations. It explains why a small cohort of electrons in a cold, collisional plasma will be accelerated to energies orders of magnitude larger than thermal energy by a sub-Dreicer electric field. Thus, the model differs from a runaway situation, i.e., from the situation where *all* electrons are accelerated to high energy. It also differs from certain previous considerations of sub-Dreicer electric fields [86–89] and is shown to provide a much stronger effect. As discussed in Section 3.4, the electric field is proposed to be the inductive electric field associated with a sudden change in electric current. This current interruption results from a fast magnetic reconnection process breaking apart the jet [18, 62]. Because the model depends only on statistics, Fokker-Planck collision theory, and current disruption, it should apply to solar and astrophysical situations as well as in the laboratory.

4.1 Overview of the Model

The experiment has a large electric current flowing along the axis of the collimated MHD-driven jet. On reaching a critical length, the jet kinks creating an effective gravity upon which a fast growing Rayleigh-Taylor instability develops. The Rayleigh-Taylor instability acts to interrupt the axial current in the jet which induces a large axial inductive electric field at the location of the interruption. For the purposes of the model presented here, the configuration will be considered one dimensional with a finite-duration electric field in the z direction having finite axial extent d. Because of Lenz's law, this electric field is oriented so as to accelerate electrons axially, i.e., in the z direction. The Dreicer electric field,

$$E_D = 0.43\frac{n_e Z e^3 \ln\Lambda}{8\pi\epsilon_0^2 \kappa T_e} = 5.6\times 10^{-18} n_e Z \frac{\ln\Lambda}{T_e} \tag{4.1}$$

in units of V/m, is the condition for runaway acceleration. When $E > E_D$, the acceleration from the electric field overpowers the drag from collisions and *all* electrons accelerate to arbitrarily high energy, regardless of each electron's initial energy.

By contrast, the statistical acceleration model to be presented here requires a sub-Dreicer electric field, $E < E_D$, and because of this, it will be shown that only a fraction of the electron population is accelerated. This fraction is determined by a statistical analysis of the acceleration process.

The sub-Dreicer electric field results from an interruption of an electric current as in an opening electric switch. In this moment of interruption when the switch is opened, the plasma transitions from behaving like an LC-circuit to behaving like an LR-circuit. Opening a switch in a circuit carrying a current I and having an inductance L produces a voltage LdI/dt so if the rate of change of current is large, a large voltage and hence a large electric field $E = (1/d)(LdI/dt)$ will develop. The initial LC-circuit analog to Fig. 3.14(a) is sketched in Fig. 4.1(a). Opening the switch is effectively the same as if one of the wires suddenly develops a large resistance, as sketched in Fig. 4.1(b), the analog to Fig. 3.14(b). The inductive energy of the circuit will be dumped into the resistance of this wire. This is seen by multiplying the circuit equation $IR + LdI/dt = 0$ by I to obtain $I^2R = -d/dt(LI^2/2)$, and then integrating in time.

4.2 Statistical Selective Acceleration Process

We now present the statistically selective process. This process accelerates a small fraction of the electrons in a cold, collisional plasma to an energy orders of magnitude greater than thermal despite: (i) $\lambda << L$ where the nominal thermal collision mean free path, $\lambda \sim \mu$m, is microscopic compared with the system size $L \sim$ cm and (ii) the electric field is much smaller than the Dreicer electric field, i.e., $E \ll E_D$.

According to Fokker-Planck theory, the slowing down time τ_s of a beam of test particles T starting with an initial velocity u greater than both electron and ion

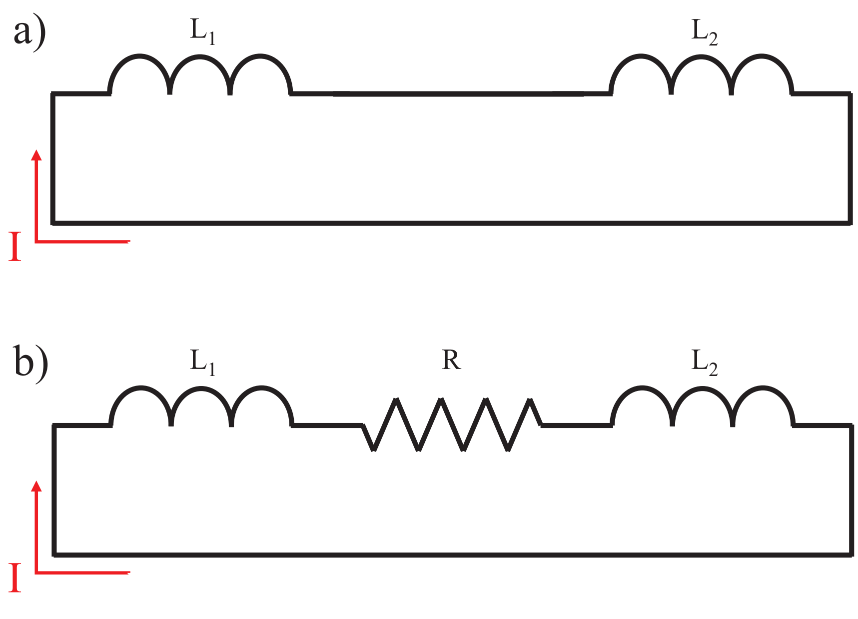

Figure 4.1: Schematic of an inductive circuit. A current will flow indefinitely in a) if there is no resistance in the wires. If the wire connecting L_1 and L_2 is replaced by a large resistance R corresponding to an opening switch, this will result in a large voltage across R and the entire inductive energy $\frac{1}{2}(L_1 + L_2)I^2$ of the circuit will be dumped into R.

thermal velocities is [1, 90, 91]

$$\tau_s \approx \frac{4\pi\epsilon_0^2}{n_e q_e^2 \ln\Lambda} \frac{m_T^2}{q_T^2} \frac{u^3}{Z + 1 + m_T/m_e}. \tag{4.2}$$

The test particles here are electrons so $m_T = m_e$ and $q_T = q_e$. We use the Caltech jet experiment parameters, namely an argon plasma with $Z = 2$ in the reconnection region, a density $n_e = 3 \times 10^{22}$ m^{-3}, and a temperature $T = 2$ eV. These give $\ln\Lambda \simeq 4.8$ where $\Lambda = 6\pi n\lambda_D^3$ and $\lambda_D = \sqrt{\epsilon_0 \kappa T/n q_e^2}$ is the Debye length.

Because $\tau_s \sim u^3$, the mean free path $\lambda = u\tau_s$ for an electron increases quadratically as it accelerates and it follows that electrons with higher initial velocities have longer mean free paths. First consider an electron having some initial velocity v_0 exceeding the thermal velocity $v_T = \sqrt{2\kappa T/m_e}$. The acceleration process will be calculated in two steps: (i) the acceleration of the electron having velocity v_0 will be determined, and then (ii) the probability of having different initial velocities v_0 will be taken into account. The first critical assumption is related to the collisional mean free path.

Since $\lambda = u\tau_s$, Eq. 4.2 shows that the initial mean free path of the electron is

$$\lambda_0 = \frac{16\pi\epsilon_0^2}{(Z+2)n_e q_e^4 \ln\Lambda} W_0^2 \tag{4.3}$$

where

$$W_0 = \frac{1}{2} m_e v_0^2 \tag{4.4}$$

is the initial electron kinetic energy. The instantaneous mean free path for the electron can therefore be written as

$$\lambda(z) = \lambda_0 \left(\frac{v(z)}{v_0}\right)^4. \tag{4.5}$$

The kinetic energy of the electron after traveling a distance z is given by

$$\frac{1}{2} m_e v(z)^2 = W_0 + q_e E z - \int_0^z m_e \left(\nu_{ee} + \nu_{ei}\right) v(z') dz' \tag{4.6}$$

where the integral on the right represents energy lost by the accelerating electron due to collisional drag via Rutherford scattering.

It will be assumed that $q_e E z >> \int_0^z m_e \left(\nu_{ee} + \nu_{ei}\right) v(z') dz'$ so the energy loss due to the drag term in Eq. 4.6 can be neglected. Of course, drag cannot be neglected for all electrons in the plasma, but neglecting drag is reasonable for the small subset of electrons that is accelerated to high energy. The conservation of energy equation becomes $\frac{1}{2} m_e v(z)^2 = W_0 + q_e E z$, so an accelerating electron has a velocity

$$v(z) = v_0 \sqrt{1 + \frac{\alpha z}{\lambda_0}} \tag{4.7}$$

where

$$\alpha = \frac{q_e E \lambda_0}{W_0}. \tag{4.8}$$

We use the thermal velocity v_T as a reference velocity and define a reference mean free path $\lambda_{0,T}$ as the initial mean free path of electrons having v_T as their initial velocity. Equation 4.3 gives $\lambda_{0,T} \approx 1$ μm using $T = 2$ eV. Equation 4.3 further shows that electrons with $v_0 > v_T$ will have a longer initial mean free path.

The probability for any single electron to collide after traveling some distance z is $P = 1 - \exp(-z/\lambda)$ where λ is the instantaneous mean free path. It follows that the electron has a $P = 0.63$ chance of colliding while traveling the first mean free path up to $z = \lambda(v_0)$. However, it is critical to note that this also means that after traveling one mean free path, the electron has an $e^{-1} = 0.37$ chance of *not* colliding.

Consider now the 0.37 fraction of the electrons with initial velocity v_0 that did not collide between $z = 0$ and $z = \lambda(v_0)$. These electrons will have gained an energy $q_e E \lambda_0$ on being accelerated collisionlessly in the electric field and so will now have a new velocity $v_1 = v_0\sqrt{1 + q_e E \lambda_0 / W_0}$. To calculate what happens next, this new velocity must be used for $v(z)$ on the right hand side Eq. 4.5 to give a new, larger $\lambda(z)$. Now consider what happens to this group of electrons when they travel this second, longer mean free path. A fraction 0.63 will collide, but a fraction 0.37 will not collide and will gain energy $q_e E \lambda_1$. This process will repeat so that each time the electrons travel a successive mean free path λ_n, they gain additional energy $q_e E \lambda_n$ if they do not collide.

Since d is the path length over which the electric field exists, the voltage drop along this path is $V = Ed$. We now consider the special subset of electrons having initial velocity v_0 that manage to travel the entire distance d without colliding. The final kinetic energy of these electrons that do not collide is

$$W_f = \frac{1}{2} m_e v_f^2 = W_0 + q_e E d \simeq q_e E d \tag{4.9}$$

if $W_f \gg W_0$. From Eq. 4.8, it is seen that $d = W_f \lambda_0 / (\alpha W_0) = v_f^2 \lambda_0 / \left(\alpha v_0^2\right)$. The number of mean free paths traveled by these electrons with initial velocity v_0 that never collide is

$$\begin{aligned} N(v_0) &= \int_0^d \frac{\mathrm{d}z}{\lambda(z)} \\ &= \frac{1}{\lambda_0} \int_0^{v_f^2 \lambda_0 / \left(\alpha v_0^2\right)} \frac{\mathrm{d}z}{\left(1 + \frac{\alpha z}{\lambda_0}\right)^2} \\ &= \frac{1}{\alpha} \left(1 - \frac{1}{\frac{W_f}{W_0} + 1}\right) \\ &\simeq \frac{1}{\alpha} \\ &= \frac{W_0}{q_e E \lambda_0}. \end{aligned} \tag{4.10}$$

This collisionless cohort will constitute a fraction $\exp(-N(v_0))$ of the electrons that had initial velocity v_0 since upon traversing each successive collisional mean free path, only a fraction e^{-1} of the electrons did not collide. Since the fraction of electrons having initial velocity v_0 is given by the Maxwell-Boltzmann distribution

$$f(v_0) = \frac{1}{\pi^{1/2} v_T} e^{-v_0^2/v_T^2}, \tag{4.11}$$

the fraction of all electrons with initial velocity $v_0 \geq v_T$ that are accelerated to final energy W_f is

$$F = \int_{v_T}^{\infty} f(v_0) e^{-N(v_0)} \mathrm{d}v_0. \tag{4.12}$$

Figure 4.2 sketches the statistical acceleration model. Only the positive half of the distribution with velocity $v_0 > 0$ is shown because the acceleration is in the positive direction and later in this section the contribution from electrons initially moving in the opposite direction will be shown to be negligible. Blue arrows represent the successive mean free paths associated with electrons having different v_0 with each initial velocity v_0 marked by a black circle. The length of the initial mean free path λ_0 increases as v_0 increases and each subsequent mean free path λ_i is larger than the previous mean free path λ_{i-1}. The relative number of electrons having a specific v_0 is indicated by the Maxwell-Boltzmann distribution (black curve), and this shows that the number of electrons having initial velocity v_0 scales as $\exp(-v_0^2/v_T^2)$.

We now define the reference number

$$N_T = \frac{\kappa T}{W_f} \frac{d}{\lambda_{0,T}} = \frac{\kappa T}{q_e E \lambda_{0,T}} = \frac{v_T^2}{v_f^2} \frac{d}{\lambda_{0,T}} \tag{4.13}$$

which is the number of mean free paths traversed by an initially thermal electron that accelerates without collisions to attain the energy W_f. Using Eq. 4.5, the mean free path λ_0 for an electron with initial velocity v_0 can be expressed as

$$\frac{\lambda_0}{\lambda_{0,T}} = \left(\frac{v_0}{v_T}\right)^4. \tag{4.14}$$

Using Eqs. 4.10 and 4.14, the number of mean free paths of an electron with initial velocity v_0 can then be expressed as

$$N(v_0) = \frac{v_0^2}{v_f^2} \frac{d}{\lambda_0} = N_T \frac{v_0^2}{v_T^2} \frac{\lambda_{0,T}}{\lambda_0} = N_T \left(\frac{v_T}{v_0}\right)^2. \tag{4.15}$$

Substituting for $N(v_0)$ in Eq. 4.12 using Eq. 4.15 gives

$$F = \frac{1}{\pi^{1/2}} \int_1^{\infty} e^{-g(\xi)} \mathrm{d}\xi \tag{4.16}$$

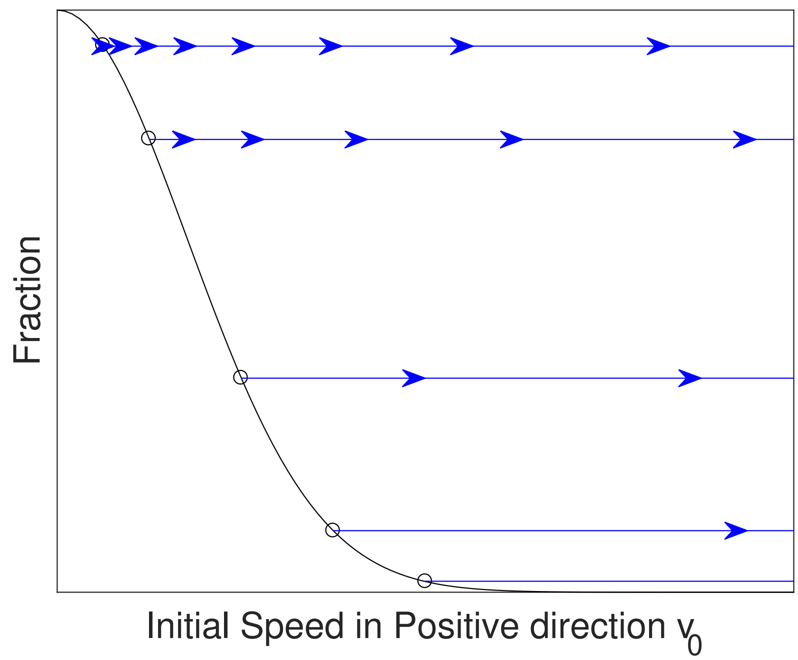

Figure 4.2: Sketch of the statistical acceleration model. The black curve represents the Maxwell-Boltzmann velocity distribution of the electrons. Five positions on the curve (circles) are chosen with distinct initial velocities v_0. The blue arrows pointing to the right from each circle represent the mean free paths for an electron that does not collide starting at initial velocity v_0 . The number of non-colliding electrons decreases by a factor e^{-1} for each successive mean free path.

where $\xi = v_0/v_T$ and

$$g(\xi) = \xi^2 + \frac{N_T}{\xi^2}. \tag{4.17}$$

Because $N_T \gg 1$ for a sub-Dreicer electric field as will be shown, the integral in Eq. 4.16 can be evaluated with high accuracy using the method of steepest descent [92]. This method exploits the property that the integrand in Eq. 4.16 has a sharp maximum when $g(\xi)$ is near its minimum $g_{\min}$ which occurs at $\xi_m = \pm N_T^{1/4}$. Figure 4.3 plots $e^{-g(\xi)}$ for $N_T = 33$ where N_T was defined in Eq. 4.13 and shows that $e^{-g(\xi)}$ is at a maximum when $\xi = N_T^{1/4}$ giving the minimum value of g to be $g_{\min} = 2N_T^{1/2}$. Since $v_0 > v_T$ is assumed, the minimum at $\xi_m = +N_T^{1/4}$ is the relevant choice and at this location $g'' = 8$. Taylor expansion of $g(\xi)$ in the vicinity of its minimum gives $g(\xi) = 2N_T^{1/2} + 4(\xi - \xi_m)^2$, so Eq. 4.16 becomes

$$F \simeq \frac{e^{-2N_T^{1/2}}}{\pi^{1/2}} \int_1^\infty e^{-4(\xi-\xi_m)^2} \mathrm{d}\xi. \tag{4.18}$$

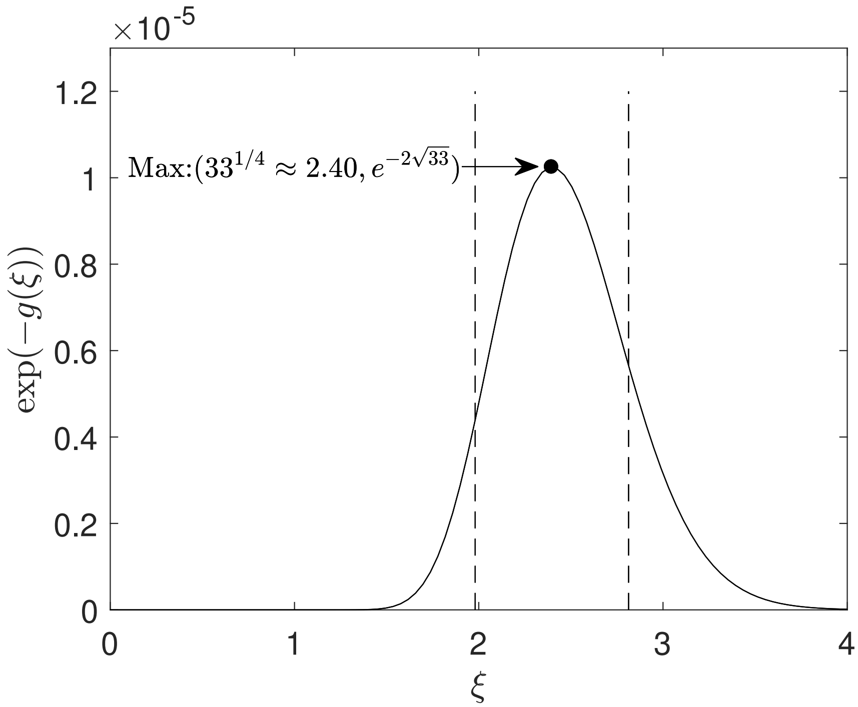

Figure 4.3: Plot of $\exp(-g(\xi))$ versus ξ for $N_T = 33$. Dashed vertical lines show the location of $\xi = 1.98$ and $\xi = 2.81$ where $\exp(-g(\xi))$ is at half its maximum.

On defining $\eta = 2(\xi - \xi_m)$, Eq. 4.18 can be written as

$$\begin{aligned} F &= \frac{e^{-2N_T^{1/2}}}{2\pi^{1/2}} \int_{2-2N_T^{1/4}}^{\infty} e^{-\eta^2} \mathrm{d}\eta \\ &\simeq \frac{e^{-2N_T^{1/2}}}{2\pi^{1/2}} \int_{-\infty}^{\infty} e^{-\eta^2} \mathrm{d}\eta \\ &= \frac{e^{-2N_T^{1/2}}}{2} \end{aligned} \tag{4.19}$$

where the lower limit of the integral has been extended to $-\infty$ because $2 - 2N_T^{1/4}$ is a large negative number. By extending the lower limit of the integrand from $2 - 2N_T^{1/4}$ to $-\infty$, a tiny error associated with integrating over the electrons moving in the opposite direction is introduced. This error is referred to as $G(N_T)$ because it is a function of N_T only and is given by

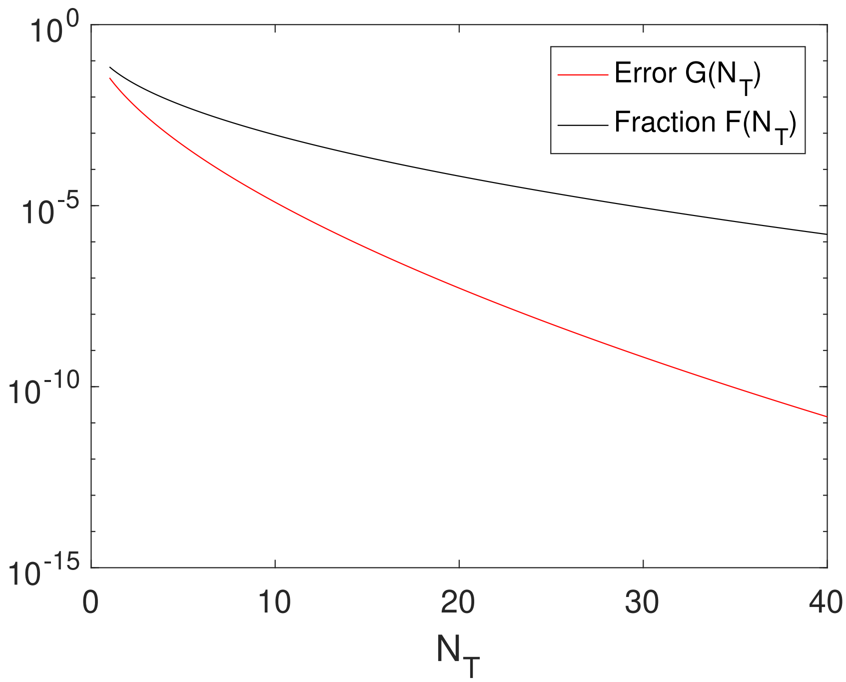

Figure 4.4: Plot of F and G from Eqs. 4.19 and 4.20, respectively, shows that G is negligible compared to F for large N_T. Error $G(N_T)$ shown in red is associated with expanding the lower limit of the integrand in Eq. 4.19 to $-\infty$. Actual values for $F(N_T)$ are shown in black.

$$
\begin{aligned}
G &= \frac{e^{-2N_T^{1/4}}}{2\pi^{1/2}} \int_{-\infty}^{2-2N_T^{1/2}} e^{-\eta^2} \mathrm{d}\eta \\
&= \frac{e^{-2N_T^{1/2}}}{2\pi^{1/2}} \int_{2N_T^{1/4}-2}^{\infty} e^{-\eta^2} \mathrm{d}\eta \\
&= \frac{e^{-2N_T^{1/2}}}{4} \mathrm{erfc}\left(2N_T^{1/4} - 2\right)
\end{aligned} \tag{4.20}
$$

where erfc is the complimentary error function.

Figure 4.4 shows that G is negligible compared to F for large N_T. As an example, for $N_T = 33$, $G \sim 10^{-10}$ whereas $F \sim 10^{-6}$. Thus the fictitious addition of a tiny number of electrons moving in the negative direction for the mathematical purpose of having a Gaussian integral makes a negligible error to the evaluation of F.

The situation where N_T is near unity corresponds to all the electrons being accelerated, i.e., to the Dreicer runaway situation whereas $N_T \gg 1$ corresponds to the statistical acceleration situation where only a fraction of the electrons are accelerated to high energy. The situation when N_T is near unity is seen by solving for E in Eq. 4.13 and then substituting for $\lambda_{0,T}$ using Eq. 4.3:

$$\begin{aligned} E &= \frac{\kappa T}{q_e N_T \lambda_{0,T}} \\ &= \frac{1}{N_T}\frac{Z+2}{0.86Z}\left(0.43\frac{n_e Z e^3 \ln\Lambda}{8\pi\epsilon_0^2 \kappa T_e}\right) \\ &= \frac{Z+2}{0.86Z}\frac{1}{N_T}E_D. \end{aligned} \tag{4.21}$$

Equation 4.21 shows that when N_T is near unity, E is close in magnitude to E_D. In this case, acceleration is no longer statistical in nature as *all* electrons are accelerated to high energy.

In order for an electron that has managed to accelerate collisionlessly through $N_T \gg 1$ successive and increasing mean paths to radiate an X-ray, it must undergo a rapid deceleration. This would happen if the electron were to make a large-angle collision. It is now recalled that the cumulative effect of small angle collisions dominates large angle collisions by a factor of 8lnΛ. Thus, the fraction of electrons that are first accelerated collisionlessly to have the full voltage drop and then have a large angle collision so as to radiate an X-ray photon is

$$F_{Xray} = \frac{e^{-2N_T^{1/2}}}{16\ln\Lambda}. \tag{4.22}$$

We believe the particle acceleration model presented here is conceptually, but not rigorously, correct for the following reasons. First, when a fast electron moves through the plasma, the fast electron generates a Langmuir wave wake as a result of the background plasma electrons rearranging their positions from the Coulomb interaction with the fast electron. This wake causes a drag on the fast electron since the wake energy comes at the expense of the kinetic energy of the fast electron. This wake drag is assumed here, as in Fokker-Planck collision theory, to be negligible. Second, the use of a collision frequency oversimplifies the real situation where a group of initially fast electrons has both drag and velocity diffusion. After one slowing-down time, velocity diffusion causes some electrons to move faster and some electrons to move slower than the average velocity of all the electrons in the group under consideration. We are effectively considering the subset of initially fast electrons for which velocity diffusion results in a slowing down much less than the average. This subset is represented in a simplified way as being a small cohort that does not slow down at all and so does not collide. This simplification comes from using a collision frequency rather than the combination of slowing down and velocity diffusion characterized by a Fokker-Planck model. Third, the Fokker-Planck slowing-down time in Eq. 4.2 depends indirectly on a Vlasov fluid treatment since Fokker-Planck collision theory incorporates Debye shielding, and Debye shielding is derived by placing a test particle in a Vlasov plasma. The collision frequency extracted from Fokker-Planck theory is used in the statistical acceleration model here as a Klimontovich-like single particle picture to describe how an individual electron in a plasma accelerates in an applied electric field. Thus, the statistical acceleration model mixes ideas from both fluid-based Vlasov theory and single-particle-based Klimontovich theory to arrive at the conclusion that there exists a subset of fast electrons which experiences much less drag than average, and this is simplified to being no drag at all. This is in qualitative agreement with reality where velocity diffusion causes a spread in drag, so some electrons experience much less drag than average. The statistical acceleration model differs from the Dreicer runaway criterion which considers only the average drag and ignores the existence of the small subset of electrons that experience much less than average drag. Appendix B provides a detailed discussion on the limitations of Debye shielding when considering collisional drag of a fast particle and provides additional support for the existence of a subset of fast electrons that effectively do not collide.

4.3 Summary of the Caltech Jet Experiment Observations

The observation of a hard X-ray burst by four different detectors during this fast magnetic reconnection event [18] serves as evidence of this statistical acceleration model. Additional evidence for the model can be found in the Chai *et al.* [61] observation of an Extreme Ultra-Violet (EUV) burst occurring at the same time and location as the RT instability. Electrons in the accelerating cohort that successfully travel a smaller number of mean free paths before colliding will attain lower energies, e.g., 10's of eV. Upon colliding with argon ions, these electrons will excite EUV atomic lines.

As reported in Ch. 3, the photons in the X-ray burst have a broad spectrum centered at about 6 keV, the burst lasts $\sim 1\ \mu$s, and the length of the presumed emitting region is determined from photos of the Rayleigh-Taylor unstable region to be 10 cm. The voltage 6 kV is consistent with interruption of the 60 kA jet current in $\sim 1\ \mu$s using a ~ 60 nH circuit inductance. By taking into account the solid angle subtended by the detector, the energy in the X-ray burst is $\sim 10^{-8}$ J which is extremely small compared to the 100 J stored in the 60 nH circuit conducting the 60 kA current.

4.4 Application of the Statistical Acceleration Model to the Caltech Jet Experiment

The inductive electric field results from a voltage drop of 6 kV in $d = 0.1$ m and so is $E = 6 \times 10^4$ V/m. Using $T = 2$ eV and $\lambda_{0,T} = 10^{-6}$ m gives

$$N_T = \frac{\kappa T}{q_e E \lambda_{0,T}} = \frac{T_{eV}}{E \lambda_{0,T}} = \frac{2}{6 \times 10^4 \times 10^{-6}} = 33. \tag{4.23}$$

Using $N_T = 33$ in Eq. 4.19 gives a fraction $F = 4.8 \times 10^{-6}$ of the original thermal electrons that are successfully accelerated up to 6 keV by accelerating collisionlessly in 10 cm. Evaluation of Eq. 4.22 using $\ln \Lambda \approx 4.8$ shows that the fraction of electrons that generate X-rays by first accelerating collisionlessly in 10 cm and then decelerating in a large angle collision is $F_{Xray} = 1.3 \times 10^{-7}$. This is consistent with the extremely small X-ray transient burst of $\sim 10^{-8}$ J compared to a stored magnetic energy $LI^2/2 = 10^2$ J. It is also possible that 6 keV X-rays have been produced by electrons that have gained more than 6 keV, but then slowed down by making less than head-on collisions so not all the energy is lost in a single collision.

4.5 How Statistical Acceleration Differs from the Modified Runaway Situation

The possibility that a sub-Dreicer electric field E will accelerate electrons having sufficiently high initial velocity to runaway has been previously discussed by many authors including Refs. [86–89]. For example, on pages 38-39 of the textbook by Helander and Sigmar [89] it is stated "However weak this [electric] field may be, it is still larger than the friction force on sufficiently fast electrons. The latter will therefore be accelerated by the electric field to arbitrarily high energy and form a population of so-called runaway electrons."As a second example, the concept that a weak electric field will accelerate sufficiently fast electrons to runaway is the basis of the analysis by Scudder and Karimabadi [88]. As a third example, Livi and Marsch [93] report a numerical calculation of the formation of a tail of high energy particles. These previous approaches did not consider time dependence of the electron distribution and only considered a time-independent competition between the accelerating force from an electric field and the drag force from collisions. We do not disagree with the conclusions of these previous discussions, but show here that the statistical acceleration mechanism is far more important than the process quoted above from the book by Helander and Sigmar [89].

The key difference between the statistical acceleration theory based on Eq. 4.2 compared with the discussion in Livi and Marsch [93] and Scudder and Karimabadi [88] is that the latter do not consider the full time-dependent Vlasov equation in their analysis whereas the statistical acceleration model effectively does. A mathematical discussion of the difference seen by considering the 1D Collisional Vlasov Equation is presented in Section 7 of Ref. [53].

Both Scudder and Karimabadi [88] and Helander and Sigmar [89] point out that a sub-Dreicer electric field will accelerate tail electrons with sufficiently fast initial velocity because collisional drag scales as $1/v^3$. We will refer to this process as 'modified runaway' to distinguish it from the statistical acceleration model presented here. The difference can be seen by carefully parsing Helander and Sigmar's previously quoted statement characterizing the modified runaway process. We agree that this modified runaway process occurs, but argue that it is far less important than the statistical acceleration effect for two reasons. First, there will be an extremely small number of electrons that are sufficiently fast to have their drag be less than the accelerating force from the electric field. Second, if the electric field is arbitrarily small, the electrons will have to travel an enormous length since the energy gained scales as qEl and this will take an enormous time. We discuss these two reasons in detail below.

First reason: In the Caltech experiment, $d \approx 10$ cm and the inductively developed accelerating electric field is 60 kV/m. Using Eqs. 4.3 and 4.5, a kinetic energy $W = 630$ eV would be required for an electron in the Caltech plasma to have a 10 cm mean free path. Electrons with initial energy exceeding 630 eV would accelerate without frictional drag in the 10 cm path length and so gain 6 kV. This 630 eV kinetic energy corresponds to a critical velocity $v_c = 1.5 \times 10^7$ m/s, i.e., 18 times faster than the thermal velocity $v_T = 8.4 \times 10^5$ m/s of the 2 eV plasma. The fraction of electrons with $v > v_c$ is

$$\begin{aligned} F_{runaway} &= \frac{1}{\pi^{1/2} v_T} \int_{v_c}^{\infty} e^{-v^2/v_T^2} dv \\ &= \frac{1}{2} \text{erfc}\left(\frac{v_c}{v_T}\right) \\ &= 5.1 \times 10^{-141}. \end{aligned} \tag{4.24}$$

The statistical acceleration theory predicts $F = 4.8 \times 10^{-6}$, 135 orders of magnitude larger! The important difference is that the statistical acceleration model predicts acceleration for the substantial number of electrons with energy only two to three times that of the thermal energy, whereas the modified runaway process relies on the virtually non-existent population of electrons having energy exceeding 300 times the thermal energy.

Second reason: According to the Helander and Sigmar description [89] of the modified runaway process, electrons with a sufficiently fast initial velocity in an arbitrarily weak constant electric field will be accelerated to arbitrarily high energy. Consider the subset of electrons in the Caltech experiment having sufficient initial kinetic energy to be collisionless, but now assume that the electric field is arbitrarily weak, say $E = 6 \times 10^{-12}$ V/m to give a precise example. In order to be accelerated to the observed $W_f = 6$ keV energy, the electrons would have to travel $l = W_f/(qE) = 10^{15}$ meters, i.e., a distance 16 orders of magnitude larger than the experiment. The time for acceleration to the final velocity is $t = \sqrt{2mW_f}/(qE) \simeq 1$ year and so is correspondingly large. We, therefore, conclude that the arbitrarily weak electric fields postulated in the modified runaway situation are not capable of accelerating electrons to arbitrarily high energies in situations having physically sensible time and length scales.

Chapter 5

APPLICATION TO THE SOLAR CORONA

[1] R. S. Marshall and P. M. Bellan. “Acceleration of charged particles to extremely large energies by a sub-Dreicer electric field”. In: *Physics of Plasmas* 26.4 (2019), p. 042102. DOI: https://doi.org/10.1063/1.5081716.

The results of the laboratory experiment and the associated statistical acceleration model can be used to propose a mechanism for the acceleration of particles in the solar corona and the solar chromosphere. The key difference is that a phenomenon that happens on the order of microseconds and centimeters in the laboratory would happen over much longer time and length scales in solar situations [52]. While MHD aspects of the experiment can be scaled directly to the solar situation, the non-MHD statistical acceleration model does not scale directly. This lack of direct scaling motivates consideration of certain additional phenomena when considering the solar situation.

The Caltech jet experiment will be scaled and compared to three previous, representative solar studies with consideration of both MHD and non-MHD behavior. The three solar studies are:

1. Kink instability in the corona: Wyper *et al.* [94] presented a numerical MHD model of a jet having a kink instability in the solar corona and provided nominal parameters of $B = 10^{-3}$ T, $n = 10^{16}$ m^{-3}, $l = 10^{6}$ m, $T = 100$ eV, jets lasting 180 s with velocities of 120-450 km/s, and instabilities with time scales of 12.5–25 s. Wyper *et al.* made no mention of the existence of Rayleigh-Taylor instabilities or of non-MHD phenomena.

2. Particle acceleration in the corona: Tsuneta [95] has used Yohkoh X-ray observations to argue that particle acceleration in the corona along a coronal loop takes place because of a 100 kV drop along field lines; this would correspond to the 6 kV voltage drop in the lab experiment. Nominal parameters for the situation described by Tsuneta are shown in the second column of the data in Table 5.1 followed by derived parameters.

3. Particle acceleration in the chromosphere: Zaitsev *et al.* [96] hypothesizes that particle acceleration takes place in the solar chromosphere rather than in the corona. The rationale underlying this hypothesis is that the flux of energetic particles leaving the sun is very large, so it would be more likely to be sourced by the chromosphere as the chromosphere density is much higher than that of the corona. Nominal parameters from Zaitsev *et al.* are shown in the third data column of Table 5.1.

5.1 MHD Scaling

Here, I will use the MHD scaling laws from Section 1.3 that result from the dimensionless nature of the MHD equations. Using reference values for the Caltech jet $n_{lab} \simeq 3 \times 10^{22}$ m^{-3}, $B_{lab} = 1$ T, and $T_{lab} = 2$ eV, we see that the lab experiment has $\beta = \mu_0 n\kappa T/B^2 = 10^{-2}$. Figure 3 from Gary [97], a plot of β versus height for a range of solar conditions, shows that it is reasonable to assume that the lab and solar plasmas have the same β. In particular, Fig. 3 from Ref. [97] shows that the nominal $\beta \sim 10^{-2}$ of the lab experiment can occur in both chromosphere and corona regions. Therefore, it will be assumed that $\beta_{lab} \approx \beta_{solar} \approx \beta \approx 10^{-2}$. The argon lab plasma has a reference mass density $\rho_{0,lab} = nm_i = 2 \times 10^{-3}$ kg m^{-3} and a reference Alfvén velocity $v_{A,lab} = B_{lab}/\sqrt{\mu_0 \rho_{lab}} = 2 \times 10^4$ m s^{-1}. We choose $l_{lab} = 0.3$ m to be the reference length (nominal jet length) so the reference time is $\tau_{lab} = l/v_{A,lab} = 15$ μs.

Scalings from the Caltech experiment to the solar corona and to the solar chromosphere of quantities described by ideal MHD are given in Table 5.2. Table 5.2 shows that the Caltech lab MHD parameters scale to quite credible solar parameters, so the lab experiment can be considered a good analog computer for solar MHD physics. In particular, the lab experiment should constitute a reasonable scale model of both the kink and the RT instability since both of these are MHD instabilities described by Eqs. 1.1 - 1.4. The three equations in Eq. 1.6 produce $c_1 = 1.875 \times 10^{-8}$, $c_2 = 1.2 \times 10^8$, and $c_3 = 66666.7$ for the scaling from the lab experiment to solar corona parameters while for scaling to solar chromosphere parameters is $c_1 = 6 \times 10^{-7}$, $c_2 = 1.2 \times 10^6$, and $c_3 = 3 \times 10^4$.

The model used by Wyper *et al.* [94] has no mass flux into the system and no electric current flowing into and out of the system. Kinking is observed and any magnetic reconnection results from numerical diffusion, an artifact of the numerical method, and not from two-fluid effects associated with ion skin depth scale lengths.

Wyper *et al.* [94] had nominal parameters of $B = 10^{-3}$ T, $n = 10^{16}$ m^{-3}, $l = 10^6$ m, $T = 100$ eV, jets lasting 180 s with velocities of 120-450 km/s, and instabilities with time scales of 12.5–25 s. These parameters are quite close to the scale-up of the lab experiment to solar corona parameters as described in Table 5.2. The lab experiment toroidal magnetic field is $B_\phi = \mu_0 I/2\pi a = 0.6$ T which means that the nominal jet velocity is $v_{jet} = v_A B_\phi / B = 0.6 v_A$, so the scaled up solar jet velocity will be $v_{jet} = 0.6 v_A = 400$ km/s which is consistent with Ref. [94]. The scale-up of the kink characteristic time to 5 s is in reasonable agreement with the 12.5–25 s time scale in Ref. [94]. The lab experiment thus scales extremely well to the solar situation from the point of view of ideal MHD.

It should be noted that Ref. [94] did not observe RT instabilities despite RT being an MHD phenomenon depending on plasma acceleration which exists in Ref. [94] as a result of the kinking. Possible reasons for the non-observation of RT in Ref. [94] are that (i) the initial density was prescribed to be uniform so that the kink-driven acceleration did not produce a ‘heavy’ fluid on ‘top’ of a light fluid, that (ii) the scale length of the RT ripples was too small to be resolved by the grid size used, or (iii) some combination of these.

5.2 Non-MHD Scaling

Using the parameters provided by Tsuneta [95] and by Zaitsev et al. [96] for the coronal and chromospheric calculations, the various derived quantities are calculated as was done for the Caltech experiment and are listed in Table 5.1. The statistical acceleration model shows that when $E \ll E_D$, it is still possible to accelerate a fraction of the original particles to energies orders of magnitude higher than thermal with this fraction given by Eqs. 4.13 and 4.22. In the Tsuneta [95] case, $N_T = 7.5$, and in the Zaitsev *et al.* [96] case, $N_T = 3.8$, so the fraction of particles that do not collide and consequently are accelerated is much higher than in the lab situation. The energy content of the small number of energetic particles is similar to or greater than the energy content of the much larger number of particles in the thermal distribution because the final energy per particle is several orders of magnitude higher than the thermal energy. The ratio of energy in the accelerated particles to that of the initial thermal distribution is FW_f/W_0 which is given in Table 5.1. This ratio can exceed unity. Thus application of the statistical acceleration model to solar situations shows that a sub-Dreicer electric field can accelerate significant numbers of solar electrons to energies orders of magnitude greater than thermal, and that it is not required to invoke a super-Dreicer field to explain the existence of such energetic particles.

Understanding the scaling of the non-MHD microphysics parameters together with the MHD parameters provides a more complete picture of how this type of particle acceleration might take place on the sun. The electron drift current v_d is a microscopic velocity and depends on discrete properties of the charge that do not appear in the MHD equations. Nevertheless, if the atomic mass number is taken into account, it is seen that the electron drift velocity scales as $J/n = m_i J/\rho$ so

$$\frac{v_{d,solar}}{v_{A,solar}} = \frac{m_{i,solar}}{m_{i,lab}} c_1 \sqrt{c_2} \frac{v_{d,lab}}{v_{A,lab}}. \tag{5.1}$$

Because collisions also depend on particle discreteness, if the order unity dependence on charge Z is ignored, the collision mean free path scales as

$$\lambda_{mfp,solar} = \frac{m_{i,solar}}{m_{i,lab}} \left(\frac{T_{solar}}{T_{lab}}\right)^2 c_2 \lambda_{mfp,lab} \tag{5.2}$$

where it is also assumed that particle speed is the same multiple of their respective thermal speeds.

Scalings of quantities that depend on particle discreteness are given in Table 5.3. Unlike the MHD situation, a simple direct scaling of non-MHD microphysics linking the laboratory experiment to the solar corona or chromosphere does not exist. The most obvious difference between the solar and lab plasmas is that the solar plasmas have very small electron drift velocity v_d, so the RT instability would have to squeeze the current channel almost completely shut before the drift velocity could be increased to be of the order of a thermal or Alfvén velocity. Another important issue is that the calculated values of N_T for the solar corona and chromosphere depend on whether the actual or scaled electric field is used to calculate N_T in Eq. 4.13. In Table 5.1, the electric field is assumed to be the observed X-ray energy divided by the assumed acceleration length, whereas in Table 5.2, the electric field is scaled up from the lab experiment using the ideal MHD electric field scaling given in Eq. 1.14. The discrepancy indicates that the rate of current interruption observed in the experiment cannot be scaled up to the solar situation since such a scaling gives too large an electric field; in effect the model works too well. This issue is partially resolved by realizing that the rate of current interruption depends on micro-physics outside the scope of ideal MHD, so it does not follow the same scaling. In particular, the Dreicer electric field scales as

$$\begin{aligned}\frac{E_{D,solar}}{E_{D,lab}} &= \frac{T_{lab} n_{solar} Z_{solar} \ln\left(\Lambda_{solar}\right)}{T_{solar} n_{lab} Z_{lab} \ln\left(\Lambda_{lab}\right)} \\ &= \frac{c_3}{c_2^2} \frac{1}{Z_{lab}} \frac{\ln\left(\Lambda_{solar}\right)}{\ln\left(\Lambda_{lab}\right)} \left(\frac{m_{i,lab}}{m_{i,solar}}\right)^2 \end{aligned} \tag{5.3}$$

which differs from the ideal MHD electric field scaling in Eq. 1.14.

The Rayleigh-Taylor instigated voltage V_{RT} is calculated assuming that the RT instability open-circuits the complete electrical current in the Rayleigh-Taylor e-folding time and this produces large electric fields at the location of the RT opening switch. Since in the solar case this would provide electric fields substantially exceeding runaway conditions, it is plausible that the RT instability does not cut off the entire current. In this case a much smaller voltage would be produced. Since the scaled potential of 10^{11} volts is 2-6 orders of magnitude larger than observed particle energies, if one assumed that the RT instability only reduced a 10^{-6} to 10^{-2} fraction of the 8×10^{10} ampere current, then correspondingly smaller voltages and electric fields would be produced, the electric field would be less than the Dreicer field, and the voltage drop appearing across the RT region would be $10^5 - 10^9$ volts which is sufficient to provide suitably energetic particles.

Thus two possible resolutions are: (i) not all the current is disrupted in the solar case so less than the maximum possible electric field is produced, (ii) the disruption of the current occurs much more slowly in the solar cases than the ideal MHD scaling predicts. A third possible resolution, discussed below, is that topological details allow for a different scaling.

5.3 Solar Braiding as the Means of Scaling

A likely way to resolve the issues discussed in the previous section is to consider that the 6 megameter radius solar flux-rope consists of a large number of braided microscopic filaments [98]. The tendency towards filamentation of a two-dimensional current sheet is the two-dimensional analog of a monolithic cylinder decomposing into a collection of braided strands and is obvious in Fig. 1 of Daughton *et al.* [99]. Solar observations support this conjecture because whenever observational resolution is increased, structures that formerly appeared to be monolithic appear to have a substructure consisting of finer-scale filaments wrapped around each other as shown for example in Fig. 1.18 of Ref. [7]. Decomposition of a flux-rope into filamentary, island-like substructures would be analogous to a commercially available type of

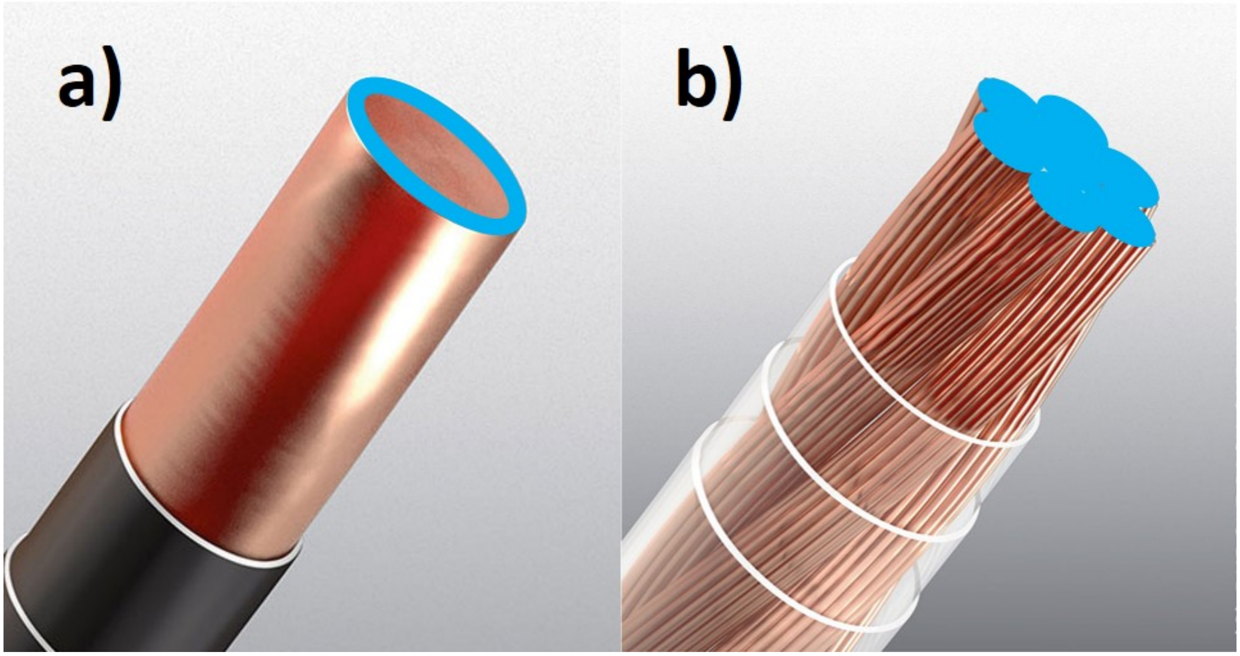

Figure 5.1: Current distributions in a) solid conductor compared with b) braided, insulated, Litz-wire. Bright blue represents where the current flows. In the solid conductor case, current only exists in a small skin layer, whereas in the case of braided, insulated Litz-wire, the current will be distributed uniformly throughout the column. Images from Rudolf Pack GMBH & Co, KG, https://www.packlitzwire.com.

braided electric cable. This braided cable is called Litz wire [100] and consists of a large number of tiny, insulated wire strands of radius smaller than a skin depth. The strands are braided in such a way that no strand is on average more inside or more outside the cable cross-section than any other strand. Because the radius of each strand is smaller than the skin depth, the current is uniform within each strand, and because there is no difference between any of the strands, each strand carries an equal proportion of the total current. The consequence is that the current is uniformly distributed across the cross-section of the cable. This is in contrast to a solid, monolithic cable which would have all the current confined within a skin depth of the surface. Figure 5.1 highlights this difference in current cross sections.

The proposal that a plasma flux-rope decomposes into braided filaments as in Litz-wire was first made by Stix [101] on considering anomalous flux penetration in a tokamak as a result of the breakup of nested flux surfaces into Litz-like helical islands. As support for this conjecture of braiding, it should be noted that a braided system has more inductance than a single monolithic conductor because the current links interior flux in a braided system, whereas the monolithic conductor has no interior flux. Having more inductance for a given amount of flux reduces the magnetic energy since magnetic energy can be expressed as $W_B = LI^2/2 = \Phi^2/(2L)$ and flux $\Phi = LI$.

Consider a solar flux-rope undergoing a kink instability producing a magnetic field $\mathbf{B}_{kink}$. If this flux-rope is constituted by an enormous number of tiny braided strands each having radius of a few ion skin depths and having current density $\mathbf{J}$, each strand would be accelerated by the kink magnetic field by a local $\mathbf{J} \times \mathbf{B}_{kink}$ force and, as in the lab experiment, each strand would experience the effective gravity associated with this kink acceleration. The ion skin depth for hydrogen with $n = 10^{16}$ m^{-3} is $c/\omega_{pi} = 2$ m. Assuming a temperature $T = 100$ eV and a magnetic field $B = 10^{-3}$ T, the ion Larmor radius is r_{Li} =1 m. The strands would thus have to be at least several Larmor radii in radius, so for example a flux-rope with radius 10^6 m might consist of strands having 10 m radius in which case the flux rope would consist of 10^{10} strands, each 10 m in radius. The strands would be braided so that each strand is statistically the same, i.e., there is no inside or outside strand. The strands could also have a web-like structure as shown in Fig. 1 of Daughton *et al.* [99].

Because there is no inside or outside to the braided strands, any externally imposed kink magnetic field will completely penetrate this structure. This is because any shielding of the externally imposed magnetic field would require a surface current, but no surface current is allowed because all strands are equally on the surface and in the interior. Each strand would then experience an identical $\mathbf{J} \times \mathbf{B}$ force from the interaction between the exterior kink-instigated magnetic field $\mathbf{B}$ and the current $\mathbf{J}$ in the strand. Each strand would have a large lateral acceleration, experience its own effective gravity, and develop its own small-scale RT ripples. These ripples would quickly grow to become comparable to c/ω_{pi} and would choke off the current in each strand because having v_d of order v_A is forbidden by kinetic considerations. The interruption of the currents in each strand when it breaks would correspond to the interruption of the current in the Caltech jet experiment when it breaks, so there would be a large electric field associated with LdI/dt. Figure 5.2(a), (b), and (c) shows what a bundle of individual filaments all undergoing the MHD kink, RT, and then breaking apart might look like. The images for each filament in Fig. 5.2(a), (b), and (c) are taken from Fig. 3.2(a), (e), and (f) respectively.

More recent experiments by Yang *et al.* [57] show a hoop force driven magnetic Rayleigh-Taylor instability in an experiment simulating solar loops at Caltech. Figure 5.3 shows the similarity between the hoop force driven RT instability on the

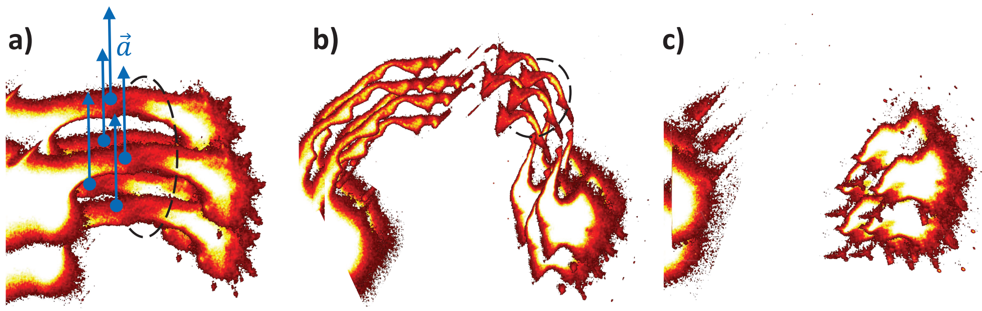

Figure 5.2: Sketch illustrating how a solar flare might evolve with a Litz-wire-like filament structure. a) is a collection of five filaments made by superposing five copies of the image from Fig. 3.2(a). This composite shows each filament undergoing an MHD kink instability and accelerating upwards. b) is the same collection of five filaments made using the image from Fig. 3.2(e) where each filament is undergoing the RT instability. c) is the same collection of five filaments made using the image from Fig. 3.2(f) where each filament has broken apart after undergoing the RT. The jet breaks apart in the microsecond between this image and the next one which is shown in c).

single loop experiment and the kink-driven RT observed on the jet experiment. While of different origin than the kink-driven RT seen on the jet experiment, it nonetheless shows that the arched geometry of current loops will provide an acceleration from the hoop force that can instigate a RT instability. If arched solar loops are composed of Litz-wire braided strands, the hoop force would affect each strand and instigate the RT instability. This RT could choke off the current in each strand on the loop producing the electric field necessary to accelerate charged particles to high energy when they break.

By imagining the braided, current-carrying strands of the Litz-wire to be like a rope, the classic slow build-up to fast-eruption behavior seen in solar flares can be explained. If a rope is supporting a large mass and something external is slowly cutting each individual strand one-at-a-time, after enough strands were cut slowly by the external factor, all the remaining strands will break in one instantaneous motion. The analogy in the case of the solar flare would be that the RT instability starts breaking a few of the braided strands in the solar prominence structure and after enough have been broken, the rest break instantaneously and the whole structure erupts producing a coronal mass ejection and solar flare.

The Litz-wire-like braiding appears to be essential because if there were no braiding

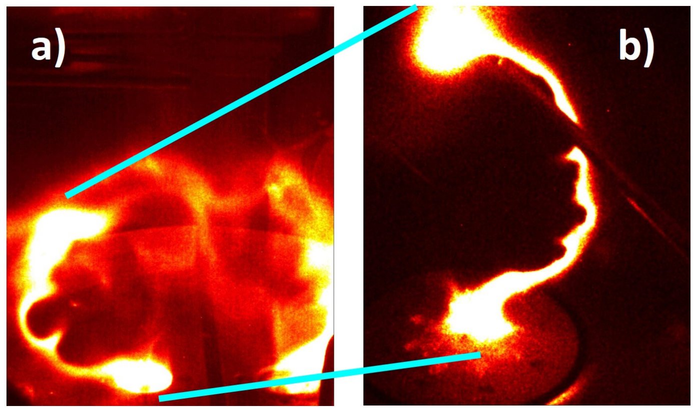

Figure 5.3: Images of Rayleigh-Taylor instability (a) at the base of the single loop and (b) on the jet experiments at Caltech.

so that a macroscopic flux-rope were a monolithic conductor, the resistive skin time would be much too long for a current to spread uniformly across the flux-rope cross-section. Specifically, the resistive diffusion time for a current to penetrate a 6×10^6 m radius 100 eV plasma is $\tau_R = \mu_0 r^2/\eta = 3$ million years which of course is many orders of magnitude larger than the time scale for currents to change in the solar corona.

Parameter	Caltech Lab	Solar Corona (Tsuneta)	Solar Chromosphere (Zaitsev)
T_e [eV]	2	90	2
n_e [m^{-3}]	3×10^{22}	10^{16}	10^{18}
W_o [eV]	2	90	2
W_f [keV]	6	100	20
l [m]	0.10	1.6×10^7	5×10^5
$E[V/m]$	6×10^4	0.006	30
Z	2	1	1
$\ln(\Lambda)$	4.8	18	10
$E_D[V/m]$	8.1×10^5	0.01	53
λ_0 [m]	1×10^{-6}	2×10^3	0.02
E/E_D	0.07	0.5	0.5
α	0.03	0.13	0.27
N_T	33	7.5	3.8
F	4.8×10^{-6}	0.002	0.010
FW_f/W_0	0.015	2.3	100
F_{Xray}	1.3×10^{-7}	1.5×10^{-5}	1.3×10^{-4}
S	10-100 [102]	$10^8 - 10^{12}$ [7]	$10^6 - 10^8$ [103]

Table 5.1: Comparison of Parameters. Rows above the first break are inputs. Rows below the first break are calculated outputs. The final row below the second break contains Lundquist Number estimates.

Parameter	**Units**	**Caltech Lab**	**Solar Corona (Tsuneta)**	**Solar Chromosphere (Zaitsev)**
a.m.u.		**40**	**1**	**1**
Z		**2**	**1**	**1**
n_e	m^{-3}	**3.0E+022**	**1.0E+016**	**1.0E+018**
T	eV	**2**	**90**	**2**
B	T	**1.0**	0.0039	0.0058
β		0.012	0.012	0.012
l	m	**0.30**	**1.6E+007**	**5.0E+005**
a	m	**0.020**	1.1E+006	3.3E+004
v_A	m/s	2.0E+004	8.5E+005	1.3E+005
τ	s	1.5E-005	19.	4.0
I	A	**6.0E+004**	1.2E+010	5.8E+008
L	H	**5.0E-008**	2.7	0.083
Φ	Wb	0.0030	3.3E+010	4.8E+007
W	J	90.	2.0E+020	1.4E+016
τ_{kink}	s	**4.0E-006**	5.0	1.1
τ_{RT}	s	**5.0E-007**	0.63	0.13
l_{kink}	m	**0.30**	1.6E+007	5.0E+005
V_{RT}	V	6.0E+003	5.3E+010	3.7E+008
l_{RT}	m	**0.10**	5.3E+006	1.7E+005
E_{RT}	V/m	6.0E+004	9.9E+003	2.2E+003
E_D	V/m	8.1E+005	0.011	28.
E_{RT}/E_D		0.074	8.8E+005	78.

Table 5.2: MHD scale-up from lab experiment. Bold numbers are inputs, all others are calculated from input numbers and from scaling relations. a is the minor radius of the current channel. These parameters do not depend on particle discreteness. E_D is the only exception to the previous statement. E_D is calculated using the referenced n_e and T, not an MHD scaling.

Parameter	**Units**	**Caltech Lab**	**Solar Corona (Tsuneta)**	**Solar Chromosphere (Zaitsev)**
λ_D	m	6.1E-008	0.00071	1.1E-005
$\ln\Lambda$		4.8	18	10
λ_{mfp}	m	1.1E-006	2.3E+003	0.021
η	Ohm-m	0.00050	2.1E-005	0.00051
c/ω_{pi}	m	0.0013	2.3	0.23
v_d	m/s	9.9E+003	2.2	1.0
v_d/v_A		0.50	2.6E-006	8.2E-006
δ_{skin}	m	0.040	9.1	21
S		15	8.2E+011	1.5E+008

Table 5.3: Microscopically-dependent parameters not in MHD. These parameters do depend on particle discreteness.

Chapter 6

DUSTY PLASMA EXPERIMENT DETAILS

The Caltech Water-Ice Dusty Plasma Experiment is the newest addition to the Bellan Plasma Physics Laboratory. 2013 marks the first publication with results from this experiment and this is the first thesis to include it. This continuous low-power ($P \approx$ Watts), capacitively coupled plasma experiment housed inside a 6” spherical-square vacuum chamber seems unimposing compared to the jet experiment with its pulsed high-power ($P \approx$ Megawatts) plasma created inside a meter-size vacuum chamber with the constant compression cycle of the cryopump compressor playing on repeat. Despite its humble stature, this table-top dusty plasma experiment demonstrates a rich variety of physics.

The dusty plasma experiment produces a plasma that will last continuously as long as the power supply is turned on. There is no μs time-scale set by a discharging capacitor bank. Interestingly, the dusty plasma experiment turns the conventional wisdom of *water vapor bad for vacuum pumps* on its head. When operating the dusty plasma experiment, water vapor is intentionally introduced into the vacuum system!

The dusty plasma experiment was designed to be an improved version of the apparatus used by Shimizu *et al.* [51]. The group at Max Planck Institute, Garching was extremely supportive of our experiment at Caltech. In fact when Kil-Byoung Chai came from South Korea to Caltech to build this experiment, he took the long way from South Korea to Pasadena traveling west to Germany first to visit Max Planck before completing the journey to Pasadena. The two main differences in the experiments are:

1. Shimizu *et al.* [51] created water vapor in-situ through the chemical reaction of $2D_2 + O_2 \rightarrow 2D_2O + 484\text{kJ/mol}$, whereas the Caltech experiment uses the vapor pressure of liquid water to diffuse water molecules into the plasma from a separate reservoir.

2. The Caltech experiment has an adjustable gap distance between the electrodes.

The dusty plasma experiment provides a unique opportunity to observe directly how ice grains in an astrophysically-relevant plasma environment grow from a few μm to hundreds of μm. Similar to terrestrial and astrophysical dusty plasmas, the Caltech dusty plasma is weakly ionized ($\sim 10^{-6}$ ionization fraction) and the dust consists of water-ice grains. The $\sim$ 150 K ambient temperature is similar to the temperature of naturally occurring ice dusty plasmas.

6.1 Experimental Hardware

Figure 6.1 shows a cutaway of the 6” spherical-square vacuum chamber with the parallel plate electrodes in brown and the purple plasma in the middle. Figure 6.2 shows a schematic of the complete system. The key hardware components that compose this relatively humble experiment will be discussed in the subsections below.

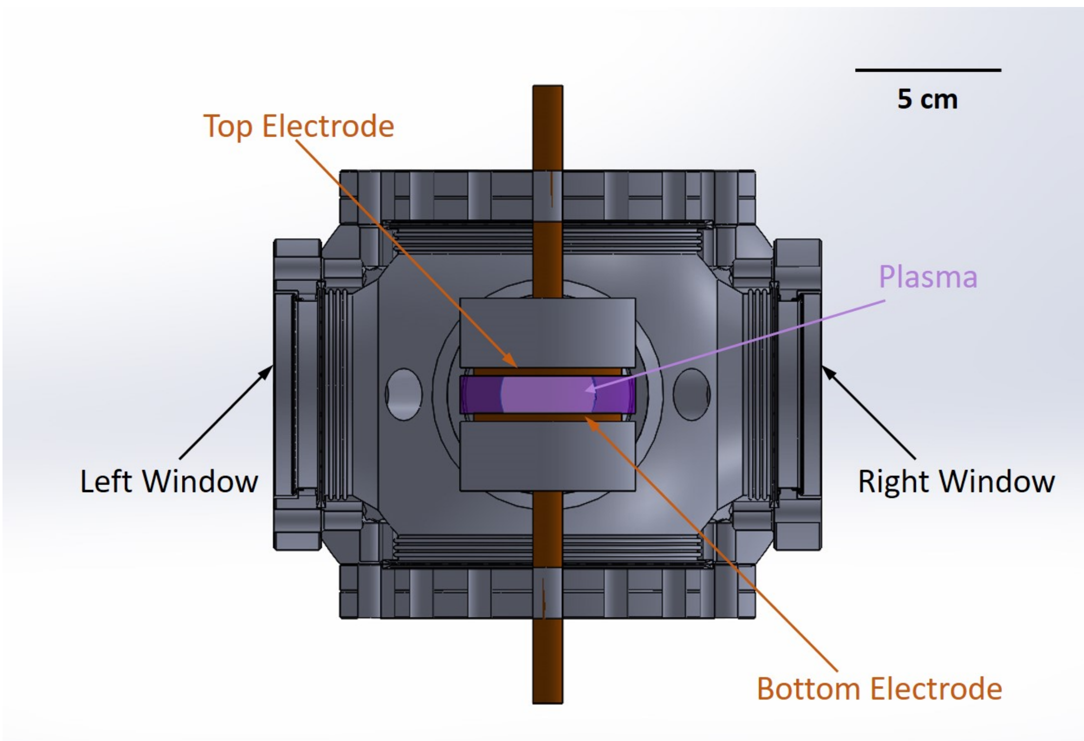

Figure 6.1: Cutaway of the Caltech Water-Ice Dusty Plasma Experiment vacuum chamber.

Vacuum Chamber

The dusty plasma experiment is housed in a Stainless Steel 316L 6.0" Spherical-Square Vacuum Chamber produced by Kimball Physics. The chamber has a volume

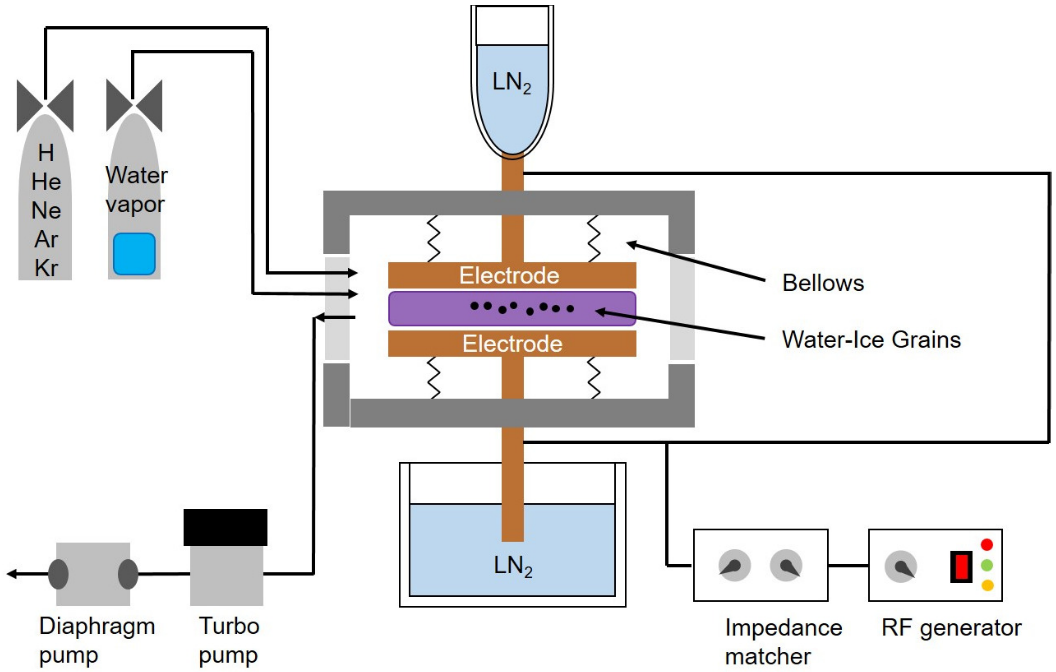

Figure 6.2: Schematic diagram showing the main components of the Caltech Water-Ice Dusty Plasma Experiment.

of 119 in^3. The vacuum chamber features two 6" ConFlat ports, four 4.5" ConFlat ports, and four 1.33" ConFlat ports which allow for the experiment hardware to be rapidly configured or changed. The chamber is oriented as in Fig. 6.1 such that the two 6" ConFlat ports are at the top and bottom. The four 4.5" ConFlat ports are situated 90° from each other in the same horizontal plane. Glass windows are mounted onto three of these 4.5" ConFlat ports. Attached to the fourth 4.5" ConFlat port is an angle valve leading to a Pfeiffer Vacuum two-stage HiCube pump system. The HiCube consists of an MVP 015 diaphragm pump and a HiPace80 turbo pump. The amount of water vapor we use does not cause difficulties with these pumps. An ion gauge shows that this pumping system achieves a base pressure of approximately 5×10^{-6} Torr.

Electrodes

Without a doubt, the electrodes are the most important components of the Dusty Plasma experiment. The 6 cm diameter parallel-plate copper disk electrodes are each built into a 6" ConFlat flange with adjustable welded bellows allowing the gap distance between them to be varied. This gap is typically ~ 1.5 cm, but can be as large as ~ 2.5 cm. A thermal finger passes all the way through the ConFlat flange from the electrode disk itself inside vacuum to atmospheric pressure where it is submerged in liquid nitrogen (LN_2). The two flanges each bolt to the 6” ConFlat ports at the top and bottom of the chamber. The electrodes and thermal fingers are electrically connected to a custom-made 1-3W 13.56 MHz radio frequency (RF) power supply while they remain electrically insulated from the rest of the vacuum chamber via kapton inserts.

An important difference from Ref. [104] is that the electrodes have been changed to be copper instead of aluminum because copper is more thermally conductive. This change results in colder electrodes because the (LN_2) cooling is more effective.

Liquid Nitrogen Cooling

A temperature gradient develops across each cold finger between the end dipped in the LN_2 bath and the end attached to the electrode disk. This gradient cools the electrode plates to nearly cryogenic temperatures. Figure 6.3 shows a plot of electrode temperature versus cooling time measured with tiny resistance temperature detectors (RTDs). The RTD has a resistance that is dependent on temperature which provides for easy measurement using a standard multimeter. The RTDs are each snaked through a small cavity in the cold fingers to sit at the base near the electrode disks. The RTDs are not regularly used because they are relatively expensive given how often they break. The important result is that it takes $\sim$ 30 minutes to an hour to cool the electrodes to $\sim$ 150 K. Equally noteworthy is the indication that the top electrode cools to a lower temperature than the bottom electrode. This is likely because there is a better thermal connection between the LN_2 and the cold finger on the top electrode compared to the bottom one.

Gas System

The other key component of the experiment is the gas system. The Caltech Water-Ice Dusty Plasma experiment can produce plasma using H, He, Ar, N, and Kr gases. Each high pressure gas bottle has a regulator with a line that leads to a switch board where the user chooses the desired gas. The gas line coming out of the switch board passes through a crucial component called a leak valve. The leak valve is a very sharp needle valve that is adjustable and allows only a minuscule amount of gas to pass through it. After passing through the leak valve, gas enters the vacuum chamber through a 1.33” CF flange to 1/4” vacuum coupling. The water vapor that will become the ice grains is produced by the vapor pressure of liquid water kept in

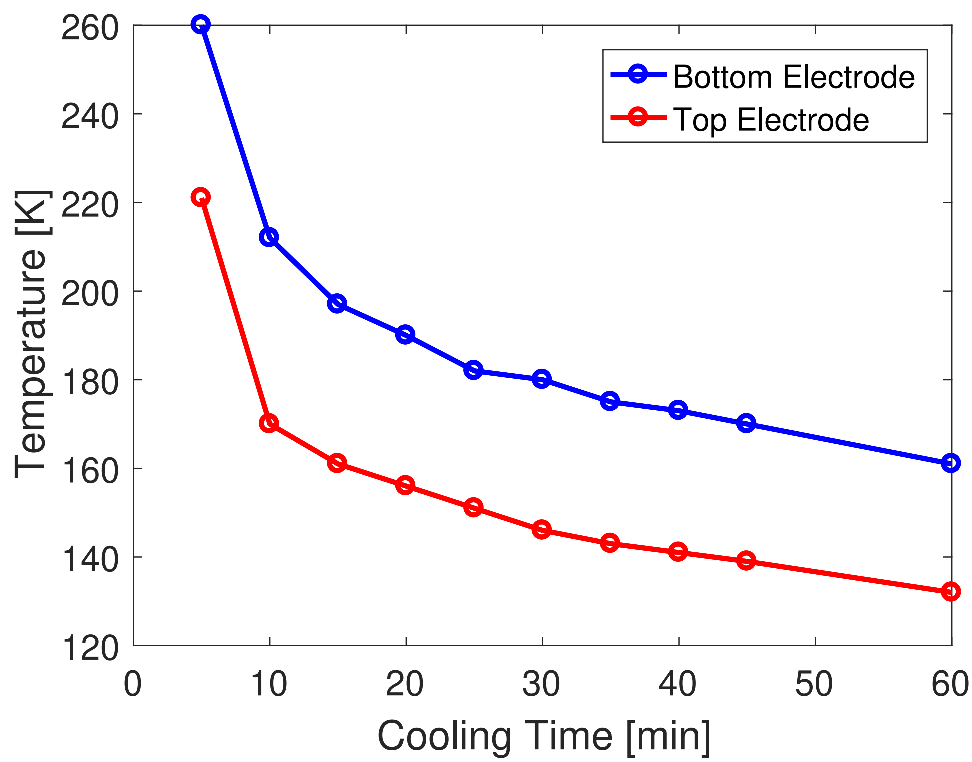

Figure 6.3: Plot of electrode temperature as a function of cooling time using the resistive temperature diodes in the top and bottom electrodes.

a separate canister. Opening a separate valve between the canister and the chamber allows water vapor to simultaneously enter into the chamber through the same 1.33" CF connection with the background gas.

While operating the experiment, chamber pressure is determined by an equilibrium between the inflow of atoms controlled by the leak valve and the outflow of atoms controlled by the angle valve that sits between the vacuum chamber and the pumps. By opening and closing this angle valve, pumping efficiency is changed. Typical operation involves setting the leak valve to a standard (unknown) inflow rate and then adjusting the chamber pressure by opening or closing the angle valve at the back. The only time the leak valve is adjusted is when operation at abnormally low pressure is attempted.

Operation

Creating a cold water-ice dusty plasma is surprisingly simple with this machine. The first step to turn on the separate vacuum pump responsible for pumping air out of the liquid water canister because this takes the longest. The pressure in the water tank falls from atmospheric pressure to $\sim$ 8 Torr in $\sim$ 45 minutes. To save time, while the water tank is being evacuated, also start the electrodes cooling by filling the top and bottom dewars with LN_2 and top off every 5 to 10 minutes. By the time that the water tank is sufficiently evacuated, the electrodes have cooled —see Fig. 6.3. After the electrodes are cold and the water tank has been evacuated, open the leak valve to 101.5[1] and use the angle valve to adjust the pressure to 200-600 mTorr. Turn on the power supplies to ignite the plasma. The final step is to open the variable valve between the water reservoir and the vacuum chamber for 10-20 seconds, and then to close it. When plasma is present, the water vapor spontaneously freezes into ice grains which levitate inside the plasma. Plasma is a requirement of ice grains like Ref. [51].

6.2 Diagnostics

Cameras serve an especially important diagnostic role in the dusty plasma experiment because the experiment is continuous and everything is more or less on the human scale. We use a standard Nikon D5300 DSLR camera and a Dalsa Falcon VGA300 camera. These cameras have helped to produce many interesting results. For standard image-taking, the Nikon D5300 is employed. The Dalsa Falcon VGA300 records video at up to 300 frames per second (FPS) at the expense of image resolution compared with the Nikon D5300 which can only record up to 60 FPS. During my tenure in the lab, we also used a Photron SA-X2 ultra-high-speed camera whose results will be featured in Ch. 7. Common lenses used on the cameras include an Infinity K2 DistaMax long-distance microscope lens and a 24 mm prime Nikon lens.

The Infinity K2 DistaMax long-distance lens is a refractor that gives a camera like the Nikon D5300 or Photron SA-X2 the capability of a microscope while keeping a relatively large distance between the subject and the camera lens itself. Rather than the tip of the microscope being millimeters away from the sample, this lens allows the sample to be $\sim$ 15 cm from the end of the lens. This is paramount at the dusty plasma experiment because the ice grains are suspended between the electrodes inside the plasma. The grains are $\sim$ 10 cm from the window and the camera is outside the vacuum chamber. The lens has a resolution down to a few microns.

The combination of the 22.4 MegaPixel Nikon D5300 camera and the Infinity K2 DistaMax long-distance microscope lens, pictured in Fig. 6.4, is commonly used

[1]Opening the leak valve past 102 will cause the turbopump to overheat.

for taking images of the ice grains. A 500 W halogen lamp back-illuminates the ice grains through the window opposite the camera lens which causes the ice grains to appear in the camera as dark silhouettes on a bright background. Figure 6.5 shows an image of the ice grains taken in this configuration with a shutter time of 1/4000 s and 2000 ISO. Figure 6.5 makes it clear that the ice grains produced in the experiment are not spherical, but rather elongated and fractal.

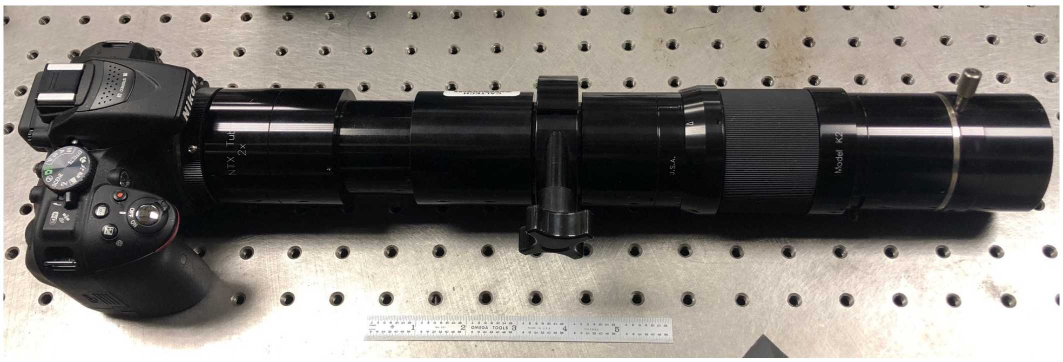

Figure 6.4: Nikon D5300 Digital Camera with the Infinity K2 DistaMax long-distance microscope lens mounted. Metal ruler in the foreground for perspective on lens' size is 6 inches long.

Other diagnostics used on the dusty plasma experiment include Langmuir probes to measure electron temperature and electron density. Spectroscopy is another commonly used tool. Light emission from the plasma has been analyzed using an Ocean Optics USB 2000 series spectrometer, a 1/2 m spectrometer, and a more capable 1 m spectrometer. However, the 1 m spectrometer is located in another room which requires coupling the light to a long optical fiber to use it. It can also only be used to study emission less than 500 nm. Laser-Induced Fluorescence is another spectroscopy-based diagnostic that has been attempted on both the water molecules in the plasma and the plasma gas species. Ch. 8 of this thesis is devoted to results from the Tuneable-Diode Laser Induced Fluorescence (TD-LIF) diagnostic that I have developed for the neutral argon species on the dusty plasma experiment.

The dusty plasma experiment has produced a number of interesting papers. Most relevant to this thesis are the results about ice grain growth that are detailed in Refs. [105] and [106]. To summarize here, Chai and Bellan found that:

1. Ice grains grow faster and to larger sizes when the background gas pressure is lower [105, 106].

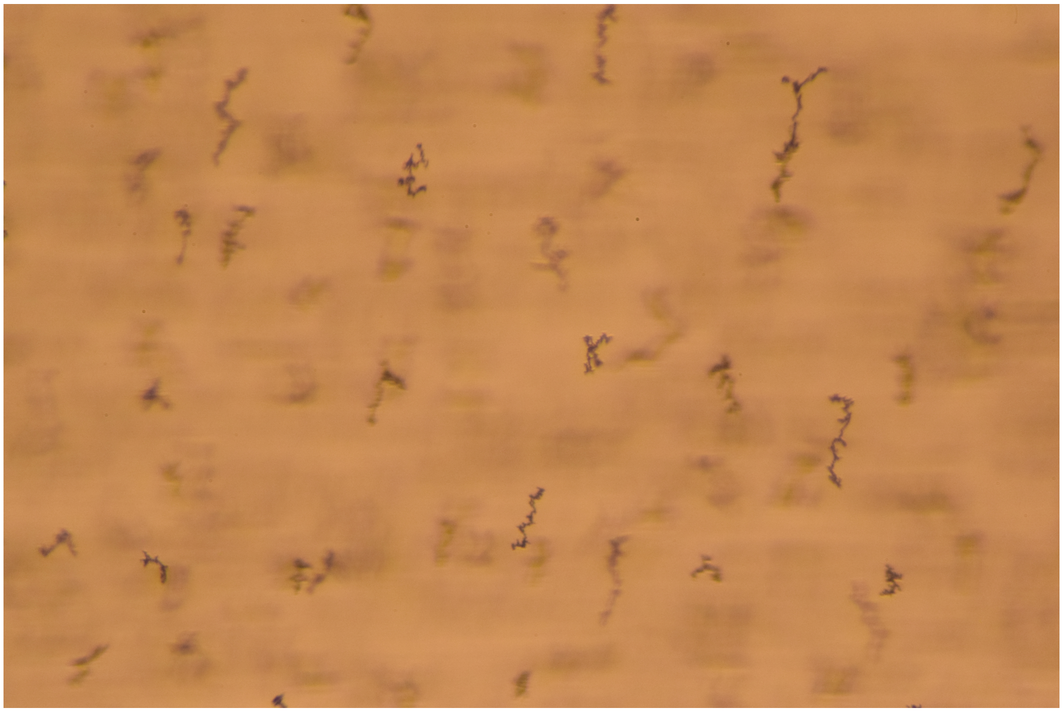

Figure 6.5: Image of the ice grains suspended in the plasma taken by the Nikon D5300 using the Infinity K2 Distamax Long-Distance Microscope lens. The ice grains are the dark silhouettes in the light background.

2. Ice grains grow faster and to larger sizes when the background gas species is lighter [105].

3. Ice grains grow quickly at the start and saturate after about 2 minutes of growth [106].

4. Higher water vapor pressure produces larger, more elongated ice grains [106].

5. Higher RF power produces faster growing ice grains that grow larger [106].

6. Applying an external magnetic field inhibits growth and produces smaller, more spherical grains [106].

Another interesting result is the observation of a vortex-like motion due to the ion density gradient and the gradient of the magnitude of the ion ambipolar velocity being non-parallel which causes a non-conservative ion drag [107].

Chapter 7

ICE GRAIN GROWTH

[1] R. S. Marshall, K. -B. Chai, and P. M. Bellan. "Identification of accretion as grain growth mechanism in astrophysically relevant water-ice dusty plasma experiment". In: *Astrophysical Journal* 837.1 (2017). DOI: https://doi.org/10.3847/1538-4357/aa5d11.

Laboratory exploration is well-suited to study the ice grain growth process in protoplanetary disks and molecular clouds because these structures are distant and the growth time scale is presumably much longer than the human scale. Two commonly made assumptions in the study of astrophysical dusty plasmas will be addressed here. The first is that water-ice dust grains are spherical with radius $0.01\mu\text{m} < r < 10$ cm where r is distributed with power-law dependence $n(r) \sim r^{-p}$ and $p = 3.5$ [108, 109]. The power law distribution is the equilibrium balance of constant collisions between ice grains where sometimes they stick together and become larger and other times they break and become smaller [110].[1] The second assumption is that plasma effects such as dust charging are considered negligible because plasma density is assumed to be low compared to dust density.

The photograph of ice grains in the dusty plasma experiment in Fig. 6.5 has already provided evidence to challenge the first assumption. In regard to the second assumption, it is postulated that the ratio of the plasma to dust density might not be small in the outer disk regions [28, 111, 112] where ice grains are thought to grow quickly to mm size and the ice grains are likely to be charged. In this region, charging occurs because the ice grains are continuously bombarded by electrons and ions that collide with and attach to the ice grains. If all ice grains are charged with the same electric polarity, there would be an electrostatic repulsive force between the grains and this force would oppose agglomeration of the ice grains. It is very important to note that, although an electrostatic repulsive force between ice grains impedes agglomeration, it does not impede another important means of ice grain growth described in Ref. [105] called accretion growth.

In particular, if ice grains grow via accretion of neutral water molecules, a mechanism which we call accretion growth, then the growth rate of the ice grains will

[1] See the Introduction of Chai and Bellan [105] for other proposed grain growth models.

increase as the grains become more highly charged. This is because neutral water molecules have a very large dipole moment, so they are attracted to charged ice grains in proportion to the degree of grain charging. Thus increasing the ice grain charge will accelerate growth by accretion and decelerate growth by agglomeration.

A situation like what is found in the outer disk regions with negatively charged ice grains arises in the Caltech Water-Ice Dusty Plasma Experiment. Prior to my arrival at Caltech, ice grain growth was studied by taking still images using the Nikon D5300 DSLR camera and the Infinity K2 Distamax Long Distance Microscope Lens. A recap of the results is enumerated at the end of Ch. 6.

The accretion growth mechanism is consistent with the enumerated results. It was concluded that plasma effects, such as charging of the dust grains negatively by electron flux bombarding them, is important, contrary to the second commonly made astrophysical assumption. Water molecules have a strong dipole moment, so water molecules will be attracted to concentrations of charge. Any water molecule that is inside the dust Debye sphere will be attracted to the negatively charged dust grain. How difficult it is for the water molecule to reach the grain surface will depend on what the background plasma gas is and how much is present. Water molecules have atomic mass $m = 18$, so in a hydrogen plasma where the background gas has $m = 2$, the water molecule colliding with a hydrogen atom is like a bowling ball hitting a ping-pong ball and the water molecule will be able to plow its way to the surface of the grain. In a plasma made of argon with atomic mass $m = 40$, now the water molecule is like the ping-pong ball and collisions make it much harder for the water molecule to reach the surface of the grain.

The specific role of electrical charge in ice-dust grain growth can be discerned by examining the dust growth process in laboratory dusty plasmas ignited with reactive gases such as SiH_4 [47, 48], C_2H_2, and CH_4 [49]. It is generally accepted that nm-sized dust particles in these plasmas form spontaneously, and then proceed to grow by continually colliding with each other [47, 49]. This growth by coagulation ceases when the ice grains become micron-sized and have acquired enough electric charge for mutual repulsion to prevent further coagulation. After this growth by coagulation, dust particles can grow further by accreting molecules and ions [47–49]. However, it has been recently reported that dust grains larger than μm immersed in a plasma can grow by the agglomeration process even though they have large electric charges [113, 114]. In order for this agglomeration growth to occur in laboratory plasmas, the kinetic energy of a dust particle must overcome the Coulomb repulsive potential energy; dust acoustic waves have been proposed as a mechanism for providing the required kinetic energy [113, 114].

Clearly, there are still many questions that can be answered by an astrophysically-relevant laboratory experiment. Attempts were made to study grain growth by capturing video using the Nikon D5300. When the Nikon D5300 was deemed too slow, the Dalsa Falcon was used instead. Unfortunately 300 FPS was not fast enough either.

7.1 Hardware

Figure 7.1 sketches the water-ice dusty plasma apparatus as it was set up to study grain growth. A 500 W halogen lamp shines through one window of the vacuum chamber to back-illuminate water-ice grains formed in helium plasma. High-speed video of a cluster of individual ice grains is recorded using the Infinity K2 DistaMax long distance microscope lens attached to a RGB Photron SA-X2 high-speed camera viewing the chamber interior through an oppositely facing window. The Photron SA-X2 camera can record 1024 x 1024 pixel images with frame rate up to 12,500 FPS and can record even faster when using decreased image resolution. The duration of video that can be recorded is limited by the internal storage capacity of the camera. This setup provides an approximately 200 μm depth of field and $1.5{\times}1.5$ mm^2 field of view to the Photron camera. The light scattered from the ice grains makes the grains appear as dark particles in a light background.

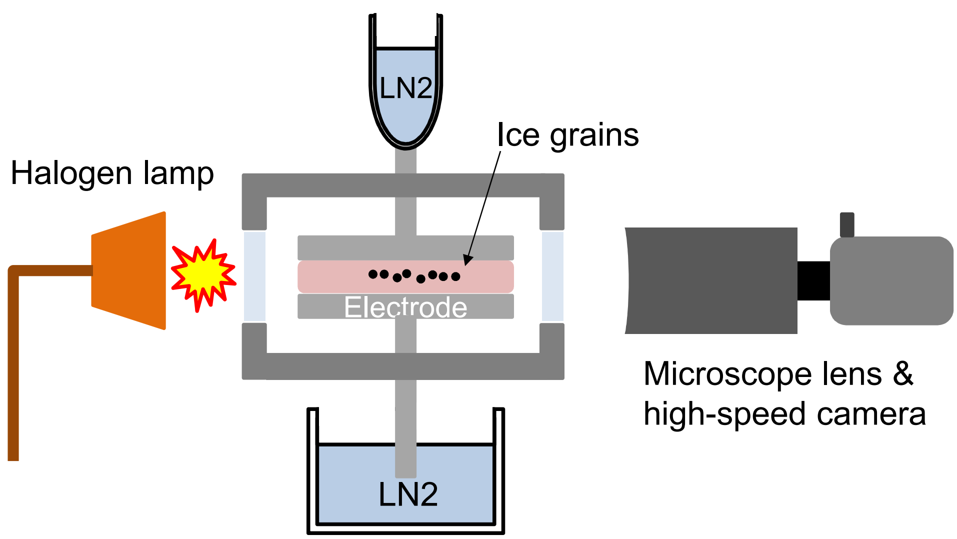

Figure 7.1: A sketch of experimental setup.

The experimental procedure is similar to Ref. [104]. After purging residual gas from the distilled water tank, liquid nitrogen is poured into the upper and lower reservoirs and the electrodes are allowed to cool for 30 minutes. The main vacuum chamber is then filled with 1 Torr helium gas and the plasma is ignited by application of 1-3 W of 13.56 MHz RF power across the electrodes. After plasma ignition, water vapor is introduced into the plasma. The amount of water vapor is gauged by the increase in reading of an MKS Capacitance Manometer. The increase in the manometer reading is 20 mTorr which implies that the ratio of the helium partial pressure to the water vapor partial pressure is 50 assuming that this increase is solely from water vapor and not from air. Immediately upon introduction of the water vapor, water-ice grains spontaneously form and grow. Ice grain formation is only observed when the ambient helium pressure exceeds 600 mTorr. After growth begins, the ambient gas pressure is lowered from 1 Torr to 200 mTorr as illustrated in Fig. 7.2. When the ambient helium pressure has decreased to 600 mTorr, the ice grains have become macroscopic and the video recording of the ice grain growth process is started. The camera records a 10-second long video at 4,000 frames per second. During the recording time, the pressure drops to 200 mTorr while the ice grains grow from 20 μm to 80 μm. The 40,000 recorded photos were analyzed and the results will now be presented and discussed.

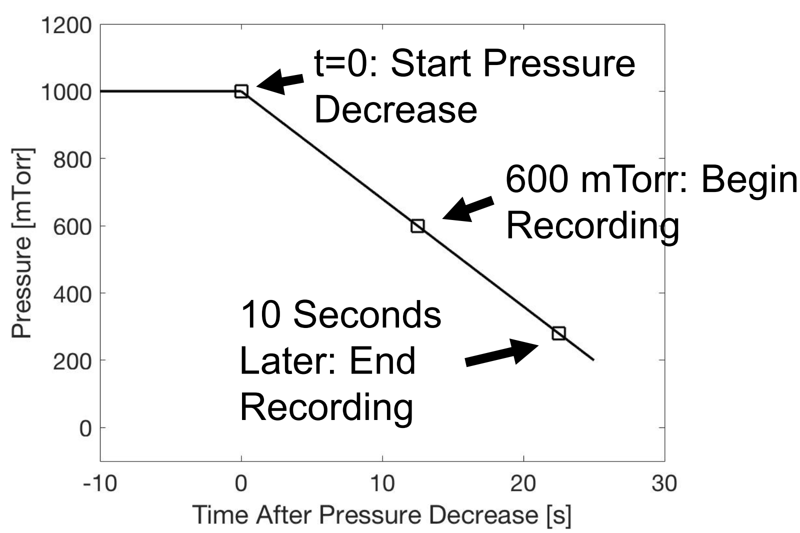

Figure 7.2: Plot of pressure in vacuum chamber as a function of time after pressure decrease.

7.2 Analysis of High-Speed Video

Watching the 4,000 frames per second video at 10 frames per second provides insights into the ice grain motion and growth process that would not otherwise be evident without the 400-fold slowdown of the motion. Figure 7.3 (movie on web and photograph from movie in print) shows a sample of the high-speed video. Unlike when recording video with the Nikon D5300 or the Dalsa Falcon, the exact trajectory of each ice grain can be identified and followed for over 50 frames and sometimes as many as 250 or more frames when recording video with the Photron camera. This is a monumental improvement over the Nikon D5300 and Dalsa Falcon where it is impossible to definitively track and follow grain motion across consecutive movie frames. The 10-second long video shows a considerable growth in particle size. This is in agreement with Ref. [104] where it was reported that when ambient pressure decreases, ice grain size increases. As the ice grains grow, a decrease in the overall ice grain number density in the plasma is also observed.

The 4,000 per second frame rate is sufficient to follow oscillatory ice grain motion caused by what are likely dust acoustic waves. Because the position of each ice grain is measured as a function of time, the velocity of each ice grain can be computed. This computation was done for every ice grain between all consecutive pairs of frames to create an evolving temporal speed distribution. The 4,000 per second frame rate provides so much detail regarding grain motion that it was actually possible to observe the ice grains vertically aligned as in Ref. [105] spinning about their vertical axis. In rarer instances, an ice grain would be observed tumbling and spinning about some other axis or combination of axes.

A critical result is that no direct collisions between ice grains were observed in the 40,000 frame video inside the camera's field of view. It is important to note that this does not preclude the possibility that collisions could occur outside the field of view. Moreover, it was not possible to locate an obvious example where two ice grains approached on a collision course, and then deflected from each other according to Rutherford scattering. There is no observational evidence of two ice grains colliding and sticking to each other, nor is there any evidence of two ice grains colliding and breaking apart. This lack of evidence for collisions between grains combined with the ability to track the grains in the camera frame for an extended period of time suggests that accretion is the dominant mode of growth, not coagulation.

Ice Grain Size, Aspect Ratio, and Number Density

The solid line in Fig. 7.4(a) shows the time evolution of the major axis length. This measurement was determined by a three-step process: every 10th video image was read into a Matlab code and sharpened to make the ice grains more distinct. The

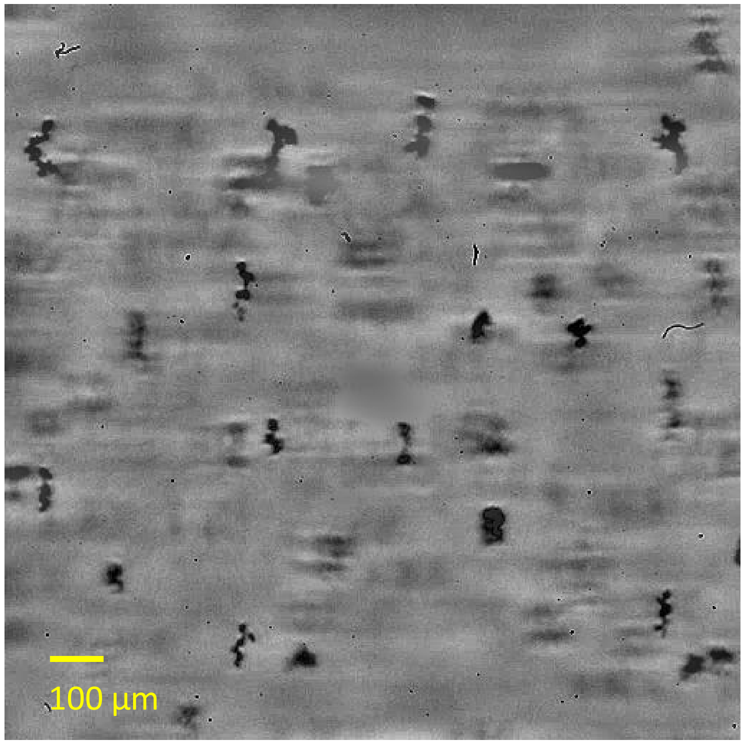

Figure 7.3: Still image frame taken from the high speed movie. A 10 fps sample of the high speed movie consisting of 6 segments of 400 frames each with 2 s intersegment time can be downloaded from the CaltechDATA repository at https://data.caltech.edu/records/1383.

images were then filtered according to particle size and partial ice grains cut off at the edges were removed. The built-in Matlab function regionprops was then used to calculate the centroid, major axis, and minor axis lengths of all the remaining ice grains in each image. The major axis values from each ice grain in the frame were then averaged and plotted. Figure 7.4(a) demonstrates that the water-ice grains grew in length from 20 μm to 80 μm at an almost constant rate as the ambient pressure decreased from 600 mTorr to 200 mTorr during 10 seconds.

Since regionprops does not give an accurate minor axis value, a different method was used to investigate the major and minor axis lengths as a function of time. This was accomplished by selecting six frames from the video corresponding to different times and physically measuring the length in pixels of the major and minor axes of a number of ice grains in each using the software *imageJ*. Only the particles that were in sufficiently sharp focus to obtain accurate dimensions were used; this selection resulted in a sample size between 16 and 32 ice grains for each frame. These hand-measured major axis lengths, indicated by square dots in Fig. 7.4(a), show the same trend and very similar values to the regionprops data as the grain length increased from 40 μm to 80 μm. Meanwhile, the minor axis length indicated by circle dots in Fig. 7.4(a) increased from 10 μm to 20 μm between 4 s and 10 s.

The average aspect ratio for each frame was calculated by dividing each respective major and minor axis length and is shown in Fig. 7.4(b). It is apparent that the aspect ratio stayed roughly constant at ~4.25 throughout the growth process.

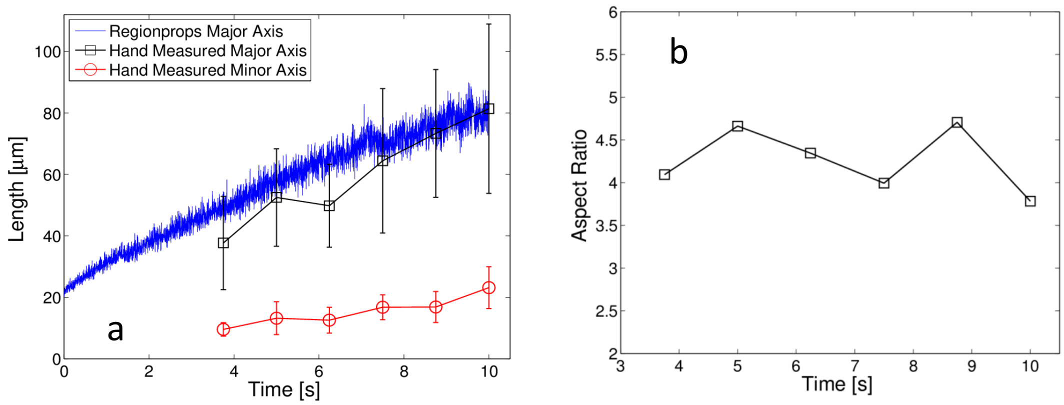

Figure 7.4: Ice grain major and minor axis length as a function of time during growth video. (a) Major axis length from *regionprops* indicated as solid line, major axis length measured by hand using *imageJ* indicated by square dots, and minor axis length measured by hand using *imageJ* indicated by circle dots, and (b) aspect ratio of ice grains calculated using *imageJ* measured values.

The number of ice grains in a frame determined by regionprops as a function of time is shown as the solid line in Fig. 7.5. In order to determine whether or not the data from regionprops is accurate, the number of ice grains in a frame is physically counted from 10 selected frames and is displayed as the circles in Fig. 7.5. The hand-measured numbers show the same trend and similar value to the regionprops data as the number of grains decreases from 120 to 30. This data can be used to quantify the water-ice grain number density because the number of ice grains in each frame is proportional to the number density in the plasma. The constant of proportionality is determined from the size of the frame (1.5×1.5 mm^2) and the depth of field of the regionprops function (1 mm); note that the regionprops function has a thicker depth of field than the camera system because regionprops logs out of focus particles outside the depth of view of the lens. The number density of ice grains decreased roughly linearly with time over most of the growth process.

The number density decreased by a factor of four while the ice grain major radius increased by a factor of four. Section 7.3 discusses the significance of the factor of four number density decrease being small compared to what might be expected from the observed change in total ice grain volume which increases by a factor of r^d where d is the fractal dimension of the ice grains.

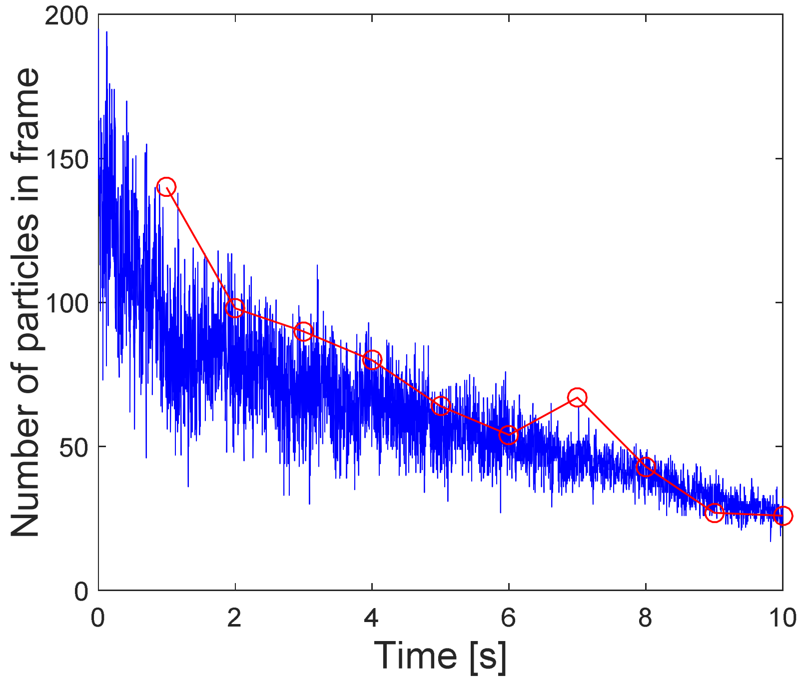

Figure 7.5: Time evolution of the number of particles in each frame.

Major Axis Length Distribution

The major axis length of all ice grains in each frame obtained from the regionprops function can be plotted as a histogram. Figures 7.6(a)-(d) show the major axis length histogram at 2.5, 5, 7.5, and 10 s. The x-axis is the major axis length in μm and the y-axis is the number of particles. As seen in Fig. 7.6, both the mean value of the major length and the FWHM of the distribution function increase with time. The distributions are approximately log-normal which significantly differs from the power-law distribution typically assumed in astrophysical contexts [34, 35, 40, 41]. This difference in distribution is presumed to result from the growth primarily coming from accretion as opposed to agglomeration. We note that the power-law distribution assumed in previous astrophysical contexts is based on the assumption that an equilibrium develops between the collisional processes of agglomeration and fragmentation. If the dust grains do not collide, there is no mechanism for establishing the power-law distribution.

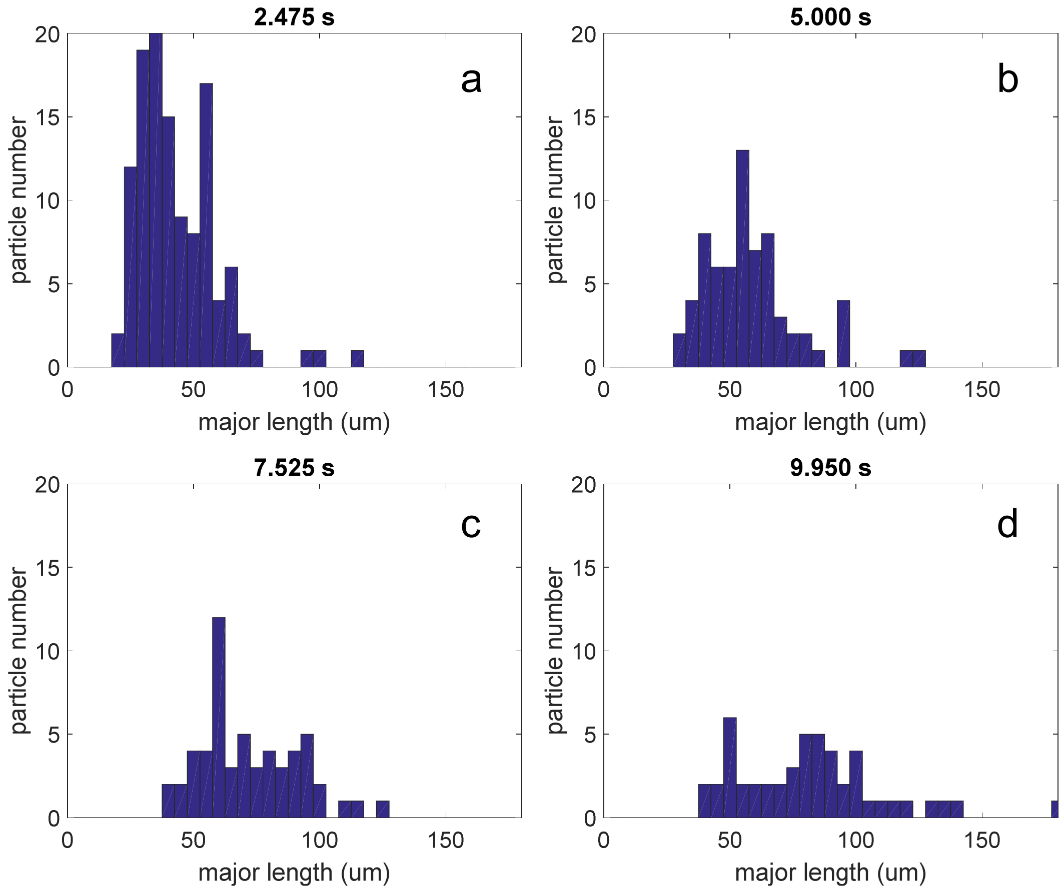

Figure 7.6: Ice grain major axis length distribution at (a) 2.5 s, (b) 5 s, (c) 7.5 s, and (d) 10 s.

Oscillation Motion and Velocity Distribution

The 4,000 frames per second video from the Photron SA-X2 camera enabled tracking the trajectories of individual ice grains. At each frame, the (x, y) position of any specific ice grain was recorded. Figure 7.7(a) shows the (x, y) trajectory of a particle starting from frame 20,000 corresponding to time 5 s while Fig. 7.7(c) shows another trajectory starting from frame 35,000 corresponding to time 8.75 s. In each case, the particle in question was followed for 100 frames and no collisions were observed. Using these position coordinates and the 0.25 ms interframe time, the speed of the ice grain was calculated. The ice grain speed for the trajectory starting at 5 s is shown in Fig. 7.7(b) and the speed of the ice grain for the trajectory starting at 8.75 s is shown in Fig. 7.7(d). The speed is found using $v = (\sqrt{(\Delta x)^2 + (\Delta y)^2} \times 2.7$ μm$)/(0.25$ ms$)$ where Δx is the difference in pixels of the x position of the ice grain between two consecutive frames and Δy is the same for the y position; 2.7 μm is the distance between pixels.

Figure 7.7(e) plots the vertical oscillation frequency of the ice grains as a function of time through the growth process. The frequency was found by watching a pair of well-defined ice grains oscillate through one whole period. The overall trend is that as the ice grains grow, the oscillation frequency drops from 260 Hz to 130 Hz.

It is possible that the observed periodic motion of ice grains in the vertical direction is a result of dust acoustic waves and the horizontal dark regions in the movie are wave fronts. However, because the camera system field of view is too small to observe more than two of these wave fronts, it is not possible to conclude for certain that the dark regions are dust acoustic waves.

The speed distributions of ice grains at 2.5, 5, 7.5, and 10 s are shown in Figs. 7.8(a)-(d), respectively; these distributions were obtained by analyzing 250 movie frames. A correlation function was used to trace ice grains between two successive frames. Not all the grains can be followed because some grains become out-of-focus and some grains cannot be distinguished from others. As a result, only ice grains with a unique shape or sharp edges were followed. However, since there is nothing special about this subset, it represents a reasonable sample. Figures 7.8(a)-(d) show that the mean speed of ice grains becomes slower and the FWHM of the speed distribution becomes narrower with time. This indicates that ice grains become slower as they grow which supports the findings presented in Fig. 7.7(e).

Global Behavior

In order to obtain information on how the ice grains grow throughout the entire plasma volume, a lens with a larger field of view was used to make a movie of the growth process; a frame from this movie is shown in Fig. 7.9. The experimental parameters were identical to those used in Fig. 7.3. The ice grains are observed to grow in size as the pressure decreased from 800 mTorr to 400 mTorr as indicated by Fig. 7.3. It is further observed that dust acoustic waves only occur in the center of the plasma for a short period of time while the ice grains show a flow-like behavior throughout the plasma almost the entire time. It is interesting to note that larger ice grains are observed near the water vapor inlet which is located on the extreme left in the movie images. The observation that dust acoustic waves only occurred in a small central portion of the plasma further indicates that the ice grains likely grow by accretion. Dust acoustic waves have been proposed to be the primary source that provides a kinetic energy for ice grains to overcome the Coulomb repulsive energy in laboratory plasmas [113, 114]. However, because the dust acoustic waves

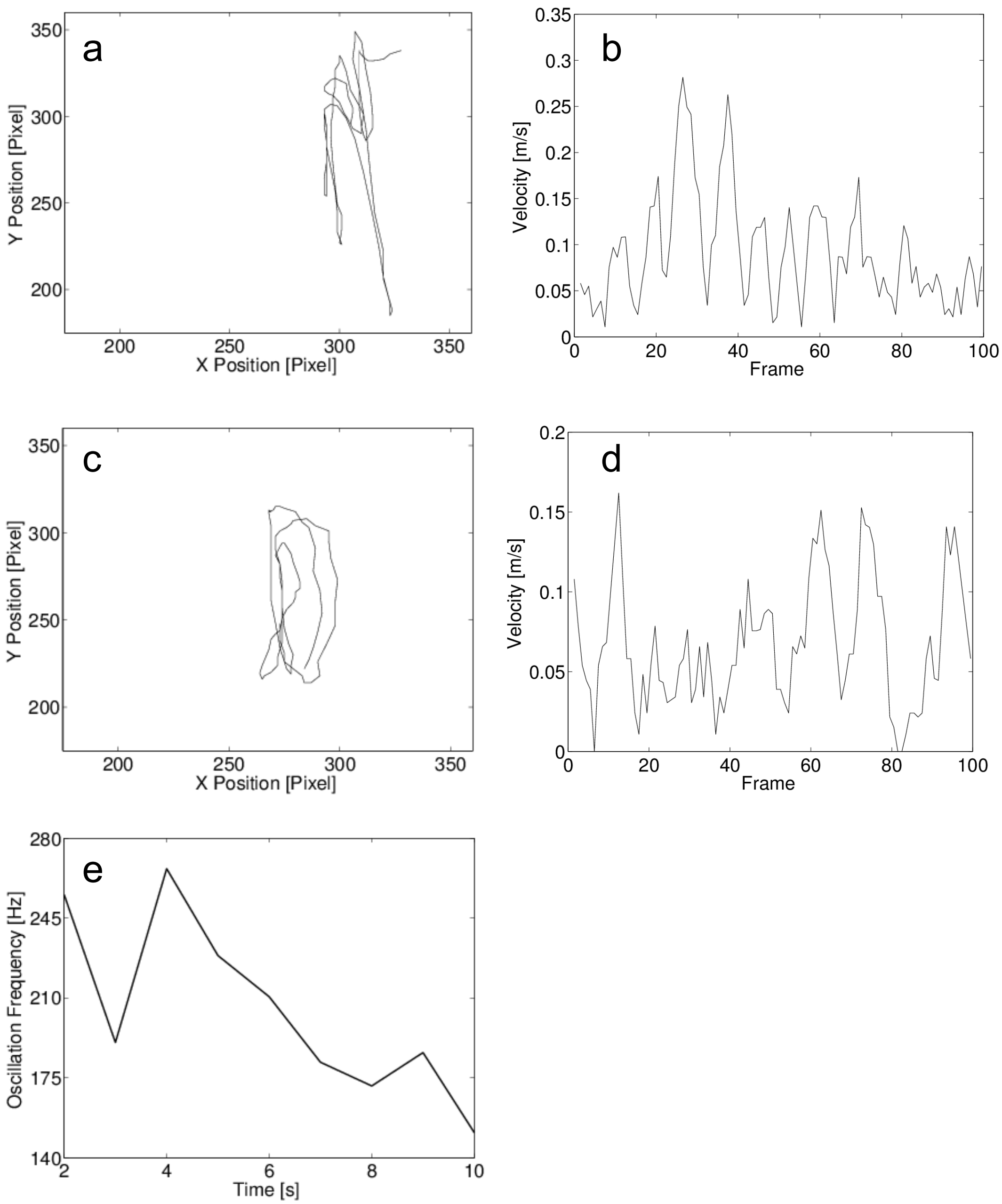

Figure 7.7: Ice grain trajectories: (a) shows a particle trajectory starting from frame 20000 (t = 5 s) tracked over 100 consecutive frames of the video. Its speed is shown in (b). (c) shows a particle trajectory starting from frame 35000 (t = 8.75 s) tracked over 100 consecutive frames of the video. Its speed is shown in (d). (e) shows the vertical oscillation frequency of the ice grains at various times in the video.

do not exist during the entire time that the ice grains grow and are localized to a small central region, it is likely that dust acoustic waves cannot be the reason for the growth here. The appearance of larger ice grains near the water vapor inlet

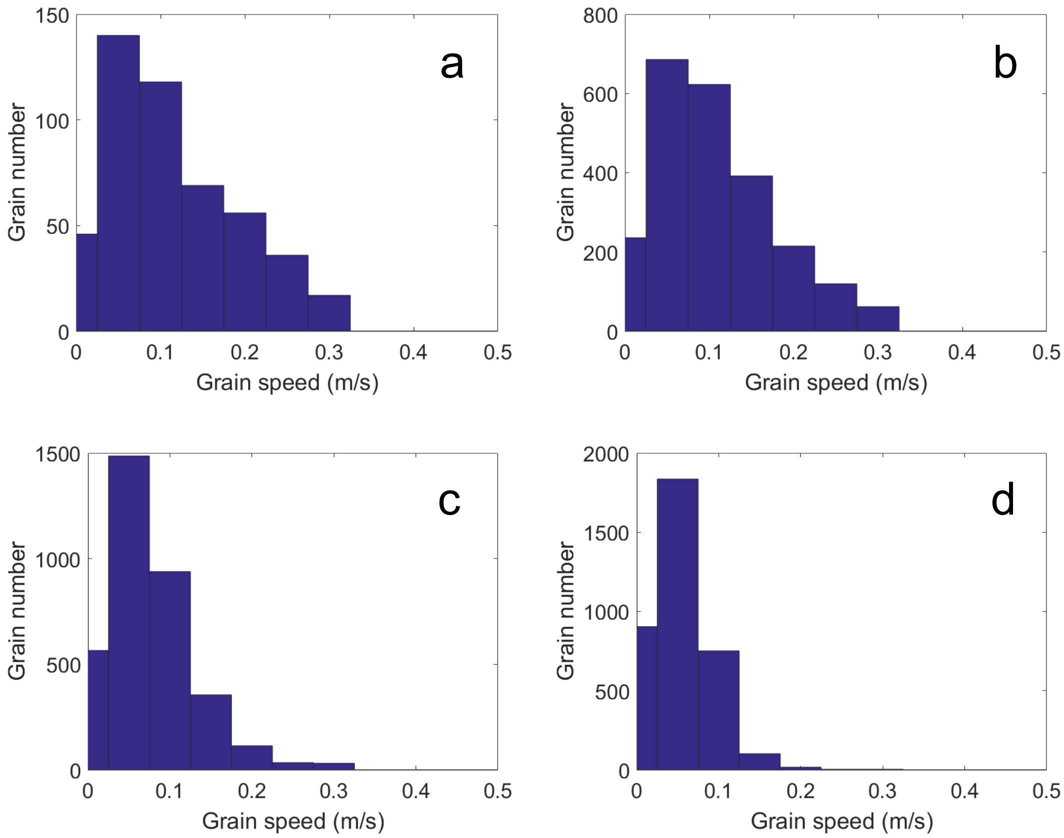

Figure 7.8: Ice grain speed distribution obtained at (a) 2.5, (b) 5, (c) 7.5, (d) 10 s.

additionally suggests that accretion growth is more important than agglomeration growth.

It is possible that differences between our experiments and Refs. [113] and [114] account for the different conclusions. For example, we use water vapor spontaneously freezing into ice grains whereas the other experiments start with pre-formed micrometer-sized spherical objects that are introduced into the plasma and they cannot undergo accretion. Another difference is that the dust particles were observed to levitate near the plasma-sheath edge in other experiments whereas, the ice grains in our experiment levitate in the bulk plasma region.

Figure 7.9 also reveals that the ice grains levitate near the top electrode, not the bottom electrode. This is different from typical laboratory dusty plasma experiments where micron-size dust particles levitate at the plasma-sheath edge near the bottom electrode. This indicates that the downward gravitational force exerted on the ice grains is overwhelmed by the upward thermophoretic force that results from the temperature difference between the top and bottom electrodes; the bottom electrode is warmer than the top electrode in our experiment.

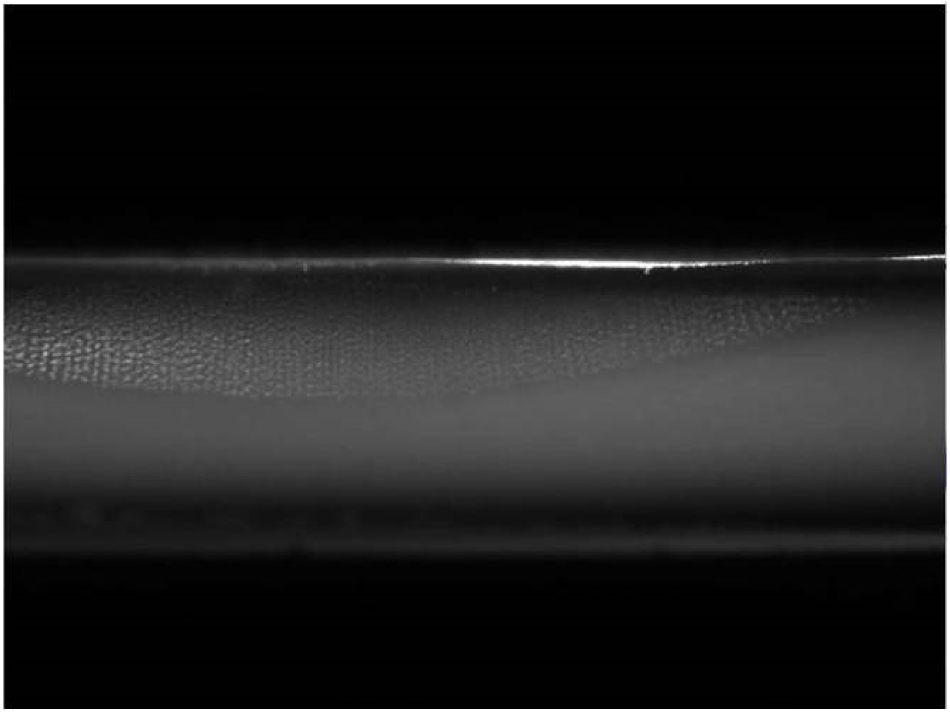

Figure 7.9: Sample picture from movie taken by Dalsa camera with wider field of view lens to observe whole plasma dynamics. The movie is slowed by 10 times.

7.3 Discussion

Ice Grain Size and Number Density

The relationship between ice grain size and ice grain number density provides insight into the dominant growth mechanism. The micron-sized ice grains recorded in the 10 s video grow in length by a factor of approximately four while the aspect ratio stays nearly constant. Also, it is presumed that new ice grains are not created in the plasma since we observed that ice grain nucleation ceases at ambient gas pressures lower than 600 mTorr as stated in Section 7.1.

If it is supposed that agglomeration causes grain growth and assuming that this growth is independent of direction, then to conserve water molecules, the number density of ice grains should drop by a factor of 4^d where d is the fractal dimension of the ice grains. Fractal dimension is used instead of a cubic relation because the ice grains generated are observed to be fractal and the volume of a fractal entity varies as r^d. The nominal fractal dimension was determined from analysis of 2D ice grain images in Ref. [105] to be $d = 1.7$. Since the 2D projection of the fractal dimension was found to be independent of the angle from which photographs were taken, the fractal dimension of the 3D grains can be estimated to be $1.7^{3/2} = 2.2$. The factor of four increase in ice grain size observed here thus corresponds to a factor of $4^{2.2} = 21$ increase in volume with corresponding increase in mass. A mass-conserving 21-fold reduction of the ice grain number density is not observed and this violation of mass conservation contradicts the supposition that agglomeration dominates grain growth. Instead a drop in number density by a factor of only four is observed which implies an increase of the total mass of all the ice grains and so is consistent with growth by accretion and some particle losses.

Consideration of the Possibility of Wave-Induced Collisions

The movies show that the ice grains oscillate quite coherently in a wave. It has been proposed by Refs. [113] and [114] that wave-induced collisions can cause two charged grains in a dusty plasma to collide with sufficient kinetic energy to overcome their mutual electrostatic repulsion and so agglomerate. The ice grains are presumed to move in a coherent wave according to the equation of motion

$$m_d \frac{d^2 y}{dt^2} = q_d E \cos\left(ky - \omega t\right), \tag{7.1}$$

and the relevant questions are (i) can two particles starting at different initial positions in this wave collide with each other and (ii) if they collide, will the collision be strong enough to overcome mutual electrostatic repulsion? The movies provide the following information: $\omega/2\pi = 175\ \mathrm{s}^{-1}$, $2\pi/k = 2000\ \mu$m, amplitude of ice grain oscillation $\tilde{y} = 125\mu$m, and nominal ice grain spacing in the compressed region of the wave $\delta = 200\ \mu$m. The movies also show that the ice grains have no average velocity, i.e., $\langle dy/dt\rangle = 0$ where the angle brackets denote time average.

We now address the above questions using the standard linear analysis of Eq. 7.1. It is first convenient to define the bounce frequency $\omega_b = \sqrt{kq_d E/m_d}$ and the following dimensionless quantities

$$Y = ky,\ \ \tau = \omega_b t,\ \ \Omega = \omega/\omega_b, \tag{7.2}$$

so Eq. 7.1 becomes

$$\frac{d^2 Y}{d\tau^2} = \cos\left(Y - \Omega\tau\right). \tag{7.3}$$

Because $\tilde{Y} = k\tilde{y} = 2\pi \times (125/2000) = 0.4 \ll \pi/2$, we may assume that $Y \approx Y_0$ in the right hand side of Eq. 7.3 where Y_0 is the particle position at $\tau = 0$ in which case Eq. 7.3 becomes

$$\frac{d^2Y}{d\tau^2} = \cos\left(Y_0 - \Omega\tau\right); \tag{7.4}$$

this is the essential approximation in the standard linear analysis. Integration of Eq. 7.4 gives

$$\frac{dY}{d\tau} = V_0 - \frac{1}{\Omega}\left[\sin\left(Y_0 - \Omega\tau\right) - \sin Y_0\right] \tag{7.5}$$

where the first and last terms are constants of integration chosen so that $dY/d\tau = V_0$ at $\tau = 0$. In general these constants of integration would cause $\langle dY/dt \rangle$ to be non-zero, but the observations show that this is not so, hence we must choose

$$V_0 = -\frac{1}{\Omega}\sin Y_0 \tag{7.6}$$

in which case Eq. 7.5 reduces to

$$\frac{dY}{d\tau} = -\frac{1}{\Omega}\sin\left(Y_0 - \Omega\tau\right). \tag{7.7}$$

Integrating again gives

$$Y(\tau) = Y_0 - \frac{1}{\Omega^2}\cos\left(Y_0 - \Omega\tau\right) + \frac{1}{\Omega^2}\cos Y_0 \tag{7.8}$$

where the last term is a constant of integration chosen so that $Y = Y_0$ at $\tau = 0$.

Let us now consider whether two grains initially separated by δ can collide, and for this purpose define the dimensionless separation $\Delta = k\delta$. Consider two particles starting at respective positions Y_{10} and $Y_{20} = Y_{10} + \Delta$ at $\tau = 0$, so their respective motions are given by

$$\begin{aligned} Y_1(\tau) &= Y_{10} - \frac{1}{\Omega^2}\cos\left(Y_{10} - \Omega\tau\right) + \frac{1}{\Omega^2}\cos Y_{10} \\ Y_2(\tau) &= Y_{20} - \frac{1}{\Omega^2}\cos\left(Y_{20} - \Omega\tau\right) + \frac{1}{\Omega^2}\cos Y_{20}. \end{aligned} \tag{7.9}$$

We now assume that the two particles collide at some collision time τ_c, i.e., $Y_1(\tau_c) = Y_2(\tau_c)$. Subtracting the above two equations at this collision time gives

$$Y_{10} - Y_{20} - \frac{1}{\Omega^2}\left\{\left(\cos\left(Y_{10} - \Omega\tau_c\right) - \cos\left(Y_{20} - \Omega\tau_c\right)\right) - \left(\cos Y_{10} - \cos Y_{20}\right)\right\} = 0. \tag{7.10}$$

Let us define

$$S = \frac{Y_{10} + Y_{20}}{2},\ T = \frac{Y_{10} + Y_{20}}{2} - \Omega\tau_c,\ D = \frac{Y_{10} - Y_{20}}{2} \tag{7.11}$$

so $Y_{10} = S + D$, $Y_{20} = S - D$, $Y_{10} - \Omega\tau_c = T + D$, $Y_{20} - \Omega\tau_c = T - D$. Noting that

$$\cos\left(S + D\right) - \cos\left(S - D\right) = -2\sin S \sin D \tag{7.12}$$

and similarly for $S \to T$, Eq. 7.10 can be expressed as

$$\Delta + \frac{2}{\Omega^2}\left\{\sin\left(\bar{Y}_0 - \Omega\tau_c\right) - \sin\left(\bar{Y}_0\right)\right\}\sin\left(\frac{\Delta}{2}\right) = 0 \tag{7.13}$$

where $\bar{Y}_0 = \left(Y_{20} + Y_{10}\right)/2$. Because $\Delta << 1$ Eq.7.13 simplifies to

$$\Omega^2 + \sin\left(\bar{Y}_0 - \Omega\tau_c\right) - \sin\left(\bar{Y}_0\right) = 0. \tag{7.14}$$

The assumption of small wave amplitude so $Y \approx Y_0$ corresponds to having $\Omega^2 \gg 1$ in which case Eq. 7.14 can never be satisfied. Denoting $\tilde{Y}$ as the oscillatory component of $Y(\tau)$, i.e., the deviation of Y from Y_0, Eq. 7.8 shows that $\left|\tilde{Y}\right| = \Omega^{-2}$. However, the measurements show that $\tilde{Y} = k\tilde{y} = 2\pi\tilde{y}/\lambda = 2\pi \times 125/2000 = 0.4$, so $\Omega^2 = 2.5$ which indicates that Eq. 7.14 cannot be satisfied. We thus conclude that coherent linear wave motion as described by Eq. 7.4 cannot produce collisions between grains for the observed wave amplitudes. Thus, if the particles collide, the cause must either be random deviations from the linear solution, more complicated waves, or $Y(\tau)$ substantially deviating from Y_0 in Eq. 7.1 which could happen if the wave amplitude were much larger.

Observational Evidence for Wave-Induced Collisions

If one of the complexities listed above were such that two particles starting at nearly the same position in a wave did collide, their relative velocity would be small because the two particles follow nearly the same trajectory. Figure 7.10 illustrates this possibility. Two ice grains that started close together were chosen from frame 21,900 of the high speed video (this frame is at approximately $t = 5.5$ seconds of the video) and the vertical position of each trajectory for the next 100 frames is plotted in Fig. 7.10.

Figure 7.10 shows that the y positions of the two particles intersect a few times indicating that there would be a collision if the particles also had the same x and z positions. Such intersections are at odds with the discussion in Sec. 7.3 and indicate existence of a random wave component or that it is incorrect to assume $Y = Y_0$ when calculating the wave phase. It is important to note that the trajectories plotted in Fig. 7.10 do not indicate actual collisions because the two ice grains have different x positions and likely different z positions as well. Direct measurements of relative velocities of the very occasional particles that do come close indicate the maximum relative velocity of approaching particles to be 0.20 m/s and numeric calculations

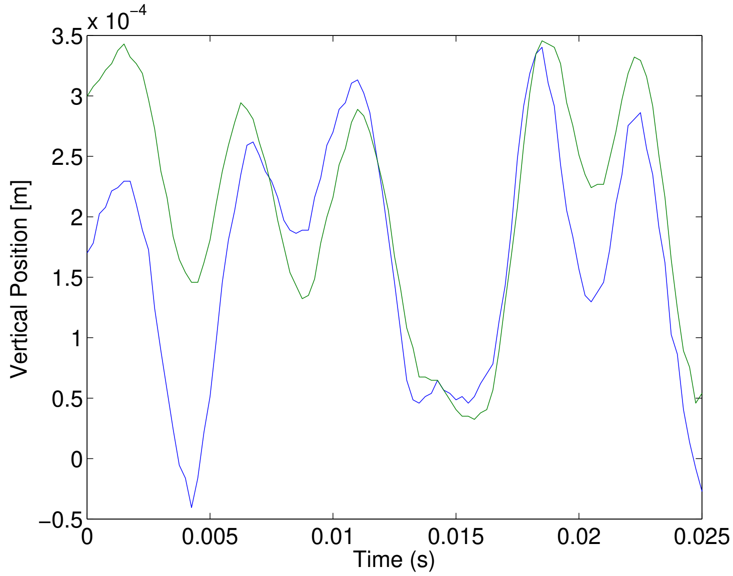

Figure 7.10: Vertical component of the trajectories of two neighboring ice grains in the plasma starting from frame 21,900 and charting for the next 100 frames. Time $t = 0$ at frame 21,900. Note that when the ice grains occupy the same vertical position (i.e., resulting in a collision in the 1D model but not in the three dimensions of the actual experiment because the grains are offset horizontally), they have nearly the same vertical velocity (slope) so their relative vertical velocity is very small.

of the wave theory solutions provide a relative velocity of 0.10 m/s. Therefore $v_{rel} = 0.15 \pm 0.05$ m/s is used for future analysis.

Packing Factor

A comparison between kinetic energy calculated in the center of mass frame and the potential energy associated with Coulomb repulsion provides information on the possibility of collisions when two ice grains approach each other. Comparing the initial kinetic energy with the potential energy at closest approach constrains the ice grain packing factor, i.e., the fraction of the ice volume that is solid. The kinetic energy of an ellipsoidal ice grain having major radius b, minor radius a, and packing factor p is

$$T = \frac{1}{2}\rho v_{rel}^2 \times \frac{4\pi a^2 b}{3} \times p \tag{7.15}$$

where v_{rel} is the initial relative velocity between the two ice grains. The potential energy at closest approach d between two dust grains having charge Z_d is

$$U = \frac{Z_d^2 e^2}{4\pi\varepsilon_0 d} \tag{7.16}$$

and at closest approach $T = U$.

Solving $T = U$ for d and noting that no collisions occur if $d > 2b$ gives

$$Z_d > \frac{4\pi}{e} abv_{rel}\sqrt{\frac{p\varepsilon_0\rho}{3}} \text{ for no collisions.} \tag{7.17}$$

The mass density of ice is $\rho = 940$ kg m^{-3}and $v_{rel} = (0.15 \pm 0.05)$ m s^{-1} will be assumed. We consider nominal grains having $b = 20$ μm and $a = 6$ μm. Inserting these values in Eq. 7.17 gives

$$Z_d > (7 \pm 2) \times 10^4 \sqrt{p} \text{ for no collisions.} \tag{7.18}$$

An estimate for the packing factor p can be obtained by calculating Z_d from capacitance and floating potential. It is presumed that the dust grain charge lies between the value predicted by a one-dimensional Langmuir probe model (slab model) and a three-dimensional orbital motion limited (OML) model. The ice grain floating potential as determined by one-dimensional Langmuir probe theory is

$$V_d = -T_e \ln\left(\frac{m_i}{2\pi m_e}\right)^{1/2}. \tag{7.19}$$

The capacitance of an ellipsoidal ice grain is

$$C = C_f \varepsilon_0 \sqrt{4\pi S} \tag{7.20}$$

where S is the ellipsoid surface area and C_f is a dimensionless factor depending on the elongation b/a [115].

The surface area of a prolate ellipsoid is

$$S = 2\pi a^2 \left(1 + \frac{\sin^{-1}\kappa}{\kappa\sqrt{1-\kappa^2}}\right) \tag{7.21}$$

where

$$\kappa = \sqrt{1 - \frac{a^2}{b^2}} \tag{7.22}$$

so for $a = 6$ μm and $b = 20$ μm, $\kappa = 0.954$ giving $S = 1.2 \times 10^{-9}$ m^2. Reference [115] gives $C_f = 1.03$ for $b/a = 3.3$. Since $Z_d e = CV_d$, Eq. 7.19 gives

$$Z_d = C_f \varepsilon_0 \sqrt{4\pi S}\frac{T_e}{e} \ln\left(\frac{m_i}{2\pi m_e}\right)^{1/2} \tag{7.23}$$

so assuming $T_e = 3$ eV for the He plasma, the grain charge calculated using this capacitance method is $Z_d = 7.4 \times 10^4$. We now use Z_d calculated from the 1D Langmuir Theory, i.e., Eqs. 7.19 to 7.23, and then after the calculation, we will show the extent to which the results differ if OML theory is used to provide a value for Z_d in Eq. 7.18 instead.

Combining Eqs. 7.17 and 7.23 and defining the aspect ratio function

$$F(\kappa) = 1 - \kappa^2 + \frac{\sqrt{1-\kappa^2}}{\kappa} \sin^{-1} \kappa \tag{7.24}$$

constrains the packing factor to

$$p < \frac{3C_f^2 \varepsilon_0}{2\rho} \frac{F(\kappa) T_e^2}{a^2 v_{rel}^2} \left(\ln \left(\frac{m_i}{2\pi m_e} \right)^{1/2} \right)^2 \text{ for no collisions.} \tag{7.25}$$

This gives

$$\begin{aligned} p &< 0.6 \text{ for no collisions if } v_{rel} = 0.2 \text{ m/s} \\ p &< 2.3 \text{ for no collisions if } v_{rel} = 0.1 \text{ m/s} \end{aligned} \tag{7.26}$$

using values of $\rho, T_e, S, a, b, v_{\max}$ given above. For $b/a = 1, F(\kappa) = 2$ while $F(k) \to 0$ when $b/a \to \infty$. For the a, b values used here $F(\kappa) = 0.493$.

If OML theory is used instead of the 1D slab model, then an important parameter is $\alpha = Z_d n_d / n_i$, the fraction of all negative charge in the plasma which is on the dust grains. If $\alpha \to 0$ is assumed, then Eqs. 17.13 and 17.27 in Ref. [1] indicate $Z_d \simeq 1.7 \times 10^4$ assuming $r_d = 6$ μm while if $\alpha = 0.2$ is assumed, then one obtains $Z_d \simeq 1.5 \times 10^4$ showing very little sensitivity to the value assumed for α so long as α is small compared to unity. Because Eq. 7.18 shows that p scales as Z_d^2 and because the OML model predicts Z_d to be four times smaller than in the 1D slab model, the OML model gives packing factors 16 times smaller, i.e., $p < 0.04$ for no collisions if $v_{rel} = 0.2$ m/s and $p < 0.14$ for no collisions if $v_{rel} = 0.1$ m/s. The lower predicted charge implies less mutual repulsion and so the dust grains would have to be fluffier in order not to collide for the same initial relative velocity.

It is clearly seen from the high resolution images of ice grains in Fig. 2 of Ref. [105] that due to their fractal nature, ice grains formed in our experiment are not completely-filled ellipsoid volumes. An estimate based on analysis of the images indicates the packing factor to be $p \approx 0.1$, i.e., an ellipsoid circumscribing the ice grain would have about 10 times the volume of the ice grain. However, the ice grain capacitance would be similar to the ellipsoid because for both the ice grain and the ellipsoid, the electric charge from the electrons is concentrated on the extremities because of the mutual repulsion of the electrons. Thus, the observed packing factor is not inconsistent with the estimated constraints on packing factor calculated above.

Additional Evidence Supporting Accretion to be the Growth Mechanism

Two additional experimental observations support the hypothesis that accretion provides the growth mechanism.

The first of these was to vary the water vapor inflow rate and observe any resulting effect on ice grain size; this test is informative because agglomeration should be insensitive to water vapor inflow rate whereas accretion would be affected. The first step in the experimental sequence was to nucleate ice grains in the He plasma as done for the high-speed movies, i.e., the background He pressure was started at 1 Torr, and then lowered. When the descending background He pressure crossed 600 mTorr which happened at approximately t=10 s as in Fig. 7.2, the water vapor valve was throttled to change the inflow rate. After waiting an additional 10 s, the ice grains were photographed (i.e., at time 20 s in Fig. 7.2). The experiment was repeated with the valve closed, half open, and fully open. Figure 7.11(a) shows the initial condition when the background pressure is 600 mTorr (this corresponds to time 10 s in Fig. 7.2). Figures 7.11(b)-(d) show the situation for the three different valve settings 10 s later (i.e. at 20 s in Fig. 7.2). Figure 7.11(b) has the valve closed and the ice grains are very small and spherical, Fig. 7.11(d) has the valve fully open and has large elongated ice grains, while Fig. 7.11(c) is intermediate. The way the valve was set greatly affected the ice grain size which is consistent with growth dominated by accretion but not with growth primarily by agglomeration.

The second of these additional observations is given in Ref. [106]. In Section 3.5 of Ref. [106], smaller and more spherical ice grains are observed when an externally produced 190 G magnetic field is applied to the experiment. This reduction in grain size can be explained by the applied magnetic field causing electrons to undergo cyclotron gyration in which case the electron flux perpendicular to the magnetic field is attenuated because gyrating electrons cannot move freely across the magnetic field. Because the ions remain essentially unmagnetized, the ion flux is unaffected by the magnetic field. This reduction of the ratio of electron to ion flux on ice grains reduces Z_d and because the ice grains are smaller when the magnetic field is applied,

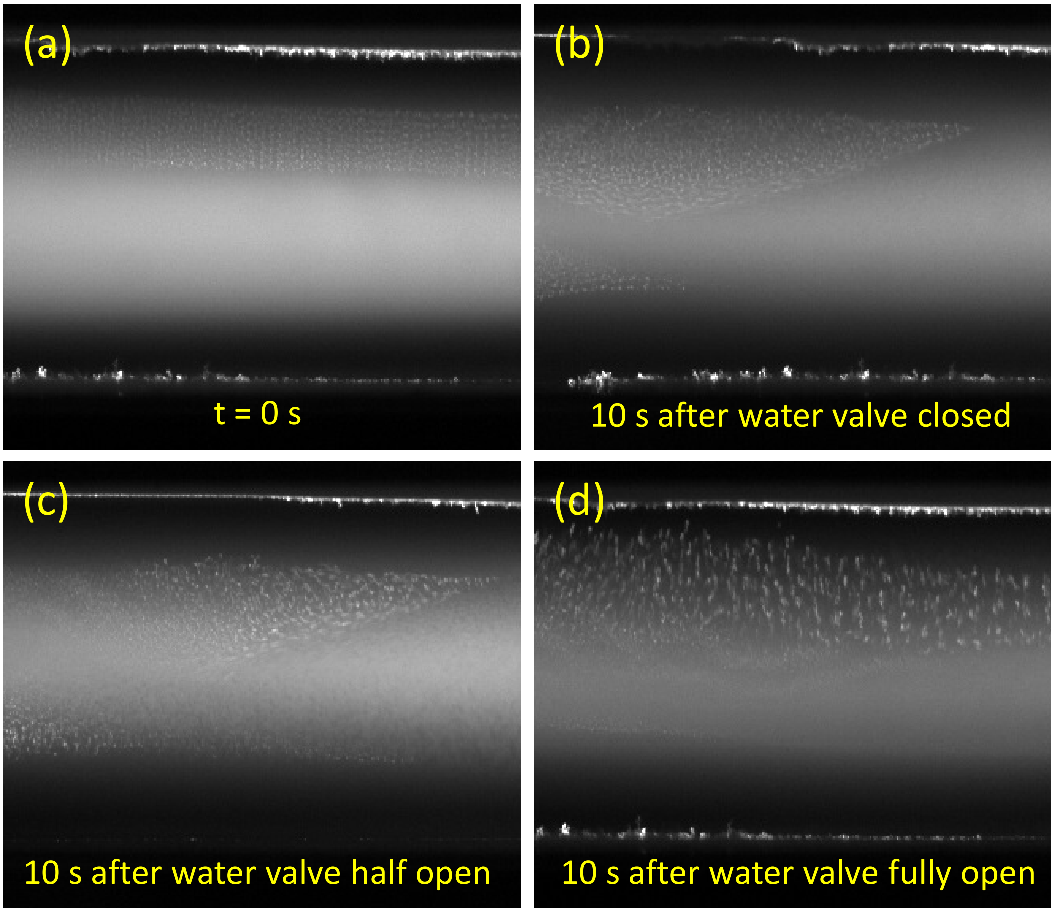

Figure 7.11: (a) Ice grains captured when the background He pressure was 600 mTorr (at t=10 s in Fig. 7.2) with water vapor supply. Ice grains imaged 10 s after (b) water vapor inflow was closed, (c) half opened, and (d) fully opened; the background pressure kept on decreasing as seen in Fig. 7.2. Larger and more elongated ice grains form with higher water vapor inflow indicating accretion is dominant over agglomeration.

it can be concluded that reduction of Z_d results in smaller ice grains. This is the opposite of what would happen if agglomeration was the main growth mechanism because reduction of Z_d reduces Coulomb repulsion between grains which would increase the collision frequency and hence the growth rate by agglomeration.

Ice Grain Observation

The ice grains in this experiment are somewhat smaller than those reported previously in Ref. [105] for similar conditions. In Ref. [105], it was stated that ice grains in a low pressure helium plasma attained maximum length of around 300 μm whereas here we only see a maximum length of 80 μm. This discrepancy arises for two reasons. First, in Ref. [105] the largest ice grains in the plasma were sought out by viewing the entire plasma. Because here the camera field of view is fixed on a small region, it is possible we are observing a different plasma region where the ice grains are smaller. Second, we are only measuring 10 seconds of growth whereas Ref. [105] waited one or two minutes until the ice grain growth had saturated. It is highly likely that the grains are still growing at the end of the measurement interval in the experiment here.

Possible Growth Mechanism for nm Ice Grains

A growth process scenario consistent with the video observations presented here is that the grains grow by coagulation when they are nanometer size, but then grow by accreting water vapor when their size exceeds some critical threshold. This two-step process is very similar to the SiH_4 and CH_4 plasmas in [47], [48], and [49]. The rationale for the two-step process is that at nanometer size, because ice grain number density is comparable to the ion number density, the water-ice grains cannot be highly charged, so the Coulomb barrier is sufficiently small to be overcome. As the ice grains grow by this first-stage agglomeration mechanism, their number density significantly decreases and they become so highly charged that the Coulomb barrier becomes unsurpassable. Despite this Coulomb barrier to collisions, it is observed that the ice grains still grow. Because agglomeration cannot be the growth mechanism when there is insurmountable Coulomb barrier, some other mechanism must take over and the evidence presented here indicates that accretion is likely to be this mechanism.

Chapter 8

LIF

[1] R. S. Marshall and P. M. Bellan. "Laser-induced fluorescence measurement of very slow neutral flows in a dusty plasma experiment". In: *Review of Scientific Instruments* 91.6 (2020), p. 063504. DOI: https://doi.org/10.1063/5.0006684.

Laser-Induced Fluorescence (LIF) is a plasma spectroscopic diagnostic that can be used to measure the velocity distribution of a target species and so give the species temperature and flow speed. LIF works by exciting an atom or ion from some initial state to an excited state, and then measuring the fluorescence photons emitted as the atom decays out of the excited state to a third, different state. LIF was first performed in the 1970's using tuneable dye lasers [116, 117]. Performance and convenience was improved when Severn *et al.* replaced the dye laser with a tuneable diode laser thereby demonstrating Tuneable Diode-Laser Induced Fluorescence (TD-LIF) on the 668.429 nm argon II ion line [118].

The temperature of argon neutral gas in both a dust-free and a dusty plasma environment has recently been measured on the ground-based PK3 experiment in Germany using absorption spectroscopy, a method similar to LIF [119]. One shortcoming associated with absorption spectroscopy is that it is a line-averaged measurement. The addition of a photomultiplier tube (PMT) perpendicular to the excitation beam in an absorption spectroscopy experiment that detects fluorescence photons turns it into an LIF experiment. This extra hardware gives LIF a measurement localized in three dimensions. The first two dimensions of localization come from the cross section of the beam itself (as in absorption spectroscopy) and the third dimension of localization comes from the location along the beam path intersected by the PMT line of sight.

Over the past few decades, LIF has been used in a myriad of different ways. LIF is an established method to measure xenon neutral and ion exit speeds from Hall thrusters [120, 121]. By splitting one beam into two and using independent chopping, LIF has been used to simultaneously measure two components of the ion velocity distribution function where the components are of the order of $\sim$ 100's of m/s [122]. Because of the localization of the beam and detector, LIF is capable of measuring density profiles in three dimensions [123]. PLIF (Planar LIF) imaging using a camera sensor to detect LIF emission from a planar excitation beam has been used to build an image of density [124]. The shift between the double-peaked LIF spectrum from Zeeman splitting can even be used to measure magnetic fields [125].

TD-LIF measurements of the temperature and flow speed of neutral argon atoms in both dust-free and astrophysically-relevant dusty environments through the introduction of frozen water-ice dust grains will be presented in this chapter. Information on the astrophysical relevance and how the dust grains grow is given in Ch. 7 of this thesis and in Refs. [105, 126]. We report results using the argon neutral LIF scheme that pumps on the $\lambda_{vac} = 696.735$ nm transition between the metastable $\left({}^2P^0_{3/2}\right)$4S level and the excited $\left({}^2P^0_{1/2}\right)$4P level. Decay from the $\left({}^2P^0_{1/2}\right)$4P excited level to the $\left({}^2P^0_{1/2}\right)$4S level produces $\lambda_{vac} = 772.633$ nm fluorescence photons that the PMT detects [127, 128]. Key results are: i) LIF works not only on a dust-free plasma, but also on an astrophysically-relevant dusty plasma, ii) exploitation of symmetry allows measurement of the in-plane two dimensional flow velocity vector as a function of position $\{x, y, z\}$ in a three-dimensional plasma volume, and iii) flow speeds are measured and resolved with sub-linewidth resolution.

8.1 Experimental Setup

Figure 8.1 shows front view (a) and top view (b) schematic diagrams of the Caltech Water-Ice Dusty Plasma Experiment as it has been set up to perform TD-LIF. A Toptica DLC Pro controller and Toptica DL Pro ultra-narrow tuneable diode laser-head are used. The DL Pro laser-head is capable of producing up to $\sim$ 35 mW of continuous beam power with a $\sim$ 150 kHz linewidth. The beam traverses a beam-splitter and a mechanical chopper that chops the two resulting beams at 1 kHz. Both beams are coupled to optical fibers with collimators that direct the beams into the plasma. The collimation is slightly less than perfect with an opening angle $\theta \approx 0.33°$. Over the distances traversed in the dusty plasma experiment, beam divergence is assumed to be negligibly small. A moveable barrier between the chopper wheel and the optical fiber entrances allows only one beam to pass through the plasma at a time. The key feature is that the fibers send the two laser beams into the plasma from opposite sides so that light from the "$+z$ beam" is traveling along the same path but in the direction opposite of the light from the "$-z$ beam." The $+z$ and $-z$ beams are named for the beam directions. Light from the $+z$ beam propagates in the positive z direction from small z to large z and light from the $-z$

beam propagates from large z to small z. A PMT utilizes a 1 nm full width half max line filter so that it only detects 772.633 nm fluorescence photons. It views the beams at a 90° angle. The PMT signal goes to a lock-in amplifier which is synchronized to the chopper.

In Fig. 8.1(b), the dashed black line and thick black dots on the optical fibers and PMT indicate that the $-z$ beam, the $+z$ beam, and the PMT are all mounted on the same rigid structure. This rigid structure is mounted on three stepper motors which allow the two beams and the PMT to move together in three dimensions. The 1D translating barrier, also shown in Fig. 8.1(b), is moved by a fourth stepper motor. With these four motional degrees of freedom, the TD-LIF diagnostic is completely automated in Labview and can scan the plasma over a three-dimensional volume with either the $+z$ or the $-z$ beam illuminating the plasma.

The three-dimensional perspective in Fig. 8.2 shows the relative orientation of the gas nozzles and the laser beams. Figures 8.3(a) and (b) shows the coordinate system; where $x = 0$ is defined to be mid-way between both nozzles, $y = 0$ is defined to be in the middle of each nozzle, and $z = 0$ is defined to be the edge of the nozzles. This origin $(0, 0, 0)$ will be used when moving the stepper motors to collect data from the plasma in a three-dimensional volume.

This motorized system can be programmed to measure LIF at any series of (x, y, z) positions in the plasma. The biggest limitation is the finite cross-sectional area of the $-z$ and $+z$ beams. This poses little challenge when measuring LIF throughout the bulk volume of the plasma, but becomes critical for measuring on length scales smaller than the diameter of the beams, for example in the plasma sheath regions. Measuring detail in the sheath would require a smaller diameter laser beam. Additionally, it is observed when measuring LIF in the sheath of the plasma that LIF signal amplitude quickly diminishes becoming too small to detect. Thus, LIF measurements in this chapter are limited to the bulk of the plasma.

The imposed symmetry between the gas inlet nozzles and the laser beam path shown in Figs. 8.2 and 8.3 will later be exploited to determine the v_x and v_z components of the in-plane flow velocity using only a single laser beam.

8.2 LIF Theory

Because of the discrete nature of atomic line transitions, LIF can be used to measure the temperature and flow speed of any specific target species in the plasma as long as an appropriate laser and defined LIF scheme both exist. In order to explain how

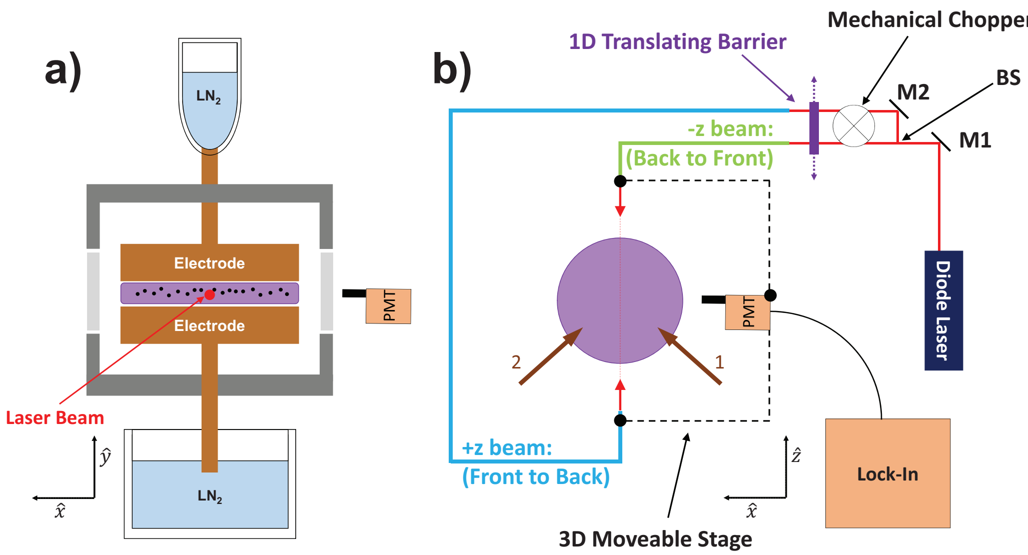

Figure 8.1: Schematic representations of the LIF experiment on the Caltech Water-Ice Dusty Plasma. a) is a view from the front and b) is a view from the top. The bold green and blue lines represent the optical fibers that direct the light to the plasma. The rigid structure that moves the fibers and PMT in unison is shown by the three black dots connected by the dashed lines. Brown arrows 1 and 2 oriented 45° inwards represent the nozzles through which argon gas enters the chamber. M1 and M2 are mirrors and BS is a beam-splitter. Coordinate directions are denoted by the set of axes on each sub-figure.

to measure target species temperature and bulk flow speed, first we will derive the mathematical form that the LIF signal should take.

As written at the beginning of the chapter, the neutral argon LIF scheme used pumps an argon neutral metastable state with λ_{vac} = 696.735 nm and observes emission at λ_{vac} = 772.633 nm. While a stationary neutral atom will absorb radiation with wavelength λ_{vac} = 696.735 nm, atoms in a plasma are moving and the light that each atom sees will be Doppler shifted based on the component of its velocity in the direction of the laser beam.

The Doppler shifted angular frequency is given by

$$\omega = \omega_0 - k_0 v_z \tag{8.1}$$

where $\omega_0 = 2\pi f_0$ is the angular frequency of the unshifted source light, $k_0 = 2\pi/\lambda_0$ is the wavenumber of the unshifted source light, and v_z is the speed of the atom

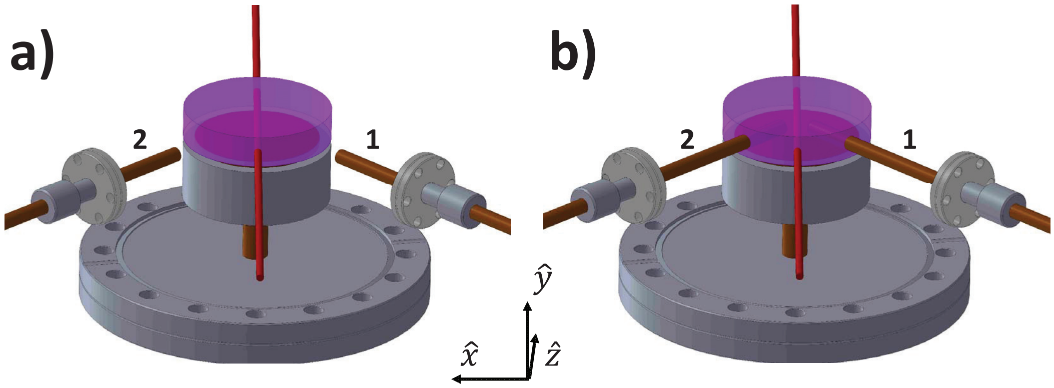

Figure 8.2: Sketch showing the bottom electrode and 6" ConFlat flange with the plasma (purple) in the middle. Top electrode is not shown because it obstructs the view. The laser beam is the red line passing through in the $\hat{z}$ direction. The numbered copper-colored tubes are the gas nozzles. a) and b) are the same, the only difference being that the copper gas nozzles are outside the plasma or inside the plasma, respectively.

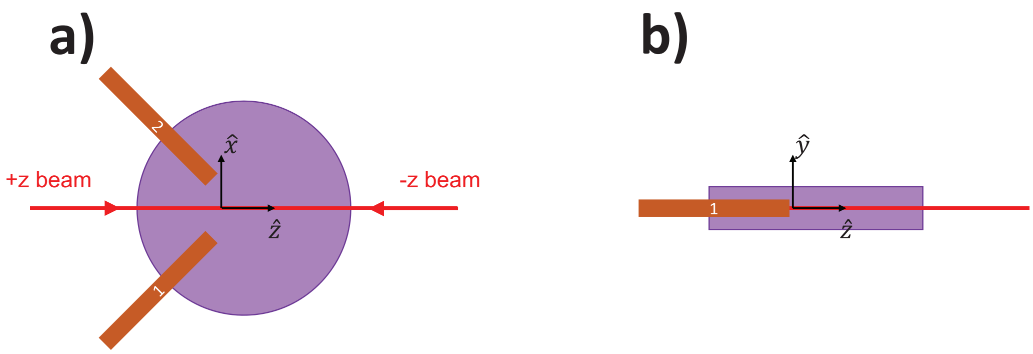

Figure 8.3: Sketch to show the origin of the stepper motor coordinate system. a) is a view from the top looking in $-\hat{y}$ and b) is a view from the side looking in $+\hat{x}$.

projected in the direction of the laser beam.

Rearranging Eq. 8.1 gives

$$v_z = c\frac{\lambda - \lambda_0}{\lambda} \tag{8.2}$$

where v_z is the speed of the atom projected in the direction of the laser beam, c is the speed of light, λ_0 is the wavelength of the unshifted light source, and λ is the wavelength of light seen by the atom.

The Maxwell-Boltzmann distribution for atoms moving in the $\hat{z}$ direction with no mean bulk flow speed is

$$f(v_z) = \sqrt{\frac{m}{2\pi\kappa T}} e^{-\frac{mv_z^2}{2\kappa T}}. \tag{8.3}$$

Substituting v_z in Eq. 8.3 with the Doppler shift relationship in Eq. 8.2 yields the mathematical form of the LIF signal:

$$f(\lambda) = \sqrt{\frac{m}{2\pi\kappa T}} e^{-\frac{(\lambda-\lambda_0)^2}{2\left(\sqrt{\frac{\kappa T}{m}}\frac{\lambda}{c}\right)^2}}. \tag{8.4}$$

The measured LIF signal is fit to the Gaussian profile in Eq. 8.4. Temperature is determined by the width of the best-fit Gaussian and bulk flow speed is determined using its center position λ_0.

Temperature

The temperature of the target species is simply the random motion of the species. This random motion corresponds to the width of the Gaussian in Eq. 8.4. Solving for the full width half max (FWHM) of the spectrum in Eq. 8.4 gives

$$\text{FWHM} = 2\lambda\sqrt{\frac{2\kappa T}{mc^2}\log(2)} = 7.7 \times 10^{-5}\lambda\sqrt{\frac{T}{m}} \tag{8.5}$$

where T has units of eV and m has units of amu (atomic mass unit).

Flow Speed

Flow speed of the target species is the bulk motion of the species. Bulk motion shifts the center position λ_0 of the Gaussian in Eq. 8.4. For the neutral argon species, there would be no bulk flow detected if the best-fit Gaussian has $\lambda_0 = \lambda_{vac} = 696.735$ nm. However for $\lambda_0 \neq 696.735$ nm, the center has been shifted due to a bulk flow. In this case, bulk flow speed is then determined using Eq. 8.2 to be $v_z = \Delta f \lambda_0 = c\left(\frac{\lambda_{vac}-\lambda_0}{\lambda_{vac}}\right)$.

8.3 Results and Discussion

The diagnostic records LIF signal amplitude from the lock-in amplifier as a function of tuneable diode laser piezo voltage. Changing the electric potential on the laser piezo alters the wavelength of light emitted by the laser. In order to convert from diode laser piezo voltage to wavelength, the user must know the exact wavelength at a single piezo voltage (typically found using a reference), and then use the factory calibration factor (21 GHz = 39.2 volts change in the potential applied to the laser piezo tuning actuator) to find the wavelength everywhere else. The LIF signal as a function of wavelength is then fit to the Gaussian in Eq. 8.4 to provide temperature or flow speed as shown in Section 8.2. The TD-LIF diagnostic developed at Caltech produces very reproducible results with signal to noise ratios routinely in excess of 100.

The Toptica DL Pro laser head has a $\sim$ 150 kHz linewidth while the natural linewidth of the neutral argon λ_{vac} = 696.735 nm absorption line is Δf = 5.6 MHz [125]. The Doppler width for thermal argon neutrals at 300 K is calculated to be $\sim$ 1 GHz, so the diode laser is emitting light as an effective δ-function compared to other line profiles.

Temperature Measurements

Doppler widths measured by the LIF diagnostic are on the order of 1 GHz. It was surprising to see that a diode laser illuminating the plasma with only a few milliwatts of pump beam was strong enough to enter a power-broadened regime and give a spurious power-dependent temperature reading [129]. Optical density filters are used to reduce the beam power to the order of 300 μW at which point the measured LIF temperature no longer depends on laser beam power and is considered accurate.

Cooling Electrodes

With no LN_2 cooling, the neutral argon temperature is typically measured to be 350 K compared with the $\sim$ 295 K room temperature. Similar results were found on the PK4 experimental setup at Baylor University where an early version of the diagnostic was installed and operated for two weeks. Upon cooling the electrodes with LN_2, the LIF diagnostic indicates that the neutral argon temperature is much lower. Figure 8.4 shows the measured neutral argon temperature as a function of time while the electrodes are cooling. It takes about 30 minutes for the electrodes to cool from room temperature to $\sim$ 150 K and it similarly takes about 30 minutes for the argon neutrals to cool from ~ 350 K to ~ 200 K.

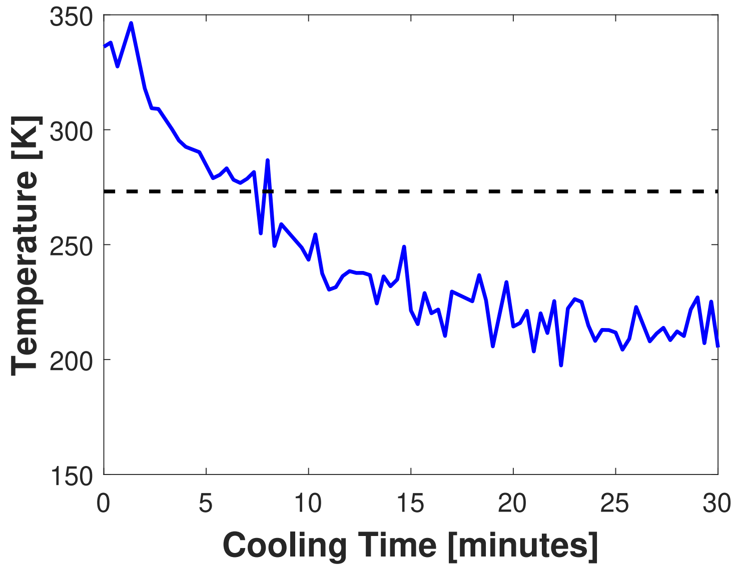

Figure 8.4: Temperature of neutral argon atoms measured by LIF as a function of the time that the electrode cold fingers have been exposed to LN_2. Over the ~ 30 minutes that the electrodes cool, the measured temperature of the neutral argon drops. The black dashed line represents water freezing at 273 K.

Demonstration that LIF Works with Ice Grains

One of the most important results is that the LIF diagnostic still works in a water-ice dusty environment. Figure 8.5 shows a measurement taken with water-ice dust present. A temperature of 192 K was determined.

Flow Measurements

While measuring neutral argon temperature via LIF proved straight-forward after accounting for power broadening, measurement of flow speed was anything but straight-forward. Prior to development of the LIF diagnostic there had not been measurements of neutral flow velocity profiles inside a dusty plasma experiment. Many experiments such as PK4 on the International Space Station use precise electronic flow controllers to carefully regulate flow entering the vacuum chamber where plasma is created [50]. These flow controllers allow the flow to be known at the inlet into the chamber, however the velocity profile after the flow leaves the nozzle and interacts with the existing plasma is still unknown. An LIF diagnostic can be used to quantify the unknown velocity profile inside the plasma. The Caltech

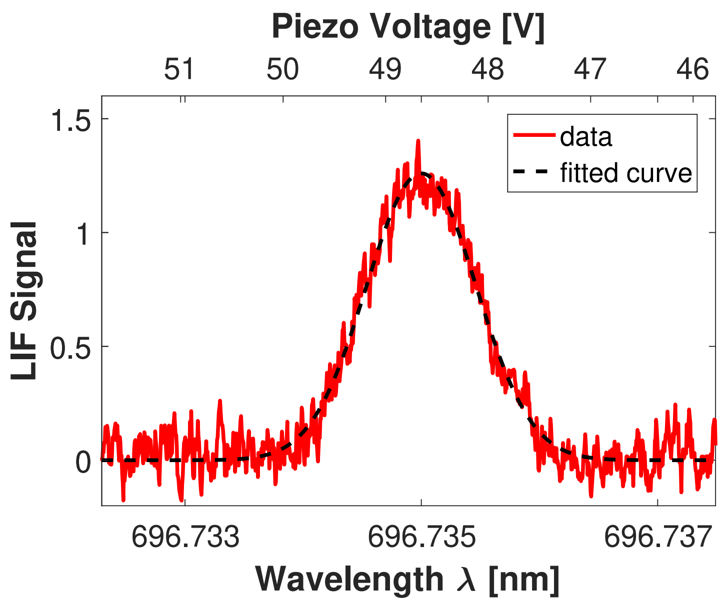

Figure 8.5: LIF signal from neutral argon species in astrophysically-relevant cold water-ice dusty plasma.

experiment lacks an electronic flow controller. Instead a mechanical leak valve is used. A consequence of this is that very little is known about how much gas passes through the leak valve control and how fast the gas is traveling. For reference, $\kappa T = m_{argon} v_{th}^2/2$ gives the room temperature thermal velocity of argon to be $v_{th} \approx 300$ m/s.

When measuring temperature, it does not matter whether the gas nozzle configuration is as in Fig. 8.2(a) where the nozzles are outside of the plasma and on the order of 5 cm away from the counter-propagating laser beams or if the configuration is as in Fig. 8.2(b) where the nozzles are immediately adjacent to the counter-propagating beams. Initial attempts to measure flow speed were made with the nozzles in the configuration of Fig. 8.2(a). In this configuration, measurement of a bulk flow proved unsuccessful.

The key parameter needed to quantify bulk flow speed is the shift of the measured Gaussian from its Doppler-free value λ_{vac}. This is challenging because diode lasers do not have an absolutely calibrated wavelength. Converting from the laser piezo voltage (frequency shift) to an absolute wavelength requires more information than the diode laser can provide. It follows that it is impossible to determine bulk flow speed simply by shining a laser beam through a plasma and then measuring a fluorescence signal, whereas this works for determining temperature.

Several different methods were attempted before a successful flow speed measurement was achieved. One unsuccessful method was to obtain an absolute calibration between piezo voltage and wavelength using the absorption spectrum from a separate plasma in a small fluorescent lamp starter as an absolute reference [130]. This requires using a beam splitter to perform LIF on the Caltech plasma and absorption spectroscopy on the lamp starter plasma simultaneously. Since the lamp starter is small and sealed, it is assumed to have no flow and thus the peak absorption would define $v = 0$. This absorption reference scheme established that the flow speed in the Caltech plasma was very small because the two spectra were perfectly superimposed within the available resolution. It was not possible to make a credible measurement of flow speed. Absolute calibration was also attempted using the Lamb Dip which has been successfully used to measure slow flows in plasma [131]. However, the Lamb Dip was relatively small and requires operation at a pressure much lower than the pressure of interest.

In addition to the difficulty of the flow velocity being very small, the measurement is challenging because the diode laser wavelength constantly drifts due to slight changes in ambient conditions. Thus any absolute calibration becomes inaccurate over time and a constant absolute calibration is required. While the diode laser has an ultra-narrow linewidth, in 20 minutes the wavelength typically drifts $\sim 10 - 20$ MHz and over the course of three hours, by over 250 MHz. This drift would be negligible for measuring $v_{flow} >> 200$ m/s flows, but makes it impossible to measure $v_{flow} \leq 5$ m/s. A 5 m/s flow corresponds to a frequency shift of 14.36 MHz between the two counter-propagating Gaussian peaks. This shift is so small that it would be masked by the laser drift.

Locking the laser wavelength to an external device seems like a logical approach to counteract the laser drifting. Unfortunately, the laser cannot be locked while scanning. An attempt was made to use the built-in PID locking capability of the DLC Pro to lock the laser wavelength using the absorption spectroscopy signal from the fluorescent lamp starter. Unfortunately, the lamp starter proved to be an unreliable reference because the plasma inside the lamp starter is not stable and its light intensity changes in the order of 10 seconds to a few minutes. We also tried to lock the laser to a specific wavelength using a wavemeter as a feedback source, and then to average over a long time to obtain LIF signal as a function of wavelength directly. This also failed because the dusty plasma light intensity changes sufficiently in a few minutes to make this data meaningless. It was determined that satisfactory results could not come from a single long-averaging method of data collection. Instead, a different technique using many 5-10 second measurements taken in succession and analyzed together was found to work and will be presented in the next section.

The final key to successfully measuring flow was to move the gas inlet nozzles from their original positions outside the plasma as in Fig. 8.2(a) to a position inside the plasma much closer to the pumping laser beam as in Fig. 8.2(b).

Single Position Measurement

A counter-propagating beam approach was developed to measure the extremely slow flows. This technique involves repeating the measurement 15 times for a total of 30 data sets at a given position. Figure 8.6 shows typical data taken with this approach. This method can be considered to be in effect a double modulation scheme where the first level of modulation is from the chopper and the second level of modulation is the alternation between the counter-propagating beams.

The diode laser is set to scan a range of $\Delta\lambda = 7$ pm around λ_{vac} over 5 seconds. Specifically, the laser scans from $\lambda = 696.7385$ nm to $\lambda = 696.7315$ nm and back to $\lambda = 696.7385$ nm in 5 seconds. The lock-in amplifier averages with a time constant $\tau = 10$ ms. The steps i taken to measure flow and how long they take to complete Δt_i are:

1. The translating barrier moves to block the $+z$ beam and to allow the $-z$ beam to pass. No measurement is made while the barrier is moving. ($\Delta t_1 = 10$ s)
2. The LIF measurement is saved and plotted in red on Fig. 8.6(a). The measurement is fit to a Gaussian and the center piezo voltage of the Gaussian is plotted in red on Fig. 8.6(b). ($\Delta t_2 = 5$ s)
3. The translating barrier moves to block the $-z$ beam and to allow the $+z$ beam to pass. No measurement is made while the barrier is moving. ($\Delta t_3 = 10$ s)
4. The LIF measurement is saved and plotted in blue on Fig. 8.6(a). The measurement is fit to a Gaussian and the center piezo voltage of the Gaussian is plotted in blue on Fig. 8.6(b). ($\Delta t_4 = 5$ s)
5. Steps 1-4 above are repeated 14 more times. The total time to complete 30 scans is $T = 15\,(\Delta t_1 + \Delta t_2 + \Delta t_3 + \Delta t_4) \approx 450$ seconds.

Figure 8.6(a) shows all 30 individual sets of data taken during the $\sim$ 450 second procedure superimposed: the 15 red traces represent measurements from the $-z$ beam and the 15 blue traces represent measurements from the $+z$ beam. Figure 8.6(a) shows that the results are extremely reproducible. Figure 8.6(b) shows the center piezo voltages for the 30 Gaussians in Fig. 8.6(a). Scan number ranges from 1 to 30 because 30 data sets were taken. The $-z$ beam (red) was taken first, so there are red data points for odd numbered scans and blue data points for the even numbered scans taken with the $+z$ beam. The black dashed lines alternating between the red and blue circles represent the order data was taken starting with the bottom red data point on the left, then the blue data point with the dashed line connecting, and so on.

The 30 LIF measurements plotted in Fig. 8.6(a) are deliberately shown as a function of piezo voltage, not wavelength. There are three reasons for this. i) Wavelength as a function of piezo voltage differs slightly for each scan because the laser is drifting, therefore piezo voltage is a natural way to look at the data because the diode laser is directly tuned by this parameter. ii) Plotting the center piezo voltage of each Gaussian fit shows how the diode laser is drifting whereas plotting LIF signal versus wavelength would obscure this important complication. iii) It takes all 30 measurements and their center piezo voltage to separate the drift out of the measurements and obtain an accurate absolute calibration that can be used to calculate flow speed as will be demonstrated next.

The data in Fig. 8.6 shows how this repeating, alternating counter-propagating beam approach allows for flow measurement even when the laser drift is non-negligible. First, the laser drift is determined by taking all 30 data points (red and blue) in Fig. 8.6(b) and fitting them to a single line $y = mx + b$. The slope of this line m represents the drift of the laser wavelength. Then the individual beam data are both fit to their own lines, shown by the dashed red and blue lines, where the slope of each best-fit line is forced to be the same slope as the linear best fit of all 30 data points m representing the laser drift. In this prescription, the vertical distance between the two fits, i.e. the y-intercepts, provides the absolute calibration required to calculate the flow speed. Thus, the laser drift (slope of the two lines) and the signed flow velocity (distance between the two lines) can both be determined individually from Fig. 8.6(b).

The uncertainty associated with the flow measurement is found by examining each pair of consecutive $-z$ and $+z$ beam LIF measurements together. The difference in volts between the center of first Gaussian for the $-z$ beam and the first Gaussian for the $+z$ beam is found. Then the difference for each subsequent pair is found. The standard deviation of the 15 differences becomes the error bar on the flow measurement.

The enumerated procedure finds the absolute calibration and statistical uncertainty error bar. The vertical distance between the blue and red dashed lines in Fig. 8.6(b) is measured to be $\Delta V = 0.0068 \pm 0.0030$ piezo volts. The piezo voltage halfway between the shifted peaks, illustrated by the solid black line in Fig. 8.6(b), corresponds to $\lambda_{vac} = 696.735$ nm. Applying the calibration factor from Toptica, the frequency shift between the two peaks is then $\Delta f = \Delta V \times \left(\frac{21\times10^9}{39.2}\right) = 3.63$ MHz. This gives $v = \Delta f \lambda_{vac}/2 = 1.3 \pm 0.6$ m/s flow speed. The Doppler shift from this flow changes the wavelength of the center of the peak by 3 femtometers = 3×10^{-15} m.

2D Plane Scan

A two-nozzle setup is used to enable measurement of the v_x and v_z flow velocity vector components. Figures 8.3(a) and (b) show the coordinate system and origin of the stepper motor axes for scanning in three dimensions. Nozzle 1 is located at (-4125,0,0) and Nozzle 2 is located at (4125,0,0) in stepper motor coordinates where 1600 stepper motor coordinates correspond to 2.5 mm so one motor step is 1.5625 μm. The stepper motors are computer controlled so high spatial precision is obtained.

The PMT and the two fibers with collimators providing the two counter-propagating laser beams were mounted on a single rigid moveable structure. This rigid structure was moved in three dimensions by stepper motors controlled by a Labview program. The LIF diagnostic took the same measurement steps described in the previous section at each of 63 positions on a grid in the xz plane. The data shown in Fig. 8.6 was taken at $(x, y, z) = (-3000, 0, 3000)$ in stepper motor coordinates which corresponds to $\mathbf{r} = -4.6875\hat{x} + 0\hat{y} + 4.6875\hat{z}$ in units of mm from the origin of the stepper motor coordinate system shown in Fig. 8.3. This also corresponds to 1.7587 mm in the $\hat{x}$ direction and 4.6875 mm in the $+\hat{z}$ direction from Nozzle 1. Figures 8.7 and 8.8 show the measured flow speeds as a contour plot for each nozzle. The diagnostic was moved over the 7x9 grid from $-3000 \leq x \leq 3000$ and $0 \leq z \leq 10000$ or equivalently $-4.6875 \leq x \leq 4.6875$ and $0 \leq z \leq 15.625$ mm at $y = 0$. It took approximately 9 hours each to repeat the procedure to deduce flow

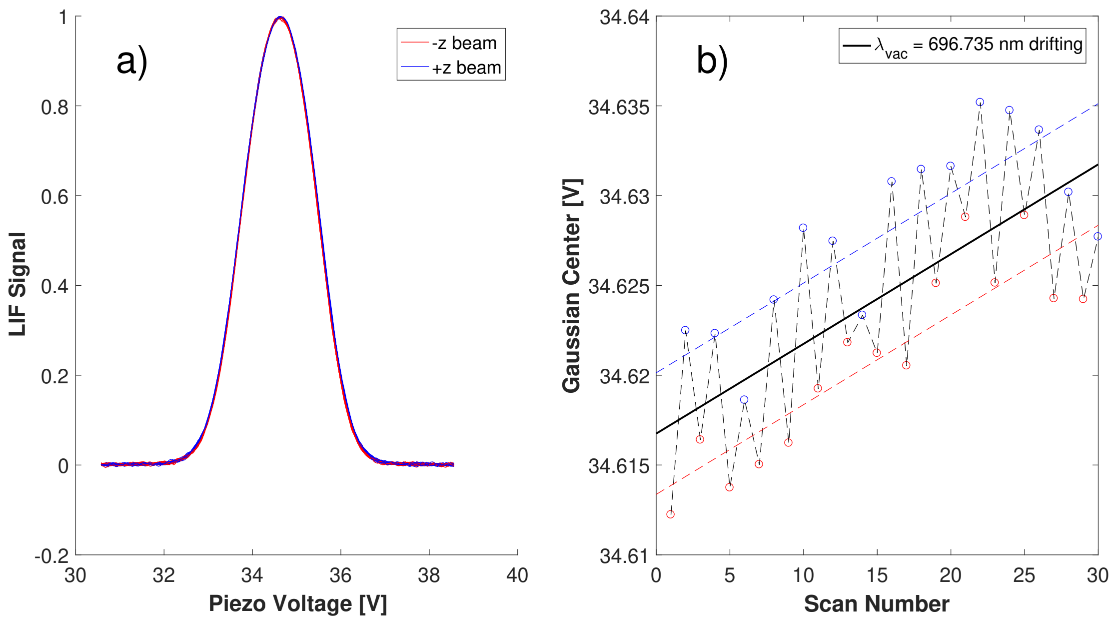

Figure 8.6: Illustration of how to calculate flow speed using the alternating counter-propagating beam approach described in steps 1-5. a) shows the 30 measured data sets taken during the $T \approx 450$ second procedure. The data is normalized and plotted on the same axes so it can be compared. There are 15 red and 15 blue traces representing data from when the $-z$ and $+z$ beams are shining, respectively. b) shows the center of the Gaussian fit from Eq. 8.4 for each of the data sets. The black dashed line represents the order data was collected starting with the red dot at scan number 1 and alternating red and blue subsequently. The slope of the best fit lines represents the drift of the laser itself and the separation of the lines represents the flow velocity. The solid black line between the dashed lines shows how the piezo voltage corresponding to λ_{vac} = 696.735 nm changes over the 30 measurements due to laser drift.

speed at each of the 63 positions in the grid and create the contours in Figs. 8.7 and 8.8.

We now describe how an imposed symmetry created by a prescribed experimental setup enables determination of both in-plane components of the flow velocity.

Consider the 1.3 m/s flow shown in Fig. 8.6 and the contour plots in Figs. 8.7 and 8.8. The flow speeds in these figures are flow speeds projected in the direction of the laser beam because LIF can only measure flow parallel to the laser beam. The data in Fig. 8.6 thus indicates 1.3 m/s = $\mathbf{v_1}\,(-3000, 0, 3000) \cdot \hat{z}$ because the laser beam propagates in the $\hat{z}$ direction. Likewise, the data that makes up the contours of Figs. 8.7 and 8.8 are contours of $\mathbf{v_i}(x, y, z) \cdot \hat{z}$ where $i = 1$ or 2, respectively.

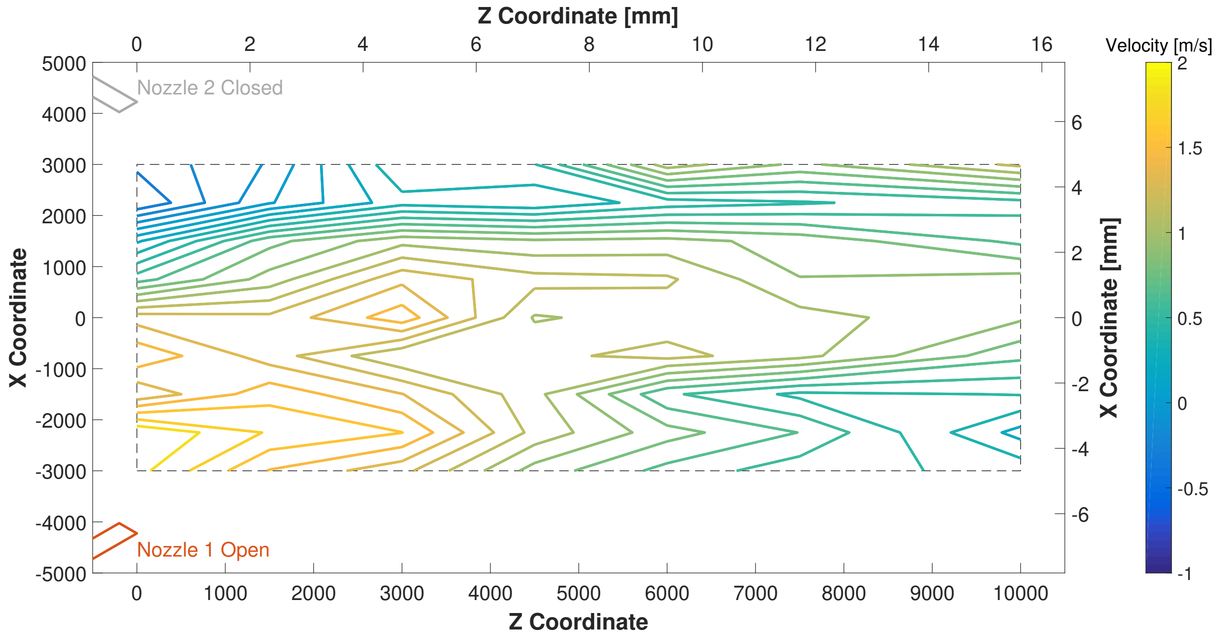

Figure 8.7: Measured $\mathbf{v_1}(x, y, z) \cdot \hat{z}$ flow contours for Nozzle 1 located at $(0, -4125)$ with Nozzle 2 closed. It took approximately 9 hours to measure the data needed to create this contour plot.

Figure 8.9 shows the two-nozzle geometry in detail. Consider measuring a 1.3 m/s = $\mathbf{v_1}(x = -3000, y = 0, z = 3000) \cdot \hat{z}$ flow from Nozzle 1. The actual velocity vector of the argon atom is illustrated by the purple arrow in Fig. 8.9, but the LIF diagnostic only measures the $\hat{z}$ component which is the green arrow and completely misses the orthogonal red $\hat{x}$ component. The key symmetry in Fig. 8.9 is that the flows from Nozzle 1 and Nozzle 2 are simply rotated by 90° with respect to each other. The two measuring positions denoted by the two black dots in Fig 8.9 are displaced from their respective nozzle by the same vector. This means that the purple arrows (flow velocity) have the same magnitude, but their orientation differs by 90°. The red and green velocity components are similarly the same magnitude. By closing Nozzle 1 and opening Nozzle 2, the red component is measured instead of the green which is now orthogonal. Thus with two nozzles 90° offset and one beam, LIF can effectively measure two components of the flow speed, v_x and v_z, from a single nozzle.

The second component of the flow velocity is obtained by rotating the $\{z, x\}$ co-ordinates of the Nozzle 2 data by 90° in the counter-clockwise direction. Figure 8.10 shows arrows made from the Nozzle 1 v_z data and the Nozzle 2 v_x data where the coordinates from Nozzle 2 have been rotated to the Nozzle 1 basis. The brown

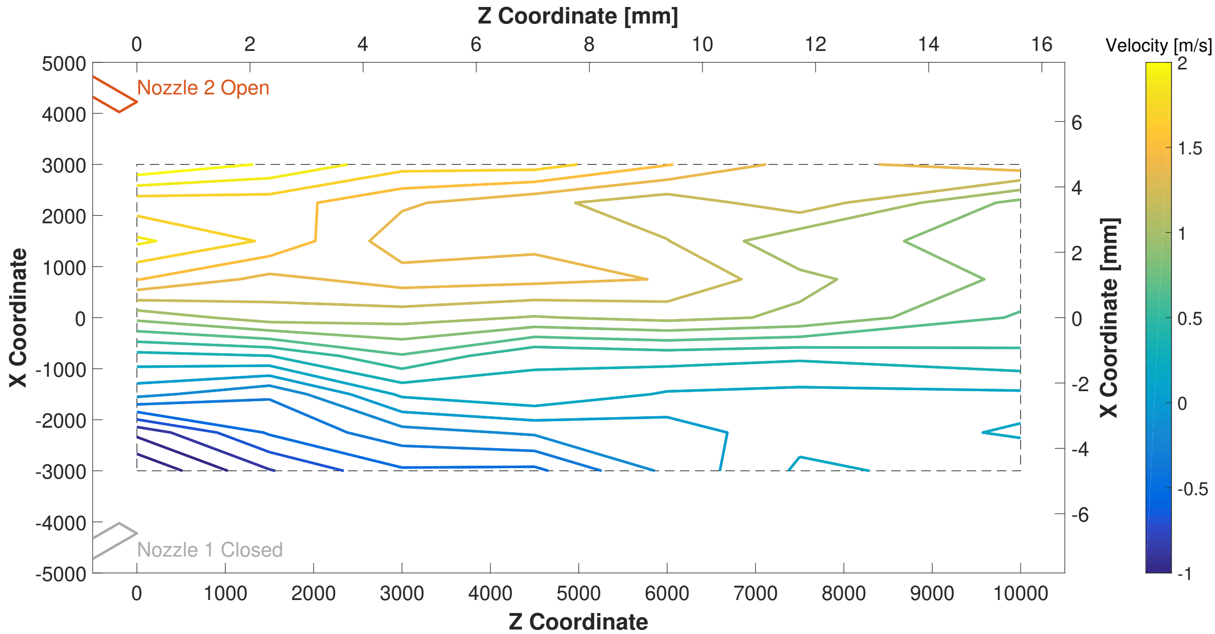

Figure 8.8: Measured $\mathbf{v_2}(x, y, z) \cdot \hat{z}$ flow contours for Nozzle 2 located at (0, +4125) with Nozzle 1 closed. It took approximately 9 hours to measure the data needed to create this contour plot.

outline represents the location of Nozzle 1. It took $9 \times 2 = 18$ hours to measure the data to create the velocity arrows in Fig. 8.10.

The nozzle orientation in the xz plane and the geometry of the electrodes leads us to believe that $v_y << v_x, v_z$. The velocity resolution of the LIF diagnostic is exhausted when trying to explore the out-of-plane y component of the flow velocity by assuming an incompressible flow and solving for $\frac{\partial v_y}{\partial y}$ in $\nabla \cdot \mathbf{v} = 0$. No conclusions are able to be drawn about v_y.

How Flow Speed Changes with Parameters

The arrows in Fig. 8.10 clearly show that the flow speed is peaked near the nozzle and decreases as the LIF diagnostic moves away in x and z. Changing the rate of inflowing gas by varying the leak valve setting and changing the rate of outflowing gas by partially valving off the turbopump are two ways to vary the neutral argon flow speed in the plasma measured by the LIF diagnostic at a given position. Chamber pressure is determined by an equilibrium between the inflow rate determined by the leak valve and the outflow rate determined by the pumping efficiency of the turbopump. Altering either changes the pressure.

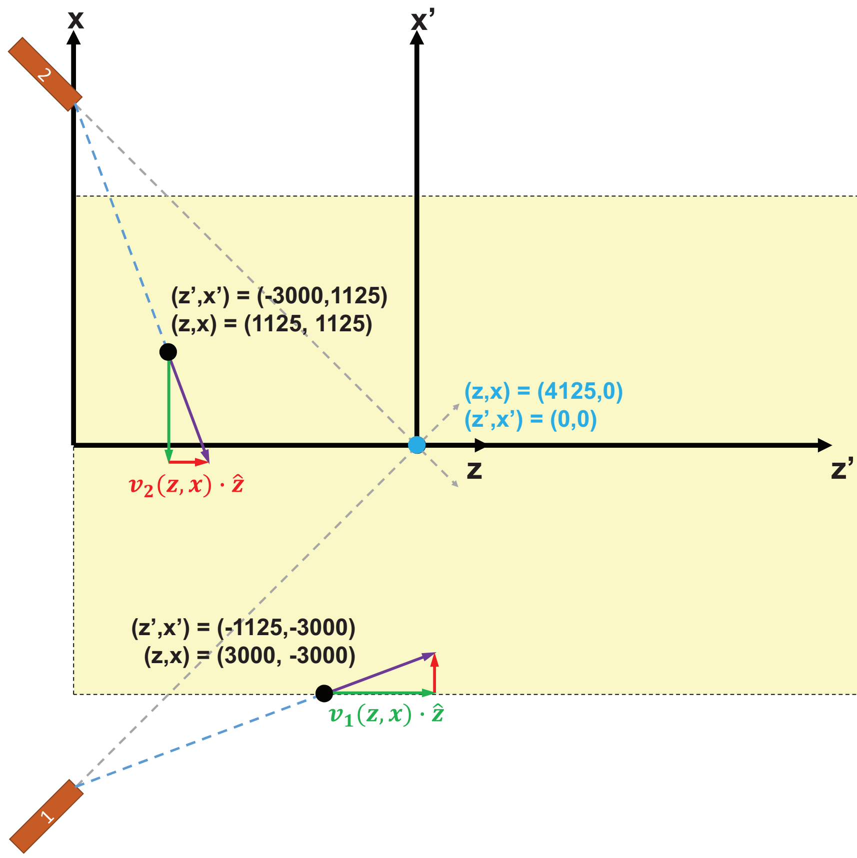

Figure 8.9: A to-scale illustration of the rotational symmetry between the nozzles using stepper motor coordinates. Measurements are made in the yellow rectangular region. The origin of the (z', x') axes sits at $(z, x) = (4125, 0)$ and represents the point of rotational symmetry for the nozzles. Each of the measurement positions denoted by black circles is the same vector from its respective nozzle. This symmetry means that the purple flow velocity vector from each position is the same, simply rotated by 90°.

First, one can vary the inflow rate of gas into the chamber by opening or closing the mechanical leak valve. By restricting the flow through the leak valve and holding chamber pressure constant by partially valving off the turbopump, it is seen that the measured flow speed drops by a factor of about three from 4.6 m/s to 1.6 m/s.

Second, one can change the pressure in the chamber while holding the inflow leak valve setting constant and partially opening the valve to the turbopump. As the chamber pressure drops from 330 mTorr to 90 mTorr, it is seen that the flow speed measured by the LIF diagnostic increases from 1.7 m/s to 4.6 m/s.

Third, it is also seen that physically reversing the direction of the flow that is

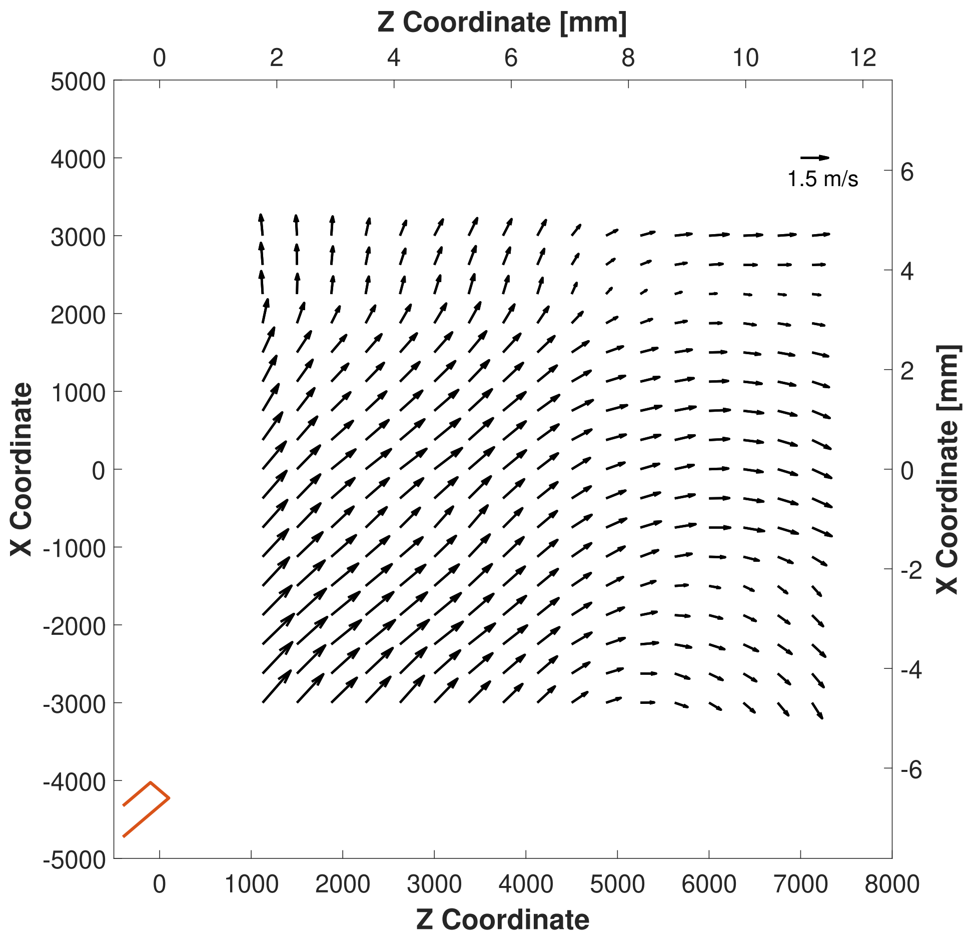

Figure 8.10: Two-dimensional in-plane flow velocity measured using the rotational symmetry between the nozzles in the xz plane at $y = 0$ represented by arrows with a scalebar in the upper right corner providing a reference. The brown outline near $(0, -4125)$ represents Nozzle 1, the source of this flow.

projected into the direction of the laser beam path produces very similar results. The only difference is that the sign of the measured flow velocity has reversed.

Figure 8.11 shows the second and third trends graphically. In the figure, flow is measured while the nozzles introduce flow in opposite directions along the axis of the LIF diagnostic separately. Unsurprisingly, the diagnostic measures flow in the opposite direction (sign) depending on which nozzle is used. Varying pressure in the chamber by partially valving off the turbopump while holding the inflow setting constant produces flow speeds of approximately the same amplitude regardless of which nozzle is used. The only difference is the sign. The negative flow datapoint at 333 mTorr with the particularly large error bar was made from data with considerably more laser drift than the other measurements.

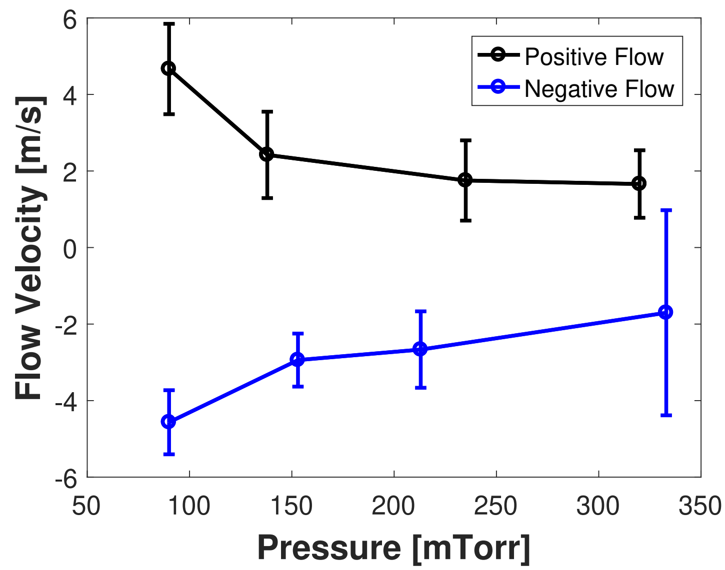

Figure 8.11: Measured flow speed with error bars as a function of chamber pressure. Inlet flow is held constant and pressure is varied by partially valving off the turbopump. The positive and negative flows are made from nozzles producing flow in opposite directions projected on the LIF beams.

Mean Free Path for Collisions

Consider the mean free path for collisions of inflowing neutral argon atoms,

$$\lambda_{mfp} = \frac{\kappa T}{\sqrt{2}\pi d^2 p}. \tag{8.6}$$

Doubling the Van der Waal's radius gives the effective diameter d of an argon atom; d = 376 pm [132, 133]. For a room temperature plasma at T = 300 K, λ_{mfp} in meters is simply inversely related to pressure by $\lambda_{mfp} = 0.049/p$ where p is in mTorr. For p = 100 mTorr, λ_{mfp} = 0.5 mm.

The flow speed decreases as the LIF diagnostic is moved away from the nozzle because the inflowing argon atoms have to travel through more mean free paths before they reach the beam. This means that they have thermalized more and have less of a bulk flow. By holding the nozzle and LIF diagnostic in the same position and increasing the background pressure, the mean free path for collisions is reduced and the inflowing argon atoms have to travel more mean free paths to get to the same position. This means that they are more thermalized, so the measured flow speed is less. When the nozzles were outside the plasma, the argon flow had to travel through $\sim$ 3 cm of plasma to reach the laser beams which is more than 30 mean free paths, so the flow was likely fully thermalized with no bulk flow left. This is presumed why the initial effort to measure flow with the nozzles in the Fig. 8.2(a) configuration failed.

Resolving Details Smaller than the Natural Linewidth

One subtle issue is that the linewidth of the 696.735 nm transition in neutral argon is $\Delta f = 5.6$ MHz [125]. One might therefore presume as in Ref. [118] that the minimum resolvable flow speed is then $v_{min} = \Delta f \lambda_{vac} = 3.9$ m/s. One would be troubled that all the flow speeds presented in this paper have $v < v_{min}$ and that we are resolving speeds of a fraction of a meter per second. However, this would only be an issue if our conclusions were based on single point measurements where one would experience the full linewidth as uncertainty. This is not the case for the methods described here because data is taken at many different wavelengths and is fitted to a Gaussian shape. The peak of the Gaussian can be resolved to much less than the transition linewidth because determining the peak involves averaging over a large number of data points.

Relative Density and Attenuation Coefficient Measurements

Figures 8.12(a)-(d) show that the measured LIF signal changes when translating the LIF diagnostic along the beam axis $\pm\hat{z}$. Figure 8.12(a) shows LIF data measured when the $-z$ beam traverses the plasma. Each color trace superimposes 15 measurements made at each of the seven z positions shown in the color bar on the right. Likewise, Fig. 8.12(c) shows the same 15 measurements for each color when the $+z$ beam traverses the plasma. Figures 8.12(b) and (d) plot the average temperature deduced from the 15 LIF measurements at each position in Figs. 8.12(a) and (c), respectively. Statistical uncertainty error bars were calculated from the standard deviation of the temperature deduced from the 15 LIF measurements at each position. These bars are not shown on Figs. 8.12(b) and (d) because they are smaller than the colored circle data point markers. For example, the blue point at $z = 0$ in Fig. 8.12(d) is $T = 427.8 \pm 1.1$ K.

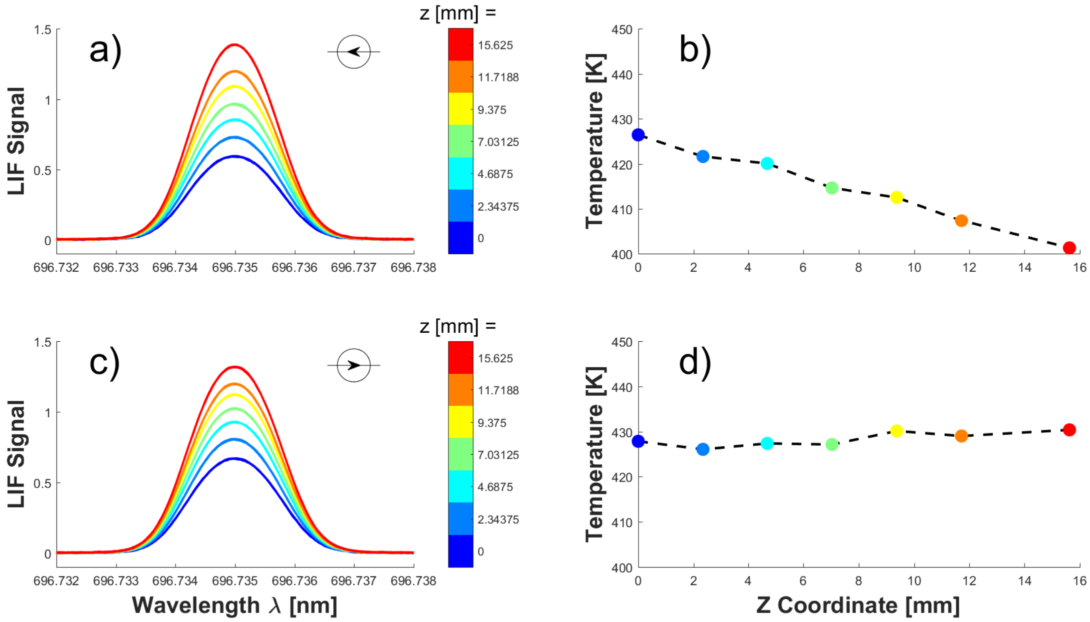

Figure 8.12: Wavelength dependent LIF signal amplitudes as a function of measurement position z for the $+z$ and $-z$ beams. a) and c) show LIF signal measured by the PMT as the LIF diagnostic is moved along the beam axis from $z = 0$ to $z = 15.625$ mm for the $-z$ beam and the $+z$ beam respectively. 15 individual data sets are superimposed in each color on both plots, showing the great reproducibility of the diagnostic. b) and d) plot the temperature deduced from the data in a) and c), respectively, with matching color. Each data point in b) and d) is found by taking the average of the 15 deduced temperatures from the 15 data sets plots on a) or c) in the same color. Error bars are found by taking the standard deviation of the 15 deduced temperatures. These statistical uncertainty error bars are not shown for the deduced temperatures plotted in b) and d) because the data point markers (colored circles) themselves are larger than the error bars.

These measurements from the $+z$ and $-z$ beams show a consistent approximately factor of two difference in LIF signal amplitude between $z = 0$ and $z = 15.625$ mm, independent of which beam is used. This indicates that there is a neutral argon density gradient along the measurement axis such that the density increases towards large z where the LIF signal is strongest.

The Doppler widths of the detected LIF signals also change with z. Both Figs. 8.12(b) and (d) show that the deduced temperature of the neutral argon atoms in the plasma increases as the pump beam is increasingly attenuated. Figure 8.12(b) shows that the deduced temperature of the neutral argon atoms measured by the $-z$ beam increases toward small z. Similarly, Fig. 8.12(d) shows that the deduced temperature of the neutral argon atoms measured by the $+z$ beam increases toward large z. In both cases, the deduced temperature increases with increasing beam travel through the plasma and therefore increasing attenuation.

The opposite temperature gradients deduced in Figs. 8.12(b) and (d) suggest that not all wavelengths of light are absorbed equally by the plasma. Moreover, it suggests a broadening mechanism whereby the deduced temperature is artificially increased as the beam is differentially absorbed by the plasma. This mechanism referred to as "absorption broadening" is a result of the attenuation coefficient κ at the center of the peak being greater than the wings. Mathematically, this means that the attenuation coefficient $\kappa = \kappa(\lambda)$ and $\kappa(\lambda_0) > \kappa(\lambda)$ for $\lambda \neq \lambda_0$.

We now present an analysis of what is happening in Fig. 8.12. This analysis will not explain everything but provides a strong foundation. $A_\pm(z)$, the amplitude of the LIF signal at position z from the $\pm$ beam, is influenced proportionally (up to saturation) by i) $n(z)$, the density of the target species at position z and ii) $P_\pm(z)$, the intensity of the $\pm$ beam at position z. The relationship between $+z$ pump beam intensity and distance z traveled through a plasma of uniform density is $P_+(z) = P_+(0)e^{-\kappa z}$. More specifically, the attenuation coefficient $\kappa = \kappa(z, \lambda) = \alpha(\lambda)n(z)$ is proportional to neutral argon density and is also a function of wavelength via the $\alpha(\lambda)$ term. Therefore the $+z$ pump beam amplitude at a given wavelength traveling through a plasma with non-uniform density is $P_+(z, \lambda) = P_+(0, \lambda)e^{-\int_0^z \alpha(\lambda)n(z)dz}$. Considering the direction each beam is traveling, it is proposed that for a given wavelength, the two functions

$$A_+(z) = A_+(0)n(z)e^{-\alpha \int_0^z n(z')dz'} \tag{8.7}$$

$$A_-(z) = A_-(0)n(z)e^{-\alpha \int_z^0 n(z')dz'} \tag{8.8}$$

quantify how the LIF signal varies along the beam axis for each beam. All multiplicative constants are included in the $A_\pm(0)$ terms. A consequence of this is that $n(z)$ is effectively a relative density at each position and not an absolute density.

It is important to explain why the limits of integration are switched between Eqs. 8.7 and 8.8. Equation 8.7 is integrated from $z' = 0$ to $z' = z$ because the $+z$ beam is exponentially attenuated as it travels in the $+z$ direction from 0 to z. The $-z$ beam travels in the opposite direction, so it is exponentially attenuated as it travels in the

$-z$ direction from $z' = z$ to $z' = 0$ which is why Eq. 8.8 has its limits of integration switched. Equations 8.7 and 8.8 can be written more compactly as

$$A_\pm(z) = A_\pm(0)n(z)e^{\mp\alpha \int_0^z n(z')dz'}. \tag{8.9}$$

Figure 8.13(a) plots the seven signal amplitudes measured at the center wavelength at each position z in Fig. 8.12(a), i.e. $A_-(z)$, and Fig. 8.12(c), i.e. $A_+(z)$, on the same set of axes. The amplitude plotted at each point is the average amplitude of the 15 LIF measurements at each position in Figs. 8.12(a) and (c). Error bars represent the standard deviation of each set of 15 amplitude measurements. $z = 0$ is the reference position for each beam, so $n(z = 0) = 1$ by definition.

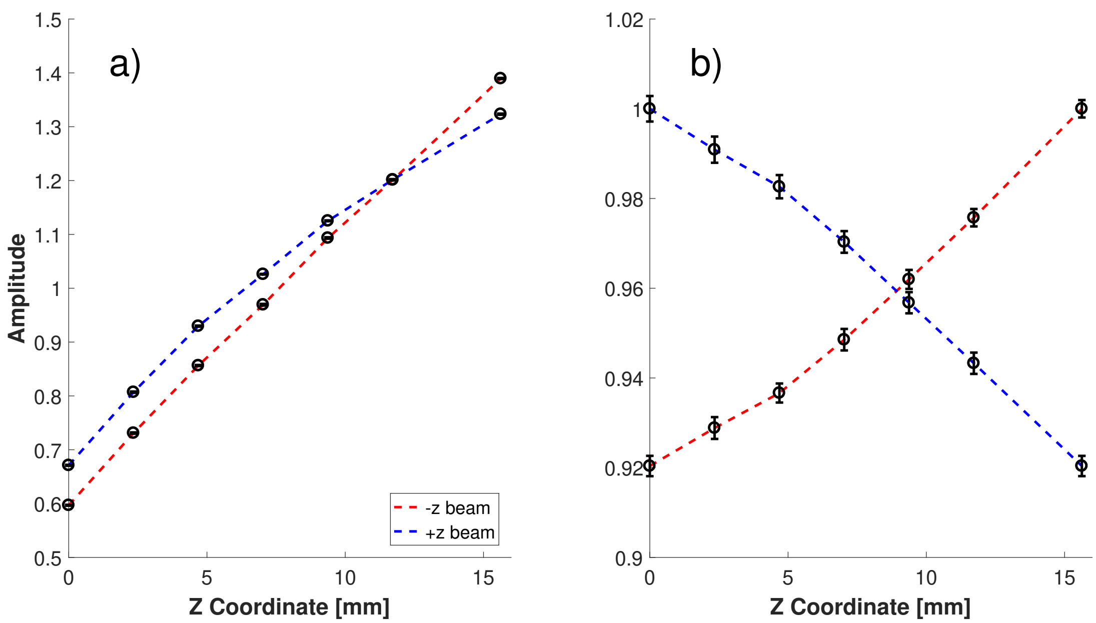

Figure 8.13: LIF signal amplitude as a function of position for the $-z$ beam in red and the $+z$ beam in blue. a) plots the signal amplitude as a function of position for the raw data shown in Figs. 8.12(a) and (c). The barely visible error bars that are smaller than the data markers show the reproducibility of the diagnostic. b) plots the signal amplitudes after they have been normalized by deduced relative density $n(z)$ values shown in Fig. 8.14. The error bars here are slightly larger as the error has been propagated through the density and normalization calculation.

For the $+z$ beam, the signal amplitude $A_+(z = 0) = A_+(0)n(0)e^0 = A_+(0) = 0.6711$. The $A_+(z)$ selection in Eq. 8.9 provides a relationship between each of the seven $(z, A_+(z))$ pairs plotted on Fig. 8.13(a) in blue where $n(z)$ and α remain unknown.

Similarly, for the $-z$ beam, the signal amplitude $A_-(z = 0) = A_-(0)n(0)e^0 = A_-(0) = 0.5969$. The $A_-(z)$ selection in Eq. 8.9 provides a relationship between each of the seven $(z, A_-(z))$ pairs plotted on Fig. 8.13(a) in red where $n(z)$ and α again remain unknown.

These relationships found using Eq. 8.9 provide 14 equations for 8 unknowns. $n(0) = 1$ is trivial by definition, so there are effectively 12 equations and 7 unknowns: $n(z)$ for each non-zero z position and α. The relative density $n(z)$ is obtained by multiplying the obtained $A_+(z)$ and $A_-(z)$ relationships for each z together. The exponential integrated attenuation terms cancel exactly, so the relative density is $n(z) = \sqrt{\frac{A_+(z)A_-(z)}{A_+(0)A_-(0)}}$ where all four numbers on the right side are known. Relative density $n(z)$ is plotted in Fig. 8.14. Statistical error from the signal amplitude measurements is propagated through the relative density calculation and found to be negligibly small compared to the size of the data point markers and thus is left off the plot. In Fig. 8.14, $n(15.625) = 2.1425$ means that the density at $z = 15.625$ mm is 2.1425 times the density at $z = 0$.

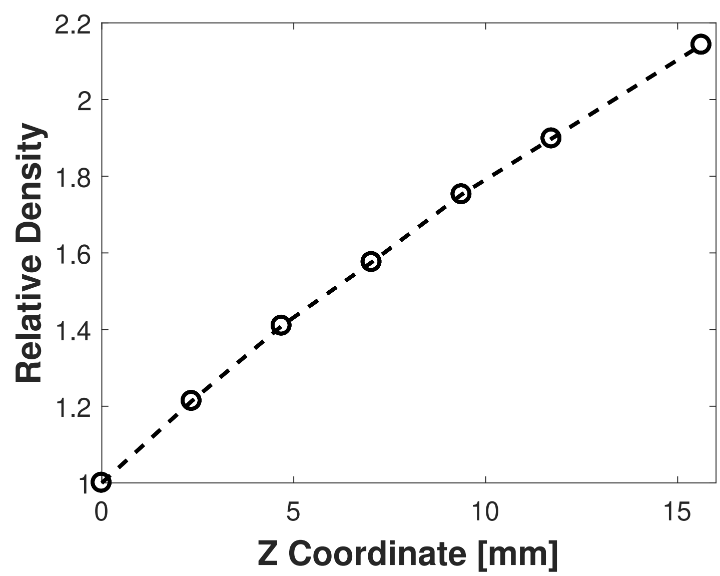

Figure 8.14: Deduced argon neutral relative density $n(z)$. $n(15.625) = 2.1425$ means that the density at $z = 15.625$ mm is 2.1425 times the density at $z = 0$. Error bars are not shown on the figure because the error bars associated with the statistical uncertainty in the density calculation are smaller than the data point markers (circles).

With $A_\pm(z)$, $A_\pm(0)$, and $n(z)$ known for each z, α up to each of the six non-zero z positions can be obtained using either the + or − selection in Eq. 8.9.

Calculating the average and standard deviation of the six obtained α values gives $\bar{\alpha} = 5.2 \times 10^{-6} \pm 2.3 \times 10^{-7}$.

Figure 8.13(b) shows the LIF signal amplitudes after they have been normalized by $n(z)$ (the relative density factors plotted on Fig. 8.14) and normalized again such that the largest signal measured for each beam is one. The error bars represent the standard deviation error propagated through the calculation to this point.

Instead of normalizing only the peak amplitude of the LIF signal, we now normalize each entire LIF measurement from Figs. 8.12(a) and (c) by $n(z)$ plotted on Fig. 8.14. This process does not affect the deduced temperature because temperature does not scale with signal amplitude.

The 15 resulting normalized data sets for the $+z$ beam and the $-z$ beam are each averaged into a separate data set and fit to a Gaussian. Because the beams are counter-propagating and there is a slow flow, the Gaussian fits all have slightly different centers. This is manually corrected for by shifting all the Gaussian fits to have their center at λ_{vac}. Shifting the Gaussian does not affect the deduced temperature because temperature does not depend on the center location. Figure 8.15 shows normalized data on the same axes after averaging and correcting for slow flow. The solid data is from the $-z$ beam and the dashed data is from the $+z$ beam.

The density gradient is not a factor affecting the data in Fig. 8.15, in contrast with the raw data in Fig. 8.12(a) and (c). In Fig. 8.15 for the $-z$ beam, the largest amplitude is at $z = 15.625$ mm whereas for the $+z$ beam the largest is at $z = 0$. The largest amplitude for each beam is thus seen where the beam enters the plasma and the LIF signal amplitude decreases as each beam is attenuated by traveling through plasma.

The last step now is to solve for the wavelength dependent part of the beam attenuation $\alpha(\lambda)$. This is done by dividing the wavelength dependent LIF signal measurements at two different positions in Eq. 8.9 to obtain

$$\alpha_{\pm} = \frac{\mp \log\left(\frac{A_{\pm}(z_2)n(z_1)}{A_{\pm}(z_1)n(z_2)}\right)}{\int_0^{z_2} n(z)dz - \int_0^{z_1} n(z)dz}. \tag{8.10}$$

Figure 8.16 shows $\alpha(\lambda)$ for the $-z$ beam and the $+z$ beam data calculated using Eq. 8.10 at each wavelength λ. There are now six rather than seven $\alpha_{\pm}$ curves because one of the seven positions is used as the reference and the other six are used to

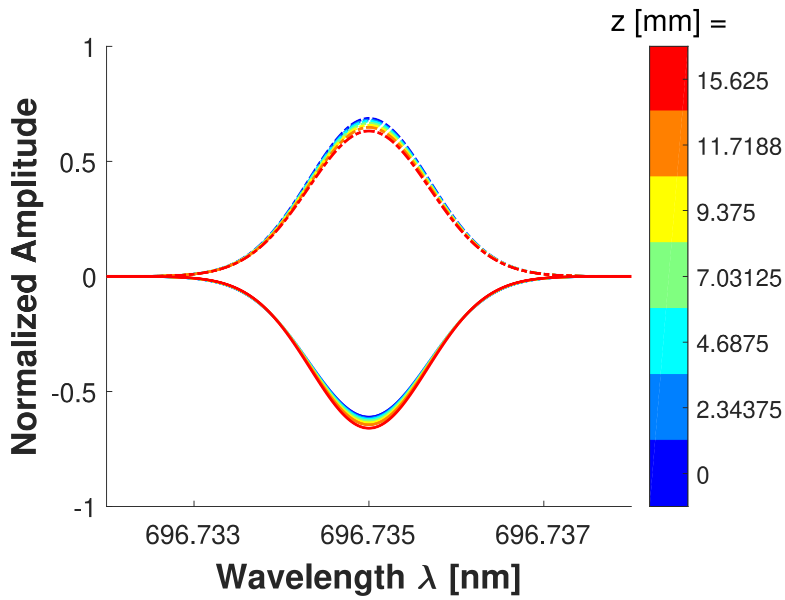

Figure 8.15: LIF signals from Fig. 8.12 (a) and (c) normalized by relative density $n(z)$. The solid lines are from $-z$ beam (inverted) and the dashed lines from the $+z$ beam.

calculate α using the + or − selection in Eq. 8.10. The plotting domain is reduced because the LIF signal peak is largely contained in this domain, and outside this domain away from the peak α does not have a physical meaning. The six curves for α from the $-z$ beam and $+z$ beam agree within the measurements of each beam and the peak magnitude of α shows excellent agreement across beam measurements.

The $\alpha_{\pm}$ curves in Fig. 8.16 quantify absorption broadening. They show that the attenuation coefficient of the pump beam α is a function of wavelength around the peak λ_{vac} absorption. Both plots show that the plasma is the most opaque absorber at λ_{vac} and becomes marginally less opaque away from λ_{vac} on the peak. That means that the detected LIF signals will get distorted as more pump beam is attenuated at λ_{vac} such that the wings of the spectrums see increased signal amplitude relative to the center resulting in artificially increasing deduced temperatures.

It is not clear why $\alpha_{-}(\lambda)$ is more sharply peaked than $\alpha_{+}(\lambda)$, or equivalently, why absorption broadening is stronger on the $-z$ beam and as a result the temperature gradient for the data measured with the $-z$ beam is larger than the temperature gradient for the $+z$ beam. Figures 8.12(b) and (d) picture this as Fig. 8.12(b) shows a larger temperature gradient than Fig. 8.12(d). It was postulated that this effect was due to the optical fibers having a finite opening angle ($\sim 0.3°$) as opposed to the light being collimated to infinity, but attempts to correct for this did not make

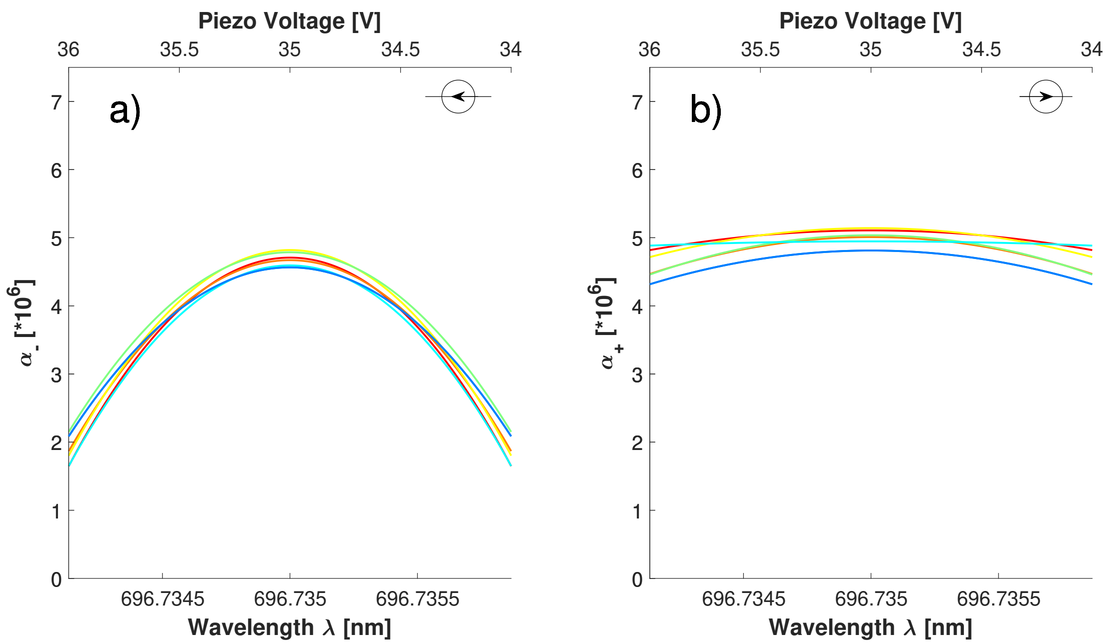

Figure 8.16: α solved using Eq. 8.9 for the $-z$ beam selection on (a) and the $+z$ beam selection on (b).

the $\alpha_\pm$ peaks match.

While the model developed has improved the understanding of how the laser beam is attenuated by the plasma, the fundamental reason for this difference in the strength of the absorption broadening mechanism for the $-z$ and $+z$ beams remains unknown. Possible explanations for the differing gradients are that there is still some power broadening or there is a hysteresis-like effect from the differential damping of the laser beam – the -z beam first travels through dense plasma and then less dense plasma whereas the +z beam first travels through less dense plasma and then higher density plasma.

With an absorption spectroscopy diagnostic, the only measurement obtained would be a line-averaged measurement of this whole effect where density gradient and absorption broadening would remain unknown.

Flow Impact on Ice Grains

To investigate how the inflowing argon atoms affect the water-ice grains, the nozzles shown in Fig. 8.2 are set into an intermediate configuration where Nozzle 2 is inside the plasma as shown in Fig. 8.2(b) and Nozzle 1 is outside the plasma as shown in Fig. 8.2(a). Argon gas flows continuously into the chamber through

Nozzle 1 throughout the experiment to sustain the plasma, and water vapor flows in when allowed to create the ice grains. The goal is to see how toggling Nozzle 2, thus creating a new flow in a different direction, affects the ice grains. After the electrodes have cooled down, water vapor is allowed to flow into the chamber for 20 seconds through Nozzle 1. The water vapor inlet is then closed and a cloud of ice grains forms and grows in the plasma. A horizontal sheet of HeNe laser illuminates a plane of ice grains. The effect of a gas flow on the ice grains can be seen by toggling Nozzle 2 on and off.

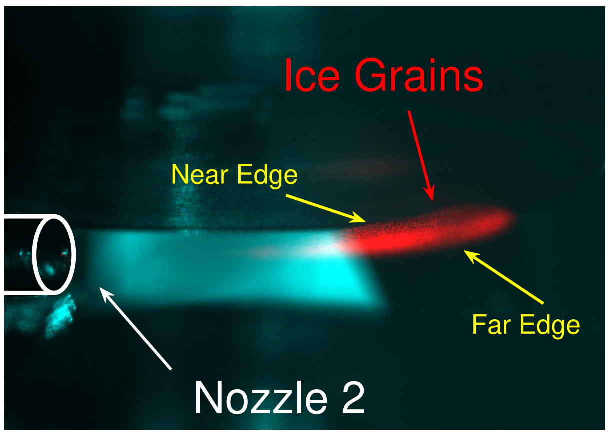

Figure 8.17: Superimposed cyan-scale (visible light) and red-scale (HeNe-filtered light) images of the dusty plasma apparatus and ice grain cloud, respectively. The cyan-scaled visible-light image shows the physical setup of the flow experiment with Nozzle 2 on the left of the frame. Because the camera is slightly below the plane of the plasma, the side of the bottom electrode is visible as is the flat disk of the top electrode. Plasma exists between the electrodes but no plasma is seen in these images. The ice grain cloud is photographed in a separate red-scale image and superimposed. The near edge of the grain cloud means closer to Nozzle 2. The far edge is on the far side.

Ice grain motion was recorded using the Dalsa Falcon VGA300 fast movie camera outfitted with a Nikon 24 mm lens and a 632 nm HeNe line filter. The lens attaches to the camera via a Nikon to C-mount adapter. The line filter only allows HeNe laser light scattered off the ice grains to be imaged by the camera. The camera is located approximately 30 cm from the center of the plasma at a position slightly below the plane of the plasma. Figure 8.17 shows the view from this position by superimposing two images. The cyan-scaled visible-light image shows the physical setup with Nozzle 2 on the left of the frame. The side of the bottom electrode is

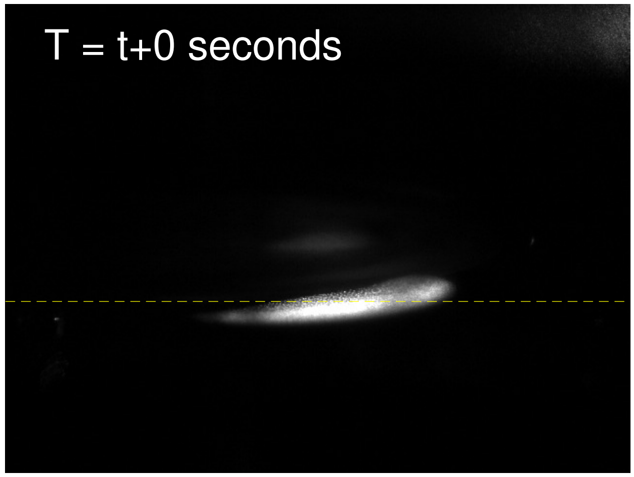

Figure 8.18: Ice grain cloud after Nozzle 2 is toggled on to allow an injected flow to move the cloud. Image shows the frame at time *t* when Nozzle 2 is toggled on. The movie showing the affect of the flow on the grain cloud can be downloaded from the CaltechDATA repository at https://data.caltech.edu/records/1423. The movie was originally recorded at 250 FPS and is played back at 10 FPS, a factor of 25 slow-down.

visible as is the flat disk of the top electrode. The ice grain cloud is photographed and superimposed in red. The near edge of the grain cloud is the edge closer to Nozzle 2. The far edge is on the far side away from Nozzle 2. The high frame rate of this camera (250 FPS used) allows for multiple frames to be taken when the flow from toggling Nozzle 2 interacts with the ice grains. The Dalsa camera takes 8-bit grayscale images.

Figure 8.18 (movie on web and photograph from movie in print) shows the motion of the grain cloud as it is exposed to a flow through Nozzle 2. The movie was recorded at 250 FPS and played back in this video at 10 FPS, a factor of 25 slow-down. The video shows the dramatic affect on the ice grain cloud from toggling on the neutral gas flow injected through Nozzle 2.

Figure 8.19 shows a set of three artificially colored images from the movie in Fig. 8.18 in the top row with key experimental features outlined including the nozzle connected to the valve that is toggled in white on the left-hand side of the each image and the electrodes in dashed yellow. The camera is below the midplane of the plasma as shown in the bottom row of Fig. 8.19 which is why it sees the side of the bottom electrode and the full flat disk of the top electrode. The red-scale images

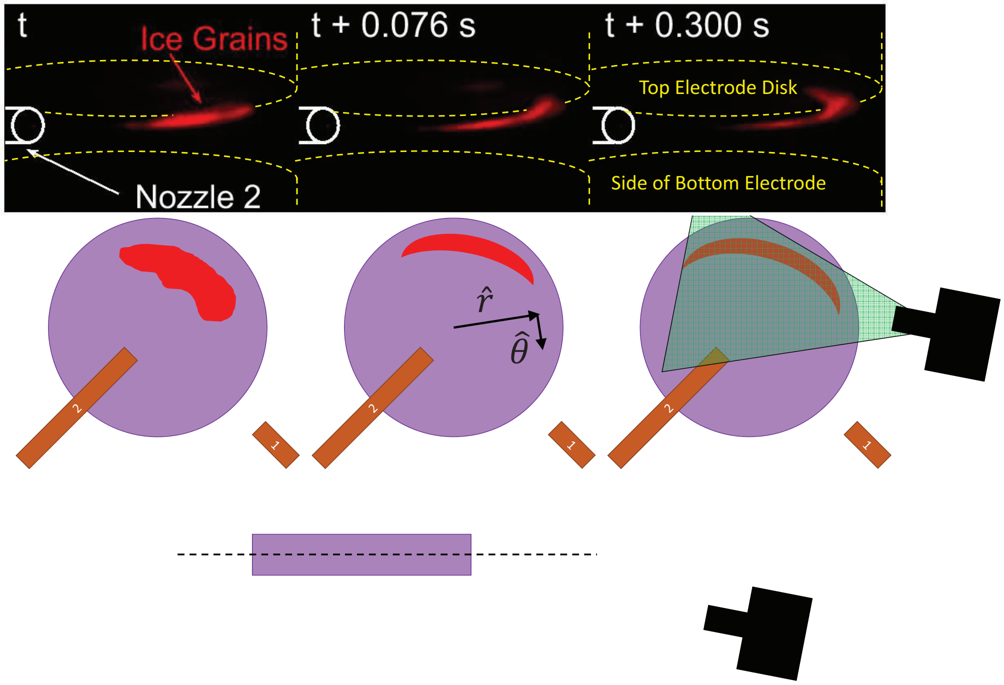

Figure 8.19: Top row: Artificially colored red-scale images of the ice grains inside the Caltech Water-Ice Dusty Plasma Experiment. Red HeNe laser light scatters off the ice grains and passes into the camera through a line filter, so the ice grains are the only thing visible. The electrodes are outlined in dashed yellow and Nozzle 2 is outlined in white for perspective. The sequence of images show how the ice grains move after Nozzle 2 is toggled open. Middle row: Top view sketches showing the estimated boundaries of the ice grains from each image in the top row. On the right is a sketch of the Dalsa Camera showing the approximate field of view. Bottom row: Sketch showing that the Dalsa Camera is below the midplane of the plasma.

were taken with a HeNe line filter to see only the ice grains. Underneath each ice grain image is a top view sketch of the estimated boundary of the ice grain cloud.

The left image in Fig. 8.19 is the frame taken at time t when the valve is opened. The middle image was taken at $t + 0.076$ s or 19 frames later and the right-hand image was taken at $t + 0.3$ s or 75 frames later. The radial $\hat{r}$ motion of the ice grains away from Nozzle 2 when it is opened takes place in the first 0.076 s of motion and the final 0.224 s of motion is primarily in the tangential $\hat{\theta}$ direction as illustrated by the unit vectors in the middle sketch on Fig. 8.19. Nozzle 2 is located on the left-hand side of the image and has diameter $d = 6.27$ mm. Thus, the radial motion appears to cease as the ice grains near the edge of the electrodes and the plasma.

Figure 8.20 quantifies the motion in the radial direction. The positions of the near and far edges of the ice grain cloud and their speeds are obtained from the video and plotted on Fig. 8.20(a). They were obtained for each frame by plotting pixel intensity as a function of position along the horizontal dashed yellow line in Fig. 8.18 and finding the pixel of the intersection between the pixel intensity trace and a selection criterion value.

Nozzle 2 is close to $z = 0$ and the flow coming out of it has in-plane flow velocity components v_x and v_z shown in Fig. 8.10 near the midplane $y = 0$. Figure 8.20(b) shows that when the valve is opened, the near edge of the ice grain cloud at the approximate center ($x = 0$) moves with speed $v_z \approx 0.25$ m/s away from Nozzle 2 and the far edge of the cloud at the approximate center ($x = 0$) moves at $v_z \approx 0.05$ m/s. The flow speed error bar on Fig. 8.20(b) is shown vertically on the right side of the plot. It was calculated by finding the distance between the pixel associated with the selection criterion and a 10% increase in pixel intensity. There is potentially some error from the fact that the camera is not looking at the grain motion from the perpendicular direction. This likely results in measuring a mix of x and z direction motion of the cloud. Nevertheless, this uncertainty is sufficiently small to conclude that there is a dust velocity gradient and that this gradient indicates that the more distant the grains are from the nozzle, the slower they move which is the same trend seen by neutral LIF in Figs. 8.7, 8.8, and 8.10.

It was challenging to find a global two-variable fit that accurately fits the measured v_x, v_z flow data in Fig. 8.10, so instead Fig. 8.21 shows an exponential fit to the relevant $v_z(x = 0, y = 0, 0 \leq z \leq 15.625 \text{ mm})$ data. The fit is made from the green data points and the red x is excluded as an outlier. Error bars calculated as in Section 8.3 are shown as well. The fit $v_z(0, 0, z) = 1.28e^{-0.0213z}$ is found with $R^2 = 0.86$ where z is in mm. Extrapolating this exponential fit of the neutral argon flow speed to the region where ice grains are present, $23.4375 \leq z \leq 31.25$ mm ($15000 \leq z \leq 20000$ stepper motor coordinates), gives $v_z(0, 0, 23.4375 \text{ mm}) \approx 0.78$ m/s which is approximately triple the speed of the near edge of the ice grains. Furthermore, $v_z(0, 0, 31.25 \text{ mm}) \approx 0.66$ m/s which is more than 10x the measured speed of the far edge. The three images in the top row and sketches in the middle row of Fig. 8.19 show how the grain motion gradient when Nozzle 2 is opened causes the ice grain cloud to compress in the $\hat{r}$ direction as the grains move towards the edge and expand in the tangential $\hat{\theta}$ direction. This bulk grain motion suggests that the grains are being held inside the plasma by a sheath force that must oppose

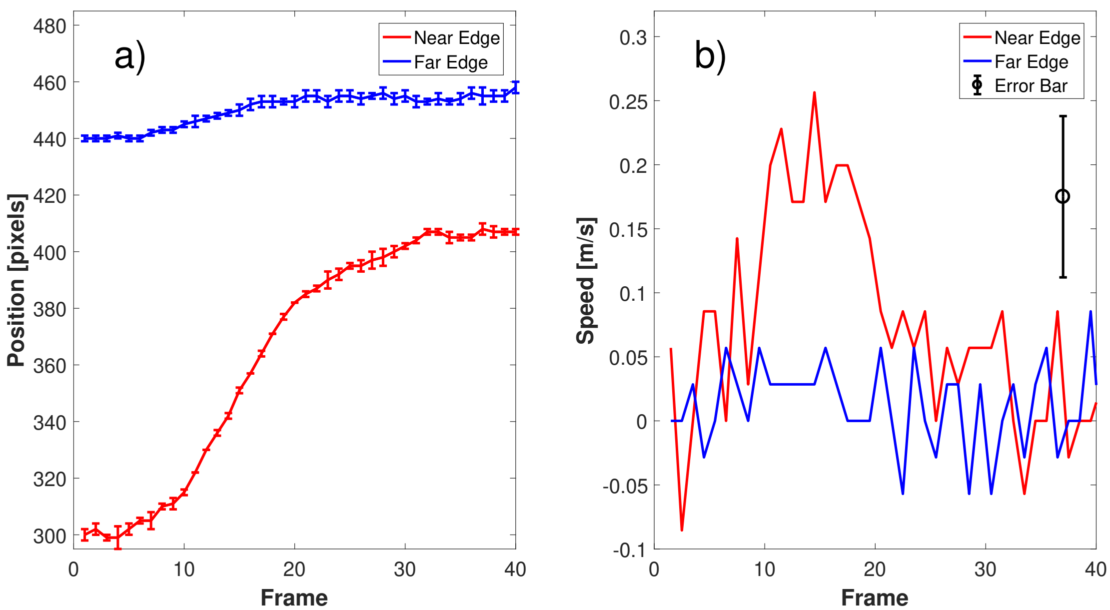

Figure 8.20: Measured impact of neutral gas flow on ice grain cloud. a) plots the position of the near and far edges (to Nozzle 2) of the ice grain cloud in each movie frame while the grains are exposed to the flow from Nozzle 2. b) plots the speed with which each edge moves. The velocity error bar (±0.075 m/s) is shown as the black vertical line on the upper right-hand side of the plot.

the force of the argon streaming towards them and that this opposing force quickly increases towards the edge of the plasma.

An interesting observation is made when Nozzle 2 is closed after the grains are in the crescent shape at the edge of the electrodes (the right-hand images of Fig. 8.19). When Nozzle 2 is closed, the ice grain cloud reverts to its original shape (the left-hand images of Fig. 8.19). The speed with which this reversion happens is slower. In fact, Nozzle 2 can be opened and closed repeatedly with minimal ice grain losses and the same motion cycle repeats each time.

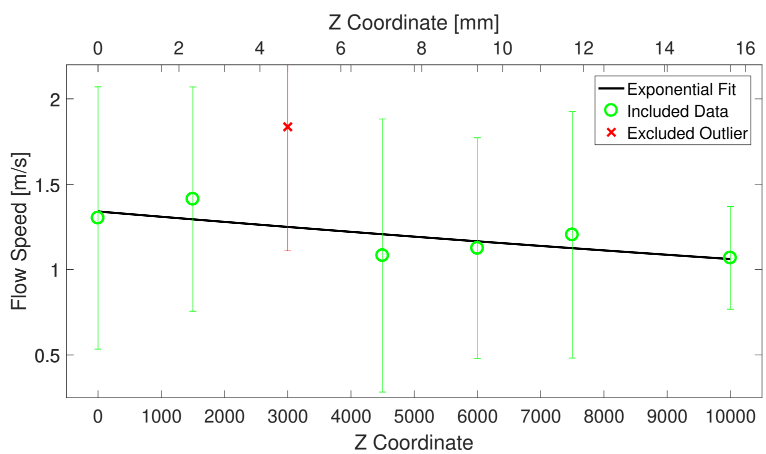

Figure 8.21: Measured $v_z(0,0,z)$ data denoted by the green o's and the red x. This data is also included on Figs. 8.7 and 8.10. The green o data is fit to an exponential curve. The single red x is excluded from the fit because it appears to be an outlier.

Chapter 9

SUMMARY

This thesis describes the development and use of new diagnostic tools for the astrophysically-relevant jet and water-ice dusty plasma experiments at Caltech. Each of three main experimental findings involved the use of new hardware and computation to uncover new physics unknown prior to implementation, thus enabling greater understandings of the astrophysical plasmas that the experiments are intended to study. An enumeration of the new hardware and the subsequent experimental finding is made:

1. A vacuum-tight, seven-channel X-ray scintillator detector measured a ~ 1 μs burst of ~ 6 keV hard X-ray photons coincident in time with a fast magnetic reconnection experiment on the jet experiment.
2. A Photron SA-X2 ultra-high-speed camera recorded a 10 second movie of the water-ice dust grains in the dusty plasma experiment as they grew by a factor of four in each dimension.
3. An automated, motorized LIF diagnostic measured neutral argon temperature to be slightly above room temperature and resolved sub-linewidth 1-2 m/s bulk flow speeds with resolution on the order of 2/3 of a meter per second.

The results from the X-ray detectors presented in Chapter 3 and the particle acceleration theory in Chapter 4 are perhaps the most exciting results in the thesis. Many theories for particle acceleration in both laboratory and astrophysical plasmas have been proposed and abandoned over the decades. D_{ext} was the first X-ray detector to be built. It was motivated by previous observations of transient phenomena occurring simultaneously with the RT instability breaking apart the jet. The goal was to determine if X-ray emission happens on the jet experiment, and if so, to understand it as best we can. Promising results from D_{ext} motivated the development of D_{int}. Its light-tight, vacuum-tight housing that allowed seven plastic scintillators to be mounted inside the vacuum chamber and the 10 meters of optical fiber transmission were both crucial to the dramatic improvement in capability that this second generation detector achieved. The combination of D_{CMOS} and D_{int} allowed us to achieve both time and energy resolution to paint a complete picture of the X-ray emission on the jet. We observed $\sim 1\mu$s burst of ~ 6 keV hard X-rays coincident in time with a fast magnetic reconnection. This observation serves as the foundation for the acceleration theory presented in Ch. 4 that shows how an electric field can accelerate electrons to high energy despite high collisionality. It is proposed that this electric field is the result of a large inductive LdI/dt voltage in the region where the plasma is breaking apart. A small fraction of the electron population is accelerated to keV energy in the plasma despite the high collisionality, and then undergoes large-angle collisions to emit hard X-rays. Finally, the Caltech experiment is scaled up to the solar case using the dimensionless nature of the MHD equations and it is found that this mechanism would be too efficient on the sun. The scaling leads to the hypothesis that the fine structure of solar prominences currently too small to be resolved via images may be composed of strands of braided plasma like a Litz-wire where the diameter of each strand is on the order of a few times the ion skin depth.

The results in Chapter 7 provide the strongest challenge to generally accepted notions among astrophysicists. Ice grains in astrophysical dusty plasmas are commonly assumed to be spherical with their radii distributed according to an inverse power law due to an equilibrium between agglomeration type collisions which can cause two grains to stick together forming a larger grain or break apart into smaller pieces. The goal of this work was to understand the growth of the ice grains in the Caltech experiment. Previous attempts to study grain growth at frame rates up to 300 frames per second failed to capture sufficient detail because it was impossible to definitively track each grain from one frame to the next. The impressive frame rate of the Photron camera made it easy to trace the exact trajectory of each grain across frames. Much effort was spent analyzing the 40,000 frames taken by the camera. We concluded, based on the evidence presented, that the ice grains in the experiment grow by accretion growth where one large grain accretes water molecules onto it. This is at odds with many experiments also studying micron-size grains where they see agglomeration growth. An important difference is that we grow ice grains from water vapor and many others use prefabricated microspheres. The conclusion that our grains grow via accretion challenges the use of a power-law size distribution describing dust grains in astrophysics as our measured distributions appear log-normal. Since dust grains in protoplanetary disks pass through the same micron-size regime, we propose that they grow via accretion in this regime rather than agglomeration.

The results in Chapter 8 are perhaps the results that I am most proud of. This motorized TD-LIF system controlled via a Labview program uses light traveling at $c = 3 \times 10^8$ m/s to measure the ~ 1 m/s bulk flow speed of argon atoms using the Doppler effect. The LIF diagnostic overcomes the lack of absolute calibration of diode lasers and the drift of emitted wavelength due to minute changes in room conditions to measure the $\Delta\lambda \approx 3$ femtometer shift between Doppler-free motion and the actual slow flows in the experiment. The goal of this work was to measure the temperature and flow speed of the neutral argon atoms and the argon ions in dusty plasma. We successfully measured the temperature and flow speed of the neutral argon species at the Caltech experiment. In addition, we successfully measured the temperature of the neutral argon species at the PK4 experimental setup at Baylor University in Waco, TX using a prior version of the diagnostic. By exploiting the symmetry of the laser beam and nozzle configuration, a single laser beam is able to deduce the two-dimensional in-plane flow velocity vector of the neutral argon species with sub-linewidth resolution. Utilizing measurements from both counter-propagating beams, the competing influences of density gradient and absorption broadening were separated and quantified. Neutral flow results compared with high-speed video of the ice grains exposed to flow reveals how ice grains respond to an imposed flow. It shows that when the grains are pushed too close to the edge of the plasma, a rapidly intensifying retaining force prevents their escape.

BIBLIOGRAPHY

[1] Paul M. Bellan. *Fundamentals of Plasma Physics*. Paperback edition. Cambridge: Cambridge University Press, 2008.

[2] J. Kataoka. "High energy observations of AGN jets and their future prospects". In: *Accelerators in the Universe*. Vol. 1040. AIP Conference Proceedings. Conference on Accelerators in the Universe, Mar 12-14, 2008, Tsukuba, Japan. 2008, pp. 191–205.

[3] B. S. Hogan et al. "Chandra discovery of 10 new X-ray jets associated with FR II Radio core-selected AGNs in the mojave sample". In: *Astrophysical Journal* 730.2 (2011). DOI: https://doi.org/10.1088/0004-637X/730/2/92.

[4] S. G. Benka and G. D. Holman. "A thermal/nonthermal model for solar hard X-ray bursts". In: *Astrophysical Journal* 435.1 (1994), pp. 469–481. DOI: https://doi.org/10.1086/174829.

[5] J. A. Miller et al. "Critical issues for understanding particle acceleration in impulsive solar flares". In: *Journal of Geophysical Research-Space Physics* 102.A7 (1997), pp. 14631–14659. DOI: https://doi.org/10.1029/97JA00976.

[6] Y. E. Litvinenko. "Electron acceleration in solar flares". In: *Energy Release and Particle Acceleration in the Solar Atmosphere - Flares and Related Phenomena*. Vol. 32. Advances in Space Research. 2nd World Space Congress/34th COSPAR Scientific Assembly, Oct 10-19, 2002, Houston, TX. 2003, pp. 2385–2391.

[7] M. J. Aschwanden. *Physics of the Solar Corona*. Springer-Verlag Berlin Heidelberg, 2005.

[8] V. Petrosian. "Stochastic Acceleration by Turbulence". In: *Space Science Reviews* 173.1-4 (2012), pp. 535–556. DOI: https://doi.org/10.1007/s11214-012-9900-6.

[9] P. C. Thonemann et al. "Production of higher temperatures and nuclear reactions in a gas discharge". In: *Nature* 181.4604 (1958), pp. 217–220. DOI: https://doi.org/10.1038/181217a0.

[10] S. A. Colgate and H. P. Furth. "Stabilized pinch and controlled fusion power". In: *Science* 128.3320 (1958), pp. 337–343. DOI: https://doi.org/10.1126/science.128.3320.337.

[11] B. Rose, A. E. Taylor, and E. Wood. "Measurement of the neutron spectrum from ZETA". In: *Nature* 181.4624 (1958), pp. 1630–1632. DOI: https://doi.org/10.1038/1811630a0.

[12] L. Spitzer. “Co-operative phenomena in hot plasmas”. In: *Nature* 181.4604 (1958), pp. 221–222. DOI: https://doi.org/10.1038/181221a0.

[13] K. A. George. “Neutron production and temperature in ZETA”. In: *Nature* 182.4637 (1958), pp. 745–746. DOI: https://doi.org/10.1038/182745a0.

[14] W. H. Bostick, V. Nardi, and W. Prior. “Production and confinement of high-density plasmas”. In: *Annals of the New York Academy of Sciences* 251 (1975), pp. 2–29. DOI: https://doi.org/10.1111/j.1749-6632.1975.tb00082.x.

[15] V. A. Gribkov et al. “Plasma dynamics in PF-1000 device under full-scale energy storage: I. Pinch dynamics, shock-wave diffraction, and inertial electrode”. In: *Journal of Physics D-Applied Physics* 40.7 (2007), pp. 1977–1989. DOI: https://doi.org/10.1088/0022-3727/40/7/021.

[16] R. E. Chrien et al. “Evidence for runaway electrons in a spheromak plasma”. In: *Nuclear Fusion* 31.7 (1991), pp. 1390–1393. DOI: https://doi.org/10.1088/0029-5515/31/7/015.

[17] R. D. Gill. “Generation and loss of runaway electrons following disruptions in JET”. In: *Nuclear Fusion* 33.11 (1993), pp. 1613–1625. DOI: https://doi.org/10.1088/0029-5515/33/11/I03.

[18] R. S. Marshall, M. J. Flynn, and P. M. Bellan. “Hard X-ray bursts observed in association with Rayleigh-Taylor instigated current disruption in a solar-relevant lab experiment”. In: *Physics of Plasmas* 25.11 (2018), p. 112101. DOI: https://doi.org/10.1063/1.5054927.

[19] A. Gibson. “Possibility of ion runaway in ZETA”. In: *Nature* 183.4654 (1959), pp. 101–102. DOI: https://doi.org/10.1038/183101a0.

[20] E. N. Parker and D. A. Tidman. “Suprathermal particles”. In: *Physical Review* 111.5 (1958), pp. 1206–1211. DOI: https://doi.org/10.1103/PhysRev.111.1206.

[21] D. E. McKenzie. “Observational studies of reconnection in the solar corona”. In: *Physics of Plasmas* 18.11 (2011), p. 111205. DOI: https://doi.org/10.1063/1.3628554.

[22] A. Stanier, P. Browning, and S. Dalla. “Solar particle acceleration at reconnecting 3D null points”. In: *Astronomy & Astrophysics* 542 (2012), A47. DOI: https://doi.org/10.1051/0004-6361/201218857.

[23] V. V. Zharkova et al. “Recent advances in understanding particle acceleration processes in solar flares”. In: *Space Science Reviews* 159.1-4 (2011), pp. 357–420. DOI: https://doi.org/10.1007/s11214-011-9803-y.

[24] J. Olson et al. “Experimental demonstration of the collisionless plasmoid instability below the ion kinetic scale during magnetic reconnection”. In: *Physical Review Letters* 116.25 (2016), p. 255001. DOI: https://doi.org/10.1103/PhysRevLett.116.255001.

[25] M. Yamada et al. “Study of driven magnetic reconnection in a laboratory plasma”. In: *Physics of Plasmas* 4.5, 2 (1997). 38th Annual Meeting of the Division-of-Plasma-Physics of the American-Physical-Society, Denver, CO, Nov 11-15, 1996, pp. 1936–1944. DOI: https://doi.org/10.1063/1.872336.

[26] I. H. Mitchell et al. “A high impedance mega-ampere generator for fiber z-pinch experiments”. In: *Review of Scientific Instruments* 67.4 (1996), pp. 1533–1541. DOI: https://doi.org/10.1063/1.1146884.

[27] O. Havnes et al. “First detection of charged dust particles in the Earth’s mesosphere”. In: *Journal of Geophysical Research-Space Physics* 101.A5 (1996), pp. 10839–10847. DOI: https://doi.org/10.1029/96JA00003.

[28] T. Sano et al. “Magnetorotational instability in protoplanetary disks. II. Ionization state and unstable regions”. In: *Astrophysical Journal* 543.1 (2000), pp. 486–501. DOI: https://doi.org/10.1086/317075.

[29] R. P. Turco et al. “Noctilucent clouds - simulation students of their genesis, properties and global influences”. In: *Planetary and Space Science* 30.11 (1982), pp. 1147–1181. DOI: https://doi.org/10.1016/0032-0633(82)90126-X.

[30] C. C. Porco et al. “Cassini observes the active south pole of Enceladus”. In: *Science* 311.5766 (2006), pp. 1393–1401. DOI: https://doi.org/10.1126/science.1123013.

[31] S. Kempf et al. “The E ring in the vicinity of Enceladus - I. Spatial distribution and properties of the ring particles”. In: *Icarus* 193.2 (2008), pp. 420–437. DOI: https://doi.org/10.1016/j.icarus.2007.06.027.

[32] G. H. Jones et al. “Fine jet structure of electrically charged grains in Enceladus’ plume”. In: *Geophysical Research Letters* 36 (2009), p. L16204. DOI: https://doi.org/10.1029/2009GL038284.

[33] T. W. Hill et al. “Charged nanograins in the Enceladus plume”. In: *Journal of Geophysical Research-Space Physics* 117 (2012). DOI: https://doi.org/10.1029/2011JA017218.

[34] S. M. Andrews and J. P. Williams. “Circumstellar dust disks in Taurus-Auriga: The submillimeter perspective”. In: *The Astrophysical Journal* 631.2 (2005), pp. 1134–1160. DOI: https://doi.org/10.1086/432712.

[35] L. Ricci et al. "Dust properties of protoplanetary disks in the Taurus-Auriga star forming region from millimeter wavelengths". In: *Astronomy & Astrophysics* 512 (2010). DOI: https://doi.org/10.1051/0004-6361/200913403.

[36] C. Ubach et al. "Grain growth signatures in the protoplanetary discs of Chamaeleon and Lupus". In: *Monthly Notices of the Royal Astronomical Society* 425.4 (2012), pp. 3137–3161. DOI: https://doi.org/10.1111/j.1365-2966.2012.21603.x.

[37] J. Blum et al. "Growth and form of planetary seedlings: Results from a microgravity aggregation experiment". In: *Physical Review Letters* 85.12 (2000), pp. 2426–2429. DOI: https://doi.org/10.1103/PhysRevLett.85.2426.

[38] T. Poppe, J. Blum, and T. Henning. "Analogous experiments on the stickiness of micron-sized preplanetary dust". In: *Astrophysical Journal* 533.1 (2000), pp. 454–471. DOI: https://doi.org/10.1086/308626.

[39] R. Schrapler and J. Blum. "The physics of protoplanetesimal dust agglomerates. VI. Erosion of large aggregates as a source of micrometer-sized particles". In: *Astrophysical Journal* 734.2 (2011). DOI: https://doi.org/10.1088/0004-637X/734/2/108.

[40] F. Brauer, C. P. Dullemond, and T. Henning. "Coagulation, fragmentation and radial motion of solid particles in protoplanetary disks". In: *Astronomy & Astrophysics* 480.3 (2008), pp. 859–877. DOI: https://doi.org/10.1051/0004-6361:20077759.

[41] T. Birnstiel, H. Klahr, and B. Ercolano. "A simple model for the evolution of the dust population in protoplanetary disks". In: *Astronomy & Astrophysics* 539 (2012). DOI: https://doi.org/10.1051/0004-6361/201118136.

[42] S. Okuzumi et al. "Rapid coagulation of porous dust aggregates outside the snow line: A pathway to successful icy planetesimal formation". In: *Astrophysical Journal* 752.2 (2012). DOI: https://doi.org/10.1088/0004-637X/752/2/106.

[43] J. M. Greenberg. *Submillimeter Wave Astronomy*. New York: Cambridge University Press, 1982.

[44] L. Testi et al. *Protostars and Planets VI*. Tucson: University of Arizona Press, 2014.

[45] J. Kong et al. "One-dimensional vertical dust strings in a glass box". In: *Physical Review E* 84.1, 2 (2011), p. 016411. DOI: https://doi.org/10.1103/PhysRevE.84.016411.

[46] E. Thomas and M. Watson. "First experiments in the dusty plasma experiment device". In: *Physics of Plasmas* 6.10 (1999), 4111–4117. DOI: https://doi.org/10.1063/1.873672.

[47] L. Boufendi and A. Bouchoule. “Particle nucleation and growth in a low-pressure argon-silane discharge”. In: *Plasma Sources Science & Technology* 3.3 (1994), pp. 262–267. DOI: https://doi.org/10.1088/0963-0252/3/3/004.

[48] J. L. Dorier, C. Hollenstein, and A. A. Howling. “Spatiotemporal powder formation and trapping in radio frequency silane plasmas using two-dimensional polarization-sensitive laser scattering”. In: *Journal of Vacuum Science & Technology A* 13.3 (1995), pp. 918–926. DOI: https://doi.org/10.1116/1.579852.

[49] S. Hong, J. Berndt, and J. Winter. “Growth precursors and dynamics of dust particle formation in the Ar/CH4 and Ar/C2H2 plasmas”. In: *Plasma Sources Science & Technology* 12.1 (2003), pp. 46–52. DOI: https://doi.org/10.1088/0963-0252/12/1/306.

[50] M. Y. Pustylnik et al. “Plasmakristall-4: New complex (dusty) plasma laboratory on board the International Space Station”. In: *Review of Scientific Instruments* 87.9 (2016), p. 093505. DOI: https://doi.org/10.1063/1.4962696.

[51] S. Shimizu et al. “Synthesis of water ice particles in a plasma chamber”. In: *Journal of Geophysical Research-Atmospheres* 115 (2010). DOI: https://doi.org/10.1029/2009JD013375.

[52] D. D. Ryutov, R. P. Drake, and B. A. Remington. “Criteria for scaled laboratory simulations of astrophysical MHD phenomena”. In: *Astrophysical Journal Supplement Series* 127.2 (2000). 2nd International Workshop on Laboratory Astrophysics with Intense Lasers, Tuscon, AZ, Mar 19-21, 1998, pp. 465–468. DOI: https://doi.org/10.1086/313320.

[53] R. S. Marshall and P. M. Bellan. “Acceleration of charged particles to extremely large energies by a sub-Dreicer electric field”. In: *Physics of Plasmas* 26.4 (2019), p. 042102. DOI: https://doi.org/10.1063/1.5081716.

[54] P. Wongwaitayakornkul. “Dynamics of an arched magnetically-twisted current-carrying plasma”. PhD thesis. California Institute of Technology, 2020. URL: https://resolver.caltech.edu/CaltechTHESIS:03042020-114816620.

[55] M. A. Haw. “Experimental and numerical studies of cavities, flows, and waves in arched flux ropes”. PhD thesis. California Institute of Technology, 2018. URL: https://resolver.caltech.edu/CaltechTHESIS:06012018-131846705.

[56] M. A. Haw et al. “Reverse current model for coronal mass ejection cavity formation”. In: *Astrophysical Journal Letters* 862.2 (2018), p. L15. DOI: https://doi.org/10.3847/2041-8213/aad33c.

[57] Y. Zhang, P. Wongwaitayakornkul, and P. M. Bellan. "Magnetic Rayleigh–Taylor instability in an experiment simulating a solar loop". In: *The Astrophysical Journal* 889.2 (2020), p. L32. DOI: https://doi.org/10.3847/2041-8213/ab6b2d.

[58] P. M. Bellan et al. "Laboratory simulations of astrophysical jets and solar coronal loops: new results". In: *Plasmas in the Laboratory and in the Universe: Interactions, Patterns, and Turbulence*. Vol. 1242. AIP Conference Proceedings. International Symposium Plasmas in the Laboratory and in the Universe: Interactions, Patterns and Turbulence, Societa Casino, Dec 1-4, 2009, Como, Italy. 2010, pp. 156–163. DOI: https://doi.org/10.1063/1.3460119.

[59] A. L. Moser. "Dynamics of magnetically driven plasma jets : an instability of an instability, gas cloud impacts, shocks, and other deformations". PhD thesis. California Institute of Technology, 2012. URL: http://resolver.caltech.edu/CaltechTHESIS:04132012-150652134.

[60] V. H. Chaplin. "Battery-powered RF pre-ionization system for the caltech magnetohydrodynamically-driven jet experiment: RF discharge properties and MHD-driven jet dynamics". PhD thesis. California Institute of Technology, 2015. URL: https://resolver.caltech.edu/CaltechTHESIS:05012015-172120954.

[61] K. -B. Chai, X. Zhai, and P. M. Bellan. "Extreme ultra-violet burst, particle heating, and whistler wave emission in fast magnetic reconnection induced by kink-driven Rayleigh-Taylor instability". In: *Physics of Plasmas* 23.3 (2016), p. 032122. DOI: https://doi.org/10.1063/1.4944390.

[62] A. L. Moser and P. M. Bellan. "Magnetic reconnection from a multiscale instability cascade". In: *Nature* 482.7385 (2012), pp. 379–381. DOI: https://doi.org/10.1038/nature10827.

[63] S. C. Hsu and P. M. Bellan. "A laboratory plasma experiment for studying magnetic dynamics of accretion discs and jets". In: *Monthly Notices of the Royal Astronomical Society* 334.2 (2002), pp. 257–261. DOI: https://doi.org/10.1046/j.1365-8711.2002.05422.x.

[64] C. A. Romero-Talamas, P. M. Bellan, and S. C. Hsu. "Multielement magnetic probe using commercial chip inductors". In: *Review of Scientific Instruments* 75.8 (2004), pp. 2664–2667. DOI: https://doi.org/10.1063/1.1771483.

[65] J. Yee and P. M. Bellan. "Taylor relaxation and lambda decay of unbounded, freely expanding spheromaks". In: *Physics of Plasmas* 7.9 (2000), pp. 3625–3640. DOI: https://doi.org/10.1063/1.1287137.

[66] G. S. Yun. "Dynamics of plasma structures interacting with external and self-generated magnetic fields". PhD thesis. California Institute of Technology,

2008. URL: https://resolver.caltech.edu/CaltechETD:etd-07242007-162442.

[67] K. -B. Chai and P. M. Bellan. “Extreme ultra-violet movie camera for imaging microsecond time scale magnetic reconnection”. In: *Review of Scientific Instruments* 84.12 (2013), p. 123504. DOI: https://doi.org/10.1063/1.4841915.

[68] D. Kumar and P. M. Bellan. “Heterodyne interferometer with unequal path lengths”. In: *Review of Scientific Instruments* 77.8 (2006), p. 083503. DOI: https://doi.org/10.1063/1.2336769.

[69] B. Seo and P. M. Bellan. “Experimental investigation of the compression and heating of an MHD-driven jet impacting a target cloud”. In: *Physics of Plasmas* 25.11 (2018), p. 112703. DOI: https://doi.org/10.1063/1.5045678.

[70] D. Kumar and P. M. Bellan. “Nonequilibrium Alfvenic plasma jets associated with spheromak formation”. In: *Physical Review Letters* 103.10 (2009). 105003. DOI: https://doi.org/10.1103/PhysRevLett.103.105003.

[71] S. C. Hsu and P. M. Bellan. “Experimental identification of the kink instability as a poloidal flux amplification mechanism for coaxial gun spheromak formation”. In: *Physical Review Letters* 90.21 (2003), p. 215002. DOI: https://doi.org/10.1103/PhysRevLett.90.215002.

[72] B.L. Henke, E.M. Gullikson, and Davis J.C. “X-ray Interactions: photoabsorption, scattering, transmission, and feflection at E = 50-30,000 eV, Z = 1-92”. In: *Atomic Data and Nuclear Data Tables* 54.2 (1993), pp. 181–342. DOI: http://dx.doi.org/10.1006/adnd.1993.1013.

[73] R. G. van Silfhout and A. S. Kachatkou. “Fibre-optic coupling to high-resolution CCD and CMOS image sensors”. In: *Nuclear Instruments & Methods in Physics Research Section A-Accelerators Spectrometers Detectors and Associated Equipment* 597.2-3 (2008), pp. 266–269. DOI: https://doi.org/10.1016/j.nima.2008.09.015.

[74] F. Nachtrab et al. “Simple solutions for spectroscopic, photon counting X-ray imaging detectors”. In: *2009 IEEE Nuclear Science Symposium Conference Record, Vols 1-5*. IEEE Nuclear Science Symposium and Medical Imaging Conference. IEEE Nuclear Science Symposium Conference, Oct 25-31, 2009, Orlando, FL. 2009, pp. 1636+. DOI: https://doi.org/10.1109/NSSMIC.2009.5402242.

[75] C. Stoeckl et al. “Operation of a single-photon-counting x-ray charge-coupled device camera spectrometer in a petawatt environment”. In: *Review of Scientific Instruments* 75.10, 2 (2004). 15th Topical Conference on High-Temperature Plasma Diagnostics, San Diego, CA, APR 19-22, 2004, 3705–3707. DOI: https://doi.org/10.1063/1.1788867.

[76] D. W. Lane. "X-ray imaging and spectroscopy using low cost COTS CMOS sensors". In: *Nuclear Instruments & Methods in Phyics Research Sections B-Beam Interactions with Materials and Atoms* 284 (2012), 29–32. DOI: https://doi.org/10.1016/j.nimb.2011.09.007.

[77] H. G. Kang et al. "An investigation of medical radiation detection using CMOS image sensors in smartphones". In: *Nuclear Instruments & Methods in Physics Research Section A-Accelerators Spectrometers Detectors and Associated Equipment* 823 (2016), 126–134. DOI: https://doi.org/10.1016/j.nima.2016.04.007.

[78] R.D. Deslattes et al. "X-ray transition energies (version 1.2)". [Online; accessed December 5, 2016]. 2005.

[79] H. Dreicer. "Electron and ion runaway in a fully ionized gas .1." In: *Physical Review* 115.2 (1959), pp. 238–249. DOI: https://doi.org/10.1103/PhysRev.115.238.

[80] K. H. Schoenbach, M. Kristiansen, and G. Schaefer. "A review of opening switch technology for inductive energy-storage". In: *Proceedings of the IEEE* 72.8 (1984), pp. 1019–1040. DOI: 10.1109/PROC.1984.12969.

[81] W. Jiang et al. "Repetitive pulsed high voltage generation using inductive energy storage with static-induction thyristor as opening switch". In: *IEEE Transactions on Dielectrics and Electrical Insulation* 14.4 (2007), pp. 941–946. DOI: https://doi.org/10.1109/TDEI.2007.4286530.

[82] K. Takaki et al. "Energy efficiency of corona discharge reactor driven by inductive energy storage system pulsed power generator". In: *IEEE Transactions on Dielectrics and Electrical Insulation* 14.4 (2007), pp. 834–845. DOI: https://doi.org/10.1109/TDEI.2007.4286514.

[83] C. Jacobsen and P. Carlqvist. "Solar flares caused by circuit interruptions". In: *Icarus* 3.3 (1964), p. 270. DOI: https://doi.org/10.1016/0019-1035(64)90023-5.

[84] H. Alfvén and P. Carlqvist. "Currents in the solar atmosphere and a theory of solar flares". In: *Solar Physics* 1.2 (1967), pp. 220–228. DOI: https://doi.org/10.1007/BF00150857.

[85] R. L. Stenzel, W. Gekelman, and N. Wild. "Magnetic-field line reconnection experiments .5. current disruptions and double-layers". In: *Journal of Geophysical Research - Space Physics* 88.NA6 (1983), pp. 4793–4804. DOI: https://doi.org/10.1029/JA088iA06p04793.

[86] H. Dreicer. "Electron and ion runaway in a fully ionized gas .2." In: *Physical Review* 117.2 (1960), pp. 329–342. DOI: https://doi.org/10.1103/PhysRev.117.329.

[87] V. Fuchs et al. "Velocity-space structure of runaway electrons". In: *Physics of Fluids* 29.9 (1986), pp. 2931–2936. DOI: https://doi.org/10.1063/1.865493.

[88] J. D. Scudder and H. Karimabadi. "Ubiquitous non-thermals in astrophysical plasmas: restating the difficulty of maintaining Maxwellians". In: *Astrophysical Journal* 770.1 (2013), UNSP 26. DOI: https://doi.org/10.1088/0004-637X/770/1/26.

[89] P. Helander and D. J. Sigmar. *Collisional Transport in Magnetized Plasmas*. Cambridge University Press, Cambridge UK, 2002.

[90] M. N. Rosenbluth, W. M. Macdonald, and D. L. Judd. "Fokker-Planck Equation for an inverse-square force". In: *Physical Review* 107.1 (1957), pp. 1–6. DOI: https://doi.org/10.1103/PhysRev.107.1.

[91] N. A. Krall and A. W. Trivelpiece. *Principles of plasma physics*. McGraw-Hill, New York, 1973.

[92] J. Matthews and R. L. Walker. *Mathematical Methods of Physics*. New York: W. A. Benjamin, 1964.

[93] S. Livi and E. Marsch. "Generation of solar-wind proton tails and double beams by Coulomb collisions". In: *Journal of Geophysical Research-Space Physics* 92.A7 (1987), pp. 7255–7261. DOI: https://doi.org/10.1029/JA092iA07p07255.

[94] P. F. Wyper et al. "Three-dimensional simulations of tearing and intermittency in coronal jets". In: *The Astrophysical Journal* 827.1 (2016), p. 4. DOI: https://doi.org/10.3847/0004-637X/827/1/4.

[95] S. Tsuneta. "Particle-acceleration and magnetic reconnection in solar-flares". In: *Publications of the Astronomical Society of Japan* 47.5 (1995), pp. 691–697.

[96] V. V. Zaitsev, P. V. Kronshtadtov, and A. V. Stepanov. "Rayleigh-Taylor instability and excitation of super-Dreicer electric fields in the solar chromosphere". In: *Solar Physics* 291.11 (2016), pp. 3451–3459. DOI: https://doi.org/10.1007/s11207-016-0983-1.

[97] G. A. Gary. "Plasma beta above a solar active region: rethinking the paradigm". In: *Solar Physics* 203.1 (2001), pp. 71–86. DOI: https://doi.org/10.1023/A:1012722021820.

[98] C. Prior and A. R. Yeates. "Twisted versus braided magnetic flux ropes in coronal geometry II. Comparative behaviour". In: *Astronomy and Astrophysics* 591 (2016). A16. DOI: https://doi.org/10.1051/0004-6361/201528053.

[99] W. Daughton et al. "Role of electron physics in the development of turbulent magnetic reconnection in collisionless plasmas". In: *Nature Physics* 7.7 (2011), pp. 539–542. DOI: https://doi.org/10.1038/nphys1965.

[100] C. R. Sullivan and R. Y Zhang. “Simplified design method for Litz wire”. In: *2014 Twenty-Ninth Annual IEEE Applied Power Electronics Conference and Exposition*. Annual IEEE Applied Power Electronics Conference and Exposition (APEC). 29th Annual IEEE Applied Power Electronics Conference and Exposition (APEC), Mar 16-20, 2014, Fort Worth, TX. 2014, pp. 2667–2674.

[101] T. H. Stix. “Magnetic braiding in a toroidal plasma”. In: *Physical Review Letters* 30.18 (1973), pp. 833–835. DOI: https://doi.org/10.1103/PhysRevLett.30.833.

[102] X. Zhai. “Experimental, numerical and analytical studies of the MHD-driven plasma jet, instabilities and waves”. PhD thesis. California Institute of Technology, 2015. URL: http://resolver.caltech.edu/CaltechTHESIS:06092015-162916583.

[103] L. Ni et al. “Fast magnetic reconnection in the solar chromosphere mediated by the plasmoid Instability”. In: *Astrophysical Journal* 799.1 (2015). DOI: https://doi.org/10.1088/0004-637X/799/1/79.

[104] K. -B. Chai and P. M. Bellan. “Spontaneous formation of nonspherical water ice grains in a plasma environment”. In: *Geophysical Research Letters* 40.23 (2013), pp. 6258–6263. DOI: https://doi.org/10.1002/2013GL058268.

[105] K. -B. Chai and P. M. Bellan. “Formation and alignment of elongated, fractal-like water-ice grains in extremely cold, weakly ionized plasma”. In: *Astrophysical Journal* 802.2 (2015). DOI: https://doi.org/10.1088/0004-637X/802/2/112.

[106] K. -B. Chai and P. M. Bellan. “Study on morphology and growth of water-ice grains spontaneously generated in a laboratory plasma”. In: *Journal of Atmospheric and Solar-Terrestrial Physics* 127 (2015), pp. 83–91. DOI: https://doi.org/10.1016/j.jastp.2014.07.012.

[107] K. -B. Chai and P. M. Bellan. “Vortex motion of dust particles due to non-conservative ion drag force in a plasma”. In: *Physics of Plasmas* 23.2 (2016), p. 023701. DOI: https://doi.org/10.1063/1.4941973.

[108] K. Miyake and Y. Nakagawa. “Effects of particle-size distributions on opacity curves of protoplanetary disks around T-Tauri stars”. In: *Icarus* 106.1 (1993), pp. 20–41. DOI: https://doi.org/10.1006/icar.1993.1156.

[109] M. K. McClure et al. “Probing dynamical processes in the planet-forming region with dust mineralogy”. In: *Astrophysical Journal Letters* 759.1 (2012). DOI: http://dx.doi.org/10.1088/2041-8205/759/1/L10.

[110] P. Biermann and M. Harwit. “On the origin of the grain-size spectrum of inter-stellar dust”. In: *Astrophysical Journal* 241.2 (1980), pp. L105–L107.

[111] S. Okuzumi. “Electric charging of dust aggregates and its effect on dust coagulation in protoplanetary disks”. In: *Astrophysical Journal* 698.2 (2009), pp. 1122–1135. DOI: https://doi.org/10.1088/0004-637X/698/2/1122.

[112] L. S. Matthews, V. Land, and T. W. Hyde. “Charging and coagulation of dust in protoplanetary plasma environments”. In: *Astrophysical Journal* 744.1 (2012). DOI: https://doi.org/10.1088/0004-637X/744/1/8.

[113] C. R. Du et al. “Agglomeration of microparticles in complex plasmas”. In: *Physics of Plasmas* 17.11 (2010). DOI: https://doi.org/10.1063/1.3495979.

[114] R. Yousefi et al. “Measurement of net electric charge and dipole moment of dust aggregates in a complex plasma”. In: *Physical Review E* 90.3 (2014). DOI: https://doi.org/10.1103/PhysRevE.90.033101.

[115] Y. L. Chow and M. M. Yovanovich. “The shape factor of the capacitance of a conductor”. In: *Journal of Applied Physics* 53.12 (1982), pp. 8470–8475. DOI: https://doi.org/10.1063/1.330495.

[116] D. D. Burgess and C. H. Skinner. “Dye laser-induced fluorescence of plasmas and its application to measurement of lower state decay-rates”. In: *Journal of Physics B-Atomic Molecular and Optical Physics* 7.9 (1974), pp. L297–L301. DOI: https://doi.org/10.1088/0022-3700/7/9/007.

[117] R. A. Stern and J. A. Johnson. “Plasma ion diagnostics using resonant fluorescence”. In: *Physical Review Letters* 34.25 (1975), 1548–1551. DOI: https://doi.org/10.1103/PhysRevLett.34.1548.

[118] G. D. Severn, D. A. Edrich, and R. McWilliams. “Argon ion laser-induced fluorescence with diode lasers”. In: *Review of Scientific Instruments* 69.1 (1998), pp. 10–15. DOI: https://doi.org/10.1063/1.1148472.

[119] A. Pikalev et al. “Measurement of gas temperatures in dust-free and dusty argon discharges”. In: *Journal of Physics D: Applied Physics* 53.7 (2019), p. 075203. DOI: https://doi.org/10.1088/1361-6463/ab59aa.

[120] R. J. Cedolin et al. “Laser-induced fluorescence study of a xenon Hall thruster”. In: *Applied Physics B- Lasers and Optics* 65.4-5 (1997), pp. 459–469. DOI: https://doi.org/10.1007/s003400050297.

[121] V. H. Chaplin et al. “Laser-induced fluorescence measurements of acceleration zone scaling in the 12.5 kW HERMeS Hall thruster”. In: *Journal of Applied Physics* 124.18 (2018). DOI: https://doi.org/10.1063/1.5040388.

[122] A. K. Hansen et al. “Simultaneous two-dimensional laser-induced-fluorescence measurements of argon ions”. In: *Review of Scientific Instruments* 81.10 (2010). 18th Topical Conference on High-Temperature Plasma Diagnostics,

Wildwood, NJ, May 16-20, 2010. DOI: https://doi.org/10.1063/1.3460630.

[123] A. Bogaerts et al. "Three-dimensional density profiles of argon metastable atoms in a direct current glow discharge: Experimental study and comparison with calculations". In: *Spectrochimica Acta Part B-Atomic Spectroscopy* 52.2 (1997), pp. 219–229. DOI: https://doi.org/10.1016/S0584-8547(96)01578-9.

[124] B. K. McMillin and M. R. Zachariah. "Two-dimensional laser-induced fluorescence imaging of metastable density in low-pressure radio frequency argon plasmas with added O-2, Cl-2, and CF-4". In: *Journal of Applied Physics* 79.1 (1996), pp. 77–85. DOI: https://doi.org/10.1063/1.360793.

[125] D. S. Thompson et al. "Laser induced fluorescence of ArI metastables in the presence of a magnetic field". In: *Plasma Sources Science & Technology* 27.6 (2018). DOI: https://doi.org/10.1088/1361-6595/aac963.

[126] R. S. Marshall, K. -B. Chai, and P. M. Bellan. "Identification of accretion as grain growth mechanism in astrophysically relevant water-ice dusty plasma experiment". In: *Astrophysical Journal* 837.1 (2017). DOI: https://doi.org/10.3847/1538-4357/aa5d11.

[127] T. Bieber et al. "Argon ion and neutral metastable levels destruction in a magnetically enhanced inductively coupled plasma reactor". In: *Open Plasma Physics Journal* 6 (2013), pp. 32–43. DOI: https://doi.org/10.2174/1876534301306010032.

[128] R. F. Kelly et al. "ArI/ArII laser induced fluorescence system for measurement of neutral and ion dynamics in a large scale helicon plasma". In: *Review of Scientific Instruments* 87.11 (2016). 21st Topical Conference on High-Temperature Plasma Diagnostics, Madison, WI, Jun 05-09, 2016. DOI: https://doi.org/10.1063/1.4959157.

[129] M. J. Goeckner, J. Goree, and T. E. Sheridan. "Saturation broadening of laser-induced fluorescence from plasma ions". In: *Review of Scientific Instruments* 64.4 (1993), pp. 996–1000. DOI: https://doi.org/10.1063/1.1144103.

[130] A. K. Chernyshov et al. "Pressure shift coefficient measurements in an RF discharge for Ar 45[3/2](2)-5p[3/2](3) transition with the help of diode-laser absorption spectroscopy". In: *26th Annual International Laser Physics Workshop (LPHYS'17)*. Vol. 999. Journal of Physics Conference Series. 26th Annual International Laser Physics Workshop (LPHYS), Kazan E K Zavoisky Phys Tech Inst, Kazan, Russia, Jul 17-21, 2017. 2018. DOI: {10.1088/1742-6596/999/1/012010}.

[131] M. Aramaki et al. "High resolution laser induced fluorescence doppler velocimetry utilizing saturated absorption spectroscopy". In: *Review of Sci-*

entific Instruments 80.5 (2009). DOI: https://doi.org/10.1063/1.3127581.

[132] A. Bondi. "Van Der Waals volumes + radii". In: *Journal of Physical Chemistry* 68.3 (1964), pp. 441+. DOI: https://doi.org/10.1021/j100785a001.

[133] P. Pyykko. "Strong closed-shell interactions in inorganic chemistry". In: *Chemical Reviews* 97.3 (1997), 597–636. DOI: https://doi.org/10.1021/cr940396v.

[134] D. R. Nicholson. *Introduction to Plasma Theory*. Malabar, FL: Krieger Publishing Company, 1992.

[135] E. S. Evans, S. A. Cohen, and D. R. Welch. "Particle-in-cell studies of fast-ion slowing-down rates in cool tenuous magnetized plasma". In: *Physics of Plasmas* 25.4 (2018). DOI: https://doi.org/10.1063/1.5022188.

Appendix A

PLASMA PHYSICS 101

This introduction to plasma physics will largely follow Ref. [1] which is an excellent resource for anyone looking for more detail on any topic presented here. Appendix A starts the introduction to plasma physics with a discussion on Debye Shielding; a topic that answers the question about when a collection of charged particles becomes a plasma. Multiple subsequent sections will present the different ways to quantify a plasma starting with the most fundamental way of tracking every single particle trajectory and then moving into the more feasible Vlasov, Two-Fluid, and Magnetohydrodynamics (MHD) theories. MHD will then be used to introduce the "magnetic flux frozen into the plasma" condition. Finally, there is a qualitative introduction to dusty plasmas.

A.1 Debye Shielding

Most plasmas are quasineutral. That is to say, when looking at length scales that are much larger than some length scale, the density of electrons and ions is approximately equal. Mathematically, this condition is written as $n_e = Zn_i$. If you take a quasineutral plasma and insert a test particle with charge q_T into the plasma, that test particle will attract the species that has the opposite charge and repel the species with the same charge resulting in a small volume around itself that violates quasineutrality. Outside of this volume, the plasma remains quasineutral and the test charge is undetected. The length scale at which the test particle perturbs the charge distribution in the plasma is called the *Debye Length*, often denoted λ_D. Thus, for a collection of charged particles to become a plasma, it must be at least a few Debye lengths in size. λ_D is calculated using the density, charge, and temperature of each species σ where $\sigma = i$ for ion species or e for electron species. λ_D is calculated by

$$\begin{aligned} \frac{1}{\lambda_D^2} &= \sum_\sigma \frac{1}{\lambda_\sigma^2} \\ \lambda_\sigma^2 &= \frac{\epsilon_0 \kappa T_\sigma}{n_{\sigma,0} q_\sigma^2}. \end{aligned} \tag{A.1}$$

One caveat to calculating λ_D is that a species cannot Debye shield a species that moves faster than itself. That means that while the electron species contributes to the ion Debye length, the ion species typically does not contribute to the electron Debye length. This is because electrons are usually moving much faster than ions. Appendix B contains an in-depth discussion on the limitations of Debye Shielding as related to the particle acceleration theory presented in Ch. 4.

A.2 Tracking All Particles

The most intensive and detailed way to quantify a plasma would be to track every single particle's motion individually. Consider a system of N particles where $N = \sum_\sigma N_\sigma$ and each σ represents either the electron or ion species. For simplicity, assume that every atom is ionized so there are no neutrals. Each species σ has some mass m_σ and some electrical charge q_σ. Every particle in the plasma can be described by a 6-dimensional vector in phase-space $\mathbf{A_i}$. The ith particle would have mass m_i, charge q_i, and $\mathbf{A_i}$ where three coordinates make up its position $\mathbf{x_i} = x_i\hat{x} + y_i\hat{y} + z_i\hat{z}$ and the following three coordinates make up its velocity $\mathbf{v_i} = \mathbf{\dot{x}_i} = \dot{x}_i\hat{x} + \dot{y}_i\hat{y} + \dot{z}_i\hat{z}$.

$$\mathbf{A_i} = \begin{pmatrix} x_i \\ y_i \\ z_i \\ \dot{x}_i \\ \dot{y}_i \\ \dot{z}_i \end{pmatrix}. \tag{A.2}$$

Because plasmas consist of positively and negatively charged particles, each particle will feel forces at its position from the superposition of the internal electric and magnetic fields created by the other $N - 1$ charged particles as well as additional forces from any externally applied magnetic fields as defined by the Lorentz Force Law

$$\mathbf{F} = q\left(\mathbf{E} + \mathbf{v} \times \mathbf{B}\right). \tag{A.3}$$

Thus an algorithm begins to take shape.

1. Start with a vector $\mathbf{A_i}$ for each of the N particles.
2. For each particle i in the set of N, utilize the superposition of electromagnetic fields to calculate the total electric and magnetic field at position $\mathbf{x_i}$ by

summing up the contributions from each of the other $N-1$ particles and any externally applied fields.

3. Use the Eq. A.3 to solve for the net force on the ith particle.

4. Apply this force to the ith particle for some small time δ_t and use its current position and speed to calculate its new position and speed.

5. Repeat steps 2-4 for the other $N-1$ particles.

6. Repeat steps 2-5 until desired time is reached.

The above algorithm works wonderfully for small systems. But using the presented algorithm on a macroscopic plasma with 10^{10}, 10^{20}, or more particles would easily overwhelm the most powerful supercomputer. This leads to the use of distribution functions and fluid models to study plasmas.

A.3 Vlasov Theory

Instead of tracking an enormous number of individual particle positions, velocities, and electric and magnetic fields, plasma physics makes use of distribution functions in xv phase-space. The distribution function $f_\sigma(x, v, t)$ is defined to be the number of particles of species σ with position between x and $x + dx$ and velocity between v and $v + dv$ at the given time t. This concept is often extended to three dimensions with the three-dimensional distribution function $f_\sigma(\mathbf{x}, \mathbf{v}, t)$. By drawing a box of length dx and height dv in phase-space and calculating the change in the number of particles in the box in time dt, the Vlasov Equation is obtained. This equation is sometimes referred to as the Boltzmann Equation or the Kinetic Description of the plasma. A collision is an instantaneous jump in the speed of a particle, and thus a collision can knock a particle into or out of the box in phase space and so the full Vlasov Equation for a species including collisions is

$$\frac{\partial f_\sigma}{\partial t} + \mathbf{v} \cdot \nabla f_\sigma + \nabla_v \cdot (\mathbf{a} f_\sigma) = \sum_\alpha C_{\sigma\alpha}(f_\sigma) \tag{A.4}$$

where $C_{\sigma\alpha}$ is the collision operator between species σ and α.

The Vlasov description gives the full picture of the plasma. Vlasov can be used to study phenomena at length scales smaller than the electron cyclotron radius and phenomena faster than the electron cyclotron frequency.

A.4 Two-Fluid Theory

The process of taking moments of f_σ, which mathematically amounts to multiplying f_σ by various powers of velocity and integrating over velocity, is very useful. The density of each species n_σ and the mean velocity of the species $\mathbf{u}_\sigma$ can be found by taking the zeroth and first moment of the distribution function, respectively.

$$n_\sigma(\mathbf{x},t) = \int f_\sigma(\mathbf{x},\mathbf{v},t)\,d\mathbf{v}. \tag{A.5}$$

Equation A.5 says that the density of species σ at position $\mathbf{x}$ and time t is equal to the integral over velocity of the distribution function f_σ. This is the zeroth moment of the distribution function because f_σ inside the integral has been multiplied by $\mathbf{v}^0$.

A useful way to imagine the distribution function is as a probability distribution which can be seen after normalizing $f_\sigma(\mathbf{x},\mathbf{v},t)$ by $n_\sigma(\mathbf{x},t)$. This function represents the probability of finding a particle with velocity $\mathbf{v}$ at position $\mathbf{x}$ at time t. As with any probability distribution, integrating this distribution over all $\mathbf{v}$ gives 1. Multiplying this probability distribution $(f_\sigma(\mathbf{x},\mathbf{v},t)/n_\sigma(\mathbf{x},t))$ by $\mathbf{v}^1$ and integrating over $\mathbf{v}$ yields the average velocity

$$\mathbf{u}_\sigma(\mathbf{x},t) = \int \mathbf{v}\frac{f_\sigma(\mathbf{x},\mathbf{v},t)}{n_\sigma(\mathbf{x},t)}d\mathbf{v} = \frac{\int \mathbf{v} f_\sigma(\mathbf{x},\mathbf{v},t)\,d\mathbf{v}}{n_\sigma(\mathbf{x},t)}. \tag{A.6}$$

In addition to taking moments of the distribution function f_σ, one can take moments of the full Vlasov Equation:

$$\int \mathbf{v}^n\left(\frac{\partial f_\sigma}{\partial t} + \mathbf{v}\cdot\nabla f_\sigma + \nabla_v\cdot(\mathbf{a}f_\sigma)\right)d\mathbf{v} = \int \mathbf{v}^n\left(\sum_\alpha C_{\sigma\alpha}(f_\sigma)\right)d\mathbf{v}. \tag{A.7}$$

Taking $n = 0$ in the Eq. A.7 produces the two-fluid continuity equation

$$\frac{\partial n_\sigma}{\partial t} + \nabla\cdot(n_\sigma\mathbf{u}_\sigma) = 0. \tag{A.8}$$

Instead taking $n = 1$ in Eq. A.7 produces the two-fluid equation of motion

$$n_\sigma m_\sigma\frac{d\mathbf{u}_\sigma}{dt} = n_\sigma q_\sigma(\mathbf{E} + \mathbf{u}_\sigma\times\mathbf{B}) - \nabla P_\sigma - \mathbf{R}_{\sigma\alpha} \tag{A.9}$$

where $\frac{d}{dt}$ is called the convective derivative

$$\frac{d}{dt} = \frac{\partial}{\partial t} + \mathbf{u}_\sigma \cdot \nabla \tag{A.10}$$

and $\mathbf{R}_{\sigma\alpha}$ is effectively a frictional drag on species σ due to collisions with species α. $\mathbf{R}_{\sigma\alpha} = \nu_{\sigma\alpha} m_\sigma n_\sigma (\mathbf{u}_\sigma - \mathbf{u}_\alpha)$ where $\nu_{\sigma\alpha}$ is the collision frequency.

Taking these moments and deriving what are known as the two-fluid equations in plasma physics is a trade-off. On one hand, obtaining a simpler set of equations to solve is valuable, but this simplification is at the expense of losing detail because now we are using average or center of mass velocities instead of the actual velocities. In practice, this means that electron cyclotron motion is lost in the two-fluid picture because the motion occurs on a time scale that is faster than the average velocity.

A.5 Magnetohydrodynamic Theory

Magnetohydrodynamic (MHD) theory is the simplest and most widely used plasma description. As suggested by the name, MHD closely resembles hydrodynamics. The MHD equation of motion and continuity equation are also derived by taking moments of the Vlasov equation. Instead of looking at the electron and ion fluids separately, i.e using the mean electron velocity $\mathbf{u}_e$ and mean ion velocity $\mathbf{u}_i$, all species in the plasma are considered together into the same fluid by taking linear combinations of $\mathbf{u}_e$ and $\mathbf{u}_i$. Current density $\mathbf{J} = \sum_\sigma n_\sigma q_\sigma \mathbf{u}_\sigma$ and center of mass velocity $\mathbf{U} = \frac{1}{\rho} \sum_\sigma m_\sigma n_\sigma \mathbf{u}_\sigma$ where $\rho = \sum_\sigma m_\sigma n_\sigma$ are used as the variables of choice. Thus instead of modeling the plasma as two fluids, the plasma is treated as one single fluid. The final set of governing equations combines a continuity equation with an equation of motion that looks similar to the Navier-Stokes equation and Maxwell's Equations with the addition of the MHD Ohm's Law.

The MHD governing equations are:

$$\frac{\partial \rho}{\partial t} + \nabla \cdot (\rho \mathbf{U}) = 0 \tag{A.11}$$

$$\frac{P}{\rho^{\gamma}} = constant \tag{A.12}$$

$$\rho\left(\frac{\partial}{\partial t} + \mathbf{U} \cdot \nabla\right)\mathbf{U} = \mathbf{J} \times \mathbf{B} - \nabla P \tag{A.13}$$

$$\mathbf{E} + \mathbf{U} \times \mathbf{B} - \frac{1}{n_e e}\mathbf{J} \times \mathbf{B} = \eta \mathbf{J} \tag{A.14}$$

$$\nabla \times \mathbf{E} = -\frac{\partial B}{\partial t} \tag{A.15}$$

$$\nabla \times \mathbf{B} = \mu_0 \mathbf{J}. \tag{A.16}$$

MHD can only be used to understand relatively large-scale phenoma that are slower than the ion cyclotron frequency. Luckily, a huge variety of plasmas can be studied with MHD.

A.6 Simplifying MHD

The most commonly used form of Eqs. A.11 - A.16 is called resistive MHD and it assumes that the $-\frac{1}{n_e e}\mathbf{J} \times \mathbf{B}$ term[1] in Eq. A.14 is negligible. Applying this assumption turns Eq. A.14 into the governing Ohm's Law for resistive MHD

$$\mathbf{E} + \mathbf{U} \times \mathbf{B} = \eta \mathbf{J}. \tag{A.17}$$

The set of equations that describe resistive MHD are the same as the general MHD equations Eqs. A.11 - A.16 except that Eq. A.14 is replaced by Eq. A.17.

Taking the curl of the resistive MHD Ohm's Law (Eq. A.17) and making substitutions using Faraday's Law (Eq. A.15) and Ampere's Law (Eq. A.16) results in an induction equation

$$-\frac{\partial \mathbf{B}}{\partial t} + \nabla \times (\mathbf{U} \times \mathbf{B}) = \nabla \times \left(\frac{\eta}{\mu_0}\nabla \times \mathbf{B}\right). \tag{A.18}$$

Many plasmas are nearly perfect conductors which means that the resistivity η is nearly zero so the $\eta\mathbf{J}$ term in Eq. A.17 and the right hand term in Eq. A.18 become negligible and can be dropped.

[1] Also called the Hall term.

This assumption leads to the ideal MHD versions of the Ohm's Law and Induction Equation

$$\mathbf{E} + \mathbf{U} \times \mathbf{B} = 0 \tag{A.19}$$

and

$$-\frac{\partial \mathbf{B}}{\partial t} + \nabla \times (\mathbf{U} \times \mathbf{B}) = 0, \tag{A.20}$$

respectively.

The set of equations that describe ideal MHD are the same as the general MHD equations Eqs. A.11 - A.16 except that Eq. A.14 is now replaced by Eq. A.19. For a more compactly written form, Eqs. A.14 - A.16 can all be replaced by the ideal MHD Induction Equation (Eq. A.20) which includes all the physics from Faraday's Law (Eq. A.15), Ampere's Law (Eq. A.16), and the ideal MHD Ohm's Law (Eq. A.19).

A key consequence of the ideal MHD Induction Equation (Eq. A.20) is the common "magnetic flux is frozen into the plasma" condition which means that magnetic field lines convect with the plasma itself. The plasma and the magnetic field lines move together as one ensemble in unison through space. This concept is the bedrock of ideal MHD. It is discussed in more detail in Section 2.6.4 of Ref. [1] and is followed by a mathematical proof proving that Eq. A.20 leads to the "flux frozen in" condition.

A.7 Magnetic Reconnection

A corollary of Eq. A.20 is that in ideal MHD, magnetic field lines cannot break. But when the right-hand side of Eq. A.20 is no longer zero, for example if in Eq. A.17 the right-hand side from the resistive term is finite or if the Hall term in Eq. A.14 is non-negligible, then the induction equation says that magnetic field lines can break and reconnect. If this process results in the magnetic field moving to a state of lower energy, this process will happen spontaneously and release energy that comes from the magnetic field itself.

A.8 Dusty Plasmas

The previous sections in this Appendix contain a quantitative introduction to conventional plasmas. In the interest of readability, this introduction to dusty plasmas will be relatively brief and remain qualitative.

A dusty plasma is a conventional plasma with the introduction of a third species. Oftentimes in the laboratory, the third species is a prefabricated plastic sphere of known mass (density) and radius. In the Caltech Water-Ice Dusty Plasma Experiment, the third species are tiny ice grains grown by freezing water vapor. In both of these cases (and with naturally occurring dusty plasmas), the dust grains are much larger and more massive than the ion or electron species.

Dust grains become charged in a plasma environment. If the charging is due to the collisional flux of electrons and ions (as is the case with most laboratory dusty plasmas, including the one at Caltech), the grains will have a negative charge because electrons travel much faster than ions, so the bombarding electron flux will be much greater than the ion flux. If the charging is due to photoionization or radiative decay, the charging of all the grains can be positive instead. The charge on the ice grains in the Caltech experiment will be estimated in Section 7.3 and background on the equations used can be found in Chapter 17 of Ref. [1].

The introduction of the third species and a new mass ratio m_d/m_i gives rise to an enormous amount of new physics whose depth cannot begin to be appreciated with the little amount of space allotted in this Appendix. For example, the regime where nearly all electrons are attached to dust grains leads to a situation very similar to but opposite from a conventional plasma where the heavy particles are now the negatively charged dust grains and the lighter particles are the positively charged ions where $m_d/m_i \neq m_i/m_e$. Much like the ion acoustic wave in a conventional plasma, this situation generates the dusty plasma equivalent: the dust acoustic wave. A unique feature of dusty plasmas arises when the grains become charged enough such that Coulomb repulsion is the dominant force on each grain. In this ordered crystallized regime, many phenomena from solid state physics come alive. The ice grains in the plasma arrange themselves into a crystal lattice structure where instead of having individual atoms at the lattice sites with lattice parameters being measured in Angstroms, there are dust grains at each lattice site with lattice parameters that might be measured in the 100s of μm. Like the lattice wave in solid state physics, this regime in a dusty plasma supports dust lattice waves.

Appendix B

DEBYE SHIELDING IN DETAIL

This Appendix section builds on Appendix A with a discussion of key concepts related to Debye Shielding that are relevant to the statistical acceleration theory presented in Ch. 4.

The derivation of Debye shielding, one of the most fundamental properties of plasmas, involves a logical argument that incorporates certain specific assumptions. When derived using fluid equations, the explanation involves the assumption of a quasi-static equilibrium so that ions and electrons have a Boltzmann density dependence $n(\phi) = n_0 \exp(-q\phi/\kappa T)$. This Boltzmann density dependence is then used in Poisson's equation with addition of a test particle to solve for potential $\phi(r)$. This results in the Debye length λ_D^2 which has the functional dependence

$$\frac{1}{\lambda_D^2} = \frac{1}{\lambda_{Di}^2} + \frac{1}{\lambda_{De}^2} \tag{B.1}$$

where $\lambda_{Di}^2 = \epsilon_0 \kappa T_i / ne^2$ and $\lambda_{De}^2 = \epsilon_0 \kappa T_e / ne^2$. If the ions are much colder than the electrons as is often the case, then $\lambda_{Di}^2 \ll \lambda_{De}^2$, so one would expect from Eq. B.1 that the ion term would dominate. However, this is not true when considering shielding of electron-related phenomena because electrons move much faster than the ions and ions cannot move fast enough to shield an electron. This suggests that Debye shielding only involves particles that have a thermal velocity exceeding the velocity of the particle being shielded. This rough concept is demonstrated in more detail in Section 9.2 of Nicholson [134] where it is shown that a test particle moving much faster than the thermal velocity has no Debye shielding. This indicates that superthermal particles have greatly reduced Debye shielding since they can only be shielded by faster particles and there are relatively few particles moving faster than a given superthermal particle.

The deflection of a test particle with charge q_T scattering off of a field particle with charge q_F is solved in the center of mass frame and results in the Rutherford scattering formula

$$\tan\left(\frac{\theta}{2}\right) = \frac{q_T q_F}{4\pi\varepsilon_0 b \mu v^2} \tag{B.2}$$

where θ is the scattering angle, b is the impact parameter, μ is the reduced mass, and v is the relative velocity. For grazing collisions where $\theta \ll 1$, this gives

$$\theta = \frac{q_T q_F}{2\pi\varepsilon_0 b\mu v^2} \tag{B.3}$$

and the impact parameter for scattering by more than $\pi/2$ is

$$b < b_{\pi/2} = \frac{q_T q_F}{4\pi\varepsilon_0 \mu v^2}. \tag{B.4}$$

In the center of mass frame, a collision simply rotates the velocity so if the initial velocity is in the z direction, the z component of the velocity after collision is $v\cos\theta$ and the change in velocity from a grazing collision is $\Delta v = v\cos\theta - v = -v\theta^2/2$. Since θ^2 scales as $1/b^2$, the average of b^2 over a circular area concentric with the scattering center involves an integral of the form $\int db/b$, so it is singular. The singularity is removed by arguing that Debye shielding screens out the potential for distances larger than the Debye length. The question now arises as to what Debye length is to be used. The reduced mass test particle is not a true particle; it is rather a fictitious particle that involves properties of both the test and field particles via the formula defining μ. The scattering center is also not a true particle since it does not move. Thus, the concept of Debye shielding which was defined in the lab frame does not really make sense in the center of mass frame, and yet it is used in a somewhat vague way where it is sometimes attributed to be a property of the reduced mass test particle and sometimes a property of the scattering center. This seems to be fine when the test particle is moving at slow velocities so all particles have the same shielding, but there is ambiguity about whether one should use the shielding of the test particle or the shielding of the field particle since these shieldings differ. In some treatments, one mentally moves to the frame of the reduced mass test particle and imagines that it has a strapped-on bulls-eye of radius λ_D and that there is a flux of field particles impacting the bulls-eye with a flux $\Gamma = nv$ where v is the relative velocity, but in other treatments, the bulls-eye is imagined to be strapped to the field particle and one makes an ensemble average over many possible test particle trajectories. In the former case, the Debye length would be that of the test particle while in the latter it would be the Debye length of the field particle.

Consider a circle of radius λ_D centered on a field particle so this circle has area $\sigma_D = \pi\lambda_D^2$; this is not yet a scattering cross-section, but is a physically sensible quantity. The average value of θ^2 over small-angle collisions within this circle is

$$\left\langle \theta^2 \right\rangle = \frac{1}{\pi\lambda_D^2}\int_{b_{\pi/2}}^{\lambda_D} \theta^2 2\pi b db = \frac{2\pi}{\pi\lambda_D^2}\left(\frac{q_T q_F}{2\pi\varepsilon_0 \mu v^2}\right)^2 \ln\Lambda \tag{B.5}$$

where $\Lambda = \lambda_D/b_{\pi/2}$. The mean free path for small-angle collisions associated with hitting these σ_D circles is

$$l_D = 1/(n_T\sigma_D)\ . \tag{B.6}$$

Because $\left\langle\theta^2\right\rangle$ is the average of small quantities, $\left\langle\theta^2\right\rangle$ must be small, so let $\left\langle\theta^2\right\rangle = 1/p$ where p is a large number. In order to have a large angle scattering, the particle would have to make p collisions with a Debye sphere, and it would have to travel a distance pl_D. Thus, the mean free path for the cumulative effect of small angle collisions making a large angle collision is $l_{eff} = pl_D = p/(n_T\sigma_D)$, so the effective cross section for making a large angle collision is

$$\begin{aligned}\sigma_{eff} &= \sigma_D/p \\ &= \sigma_D\left\langle\theta^2\right\rangle \\ &= 2\pi\left(\frac{q_Tq_F}{2\pi\varepsilon_0\mu v^2}\right)^2\ln\Lambda.\end{aligned} \tag{B.7}$$

The probability of not hitting *any* Debye spheres on traveling a distance l_{eff} is $\exp(-l_{eff}/l_D) = \exp(-p)$. This causes a problem because p is large and in order to be completely collisionless, the particle must avoid hitting any Debye spheres. This suggests that σ_{eff} is not quite like a normal cross-section because a normal cross-section has the property that a particle either hits or does not hit the cross-section after traveling some distance whereas here a particle appears to always be hitting it. For example, suppose $p = 10^6$, so a particle would have to travel a million times l_D to change its trajectory by 90°, but if it traveled only $100l_D$, the particle would not have a 10^{-4} chance of scattering by 90°, but rather would have scattered by some angle much smaller than 90°.

The above picture breaks down when the test particle is superthermal. It was shown above that for a test particle to scatter by 90°, it must make p collisions with field particles where p is a large number. Each of these p steps involves the test particle colliding with a different field particle and each of these p collisions is considered to be statistically independent. In the Fokker-Planck model of collisions, the $\ln\Lambda$ term is assumed to involve the Debye length associated with the field particles, i.e., Λ is a function of the field particle density and temperature. The picture is visualized as a circle of area σ_D that is like a bulls-eye which gets attached to each field particle. As an example, if there are four field particles in a Debye sphere denoted as A, B, C, and D, the test particle will first collide with A and be scattered by $\left\langle\theta^2\right\rangle$, then with B and be scattered by another $\langle\theta^2\rangle$, then with C and be scattered by another $\langle\theta^2\rangle$, and then with D and be scattered by another $\langle\theta^2\rangle$ to give a total scattering of $4\langle\theta^2\rangle$. However, intrinsic to this argument is that each of A, B, C, and D have their own Debye bulls-eye. This means that the electron at A is at the center of a spherical region depleted of electrons in a spherically symmetric manner, and so are B, C, and D. However, if the separation between A, B, C, and D is less than a Debye length, it is physically impossible for A, B, C, and D to each be at the center of spherical regions that are depleted of electrons. The only way this could happen is to wait some time after the test electron has scattered from A so that A, B, C, and D undergo random motion and re-arrange so that when the test electron interacts with B, B is at the center of a region that is spherically depleted of electrons. Thus, the positions of A, B, C, and D must randomize between encounters with the test particle if each of A, B, C, and D is to be surrounded by a Debye shielding cloud. A sufficiently fast test particle will see A, B, C, and D as being immobile, so during the time that the test particle traverses the shielding cloud surrounding A, particles B, C, and D cannot be considered to be at the centers of some other shielding clouds. The fast test particle must leave the shielding cloud surrounding A before it can undergo another statistically independent scattering. Similarly, if every fast particle were simultaneously surrounded by a Debye sphere, then the interparticle separation between the particles would be approximately λ_D and the density of field particles would be λ_D^{-3} which would give $n\lambda_D^3 = 1$ which is inconsistent with the assumption that $n\lambda_D^3 >> 1$. This reduction in the number of independent scattering events will greatly reduce the amount of scattering experienced by a fast test particle compared to a slow test particle in addition to the reduction associated with speed alone.

Because of these considerations of (i) reduction in Debye shielding of a superthermal particle, (ii) ambiguity of whether to use the test particle Debye length or the field particle Debye length, and (iii) failure to have statistical independence of the field particles interacting with a very fast test particle, it is seen that representation of collisions by an effective cross section σ_{eff} with associated collision frequency υ and mean free path $\lambda = 1/n\sigma_{eff}$ must be considered approximate. However, this approximation and Fig. 3 of Ref. [135] are consistent with the essential concept that a small fraction of an initial cohort of fast particles have much less slowing down than the average slowing down. This small fraction can be considered as the particles that do not collide. In the presence of an electric field, this small fraction of particles accelerate to even higher energies.

Appendix C

D_{INT}

This Appendix section will describe the physical design and construction of D_{int}. At the heart of D_{int} are six Eljen Technology EJ-200 scintillators arranged in a circular pattern with the seventh in the center. Each 1" diameter cylindrical scintillator has a tapered end that couples to its own 10 m long and 2 mm diameter plastic optical fiber that carries scintillated photons to one of seven Hamamatsu H10721 photomultipliers. Each PMT's electrical output is connected via BNC cable to an input channel of the SIS3100 VME.

Figure C.1 shows a schematic of the setup. An X-ray emitted from the jet enters one of the seven scintillators inside D_{int} where it is scintillated into many blue photons. The optical fiber coupled to the back of the scintillator carries the blue photons $\sim$ 10 meters away to photomultipliers which are located inside a shielded metal box. Each PMT outputs an electrical signal to a different channel of the SIS3100 VME data acquisition system.

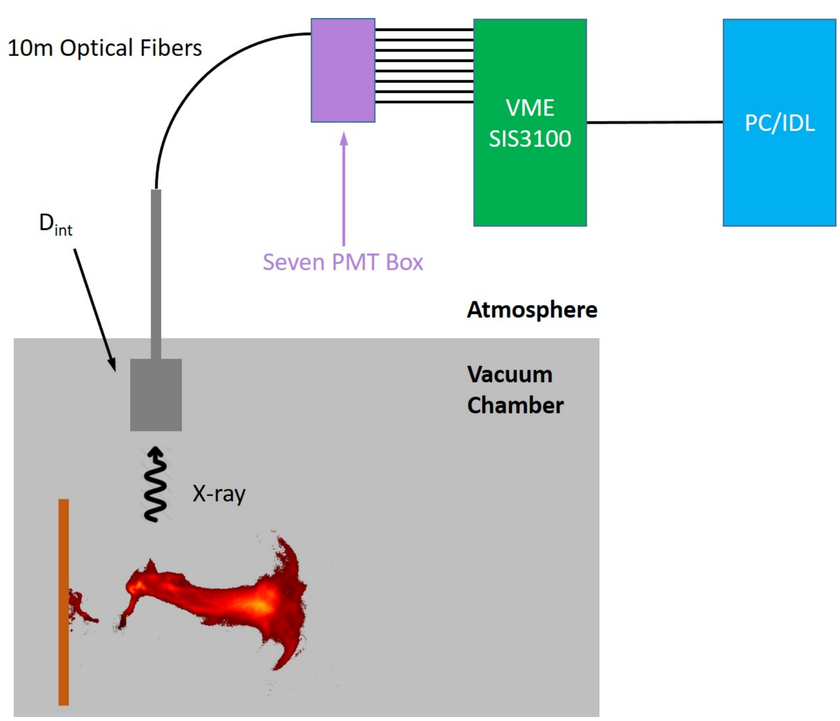

Figure C.1: Schematic diagram of the main components of D_{int}.

C.1 Design and Construction

Figures C.2(a) and (b) and C.3(a) and (b) show Solidworks renderings and actual images of the assembled detector. Numerous iterations of D_{int} were built upon with machining feasibility feedback provided by the campus machine shop before the design was finalized. The main challenge was that we wanted D_{int} to be mounted inside the vacuum chamber closer to the jet without the bottleneck of a 2.75" CF flange. That means that the detector needed to be vacuum-tight and light-tight while passing X-rays into securely held scintillators. Optical fibers coupled to the scintillators inside the detector body need to reach the photomultiplier tubes away from the vacuum chamber. The cutaway in Fig. C.2(b) shows how the scintillators (colored yellow in the image) are mounted inside the main body of the detector.

D_{int} is largely constructed from four custom-fabricated 6061 Aluminum pieces: a front plate, a body piece that holds the scintillators called the *scintillator holder*, a backing piece, and a three foot long 1” diameter round tube. Aluminum was chosen because the same design would have cost triple to be machined from stainless steel instead.

After inserting each scintillator into one of the seven slots in the scintillator holder and coupling them to fibers, the fibers are snaked through the hole at the center of the backing piece and it is attached to the scintillator holder by 12 4-inch 18-8 stainless steel 1/4-20 bolts. There is a circular groove on the scintillator holder side near the perimeter and a large o-ring is sandwiched in the groove between the two pieces. The slits seen cut in the side of the backing piece and the holes on the side of the scintillator holder are there so that any trapped air around the bolts can escape. On the other side, the front plate, seen in Fig. C.3(a) is held onto the main body by 18 18-8 stainless steel vented screws. These screws have holes down their center so that trapped air can escape. The scintillator holder has an o-ring groove and an o-ring around each scintillator slot. A single orange colored kapton sheet is sandwiched between the front plate and the scintillator holder. Clamping the front plate onto the scintillator holder with the kapton sheet sandwiched in between using the 18 screws holds the pressure gradient between vacuum outside the detector in the chamber and atmospheric pressure inside it. The backing piece is designed to be long enough so that the optical fibers coupled to the scintillators can bend with a reasonable radius of curvature inside it, and then travel through the tube into the laboratory and away from the experiment.

Welding the round tube to the designed protrusion on the aluminum backing piece and holding vacuum proved to be a challenge since aluminum is not trivial to weld. The campus welder was not comfortable performing this weld so I had to go into Los Angeles to find someone who would do it. CSM Works did a good job and the detector has been functional ever since. The weld is highlighted in Fig. C.3(b).

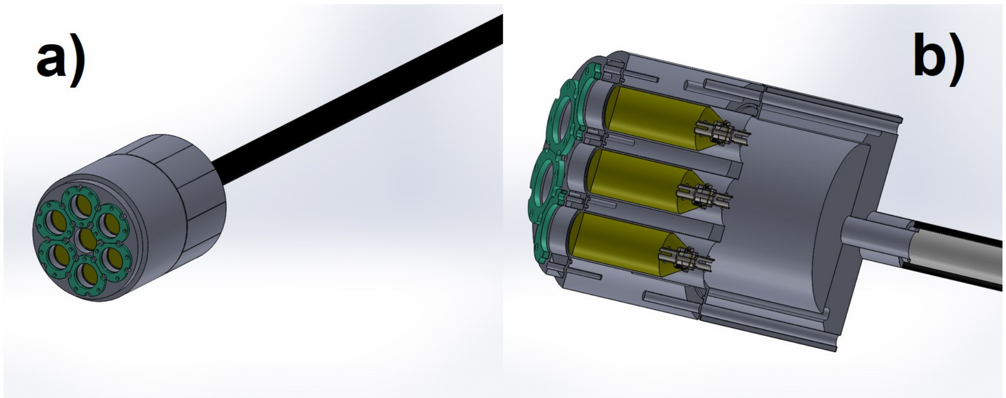

Figure C.2: Drawings of D_{int}. a) is a drawing of the complete detector and b) is a cutaway to show the inside. The yellow cylindrical shapes in b) are the scintillators mounted inside the chassis.

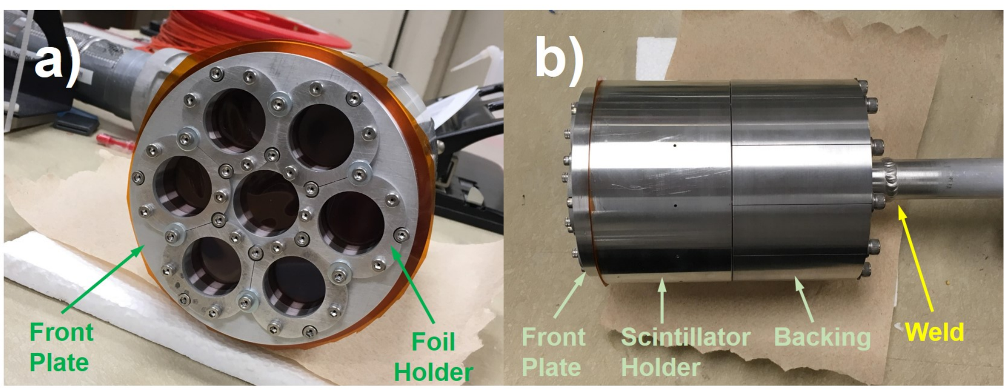

Figure C.3: Images of a constructed D_{int} from the front and side in a) and b), respectively. a) shows the front plate and the foil holders that bolt onto the front plate. The orange color is the kapton window that is sandwiched between the front plate and the scintillator holder. b) shows the four key components assembled.

C.2 Vacuum Chamber Mount

Figure C.4 shows how D_{int} is mounted inside the vacuum chamber. Figure C.4(a) is an inside view showing where D_{int} is located relative to the electrodes and Fig. C.4(b) shows the 2.75" ConFlat to 1" quick connect flange that the 1" diameter tube welded to the backing plate of the detector is mounted through. By loosening the quick connect, the detector can be moved along its axis closer to or farther away from the plasma inside. The shaft collar is there so the detector does not move when it is set in position. Unfortunately, the three-foot stainless steel tube welded to the back of the backing piece makes the assembled detector too large to be mounted from the inside of the chamber with the tube pushed out through the quick connect flange. So the detector has to be assembled inside the vacuum chamber.

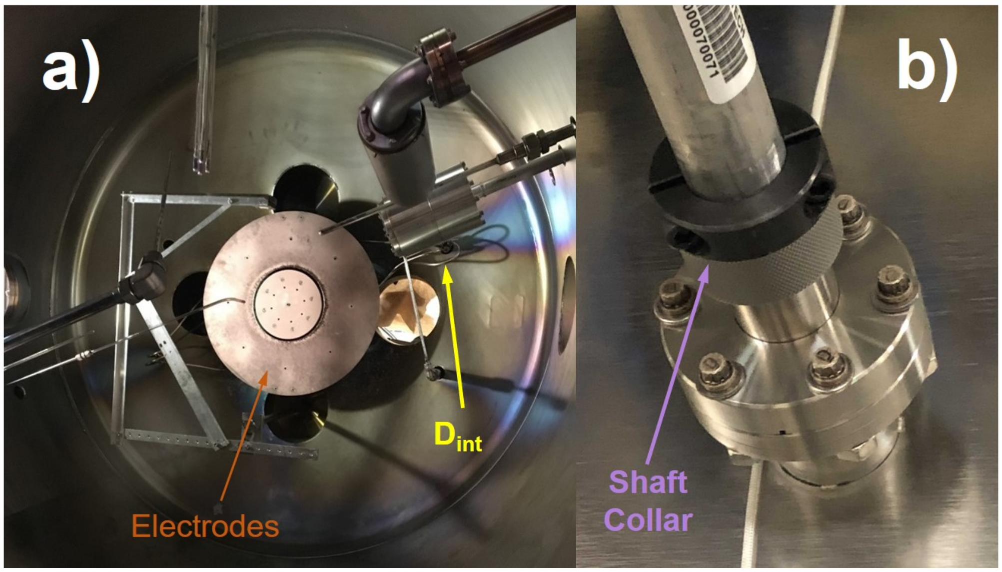

Figure C.4: D_{int} mounted on the vacuum chamber. a) shows an inside the chamber view of where D_{int} is mounted relative to the electrodes. b) shows how the aluminum tube that extends outside the chamber is mounted with a quick connect flange and a shaft collar.

C.3 Electronics Box

Figure C.5 shows the box where the scintillated blue photons are turned into an electrical signal and then sent to the VME. Because the detector has seven channels, there is seven of everything in the box: one for each channel. The photomultipliers are at the bottom of the image coupled to the black optical fibers that shine light on them. There are seven potentiometers that can vary the gain of the photomultipliers independently and seven on-off switches below them on the left. Each PMT is powered by $\sim$ 6 V from four AA batteries in series where a diode is included to reduce the voltage down to the correct 4.5 – 5.5 volt range. At the top of the image are the BNC outputs that take the electrical signals to the VME or fast oscilloscope. This system has time resolution on the order of ns. Figure C.6 shows three sample 662 keV gamma rays from a Cs-137 source.

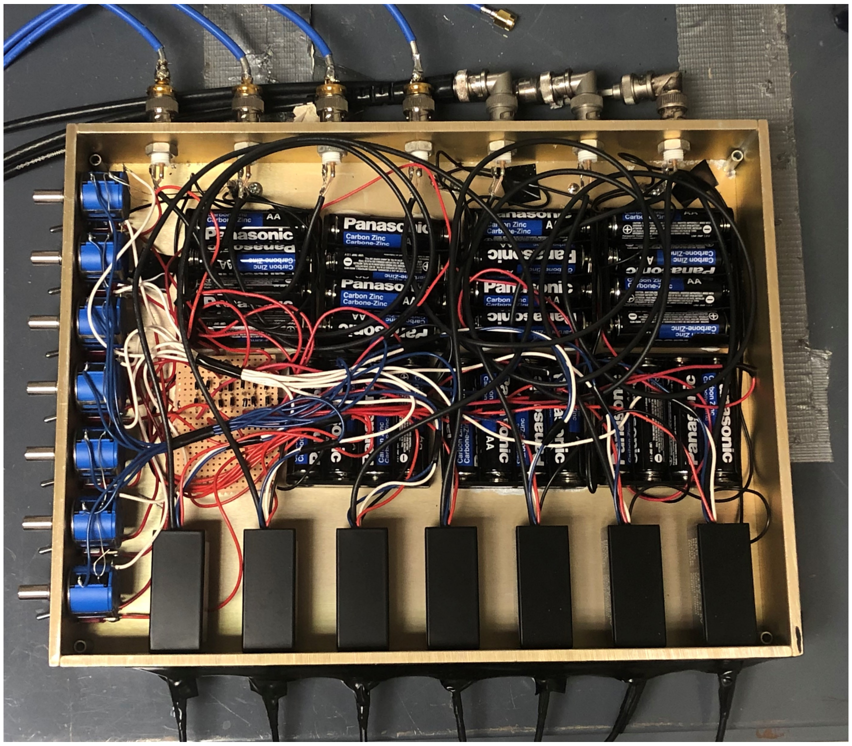

Figure C.5: Photograph of a 9”x12”x1.75” box housing the seven PMTs. The 7 optical fibers at the bottom of the image are each coupled to a PMT. Each PMT is powered by four AA batteries. Each PMT has a potentiometer and individual on-off switch. The BNC connections at the top of the image take the electrical signal from the PMT to the VME or fast oscilloscope to be recorded.

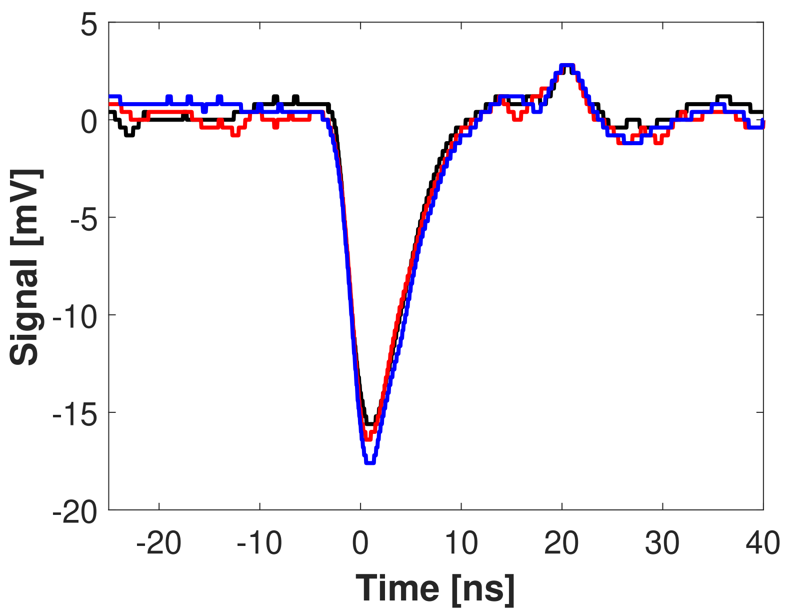

Figure C.6: Three sample 662 keV gamma rays from a Cs-137 source.

Appendix D

LIF HARDWARE

I am particularly proud of this Labview controlled, motorized four-axis tuneable diode laser-induced fluorescence system because I built this system from the ground up and I got to struggle with it mightily before seeing it all come together to work. This TD-LIF system has produced exciting measurements of neutral argon temperatures and flows in the Caltech Dusty Plasma Experiment, but I think the hardware itself is equally exciting. Figure D.1 shows a schematic diagram of the key pieces of the system and how they connect. Broadly speaking, the TD-LIF hardware can be split into four major components: the motorized 3D scanning system, the box that controls and powers the stepper motors, the optical table arrangement, and the PC that controls everything via Labview code.

D.1 Stepper Power Box

Three Nema 23 stepper motors with 100 mm travel provide the linear motion in each dimension for the motorized 3D system and an identical fourth stepper motor moves a barrier so that only one laser beam can shine through the plasma at a time. Figure D.2 shows a photograph of one of these motors. The three motors that move the LIF beams and PMT are denoted as x, y, and z. The fourth motor that moves the separate barrier is denoted as w. These four motors each run on 2 A of current and are powered by the box shown with its top removed in Fig. D.3. The box is wired to operate up to 5 stepper motors simultaneously, but it can be adapted to control up to 8 stepper motors by drilling more holes through the box and adding new XLR connectors for each additional motor.

The key components in the box are the two Peter Norberg four-motor AR-BC4E20EU circuit boards at the bottom. These boards serve as the hardware interface between the Labview program on the PC and the stepper motors. The two boards can handle up to four motors each which limit the maximum number of motors to 8. The boards connect to the PC via USB cable which powers their logic component and serves as the command interface. One nice feature of these boards is that they keep track of the current position of each motor relative to an origin.

Each interface board has access to a single 240W 12V power supply that can provide

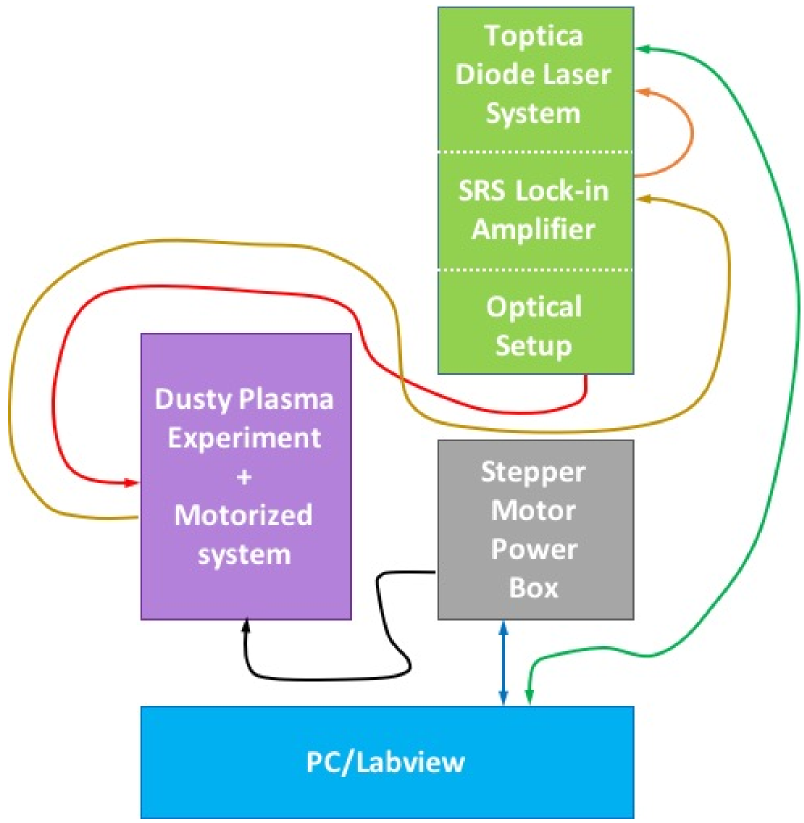

Figure D.1: Schematic of the components of the LIF diagnostic. The PC/Labview interfaces with both the stepper motor power box and the Toptica diode laser system. The stepper motor box controls the motorized system position. The optical setup takes the light from the DL Pro and carries it to the experiment. The SRS lock-in amplifier locks in to the chopper frequency and the locked-in output LIF signal is fed back into the Toptica diode laser where the PC/Labview fetches it.

up to 20 A DC to turn the stepper motors. These extra power supplies are necessary because a computer USB port cannot provide enough power to turn the motors. These power supplies are located directly adjacent (above) to their respective board in Fig. D.3. The two power supplies are powered by standard 120V AC wall power.

The stepper boards output power to four wire stepper motors through five-wire XLR cables which connect to the stepper motors with one of the five wires remaining unused. These cables connect to the bottom set of connections on the left side of Fig. D.3. The top five connectors are three-pin XLR connectors which are wired to the Peter Norberg boards to be used with limit switches. XLR cable is chosen because it is standard and easy to work with. The box has two 90 mm computer fans on the right side that move air through the box to keep everything cool. There are two mesh cutouts on the opposite side where the air can escape.

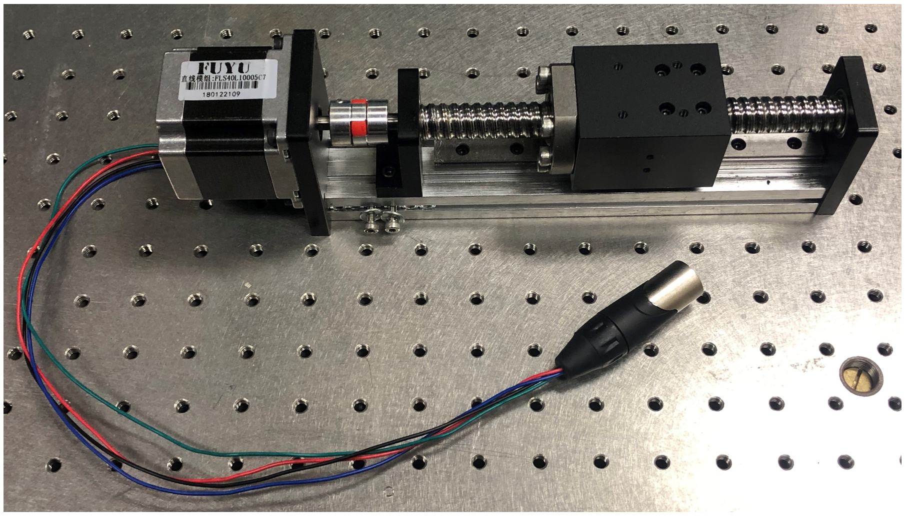

Figure D.2: Photograph of one of the four stepper motors used to automate data collection.

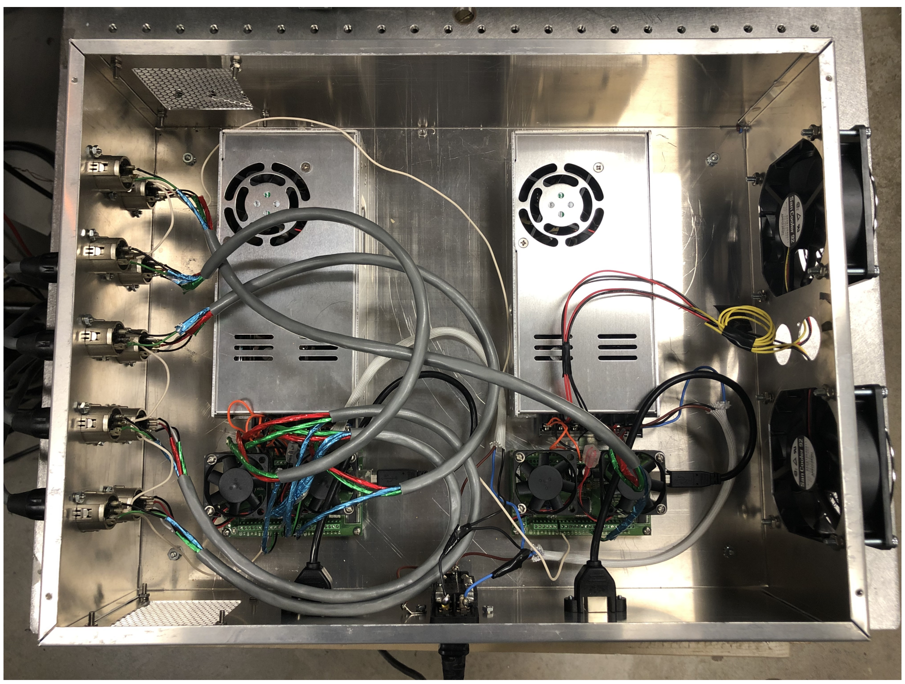

Figure D.3: Photograph of the stepper motor power box. The box contains two Peter Norberg boards and two power supplies. Each board connects via USB to the PC/Labview. The XLR connections on the left side are for limit switches and to power the stepper motors. The fans on the right side are for cooling.

D.2 Motorized 3D System

Three stepper motors are bolted together providing a stage with 100 mm of travel in three independent directions (x, y, z). The actual distance traveled by each motor when performing an LIF scan on the experiment is much smaller than this because the experiment is small. The Peter Norberg boards keep track of position relative to an origin which makes performing a scan easy. The boards work by microstepping the stepper motors. It works out that 1600 micro steps on the Peter Norberg board corresponds to 2.5 mm of actual motion.

A 50 cm rigid rail is bolted onto the stage of the stepper motor system. The optical fibers carrying light from the diode laser are mounted at each end of the rail and oriented such that the light shines through the vacuum chamber onto the other fiber. Neutral density filters are mounted next to each optical fiber so that the beams can be attenuated to negate power broadening. The PMT that detects the LIF photons is also mounted onto the same rail system in between the fiber mounts so that everything moves together.

Figure D.4 shows a photograph of the motorized system with the x, y, and z motion directions clearly marked. The vacuum chamber is in the middle and the LIF system is built so that it fits around the existing chamber. The red arrows on either side of the chamber show how the chopped light shines into the plasma and the purple arrow perpendicular shows where the LIF photons that PMT detects come from.

D.3 Optical Table Arrangement

The optical table arrangement that houses the Toptica DLC Pro, the Stanford Research Systems SR 830 Lock-in Amplifier, Toptica DL Pro laser-heads 1 and 2, and the actual optomechanical hardware is shown in Fig. D.5. The beam emitted from the DL Pro laser-head passes through two 50/50 beam splitters. The first 50% split beam shines into a High Finesse WS-6 wavemeter that interfaces with the PC. The main beam, now also at 50% intensity, travels through a second 50/50 beam splitter. Both of these 25% beams pass through a mechanical chopper and are then coupled to optical fibers which carry the chopped light to one of the optical fibers whose other ends are mounted on the motorized 3D system. Even at 25% beam power, neutral density filters are necessary to eliminate power broadening.

In between the mechanical chopper and the optical fibers is the fourth stepper motor. A physical barrier is affixed to this motor and the motor moves the barrier to the left and the right. Moving the barrier allows only one of the two beams to pass by into its optical fiber while keeping the other beam blocked.

The LIF signal emitted from the plasma is collected by the PMT that is oriented perpendicular to the laser beam path. The signal is transmitted into a Stanford

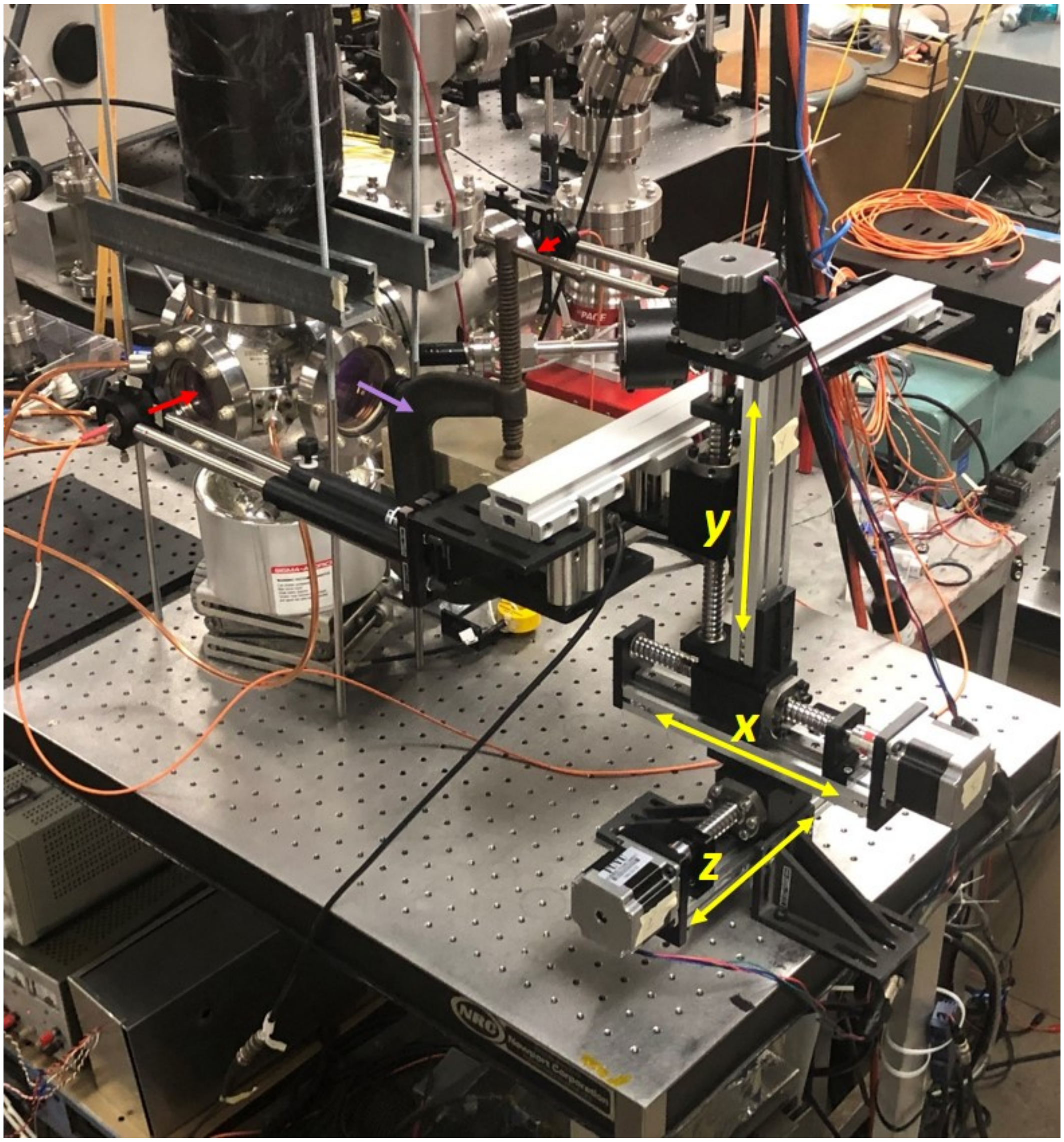

Figure D.4: Photograph of the dusty plasma experiment and the motorized LIF diagnostic. The red arrows represent the laser light being directed through the plasma. The purple arrow denotes the LIF photons that the PMT will detect. The x, y, and z stepper motors are labeled and the rigid structure mounted on them is apparent.

Research Systems SR830 lock-in amplifier which locks into the frequency from the mechanical chopper and pulls the LIF signal out of the noise. The lock-in amplifier outputs the cleaned up LIF signal into an input channel on the Toptica DLC Pro laser controller which can then plot and save LIF signal amplitude as a function of piezo voltage [1].

[1] Frequency and wavelength are related non-trivially to piezo voltage

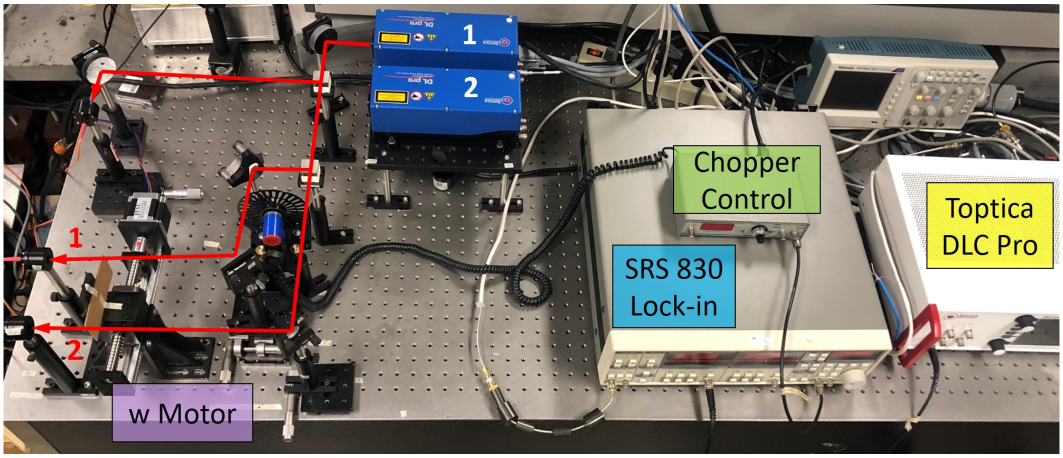

Figure D.5: Photograph of the optical table with DL Pro laser-heads 1 and 2 labelled in white. The bold red line shows the laser path through the optics. The *w* stepper motor moves the barrier in front of optical fibers 1 and 2 to allow only one beam to pass. On the right is the Toptica DLC Pro laser controller, the SRS 830 lock-in amplifier, and the mechanical chopper controller.

D.4 Labview Program

The final piece of the puzzle that ties everything together is the Labview program on the PC. The Labview program moves the motorized 3D system shown in Fig. D.4 into place using the Peter Norberg hardware interface. Once the diagnostic is in place, the Labview program moves the barrier on the *w* stepper motor to allow only one beam to excite the LIF transition in the plasma. The scanning laser records LIF signal as a function of piezo voltage coming out of the lock-in amplifier. The Labview program then interfaces with the Toptica DLC Pro via ethernet cable to save the spectrum. Then the *w* motor moves the barrier to allow the other beam to shine and the Labview program saves the spectrum. This repeats. After 30 saved scans, the Labview program instructs the 3D motorized system to move the main diagnostic to a different position and the process repeats.